



सत्यमेव जयते

**INDIAN AGRICULTURAL
RESEARCH INSTITUTE, NEW DELHI**

I.A.R. I.6.

GIP NLK—H-3 I.A.R.I.—10-5-55—15,000

CANADIAN JOURNAL OF RESEARCH

VOLUME 27

1949

SECTION A



CANADA

Liaithgow Library.
Imperial Agricultural Research Institute
New Delhi.

49426

Published by the

**NATIONAL
RESEARCH COUNCIL
of CANADA**

Canadian Journal of Research

Issued by THE NATIONAL RESEARCH COUNCIL OF CANADA

VOL. 27, SEC. A.

JANUARY, 1949

NUMBER 1

SOME QUALITATIVE RESULTS ON THE ELECTRIFICATION OF SNOW¹

BY D. C. PEARCE² AND B. W. CURRIE

Abstract

This paper reports on observations of the electrical charges on falling and drifting snow, and gives the results of laboratory experiments designed to determine the relative importance of possible charge-producing mechanisms in the atmosphere when snow and ice crystals are present. These mechanisms include impacts of snow particles on one another, melting of snow as it falls, and condensation of water vapor and formation of rime on falling snow. Apparently a large fraction of the snowflakes falling during the cold part of the winter in Saskatchewan has a charge less than 2×10^{-4} e.s.u. per flake. During blizzards the snow particles blowing along or just above the hard surface of the drifted snow carry a net negative charge and the air at the 1 m. level has positive space charge densities that are from 10 to 100 times the normal, positive space charge density. Very large charge separations can occur when a snow surface is eroded by an air blast and when snow is blown against snow and metal surfaces, a resultant negative charge appearing on the heavier particles and the corresponding positive charge on either very small ice particles or ions. This charge-producing mechanism is most effective at high air velocities and at low temperatures. The melting of newly fallen snow under conditions favorable to the escape of air bubbles does not show a charge separation. Condensation of water vapor and formation of rime on snow surfaces result in only very small charge separations for the conditions readily obtained in laboratory experiments.

Introduction

Large, and sometimes rapid, separations of electrical charges are known to occur in the atmosphere when snow particles are present, and when the presence of snow particles is surmized. Steady streams of sparks can be drawn from the lead-in wires to radio receivers and sometimes from stoves and other metal objects inside buildings when they are connected electrically to objects exposed to blizzards (3). On such occasions, positive electric fields (corresponding to a negatively charged earth and a positively charged atmosphere) as high as 10,000 v. per m. have been measured at levels close to the earth's surface (7, p. 62). Electrical discharges to the air from an aircraft that is flying through clouds of snow often make radio reception on the aircraft either difficult or impossible. It is generally agreed that the upper part of thunder clouds consists of ice crystals and that these ice crystals are required for the formation of raindrops (1). Since lightning discharges

¹ Manuscript received in original form July 14, 1948, and, as revised, October 28, 1948.

Contribution from the Department of Physics, University of Saskatchewan, Saskatoon, Sask.

² Holder of a Bursary under the National Research Council of Canada; now on the staff of the National Research Council of Canada.

begin at about the same time as the raindrops start to fall, the possibility exists that the ice crystals are a factor in the development of the large electric fields required for the discharges.

Practically all investigators in this field have assumed that the snow rather than some associated meteorological condition is essential to the charge-producing mechanism. Starting with this assumption, a number of different physical processes by which the charges may be produced and then separated have been suggested, although both observational data from the atmosphere and experimental data from the laboratory in support of these suggestions are either lacking or inconclusive. They include, (*a*) small-scale separations of charges due to impacts of snow particles on one another that are followed by large-scale separations due to differential gravitational and turbulent actions on the charged particles; (*b*) escape of charged air bubbles from snow particles as they melt on their way to the ground; (*c*) condensation of water vapor on snow particles with the particles acquiring charges of a sign different from that of air, the fall of the particles giving the large-scale separation; and (*d*) formation of rime on snow particles, the fog particles that constitute the rime having charges predominantly of one sign and the large-scale separation taking place as in (*c*). Obviously, (*a*) is the only process that is applicable to all the aforementioned cases of charge separation, (*b*), (*c*), and (*d*) playing no effective part in the electrical phenomena of blizzards.

Process (*a*) was suggested originally by Simpson (8) as a probable explanation of the large electric fields that he had observed in Antarctic blizzards. Recently, he has described the process in greater detail, and indicated its possible application to thunderstorm electricity (9). Essentially, a resultant negative charge should appear on snow particles after impacts with one another, the equivalent positive charge appearing on either small ice particles or ions that can be carried upward by air currents or left behind as the heavier particles fall. The few sets of observations that have been made on blowing snow are either contradictory or limited to one level in the atmosphere (9, 10, 11, 12). Laboratory experiments to see if snow particles charge by impact have apparently never been made.

Process (*b*) has been demonstrated for ice from distilled water that had been rapidly frozen (4). Air, drawn from above the melting ice, was charged owing to the escape of small, charged air bubbles that had been entrapped in the ice. Evidence does not exist that this process occurs as snow particles melt.

Processes (*c*) and (*d*) have been demonstrated in laboratory tests with frost and rime formations on metal and ice surfaces (2, 5, 13). The physical conditions involved in the observed electrifications are uncertain. In addition, no direct evidence exists that a corresponding electrification occurs on snow particles or surfaces.

Winter weather conditions in the Prairie Provinces of Canada are particularly suitable for the examination of these processes. Falls of light, fluffy snow that is readily drifted by the wind occur at frequent intervals. Occasionally the drift reaches blizzard proportions, when the air is filled to a height of 100 ft. or more with flying particles of snow. In addition, snow that has not been modified by some melting either on its way to the surface or at the surface is available for experimental work during at least three months of the year.

Process (a) was investigated by measuring the charges on individual snowflakes as they fell to earth, and the resultant charges during blizzards on snow blowing along or immediately above hard-packed drift snow and on snow particles and ions at the 1 m. level. Additional information on this process was obtained by eroding snow surfaces with an air blast and by blowing air through and over snow surfaces and then measuring the charges that were developed. Process (b) was tested by melting newly fallen snow under conditions similar to the ones that give a charge when ice is melted. Processes (c) and (d) were tested by drawing saturated air and air containing fog particles past blocks of snow and measuring the charges acquired by the snow.

Experimental

Charges were measured by means of a Lindemann electrometer, its portability and the ease with which its sensitivity could be changed making it convenient for the work on snow. In addition to all the usual precautions to avoid spurious effects due to stray and contact potentials, special care was taken to prevent condensation of moisture on insulators at low temperatures, the moisture coming mostly from the observer's breath. Wherever artificial heat could not be used for this purpose, ceresin wax proved a much better insulator than other materials. Where a low capacity was not a vital consideration, coaxial cable was used to connect experimental equipment to the electrometer.

Charges on Falling Snow

The snow receiver, shown in Fig. 1, was essentially a Faraday chamber with an opening at the top into which the snow could fall. It was supported by a cylindrical block of sulphur that was wound with several turns of resistance wire through which a current was passed to keep the surface of the sulphur dry. Both the receiver and the lead to the electrometer were shielded from the earth's electric field and other stray fields by grounded, metallic casings. The receiver was mounted on the roof of a low hut that was so located that the turbulence about neighboring buildings would not appreciably affect the representativeness of the catch. The receiver was also surrounded by a shield of heavy cotton to minimize the effects of turbulence due to the receiver itself.

Observations of the charges on individual snowflakes and ice crystals were made during nine storms in December, 1947, and January, 1948, the air

temperatures varying from a low of -2°F. to a high of $+22^{\circ}\text{F.}$, and the wind velocities from a low of 7 m.p.h. to a high of 24 m.p.h. Charges as low as 2×10^{-4} e.s.u. were detectable. Visual observations of the snow entering

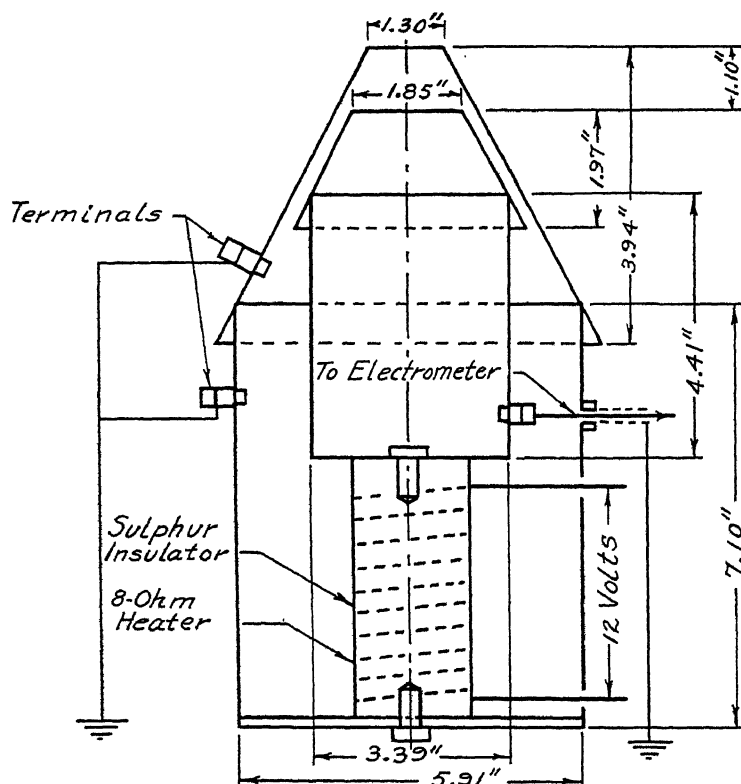


FIG. 1. Receiver for measuring the electrical charges on snowflakes.

the receiver, as the charges were measured, showed that a very large number of the particles were neutral or had charges less than the detectable value. For the particles with charges that could be measured, the average charge was $+9 \times 10^{-4}$ e.s.u. The maximum observed charge on a single flake was $+4.5 \times 10^{-2}$ e.s.u. During each storm, both positively and negatively charged particles were observed, the ratio of the former to the latter being equal to 1.9 (particles with charges below 2×10^{-4} e.s.u. being neglected). A preponderance of negatively charged flakes occurred on one occasion when the wind velocities were high and the possibility existed that particles swept upward from the roof of the hut were entering the receiver.

Charges on Drifting Snow

For snow blowing along the surface, condenserlike cups were placed in metal pails with small openings in their lids so that snow could fall into the cups. The pails were placed in small excavations on the leeward sides of

drifts, so that practically all the snow falling into a cup had been wind driven and only in contact with snow and air. Any charge transferred to the cup by the snow remained as a bound charge until it either leaked through the dielectric to the outer plate, or was neutralized by connecting the inner plate to ground. To make a measurement, a cup with its catch was placed on a metal plate connected to the electrometer. The inner plate of the cup was then grounded. This caused an electrometer deflection proportional to the charge on the snow. The observations on all except one occasion showed that the drift snow (caught in this way) had a negative charge. The exception occurred when the air temperature was above 32° F. and the snow temperature was below 32° F. Although the observed magnitudes of the charges varied greatly because of the changing intensity of the drift, they indicated an increasing separation of charge with increasing wind velocity, and with decreasing temperature.

In order to measure the charges at the 1 m. level in the drift, the device shown in Fig. 2 was used. Air was drawn through it at constant and known rates, snow particles and ions in the air stream being trapped by copper

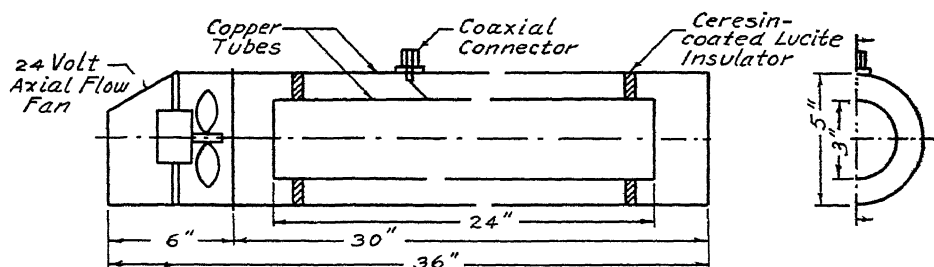


FIG. 2. Device for measuring the space charge density in the air. Copper turnings placed in the inner tube were used to trap ions and ice particles in the air.

turnings inside the inner copper tube. On occasion, the larger particles were removed from the air stream by placing either cheesecloth or metal screens over the end of the electrostatic shield. The tube was mounted with its axis horizontal and at a height of 1 m. The space charge density was computed from the charge acquired by the tube and electrometer in a known time and the rate of flow of the air. Since the space charge density in the atmosphere is normally positive, numerous measurements were made at different times and under various weather conditions to determine the values that occur when snow is not drifting.

The average space charge density at Saskatoon during daylight hours for a period from the third week of February to the second week of April was $+ 3.6 \times 10^{-8}$ e.s.u. per cm.³ In computing this average, all observed values when either ice crystals or fog droplets were visible in the atmosphere and when snow was drifting were excluded. As soon as the surface snow started to drift or falling snow was broken as it hit the surface and then started to drift, the space charge density became strongly positive, values as high as

$+ 10^{-5}$ e.s.u. per cm.³ occurring with moderate drift. With very strong gusts the rate of charging of the collector either decreased or changed its sign temporarily, indicating that the proportion of negatively charged particles entering the collector increased at such times. In addition, there was some indication that the space charge densities were greatest during drifting with the lowest temperatures. The observations with layers of cheesecloth over the open end of the collector showed conclusively that large particles of snow were not responsible for the positive space charge. Similar observations with a metal screen, consisting of a layer of copper turnings between two wire grids, indicated that the positive space charge was not due to a separation of charges by impacts of ice particles on copper with the negative charge being carried through the copper turnings by the air stream.

Electrification by Use of an Air Blast

Qualitative verification of the observations on drifting snow was obtained by eroding the surface of a snow block by an air blast. The snow block was placed on a copper tray, and air at a pressure of 25 p.s.i. and about the same temperature as the snow was directed against its upper surface through a $\frac{1}{4}$ in., grounded brass tube. The charges on the visible particles swept off the block, on air and small ice particles that could be sucked upward from above the eroding snow surface and into the device for measuring space charges, and on the block were measured. The particles swept off the block carried a net negative charge, the air and any small ice particles sucked into the collector carried a net positive charge, and the block was left with a positive charge. The magnitudes of the charges varied directly with the intensity of the erosion and the amount of the snow swept off the block, and decreased with increasing temperature. The positive charge on the block was apparently due to positive ions, or small ice particles with positive charges, that were driven into the air spaces in the snow block by the air blast.

The possibility that an appreciable charge separation could result by friction between air and snow without fracture of the snow or collisions of snow particles was eliminated by the following tests. An air-tight Faraday chamber, except for two quartz tubes by which air could be sucked through the chamber, was connected to the electrometer. The first test consisted of packing the inner end of one quartz tube with snow so that air had to pass through the snow before it could enter the chamber; the second consisted of placing a block of snow inside the chamber so that the incoming air blast struck it at a glancing angle; and the third consisted of placing loose snow in the chamber so that the incoming air was sucked through it before leaving the chamber. Invariably, charging was not detected in any of the tests until the air velocity was increased sufficiently to fracture the snow surfaces or to cause a motion of the snow particles relative to one another. As soon as such a fracture or motion took place, negative charges beyond the range of the electrometer were observed.

Still another series of tests involved the blowing of snow along a copper plate, against a copper plate, and against blocks of drift snow. Small negative charges were observed on both the copper plate and the snow in the first case, the corresponding positive charge apparently being carried away in the air stream. In comparison, very large negative charges were observed on the copper plates, the snow blocks, and the projected snow in the impact tests, the corresponding positive charges again apparently being carried away by the air.

Charges on Melting Snow

A beaker containing either a sample of snow or ice was placed inside a Faraday chamber. Heat sufficient to melt the snow or ice was obtained by pouring warm water into the space surrounding the beaker. A steady stream of air was drawn over the snow or ice by means of an air-pump, the connections to the air-pump and the open air being made by quartz tubes fastened into the walls of the Faraday chamber. Tests of the original observations of Dinger and Gunn (4) on melting ice were made by quickly freezing several grams of distilled water in a beaker, placing the beaker in the chamber, and measuring the charge acquired by the Faraday chamber as the ice melted. Invariably a positive charge was observed. On substituting snow for the ice no charge was detected. Various samples of newly fallen snow, drift snow, and old snow from the bottom of drifts where grains of ice were beginning to form were used.

Charges Resulting from Frost Deposits on Snow

The charging effect of deposits of hoarfrost and of rime on a snow surface was measured by placing a small block of drift snow on an insulated metal plate inside a Faraday chamber, and then drawing either moist air or air filled with small water droplets through the chamber. The charge due to the frost deposits on the snow and the inner surface of the chamber was measured by connecting the chamber directly to the electrometer, and on the snow by connecting the metal plate to the electrometer and grounding the chamber. A small charge (usually positive) appeared during the first few minutes of each test, reached a maximum value, and then disappeared apparently owing to the melting of the frost deposits by the heat transfer to the metal and snow surfaces from the air. However, large variations in the rate of charging and even negative charges were occasionally observed. Presumably these were due to the lack of controlled temperatures, the temperature of the metal and snow surfaces depending on the out-of-door temperatures at the time of the test. In addition, the air temperature was always above 32° F. when it entered the Faraday chamber.

Results

The aforementioned observations indicate that process (a) operates during blizzards, and probably in any atmospheric condition where snow particles can strike one another, or other objects; that process (b) does not operate

when the precipitation is in the form of melting snow; and that processes (c) and (d) can take place when the snow is in the form of an extended surface. The mechanism by which the initial charge separation takes place in process (a) evidently involves fractures of the snow particles, since ordinary frictional interactions between snow and air, and snow and metal, give only very small charge separations. The effectiveness of (a) increases with increasing wind velocity and decreases with increasing temperature. The fact that about twice as many falling snowflakes carry positive charges as negative charges is unfavorable to the view that process (a) operates in thunderstorms. Although the highest wind velocity (24 m.p.h.) at which charges were observed on falling snowflakes was much smaller than velocities occurring in thunderstorms, the increased turbulence close to the surface must have greatly increased the probability of collisions. Since a preponderance of negatively charged flakes was not observed, it is likely that the particles in a snow cloud either do not collide with one another or do not collide with sufficient relative velocities to cause charge separation.

Acknowledgment

This investigation was supported in part by a grant from the National Research Council of Canada.

References

1. BERGERON, T. *Mémoires de l'Union Géodésique et Géophysique Internationale*, Lisbon. 1933.
2. CLAY, J. and KRAMER, C. *Physica*, 13 : 508. 1947.
3. CURRIE, B. W. Unpublished correspondence with residents of Saskatchewan.
4. DINGER, J. E. and GUNN, R. *Terr. Magn. Atmos. Elec.* 51 : 477. 1947.
5. FINDEISEN, W. *Meteor. Z.* 57 : 201. 1940.
6. KÄHLER, K. and DORNO, C. *Ann. Physik*, 77 : 71. 1925.
7. SCHONLAND, B. F. J. *Atmospheric electricity*. Methuen & Co. Ltd., London. 1932.
8. SIMPSON, G. C. *British Antarctic Expedition 1910-1913*. Vol. 1, *Meteorology*. Harrison & Sons, Ltd., London. 1921.
9. SIMPSON, G. C. *Quart. J. Roy. Meteor. Soc.* 68 : 1. 1942.
10. STÄGER, A. *Ann. Physik*, 76 : 49. 1925.
11. STÄGER, A. *Ann. Physik*, 77 : 225. 1925.
12. SVERDRUP, H. U. *Carnegie Inst. Wash. Pub.* 175 (Vol. 6, p. 425). 1927.
13. WOLF, F. *Naturwissenschaften*, 31 : 223. 1943.

Canadian Journal of Research

Issued by THE NATIONAL RESEARCH COUNCIL OF CANADA

VOL. 27, SEC. A.

MARCH, 1949

NUMBER 2

SPECIFIC HEATS OF MANGANESE AND BISMUTH AT LIQUID HYDROGEN TEMPERATURES¹

BY L. D. ARMSTRONG AND H. GRAYSON-SMITH

Abstract

New measurements of the specific heats of manganese and bismuth in the temperature range 14° to 22° K. are reported. The specific heats of these metals are compared with theory. In both cases the approximate theoretical formula

$$C_v = C_D(T/\Theta) + AT,$$

where $C_D(x)$ is the Debye function, is accurately obeyed over the limited temperature region concerned. However, comparison with measurements at other temperatures shows that this may lead to erroneous conclusions. For manganese a precise conclusion is not possible, and it is estimated that the electronic specific heat coefficient A lies between 0.0035 and 0.0040, while Θ varies with temperature from 365 to 390 degrees. For bismuth it is concluded that the electronic specific heat is negligible. This permits an accurate determination of Θ , and it is found that the variation of Θ with temperature is remarkably similar to that predicted by Blackman for a simple cubic lattice.

Introduction

The investigation to be reported here is part of a program of research on the specific heats of metals, and is a continuation of the work of Elson, Grayson-Smith, and Wilhelm (4) on the specific heat of manganese.

According to the approximate theoretical treatment (8, Chaps. I and IV) the specific heat at constant volume of a metal should be given by

$$C_v = C_D(T/\Theta) + AT. \quad (1)$$

The first term represents the vibrations of the crystal lattice, where $C_D(x)$ is the Debye specific heat function, and Θ is the Debye characteristic temperature. The second term represents the contribution of the conduction electrons, which is linear in T except at very high temperatures. For low temperatures, $T \ll \Theta$, Equation (1) reduces to

$$C_v = 464(T/\Theta)^3 + AT \text{ cal. per mole per deg.} \quad (2)$$

Equations (1) and (2), with constant Θ , are derived on the assumption that the lattice vibrations have a frequency distribution given by the function

$$q(\nu) = b\nu^2, \quad (3)$$

as for a continuous medium in which the velocity is independent of frequency. Blackman (2, 3) has examined in detail the vibration spectra of some of the common crystal lattices, and has shown that the approximation of Equation

¹ Manuscript received August 30, 1948.

Contribution from the McLennan Laboratory, University of Toronto, Toronto, Ont.

(3) is unsatisfactory in many cases. This causes deviations from the Debye formula, and it has become customary to take these into account by treating Θ as a function of temperature. For example, Blackman has shown that the curve of $\Theta(T)$ against T may have the form shown in Fig. 1, for a simple cubic lattice with certain assumed values of the interatomic forces.

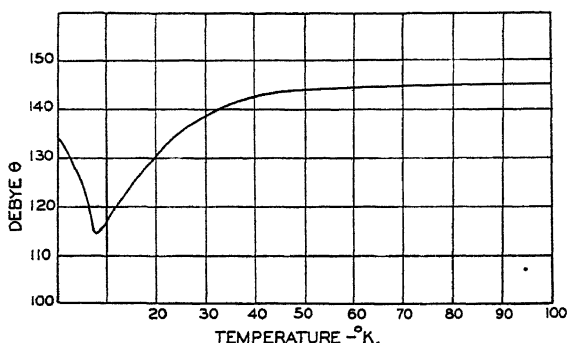


FIG. 1. The Debye constant Θ as a function of temperature for a simple cubic lattice (after Blackman).

For comparison with experiment a useful theoretical approximation for the electronic specific heat is (8, p. 181).

$$AT = 3.61 \times 10^{22} (m/\alpha) n^{1/3} V^{2/3} T, \quad (4)$$

where n is the number of conduction electrons per atom, and V is the atomic volume. m/α is the "effective mass", that is, the average inertial mass as determined by the quantum-mechanical relation between the energies and momenta of electron-waves moving through the crystal lattice. A contribution of the form (4) is expected from each unfilled electronic energy band; where the band is nearly filled, n is the number of unoccupied "holes". For a monovalent metal, assuming $\alpha = 1$, A is of order 10^{-4} cal. per mole per deg.², but much larger values can be obtained for metals which have overlapping energy bands. This is the case for the transition metals, where large values of the electronic specific heat are attributed to unoccupied holes in the low-lying d -band.

Method

The apparatus and method used were identical with those described by Elson *et al.* (4). The manganese was in the form of a fine powder. It was believed to be of high purity, but an analysis was not available; it may have contained a certain amount of oxide owing to the large proportion of surface exposed. For the measurements, 44.188 gm. of the powder was compressed into the calorimeter. The bismuth was Hilger spectroscopic material, with a purity of 99.998%. It was melted in vacuum to the approximate shape, and machined to fit tightly into the tapered calorimeter chamber. The mass of the sample was 56.258 gm.

The temperatures were determined by the same constantan resistance thermometer as used by Elson. This thermometer has a nearly linear resistance-temperature curve over the range concerned, with an average increase of resistance of about 0.07 ohm per deg. Owing to the excellent thermal contact within the calorimeter, and the small temperature intervals used (about $\frac{1}{2}^{\circ}$), the cooling curves were nearly straight lines, and the corrected temperature rise could be calculated with ease.

The quantity measured is the specific heat at constant pressure, but the correction to constant volume is negligible at the temperatures concerned, and the measured values may be compared directly with the theoretical formulae.

Manganese

The measurements for manganese are given in Table I, and the experimental values of the specific heat are shown graphically in Fig. 2. Included in the graph are the values given by Elson *et al.* (4), which are about 2% lower than the present measurements. The scattering of the individual values is appreciably less for the present measurements, and it is believed that more time

TABLE I
SPECIFIC HEATS OF MANGANESE

Run No.	Temperature, degrees Kelvin	Time of heating, sec.	Change in temperature, degrees Kelvin	Total heat capacity, Cal./°K.	Calorimeter heat capacity, Cal./°K.	Sample heat capacity, Cal./°K.	Specific heat $C_p = C_v$, Cal./mole/°K.
1	16.24	11.63	0.5180	0.1581	0.0745	0.0836	0.1039
	17.07	12.31	0.4878	0.1747	0.0878	0.0869	0.1080
	17.65	12.58	0.4609	0.1892	0.0973	0.0919	0.1143
	18.08	14.15	0.4932	0.1984	0.1046	0.0938	0.1166
	18.43	16.12	0.5341	0.2092	0.1108	0.0984	0.1224
1	18.62	13.89	0.4522	0.2130	0.1143	0.0987	0.1228
	18.92	14.48	0.4497	0.2232	0.1199	0.1034	0.1287
	19.25	15.28	0.4551	0.2330	0.1263	0.1067	0.1327
	19.53	15.62	0.4492	0.2413	0.1320	0.1093	0.1398
	19.83	16.23	0.4499	0.2507	0.1384	0.1123	0.1359
1	20.14	16.97	0.4538	0.2598	0.1451	0.1147	0.1426
	20.55	15.65	0.4868	0.2750	0.1546	0.1204	0.1497
	20.80	13.97	0.4213	0.2836	0.1670	0.1229	0.1528
	21.14	15.76	0.4541	0.2969	0.1697	0.1272	0.1582
	21.39	16.26	0.4558	0.3052	0.1750	0.1302	0.1619
1	21.32	15.46	0.4385	0.3018	0.1733	0.1270	0.1590
	22.02	16.68	0.4460	0.3205	0.1974	0.1331	0.1655
	22.16	16.20	0.4077	0.3403	0.2024	0.1379	0.1715
	22.48	15.35	0.3717	0.3540	0.2141	0.1399	0.1740
2	15.52	9.15	0.4525	0.1418	0.0636	0.0782	0.0973
	16.34	10.14	0.4530	0.1570	0.0745	0.0825	0.1026
	16.81	10.89	0.4502	0.1697	0.0835	0.0862	0.1072
	17.29	11.72	0.4538	0.1811	0.0914	0.0897	0.1115
	17.64	12.34	0.4563	0.1892	0.0972	0.0920	0.1143

and care in making the measurements, and a more careful interpretation of the cooling curves, have resulted in improved accuracy.

The solid curve in Fig. 2 is plotted from the theoretical formula (2), with $\Theta = 417^\circ$ and $A = 0.00441$, and it can be seen that the experimental

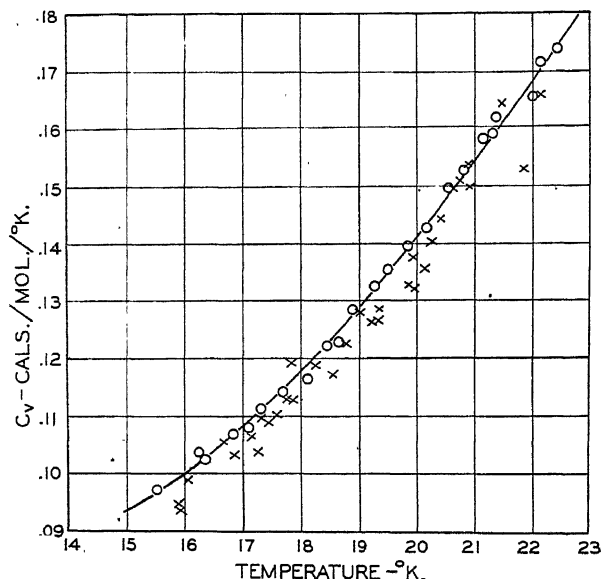


FIG. 2. Specific heat of manganese; X—Elson, Grayson-Smith, and Wilhelm, O—Armstrong and Grayson-Smith.

specific heat is well represented over this limited temperature range by such an equation. However, these figures have been compared with the measurements made by Kelley (7) in the temperature range 50° to 300° K., and it is evident that the values of Θ and A quoted above are both too large. It is also evident that there is a sharp variation in $\Theta(T)$ between 15° and 50° K., which makes it impossible to deduce the true value of A accurately. When Kelley's measurements are corrected to constant volume it is found that $C_v = 6.10$ cal. per gm. per deg. at 290° K. This implies the existence of a rather large electronic specific heat, and is consistent with a value $A \sim 0.0025$. On the other hand, this very doubtful estimate is clearly too low to agree with the low temperature measurements. Until measurements in the liquid helium temperature range are available, all that can be done is to assume a value of A , and examine whether $\Theta(T)$, derived from values of $C_v - AT$, has a reasonable temperature dependence. The conclusion is that A probably lies between 0.0035 and 0.0040. The derived values of $\Theta(T)$ then vary from 365° to 390° , with a sharp increase through the liquid hydrogen temperature range, and a flat maximum above 22° K.

With this approximate value for the coefficient of the electronic specific heat it is possible to make an estimate of the effective mass coefficient, α , in

Equation (4). By analogy with the neighboring metals (iron, cobalt, nickel) in the periodic table, manganese should have between 0.5 and 1 free electron per atom in the conducting s -band. This leaves in the d -band 3.5 to 4 unoccupied holes, which are mainly responsible for the specific heat. Assuming $n = 3.5$ and $A = 0.0038$ gives m/α approximately equal to 20 electron masses for the electron levels near the top of the occupied region in the d -band.

Bismuth

The measurements for bismuth are given in Table II, and the specific heats are plotted against temperature in a part of Fig. 3. The curve in this

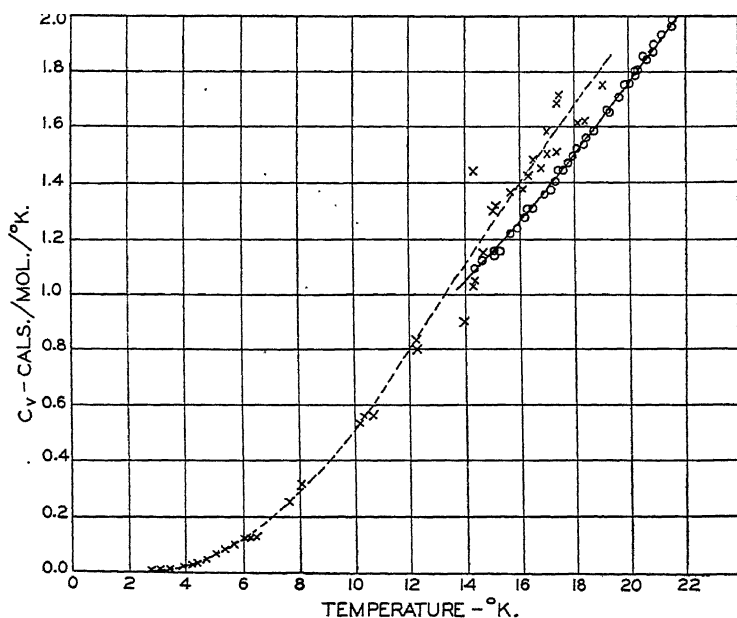


FIG. 3. Specific heat of bismuth; X—Keesom and van den Ende, O—Armstrong and Grayson-Smith.

figure is empirical, the average deviation of individual values from the smooth curve being 0.6%. Fig. 3 shows also the measurements made by Keesom and van den Ende (6). At temperatures where the two sets of measurements overlap, the internal consistency of the present measurements is clearly the better, but the discrepancy still exceeds the probable error of Keesom's measurements. Keesom did not state either the source or the estimated purity of the material used, and it is possible that the discrepancy is due to impurities.

Over the limited temperature range reported in this paper the measured specific heats agree very accurately with the theoretical formula (1), with $A = 0.060$. However, when the measurements are compared with those of

TABLE II
 SPECIFIC HEATS OF BISMUTH

Run No.	Temperature, degrees Kelvin	Time of heating, sec.	Change in temperature, degrees Kelvin	Total heat capacity, Cal./°K.	Calorimeter heat capacity, Cal./°K.	Sample heat capacity, Cal./°K.	Specific heat $C_p = C_v$ Cal./mole/°K.
1	14.60	15.19	0.3564	0.3558	0.0519	0.3039	1.123
	15.24	15.87	0.3559	0.3719	0.0600	0.3119	1.152
	15.88	17.12	0.3530	0.4042	0.0688	0.3354	1.240
	16.43	18.74	0.3633	0.4300	0.0770	0.3530	1.304
	16.86	17.92	0.3300	0.4524	0.0840	0.3684	1.363
1	17.27	20.87	0.3689	0.4710	0.0907	0.3804	1.406
	20.35	28.32	0.3731	0.6388	0.1494	0.4894	1.809
	20.65	27.87	0.3583	0.6565	0.1563	0.5002	1.850
	20.97	28.41	0.3552	0.6720	0.1644	0.5076	1.876
	21.24	25.10	0.3462	0.6940	0.1716	0.5224	1.931
1	21.60	25.88	0.3482	0.7160	0.1824	0.5336	1.972
	21.91	27.01	0.3501	0.7381	0.1927	0.5454	2.043
	22.23	27.69	0.3487	0.7598	0.2038	0.5560	2.057
2	17.76	20.01	0.3384	0.4997	0.0986	0.4011	1.476
	18.08	21.16	0.3550	0.5174	0.1043	0.4131	1.526
	18.47	21.82	0.3436	0.5364	0.1109	0.4255	1.564
	18.88	24.06	0.3753	0.5508	0.1183	0.4225	1.509
	19.23	23.46	0.3442	0.5748	0.1243	0.4495	1.653
	20.00	25.03	0.3397	0.6204	0.1414	0.4790	1.762
3	15.07	15.75	0.3542	0.3711	0.0577	0.3134	1.158
	15.59	17.31	0.3653	0.3953	0.0643	0.3310	1.223
	16.26	17.29	0.3372	0.4274	0.0744	0.3530	1.304
	17.38	20.04	0.3442	0.4847	0.0924	0.3923	1.450
	20.25	22.73	0.3434	0.6306	0.1470	0.4836	1.789
3	20.59	22.90	0.3288	0.6532	0.1547	0.4985	1.843
	21.21	24.72	0.3382	0.6952	0.1709	0.5243	1.939
	21.64	25.52	0.3360	0.7229	0.1837	0.5392	1.993
	21.96	26.39	0.3376	0.7425	0.1944	0.5481	2.027
	22.25	27.40	0.3402	0.7642	0.2026	0.5616	2.080
4	14.40	13.06	0.3225	0.3415	0.0494	0.2921	1.091
	15.09	15.08	0.3460	0.3678	0.0583	0.3096	1.144
	15.62	16.62	0.3572	0.3922	0.0646	0.3276	1.212
	16.14	17.59	0.3552	0.4180	0.0725	0.3455	1.277
	17.04	18.12	0.3320	0.4597	0.0869	0.3728	1.378
4	17.53	19.84	0.3448	0.4851	0.0948	0.3903	1.443
	17.99	20.36	0.3396	0.5071	0.1025	0.4046	1.495
	18.33	22.93	0.3674	0.5269	0.1085	0.4184	1.547
	18.72	23.43	0.3620	0.5450	0.1155	0.4295	1.589
	19.20	23.60	0.3452	0.5754	0.1247	0.4507	1.667
4	19.62	22.80	0.3642	0.5947	0.1332	0.4615	1.707
	19.93	21.86	0.3386	0.6145	0.1398	0.4747	1.756
	20.26	22.61	0.3392	0.6343	0.1472	0.4871	1.802
	20.58	23.30	0.3382	0.6548	0.1545	0.5003	1.860
	20.91	24.64	0.3467	0.6765	0.1628	0.5137	1.900

Keesom and van den Ende in the liquid helium range, and with those of Anderson (1) at higher temperatures, it is evident that the apparent linear term cannot be attributed to an electronic specific heat. The original measurements of Keesom below $5^{\circ} K.$ have been carefully re-examined for any evidence of a linear term, and the conclusion is that the true value of A is less than 5×10^{-5} . This is consistent with estimates of the number of conduction electrons in bismuth. On the basis of measurements of the diamagnetic susceptibilities, Jones (5) estimated 0.0013 electron per atom in the partly filled electronic energy band which is responsible for the conducting properties. Later, Mott and Jones (8, p. 213) gave the still smaller estimate of 10^{-4} . Presumably, the electronic specific heat, if any, would be due to an equal number of unoccupied holes in the nearly filled lower band, but the effective mass would have to be extremely large in order to produce an observable contribution to the specific heat.

It is concluded that the form of the observed specific heat curve of bismuth is entirely due to peculiarities in the spectrum of vibration frequencies in the crystal lattice. Fig. 4 shows the experimental values of $\Theta(T)$, calculated from the smoothed specific heat curve at different temperatures. The similarity of this curve to that calculated by Blackman (Fig. 1) for a simple cubic lattice is remarkable.

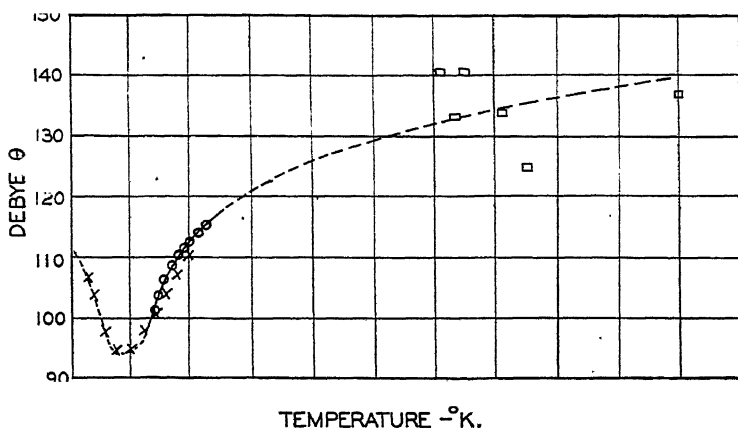


FIG. 4. Variation of Θ with temperature for bismuth; \times —Keesom and van den Ende, \square —Anderson, \circ —Armstrong and Grayson-Smith.

Acknowledgments

The authors wish to express their appreciation of the continued advice of Prof. J. O. Wilhelm, and of the assistance that he gave during liquid hydrogen runs. They also wish to acknowledge the support given by the late Prof. E. F. Burton. The senior author completed the calculations for this paper while holding a research Fellowship from the National Research Council, and he wishes to express his thanks to the Council for this assistance.

References

1. ANDERSON, C. T. J. Am. Chem. Soc. 52 : 2720. 1930.
2. BLACKMAN, M. Proc. Roy. Soc. (London), A, 148 : 384. 1935. 159 : 416. 1937.
3. BLACKMAN, M. Proc. Cambridge Phil. Soc. 33 : 94. 1937.
4. ELSON, R. G., GRAYSON-SMITH, H., and WILHELM, J. O. Can. J. Research, A, 18 : 83. 1940.
5. JONES, H. Proc. Roy. Soc. (London), A, 147 : 396. 1934.
6. KEESOM, W. H. and VAN DEN ENDE, J. N. Proc. Acad. Sci. Amsterdam, 33 : 243. 1930. 34 : 210. 1931.
7. KELLEY, K. K. J. Am. Chem. Soc. 61 : 203. 1939.
8. MOTT, N. F. and JONES, H. Theory of the properties of metals and alloys. Oxford at the Clarendon Press. 1936.

ON THE NUMERICAL CALCULATION OF THE INTERNAL CONVERSION IN THE K-SHELL— THE ELECTRIC DIPOLE CASE¹

BY J. P. STANLEY

Abstract

Hulme's formula for the internal conversion of γ -radiation is simplified and used to calculate the internal conversion coefficient in the electric dipole case for electrons in the K -shell. For each of the elements $Z = 69, 74, 79, 84, 89$, I_K is calculated for 10 values of the variable $\theta = \frac{mc^2}{h\nu}$ and a table obtained by interpolation is given for $\theta = 0.05$ to $\theta = 1.70$.

1. Introduction

The theoretical evaluation of the internal conversion of γ -radiation in an atomic system is a well known problem and has been treated by a number of writers. In particular, the case in which the atomic nucleus is assumed to radiate the field of an electric dipole has been treated exhaustively in a paper by H. R. Hulme (1). In his paper, Hulme employs Dirac's relativistic equations and derives formulae for the conversion coefficients I_K and I_{L_I} , corresponding to the electrons of the K - and L_I -shells, respectively. Except that screening effects have been neglected, these formulae are exact and enable us to calculate numerical values for I_K and I_{L_I} , if the atomic number Z and the energy of the γ -radiation are assigned.

The quantity which Hulme denotes by I_K and which we use here is such that $2I_K$ corresponds to the ratio of the number of observed K -electrons to the number of observed photons of energy $h\nu$. It is perhaps more usual to apply the term 'internal conversion coefficient' to the ratio of the number of observed electrons to the sum of the observed electrons and observed photons (2).

The expressions for I_K and I_{L_I} are extremely complex and the task of calculating numerical values for the various conversion coefficients from such expressions is a formidable one. Although Hulme himself gives the results of calculations for six (6) separate values of I_K corresponding to $Z = 84$ and at least one value for the 'exact' ratio $I_K : I_{L_I}$, in the 16 years since the publication of these results only a very few additional values have been worked out from the 'exact' formulae: however, values of conversion coefficients for other atomic numbers have been estimated from asymptotic formulae and/or by rough interpolation.

Recently, considerable importance has been attached to more exact calculations of conversion coefficients and the present paper contains the results of work done in an attempt to provide a table of I_K values in the electric dipole case.

¹ Manuscript received November 10, 1948.

Contribution from the Computation Centre, McLennan Laboratory, University of Toronto, Toronto, Ont.

As a preliminary to the calculations reported here, the formula for I_K , given by Hulme, was simplified. A brief account of the method used and the resulting modified expression for I_K are given in Section 3; Section 2 is devoted to a summary of Hulme's formula. The calculations based on the modified expression for I_K are tabulated in Section 4 and cover the range of atomic numbers from $Z = 69$ to $Z = 89$.

It was originally intended that these calculations should include the tabulation of I_K in the electric dipole case for the complete range of atomic numbers and also tables of conversion coefficients for other electron shells. However, when the work had progressed to the stage reported here, it was learned that one of the large-scale digital computers was being coded to carry out these and more extensive calculations of internal conversion coefficients. Accordingly, the basis of calculation was more or less arbitrary and further work on this problem has been suspended pending a report on progress of the above.

Since some interest may attach to the simplified form of Hulme's expression for I_K which has been obtained, it was decided that these incomplete results should be published. Further, the values of I_K tabulated may be of some value as a rough check on more extensive calculations.

2. Summary of Hulme's Formula for I_K

In the paper referred to earlier, Hulme quotes a final expression for the conversion coefficient I_K which may be written in the form:

$$(2.1) \quad I_K = \frac{1}{24} \frac{\gamma b \theta}{Z} \cdot \frac{(2\gamma)^{2-2\beta}}{\Gamma(3-2\beta)(2-\beta)} \cdot \frac{|\Gamma(1-\beta-ib)|^2}{\left\{ \gamma + \frac{i}{\theta} \left(\frac{a}{q} - 1 \right) \right\}^{2(1-\beta-w)}} \times \left\{ \frac{2A^2|B|^2}{A^2 + |B|^2} \right\} (2|A|^2 + |B|^2),$$

where

(2.2)

$$A = I_1 \left\{ \gamma \left(\frac{1}{A} - \frac{2}{|B|} \right) - i \frac{2-\beta}{|B|} \right\} + I_2 \left\{ \gamma \left(\frac{1}{A} + \frac{2}{|B|} \right) + i \left(\frac{2-\beta}{|B|} \right) \right\} \\ + I_3 \left\{ \frac{2-\beta}{|B|} + \frac{i\gamma}{A} \right\} + I_4 \left\{ -\frac{2-\beta}{|B|} + \frac{i\gamma}{A} \right\},$$

and

(2.3)

$$I_1 = I_1' \left\{ \gamma \left(\frac{1}{A} + \frac{1}{|B|} \right) + i(2-\beta) \left(\frac{3}{A} - \frac{1}{|B|} \right) \right\} \\ + I_2' \left\{ \gamma \left(\frac{1}{A} - \frac{1}{|B|} \right) + i(2-\beta) \left(\frac{3}{A} + \frac{1}{|B|} \right) \right\} \\ + I_3' \left\{ \frac{2-\beta}{|B|} + \frac{i\gamma}{A} \right\} + I_4' \left\{ -\frac{2-\beta}{|B|} + \frac{i\gamma}{A} \right\}.$$

The notation used above is essentially the same as that employed by Hulme. For ease of reference this notation is explained below: thus

Z = the atomic number.

$$\gamma = \frac{2\pi Z e^2}{ch} = \frac{Z}{137} \quad (\text{approximately}), \quad \theta = mc^2/h\nu,$$

where e , m denote the charge and mass of an electron, respectively, and c , h , ν denote, as usual, the velocity of light, Planck's constant, and the frequency of the γ -radiation. It will be noted that θ is a dimensionless parameter corresponding to the energy of the γ -radiation.

$$\beta = 1 - \sqrt{1 - \gamma^2}. \quad (\text{This quantity is the negative of that used by Hulme}).$$

$$q = 2\pi\nu/c.$$

$$A^2 = \frac{2\pi}{h} \left(mc + \frac{E}{c} \right) \quad B^2 = \frac{2\pi}{h} \left(mc - \frac{E}{c} \right),$$

where E denotes the final energy of the system considered, i.e., when the electron originally in the K -shell is a free electron outside the atom, and has the value

$$E = mc^2\sqrt{1 - \gamma^2} + h\nu.$$

Three particular expressions involving the quantities A and B are of common occurrence and have been denoted by a , b , and c in Hulme's paper. To avoid possible confusion with the velocity of light, we shall denote these expressions by a , b , and d ; they are defined by:

$$AB = ia, \quad \frac{\gamma}{2} \left(\frac{A}{B} - \frac{B}{A} \right) = -ib, \quad \frac{\gamma}{2} \left(\frac{A}{B} + \frac{B}{A} \right) = -id.$$

Since, for a free electron, $E \geq mc^2$, it follows that B is a pure imaginary and hence that a , b , and d are real.

It remains to define the quantities I_1, I_2, \dots, I_4 : these are complicated expressions involving Gamma functions and hypergeometric functions. In particular

$$\begin{aligned} I_1 &= \left\{ F(s + ib + 1, \quad ib - s - 1; \quad ib + \beta; \quad z^{-1}) \right. \\ (2.4) \quad &+ \frac{\Gamma(s + 2 - \beta) \Gamma(ib + \beta - 1) \Gamma(s + 2 - ib)}{\Gamma(s + 1 + \beta) \Gamma(s + 1 + ib) \Gamma(1 - \beta - ib)} \cdot (-z)^{-(1 - \beta - ib)} \\ &\times F(s + 2 - \beta, \quad -s - \beta; \quad 2 - \beta - ib; \quad z^{-1}) \Big\} \\ I_2 &= \left\{ \frac{s + 1 + ib}{\beta + ib} \cdot z^{-1} \cdot F(s + 2 + ib, \quad ib - s; \quad ib + 1 + \beta; \quad z^{-1}) \right. \\ (2.4) \quad &+ \frac{\Gamma(s + 2 - \beta) \Gamma(ib + \beta) \Gamma(s + 1 - ib)}{\Gamma(s + 1 + \beta) \Gamma(s + 1 + ib) \Gamma(1 - \beta - ib)} \cdot (-z)^{-(1 - \beta - ib)} \\ &\times F(s + 2 - \beta, \quad -\beta - s; \quad 1 - \beta - ib; \quad z^{-1}) \Big\} \frac{(k - s) + i(b + d)}{(k - s) - i(b + d)}, \end{aligned}$$

where

$$s = \sqrt{4 - \gamma^2} - 1,$$

k = an integer which in all cases considered here has the value $+1$,

$$z = \frac{2}{1 - \frac{q}{a} - i\delta},$$

$$\delta = \frac{1}{a a_0},$$

$$a_0 = \frac{h^2}{4\pi^2 m Z e^2},$$

and

$\arg(-z)$ is chosen so that $|\arg(-z)| < \pi$.

Similar definitions may be given for I_3 and I_4 , but these quantities may be calculated from the values of I_1 and I_2 , by means of the formulae

$$(2.5) \quad \begin{aligned} I_3 &= \frac{\frac{a}{q} \left[\delta - i \left(\frac{q}{a} - 1 \right) \right]}{(s - \beta + 1)(s + \beta + 1)V} \cdot \{(\beta - ib) \cdot V I_1 + (s - ib + 1)(1 - z)I_2\}, \\ I_4 &= \frac{\frac{a}{q} \left[\delta - i \left(\frac{q}{a} - 1 \right) \right]}{(s - \beta + 1)(s + \beta + 1)} \cdot \{(s + ib + 1) \cdot V I_1 + (\beta + ib)(1 - z)I_2\}, \end{aligned}$$

where

$$V = \frac{(k - s) + i(b + d)}{(k - s) - i(b + d)}.$$

The remaining quantities I'_1 to I'_4 are given by formulae analogous to (2.4) and (2.5); we have merely to replace s by s' and $[(k - s) - i(b + d)]$ by $[(b - d) + i(k - 1 - s')]$ in the formulae for I_1 and I_2 and the equations expressing I_3 and I_4 in terms of I_1 , I_2 . Here, s' is used to denote $[1 - \gamma^2]^{\frac{1}{2}} - 1$, i.e., the negative of β .

3. Modification of Hulme's Formula

Let us begin by defining a new variable ψ , given by

$$\psi = 1 - \beta + 1/\theta.$$

We note that E , the energy of the electron in its final state outside the atom, is given by $mc^2\psi$. Thus ψ is a parameter which measures the ratio of the electron's energy in its final state to the "rest" energy. ψ can have any real value greater than unity: the value unity for ψ is actually critical since it corresponds to a state in which the electron, outside the atom, has no kinetic energy.

In terms of ψ we note the following expressions:

$$\begin{aligned} A &= [q\theta(\psi + 1)]^{\frac{1}{2}}, \\ |B| &= [q\theta(\psi - 1)]^{\frac{1}{2}}, \\ \frac{2A^2|B|^2}{A^2 + |B|^2} &= \frac{q\theta}{\psi} (\psi^2 - 1), \end{aligned}$$

$$a = q\theta(\psi^2 - 1)^{\frac{1}{2}}$$

$$b = \gamma\psi(\psi^2 - 1)^{-\frac{1}{2}},$$

$$d = \frac{b}{\psi},$$

$$z^{-1} = \frac{1}{2} - \frac{1}{2\sqrt{\psi^2 - 1}} \left(\frac{1}{\theta} + i\gamma \right)$$

$$\frac{1}{\left| \left\{ \gamma + \frac{i}{\theta} \left(\frac{a}{q} - 1 \right) \right\}^{2(1-\beta-ib)} \right|} = \frac{1}{|(-z)^{-(1-\beta-ib)}|^2} \left[\frac{1}{2(\psi^2 - 1)^{\frac{1}{2}}} \right]^{2-2\beta} e^{i\pi}.$$

Let us now take a factor $\sqrt{q}\theta(\psi^2 - 1)^{\frac{1}{2}}$ into $|\mathfrak{A}|$ and $|\mathfrak{B}|$, combining it with the coefficient of the I 's in formulae (2.2) and (2.3). These coefficients now become

$$\begin{aligned} (3.1) \quad J_1 &= -\gamma(2\mu - \lambda) - i(2 - \beta)\mu, \\ J_2 &= +\gamma(2\mu + \lambda) + i(2 - \beta)\mu, \\ J_3 &= + (2 - \beta)\mu + i\gamma\lambda, \\ J_4 &= - (2 - \beta)\mu + i\gamma\lambda, \\ J'_1 &= + \gamma(\mu + \lambda) + i(2 - \beta)(3\lambda - \mu), \\ J'_2 &= - \gamma(\mu - \lambda) + i(2 - \beta)(3\lambda + \mu), \\ J'_3 &= J_3 \\ J'_4 &= J_4, \end{aligned}$$

where

$$\lambda = [\theta(\psi - 1)]^{\frac{1}{2}} \quad \text{and} \quad \mu = [\theta(\psi + 1)]^{\frac{1}{2}}.$$

Formulae (2.5), which give I_3 and I_4 in terms of I_1 and I_2 , become:

$$\begin{aligned} (3.2) \quad I_3 &= \frac{i\theta(\psi^2 - 1)^{\frac{1}{2}}}{(2 - \beta)V} [(\beta - ib)z^{-1} V I_1 + (s + 1 - ib)(z^{-1} - 1)I_2], \\ I_4 &= \frac{i\theta(\psi^2 - 1)^{\frac{1}{2}}}{(2 - \beta)} [(s + 1 + ib)z^{-1} V I_1 + (\beta + ib)(z^{-1} - 1)I_2]. \end{aligned}$$

We also define

$$(3.3) \quad W = \frac{\Gamma(s + 2 - \beta)}{\Gamma(s + 1 + \beta)} \frac{\Gamma(\beta - 1 + ib)}{\Gamma(s + 1 + ib)} \frac{\Gamma(s + 2 - ib)}{\Gamma(1 - \beta - ib)} (-z)^{-(1-\beta-ib)}$$

Combining formulae (2.2), (2.4), and (3.1), we may write, using (3.3),

$$\mathfrak{A}' = \mathfrak{A}_1 + W \mathfrak{A}_2,$$

where $\mathfrak{A}' = \theta [q(\psi^2 - 1)]^{\frac{1}{2}} \mathfrak{A}$ and \mathfrak{A}_1 , \mathfrak{A}_2 are complex expressions, which, however, can readily be deduced.

In particular:

(3.4)

$$\begin{aligned} \mathfrak{A}_2 = & J_1 F_2 + V J_2 \left(\frac{\beta - 1 + ib}{s + 1 - ib} \right) F_4 \\ & + i\theta \frac{(\psi^2 - 1)^{\frac{1}{2}}}{(2 - \beta)} J_3 [(\beta - ib)z^{-1}F_2 + (\beta - 1 + ib)(z^{-1} - 1)F_4] \\ & + i\theta \frac{(\psi^2 - 1)^{\frac{1}{2}}}{(2 - \beta)} V J_4 \left[(s + 1 + ib)z^{-1}F_2 + (\beta + ib)(z^{-1} - 1) \right. \\ & \quad \left. \left(\frac{\beta - 1 + ib}{s + 1 - ib} \right) F_4 \right], \end{aligned}$$

where the F_i stand for the following complex hypergeometric functions:

$$F_1 = F(s + 1 + ib, \quad ib - s - 1, \quad ib + \beta, \quad z^{-1}),$$

$$F_2 = F(s + 2 - \beta, \quad -s - \beta, \quad 2 - \beta - ib, \quad z^{-1}),$$

$$F_3 = F(s + 2 + ib, \quad ib - s, \quad ib + \beta + 1, \quad z^{-1}),$$

$$F_4 = F(s + 2 - \beta, \quad -s - \beta, \quad 1 - \beta - ib, \quad z^{-1}).$$

F_1 and F_3 are involved in the corresponding formula for \mathfrak{A}_1 . If we collect together the coefficients of F_2 and F_4 , formula (3.4) may be written in the form

$$\begin{aligned} \mathfrak{A}_2 = & F_2 \left\{ J_1 + \frac{i\theta(\psi^2 - 1)^{\frac{1}{2}}}{z(2 - \beta)} [(\beta - ib)J_3 - (s + 1 + ib)\bar{J}_3 V] \right\} \\ & + V \frac{(\beta - 1 + ib)}{(s + 1 - ib)} F_4 \left\{ J_2 - i \frac{(z^{-1} - 1)\theta(\psi^2 - 1)^{\frac{1}{2}}}{(2 - \beta)} [(\beta + ib) \right. \\ & \quad \left. \bar{J}_3 - \bar{V}(s + 1 - ib)J_3] \right\} \end{aligned}$$

where the bar denotes the complex conjugate.

Let us now introduce

$$(3.5) \quad g = \frac{i\theta(\psi^2 - 1)^{\frac{1}{2}}}{(2 - \beta)} \{ (\beta - ib)J_3 + (s + 1 + ib) \cdot VJ_4 \}.$$

We then have

$$(3.6) \quad \mathfrak{A}_2 = F_2 \{ J_1 + z^{-1}g \} + V \frac{(\beta - 1 + ib)}{(s + 1 - ib)} F_4 \{ J_2 + (z^{-1} - 1)\bar{g} \}.$$

In a similar manner, we obtain the following formula for \mathfrak{A}_1 ,

$$(3.7) \quad \mathfrak{A}_1 = F_1 \{ J_1 + z^{-1}g \} + z^{-1}V \frac{(s + 1 + ib)}{(\beta + ib)} F_3 \{ J_2 + (z^{-1} - 1)\bar{g} \}$$

By means of (3.1) we may simplify (3.5); after some algebra, we obtain

$$g = 2\gamma\lambda^2\mu + 2i(1 + \beta)\lambda\mu^2,$$

so that

$$(3.8) \quad J_1 + z^{-1}g = \gamma\mu(\theta - 1) + i[-3\mu + \lambda(1 + \beta + \theta\{2 - \beta\})]$$

$$(3.9) \quad J_2 + (z^{-1} - 1)\bar{g} = -\gamma\mu(\theta - 1) + i[+3\mu + \lambda(1 + \beta + \theta\{2 - \beta\})].$$

Let us denote the quantities given by (3.8) and (3.9) v and w respectively.

Then we have, finally,

$$(3.91) \quad |\mathcal{A}'|^2 = |\mathcal{A}_1 + W\mathcal{A}_2|^2$$

where

$$\mathcal{A}_1 = F_1 v + z^{-1} V \frac{(s+1+ib)}{(\beta+ib)} F_3 w$$

$$\mathcal{A}_2 = F_2 v + V \frac{(\beta-1+ib)}{(s+1-ib)} F_4 w$$

and W is given by (3.3)

In an exactly parallel manner, we obtain

$$\mathcal{B}' = \mathcal{B}_1 + W'\mathcal{B}_2,$$

where

$$\mathcal{B}' = \theta[q(\psi^2 - 1)]^{\frac{1}{2}} \mathcal{B},$$

$$(3.92) \quad \mathcal{B}_1 = G_1 \{J'_1 + z^{-1} \cdot g'\} + z^{-1} V' \left(\frac{1 - \beta + ib}{\beta + ib} \right) G_3 \{J'_2 + (z^{-1} - 1) \bar{g}'\}$$

$$\mathcal{B}_2 = \{J'_1 + z^{-1} \cdot g'\} - V' \{J'_2 + (z^{-1} - 1) \bar{g}'\},$$

and

$$g' = i\theta \frac{(\psi^2 - 1)^{\frac{1}{2}}}{\frac{1}{2} - \beta} \{(\beta - ib)J_3 + (1 - \beta + ib)V'J_4\},$$

$$V' = \frac{(b-d) - i(k-1+\beta)}{(b-d) + i(k-1+\beta)},$$

$$G_1 = F(1 - \beta + ib, \beta - 1 + ib, \beta + ib, z^{-1}),$$

$$G_3 = F(2 - \beta + ib, \beta + ib, \beta + 1 + ib, z^{-1}),$$

W' is obtained by replacing s by $(-\beta)$ in Formula (3.3).

After some algebra, we find

$$g' = \frac{2\gamma}{\beta} \lambda \mu (\beta \lambda - i\gamma \mu);$$

whence

$$J'_1 + z^{-1} g' = 2(1 - \theta)[\gamma \mu + i\lambda(2 - \beta)]$$

and

$$J'_2 + (z^{-1} - 1) \bar{g}' = -2(1 - \theta)[\gamma \mu - i\lambda(2 - \beta)].$$

Substituting in (3.92), we see that

$$\mathcal{B}_2 = 0$$

Hence

$$|\mathcal{B}'|^2 = |\mathcal{B}_1|^2 = 8(2 - \beta)(1 - \theta)^2 \left| G_1 + z^{-1} \frac{(1 - \beta + ib)}{(\beta + ib)} G_3 \right|^2.$$

But G_1 and G_3 are related by the formula

$$G_1 + z^{-1} \left(\frac{1 - \beta + ib}{\beta + ib} \right) G_3 = (1 - z^{-1})^{-(1-\beta+w)}.$$

Therefore

$$(3.93) \quad |\mathcal{B}'|^2 = 8(2 - \beta)(1 - \theta)^2 |(1 - z^{-1})^{-(1-\beta+w)}|^2.$$

Collecting our results, the final formula for the coefficient of internal conversion in the two electrons of the K -shell is

$$(3.94) \quad 2I_K = \frac{\gamma^{3-2\beta}(\psi^2 - 1)^{-(3/2-\beta)} e^{\beta\pi} |\Gamma(1 - \beta - ib)|^2}{12(137)(2 - \beta)\Gamma(3 - 2\beta)|(-z)^{-(1-\beta-ib)}|^2} [2|\mathcal{A}'|^2 + |\mathcal{B}'|^2]$$

where

$|\mathcal{A}'|^2$ and $|\mathcal{B}'|^2$ are given by (3.91) and (3.93) respectively.

Hulme's formula is far from being stated in its simplest terms and the above modification has simplified the algebra considerably. In particular, we note that the expression for $|\mathcal{B}'|^2$ no longer involves either Gamma functions or hypergeometric functions. The corresponding simplification holds in the

TABLE I

VALUES OF $2I_K$ (OBSERVED K -ELECTRONS/OBSERVED PHOTONS OF ENERGY $h\nu$)

Z $\theta = \frac{mc^2}{h\nu}$	89	84	79	74	69
0.05	0.00007429	0.00006297	0.00005390	0.0000439	0.0000354
0.10	0.0002008	0.0001667	0.0001393	0.000113	0.0000914
0.15	0.0003772	0.0003056	0.0002530	0.000206	0.000166
0.20	0.0005938	0.0004769	0.0003941	0.000321	0.000259
0.25	0.0008497	0.0006773	0.0005611	0.000457	0.000368
0.30	0.00115	0.000926	0.000759	0.000616	0.000495
0.35	0.00148	0.00120	0.000983	0.000797	0.000640
0.40	0.00185	0.00151	0.00123	0.00100	0.000805
0.45	0.00226	0.00185	0.00151	0.00123	0.000988
0.50	0.002706	0.002228	0.001825	0.001485	0.001198
0.55	0.00319	0.00264	0.00217	0.00177	0.00143
0.60	0.00372	0.00309	0.00255	0.00208	0.00169
0.65	0.00430	0.00358	0.00296	0.00242	0.00197
0.70	0.004922	0.004112	0.003405	0.002797	0.002280
0.75	0.00559	0.00469	0.00389	0.00321	0.00262
0.80	0.00632	0.00532	0.00442	0.00365	0.00299
0.85	0.00709	0.00599	0.00499	0.00413	0.00339
0.90	0.00792	0.00671	0.00560	0.00465	0.00383
0.95	0.00880	0.00749	0.00625	0.00521	0.00430
1.00	0.009736	0.008304	0.006956	0.005810	0.004805
1.05	0.0107	0.00917	0.00771	0.00645	0.00535
1.10	0.0118	0.0101	0.00851	0.00714	0.00593
1.15	0.0129	0.0111	0.00936	0.00787	0.00655
1.20	0.0141	0.0121	0.0103	0.00865	0.00722
1.25	0.0153	0.0132	0.0112	0.00948	0.00792
1.30	0.0166	0.0143	0.0122	0.0104	0.00867
1.35	0.0180	0.0155	0.0133	0.0113	0.00947
1.40	0.0194	0.0168	0.0144	0.0123	0.0103
1.45	0.0209	0.0182	0.0156	0.0133	0.0112
1.50	0.02248	0.01956	0.01687	0.01440	0.01214
1.55	0.0241	0.0210	0.0182	0.0156	0.0131
1.60	0.0258	0.0226	0.0196	0.0168	0.0142
1.65	0.0276	0.0242	0.0210	0.0180	0.0153
1.70	0.02949	0.02593	0.02253	0.01936	0.01642

case of the L_I -shell and will shortly be published. It would seem that the formulae for the other shells can probably be simplified in an exactly parallel manner.

4. The Numerical Calculation of the Coefficients

For each of atomic numbers 89, 84, 79, 74, and 69, formula (3.94) was used to calculate the I_K corresponding to certain selected energy parameters θ . These are shown in bold face in Table I.

The work was carried to five significant digits. It is believed that the fourth digit quoted in the final result is of some value.

The values of the coefficient for intermediate energies were obtained by interpolation, and are quoted to three figures. The interpolation was based on two cubic curves, through the points given by $\theta = 0.25, 0.50, 0.70, 1.00$, and $\theta = 0.70, 1.00, 1.50, 1.70$. It was found that the two arcs agreed very closely in the common range from $\theta = 0.70$ to $\theta = 1.00$, which perhaps lends some justification to the method. Moreover, the calculated values for $\theta = 0.05$ to $\theta = 0.20$ blended fairly well into the interpolation arcs.

The value $1/137$ was assumed for the fine structure constant.

Acknowledgment

The author wishes to express his appreciation for the interest and valuable suggestions of Dr. B. A. Griffith of the University of Toronto and for the work done by Mr. H. Gellman of the Computation Centre in checking the manuscript and reading the proofs. He also would like to thank Dr. L. G. Elliott, Mr. Harold Coish, and Dr. W. H. Watson, of the staff of the National Research Council of Canada, who suggested the problem. This project was carried out under a grant from the National Research Council of Canada.

References

1. HULME, H. R. Proc. Roy. Soc. (London), A, 138 : 643. 1932.
2. MOTT, N. F. and SNEDDON, I. N. Wave mechanics and its applications. Oxford University Press, London. 1948.

Canadian Journal of Research

Issued by THE NATIONAL RESEARCH COUNCIL OF CANADA

VOL. 27, SEC. A.

MAY, 1949

NUMBER

THE RESONANCE METHOD OF MEASURING THE RATIO OF THE SPECIFIC HEATS OF A GAS, C_p/C_v ¹

PART V

SECTION A: AN IMPROVED APPARATUS FOR MEASURING THE RATIO OF THE SPECIFIC HEATS OF A GAS

SECTION B: THE USE OF ELECTRONIC COUNTER CIRCUITS TO MEASURE LOW FREQUENCIES AND A VARIABLE LOW FREQUENCY OSCILLATOR

By L. KATZ, S. B. WOODS, AND W. F. LEVERTON

Abstract

This paper describes an improved apparatus for the determination of $\gamma = C_p/C_v$, the ratio of the specific heat at constant pressure to the specific heat at constant volume for a gas. With this apparatus, γ is determined by the resonance method of Clark and Katz. The new apparatus is constructed of stainless steel and is designed to withstand pressures up to 100 atm. This new apparatus is more compact and can be used with corrosive gases. Provision is made for the control and accurate measurement of the temperature of the enclosed gas over a wide range of temperatures. An electronic counter which will measure time intervals, in units of 10 $\mu\text{sec.}$, from 100 $\mu\text{sec.}$ to several seconds in length is described in Section B. An unknown frequency may be determined by measuring the time interval in which a preselected number of cycles occurs. The accuracy is such that frequencies may be measured to within approximately 1 part in 10⁵. The circuit for a variable frequency transistor oscillator with an output of 30 w. in a range of 15 to 250 c.p.s. is shown. The stability of the oscillator is such that the frequency may easily be maintained within 1 part in 10,000 for long periods, and with care in temperature control and choice of electrode voltages much greater stabilities may be obtained.

Introduction

This paper describes an improved apparatus for the determination of $\gamma = C_p/C_v$, the ratio of the specific heat at constant pressure to the specific heat at constant volume of gases. With this apparatus γ is determined by the resonance method (5, 6, 7). This consists essentially of a determination of the resonant frequency of a piston separating equal volumes of the gas at the desired pressure and temperature.

The new apparatus is designed to operate at pressures up to 100 atm. The temperature can be determined accurately and controlled over a range from -40 to $+100^\circ\text{C.}$ This is in strong contrast to the old apparatus, which operated only at temperatures in the immediate neighborhood of room temperature (5).

¹ Manuscript received in original form September 14, 1948, and, as revised, January 20, 1949.
Contribution from the Department of Physics, University of Saskatchewan, Saskatoon, Sask.

The ratios of specific heats at zero pressure have been determined from spectroscopic data for many monatomic and diatomic gases, and more recently, for triatomic and a few more complicated gases. The latter calculations are extremely involved and depend upon the proper assignment of fundamental frequencies to the molecule. Our results upon extrapolation to zero pressure should serve as a check on the spectroscopic work, especially in the case of triatomic and higher order molecules. Such a check is desirable because spectroscopists use these same fundamental frequencies to calculate moments of inertia and internuclear distances of the various molecules.

Clark and Katz (4) have described an accurate method of measuring low frequencies which requires a darkroom and necessitates the development of photographs before the frequency is known. While engaged in wartime research, the senior author of the present paper employed several electronic counter circuits and recognized their application to frequency measurement. With such a counter the frequency is obtained immediately by means of one simple arithmetical operation.

The dynatron oscillator described by Clark and Katz (4) for the production of low frequency currents has been replaced by a transitron oscillator. The latter type of oscillator is not critical to electrode voltages nor to individual tube characteristics. It will operate over an extended range of frequencies with good stability and provide an excellent laboratory oscillator where elaborate circuits are not desirable.

Simple and accurate methods of calibrating the frequency meter and testing the operation of the meter and oscillator, using the standard signals broadcast by WWV, the Washington Bureau of Standards transmitter, have been employed.

Section A

MECHANICAL DESIGN OF THE NEW APPARATUS

Theoretical considerations on which the design of a sharply resonant system is based were outlined in a previous paper (5). The present apparatus was constructed with these limitations in mind. The values of the pertinent design factors are, approximately:

Gas volume.....	34 cm. ³
Piston mass.....	95 gm.
Piston area.....	7.9 cm. ²
Range of resonant frequency	
at 1 atm.....	45 c.p.s.
at 20 atm.....	180 c.p.s.

The general outline of the new apparatus is shown in Fig. 1. The piston (*P*) was made of stainless steel type 410 (S.A.E.). This steel is ferromagnetic. The inner cylinder (*C*₁) was made of stainless steel type 330, which is non-magnetic. Both types are noncorrosive, thus making it possible to use the

apparatus for the study of gases such as chlorine. These materials have nearly equal coefficients of thermal expansion,

Type	Coefficient of expansion/ $^{\circ}\text{C}$.
410	10.9×10^{-6}
330	11.3

making it possible to use the apparatus over a wide range of temperatures with little change in the clearance between piston and cylinder.

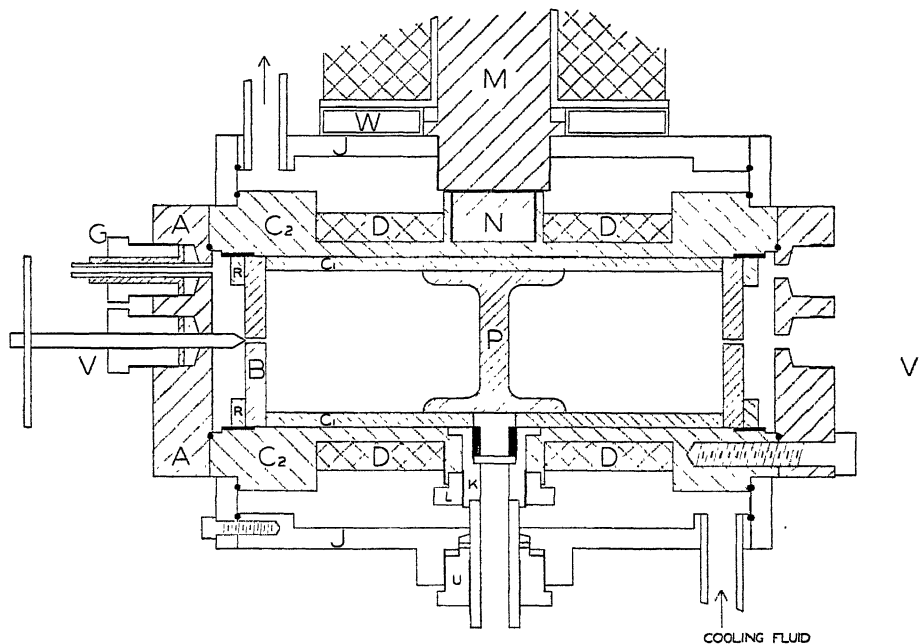


FIG. 1. Construction of the apparatus

Piston and cylinder must fit very closely (all around clearance of a few ten-thousandths of an inch) in order that error due to excessive gas leakage past the piston will be avoided. This necessitated that both piston and inner cylinder surface be machined round to a very fine tolerance. Further, friction must be kept to a minimum, thus requiring that these surfaces be very smooth. The piston was lightly plated with chromium to give a good wearing surface and to reduce the possibility of the piston's sticking. The ends of the resonator cylinder must be flat and parallel to ensure that the end plates (B, B) form a good seal and to make possible an accurate determination of the volume of the enclosed gas.

The diameter of the piston and the length of the resonator cylinder were measured by means of a set of gauge blocks accurate to $\pm 4 \times 10^{-6}$ in. and a comparator with smallest divisions equivalent to 50×10^{-6} in. The mean clearance of the piston within the cylinder, and hence the inside diameter of

the cylinder, was determined by measuring the rate of gas leakage past the piston under a known pressure head. The mean all around clearance was found to be 3.3×10^{-4} in.

A fine scratch was machined around the piston midway along its length. Observation of the amplitude of motion of this scratch when the piston is oscillating enables one to determine the resonance frequency.

The outer cylinder (C_2), of noncorrosive, nonmagnetic stainless steel, serves as the high pressure container. It carries the coils (D) through which an alternating current is passed to drive the piston. Each coil consists of 5900 turns of No. 34 enamelled copper wire. (R,R) are rings to hold the end plates of the resonating chamber in place. The outer end plates (A,A) serve to seal off the pressure cylinder. These end plates also carry the gas inlets (G,G) and the inlet valves (V,V).

(J) is a brass cylinder. The annular space between this cylinder and the pressure cylinder is closed off at the ends by brass rings. Oil circulated through this space controls the temperature of the apparatus.

(M) is an electromagnet. The current through the electromagnet coil is adjusted so that the force on the piston due to the magnet is just sufficient to counterbalance the force due to gravity. This causes the piston to "float" in the cylinder and greatly reduces the friction. (N) is a plug of ferromagnetic material tapped into the pressure cylinder wall directly below the core of the lift magnet. Its purpose is to extend the core of the lift magnet nearer to the piston. Water may be circulated through the hollow brass ring (W) to reduce the flow of heat from the lift magnet coil to the apparatus.

Directly opposite the lift magnet, a glass window is sealed into the wall of the pressure cylinder to permit observation of the motion of the piston. The window is sealed into the boss (K) between "silastic" washers. The nut (L) holds K in position. A brass tube and boss (U) provide a clear optical path through the cooling chamber.

Fig. 2 shows the optical system used to view the motion of the piston in the apparatus. A beam of light from a projection lamp is reflected vertically

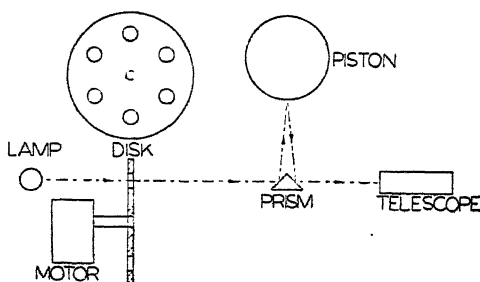


FIG. 2. Optical system.

upward by one face of a small 90 degree aluminized glass prism. The light passes through the window, is reflected by the piston surface, and returns

through the window to the prism. Part of the returning beam is reflected out horizontally by the second face of the prism into the telescope.

A wooden disk with six uniformly spaced $\frac{1}{2}$ in. holes near its circumference is placed between the light source and the prism. By adjusting the rate of rotation of the disk, i.e., the number of interruptions of the light beam, to match the frequency of the piston, the apparent motion of the latter can be made as slow as desired stroboscopically and the amplitude of its excursion measured with precision.

TEMPERATURE CONTROL

The apparatus is maintained at any desired temperature by circulating oil from a thermostatically controlled tank through the outer jacket. The temperature of the interior of the apparatus is determined as follows. A copper-constantan junction is set in the wall of the pressure cylinder (C_2) and is connected through a sensitive galvanometer to a similar junction which is suspended in the oil tank near the bulb of a thermometer. The thermometer indicates the temperature of the oil in the tank and the galvanometer deflection gives the difference between this and the temperature of the apparatus. We are able to maintain and determine the temperature of the apparatus within 0.05°C .

DETERMINATION OF γ

In the earlier papers (5, 6, 7) it was shown that:

$$\gamma = \frac{m V_0 \omega_m^2}{2a^2 P_0} \Lambda \chi G \Gamma,$$

where m = mass of piston,

V_0 = volume of gas on either side of piston,

ω_m = frequency at maximum amplitude of piston motion,

a = effective area of end of piston,

P_0 = pressure of gas,

$\Lambda = \frac{m + m_g}{m}$, where m_g is the mass of a volume V_0 of the enclosed gas,

χ = correction for the effect of friction between piston and cylinder,

G = correction for nonideal behavior of the gas,

Γ = correction for nonadiabatic change of the gas.

The pressure is measured by means of a mercury and glass manometer up to 6 atm., and at higher pressures by means of the Amagat gauge used in the earlier work.

The alternating current to drive the piston is supplied by a transitron oscillator of very high stability. The oscillator and the method of measuring its frequency are described in Section B of this paper.

PERFORMANCE OF THE NEW APPARATUS

This method is absolute in the sense that it is not necessary to calibrate the apparatus by means of measurements with a gas for which γ is already known. The different correction factors involved are also obtained from the experimental set-up and various quantities which can be calculated. In order to check the functioning of the new apparatus and the values of the constants m , V_0 , and a , a series of measurements was made of γ at various pressures from 1 to 5 atm. for argon. A straight line was fitted to the experimental points (γ vs. pressure) by the method of least squares. The mean variation of the experimental points from this straight line was 0.06%. Extrapolation yielded $\gamma = 1.6662$ at zero pressure. This differs by 0.03% from $\gamma = 1.667$ obtained previously by this method and also by the spectroscopic method.

Section B

THE ELECTRONIC FREQUENCY METER AND INTERVAL TIMER

Electronic counter circuits and associated equipment for their use in many applications have been described in the literature recently. The complete circuits for an instrument suitable to use as a frequency meter have not yet appeared.

The block diagram of Fig. 3 shows the sequence of operation of the circuits in the meter. The signal of unknown frequency is connected to a pulse

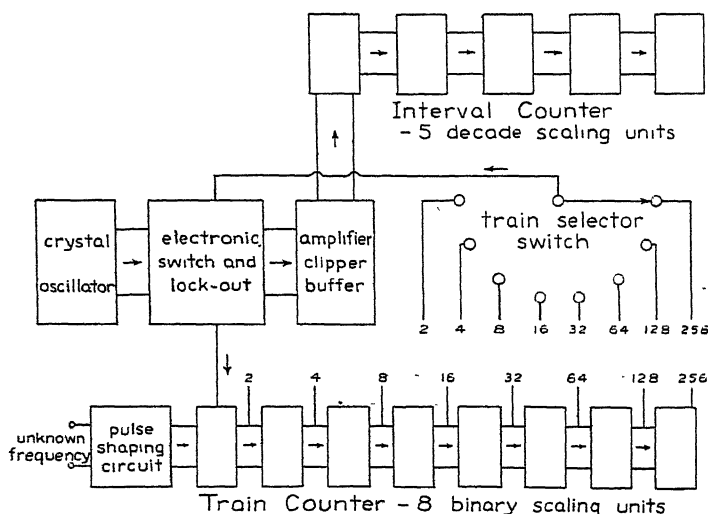


FIG. 3. Block diagram of the frequency meter.

forming circuit, the output of which has the same wave form irrespective of the input wave form. The output is then applied to the train counter, which consists of eight scale-of-two frequency dividing circuits. The output of

any one of these scaling circuits may be chosen, by means of the train selector switch, to operate the electronic switch. When the first pulse is received by the electronic switch, a gate circuit opens, allowing the pulses from the 100 kc. crystal oscillator to be counted and recorded by the interval counter. The next pulse closes the gate so that the 100 kc. pulses are no longer counted. The lockout circuit operates at the same time and prevents further operation of the meter until it is manually reset. The number of cycles of the 100 kc. oscillator that occurred in the time interval between the pulses which operated the electronic switch is recorded by means of neon lights on the interval timer. This corresponds to a train of 2, 4, 8, 16, 32, 64, 128, or 256 cycles of the unknown frequency, depending on the position of the train selector switch. Dividing the number of cycles in the train by the time interval during which they occurred, as indicated by the neon lights of the interval counter, gives immediately the frequency of the source.

Figs. 4, 5, 6, and 7 are the diagrams of the circuits used in the counter. V. H. Regener (12) discusses thoroughly the choice of design parameters for the pulse forming circuit used here. The frequency scaling stages of the train counter use the circuit originally developed by Eccles and Jordan (8) and modified by Potter (10, 11). The action of dual triode trigger pairs such as this circuit employs is described by B. E. Phelps (9). The electronic switch employs a similar circuit. The potentials shown in Fig. 6 are those obtained with the gate circuit in the closed condition. The decade frequency scaling circuits used in the interval counter were developed by Potter (10, 11) and are described by him together with the method of reading the neon lights. G. T. Baker (1) discusses a method of design procedure for this circuit. The method used by Regener (12) may also be adapted for use with triode trigger circuits such as employed in the interval and train counters.

A Bliley Type FM6-S 100 kc. standard frequency crystal, with the oscillator circuit suggested by the manufacturers is used as the standard source. This oscillator maintains a frequency stability of $\pm 0.005\%$ over a temperature range of 0 to 50° C.

The oscillator was calibrated by beating the fiftieth harmonic of its output against the 5 megacycle carrier broadcast from WWV. A wire carried from the output of the 6AG7 clipper amplifier alongside the antenna of a receiver tuned to WWV radiated enough energy to produce the beat note. In this manner, the oscillator could be adjusted to within one part in five million of the WWV signal. Subsequent checks over a period of a year showed it always to be within one part in one million of this frequency.

Since the gate circuit may open part way through a cycle of the standard oscillator which will not be counted or close part way through a cycle which is already counted there may be an error of ± 1 count in the reading of the interval counter. This represents an error of $\pm 10 \mu\text{sec.}$ in the measurement of the time interval, which should normally be the largest error.

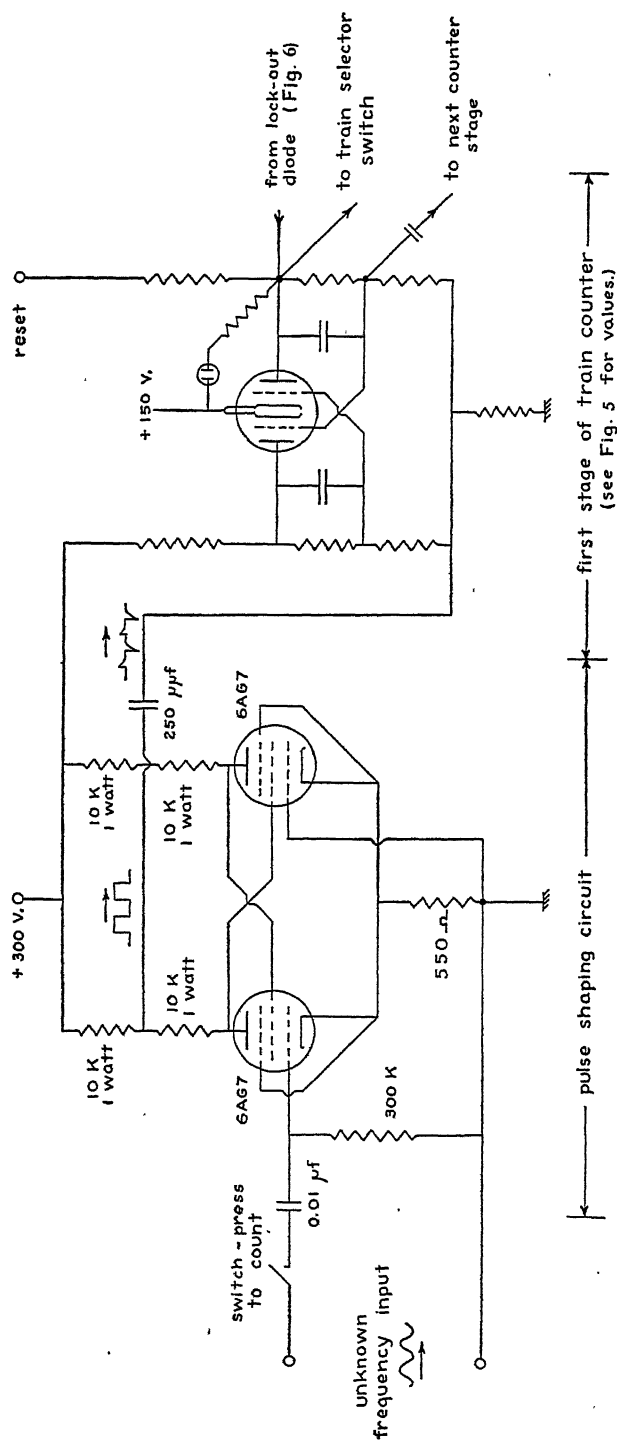


FIG. 4. Pulse forming circuit and the first stage of the train counter. All resistors are $\frac{1}{4}$ w. unless otherwise specified.

If a well filtered power supply is employed, dependable operation is obtained with voltage variations of $\pm 10\%$ without special regulation equipment. The total power consumption is less than 150 w.

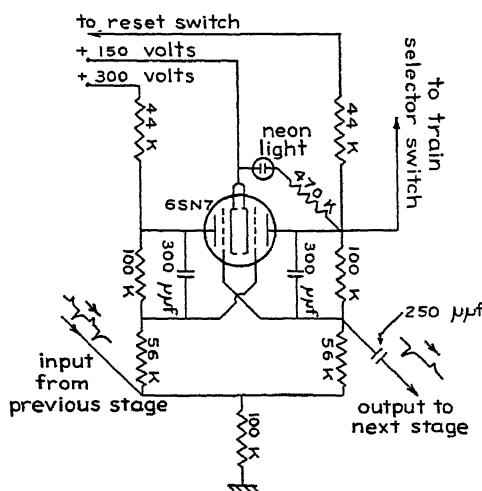


FIG. 5. Binary frequency scaling unit. All resistors are $\frac{1}{2}$ w.

TRANSITRON OSCILLATOR

The oscillator with a three stage amplifier is shown in Fig. 8. For stability the oscillator is powered entirely by batteries and very lightly coupled to the amplifier. The correct voltages were located experimentally and are not critical. The tuned circuit consists of the inductance and condensers used by Clark and Katz (4). At low frequencies a resistance in series with the tuned circuit is necessary to satisfy the conditions for oscillation given by Brunetti (2, 3). The amplifier has been changed only slightly from that shown by Clark and Katz, in order to obtain greater power output.

MEASUREMENTS AND RESULTS

The consistency of the results obtained when measuring the frequency of the transitron oscillator with the meter was used as a test of their combined performance. Both the oscillator and counter were allowed a one hour warm-up period before the readings were taken. Ten measurements were made at each of 22 different frequencies between 25 and 250 c.p.s. The maximum departure of any reading from the mean value for the 10 trials was always less than 0.01% and, for several frequencies, corresponded to an error of 10 μ sec. in the measurement of the time interval.

To ensure that there was no systematic error in the determinations, a known frequency was obtained and measured. A receiver was tuned to WWV on 5 megacycles and the output of the audio amplifier, which contained the standard frequency of 440 c.p.s., was connected to the vertical plates of an

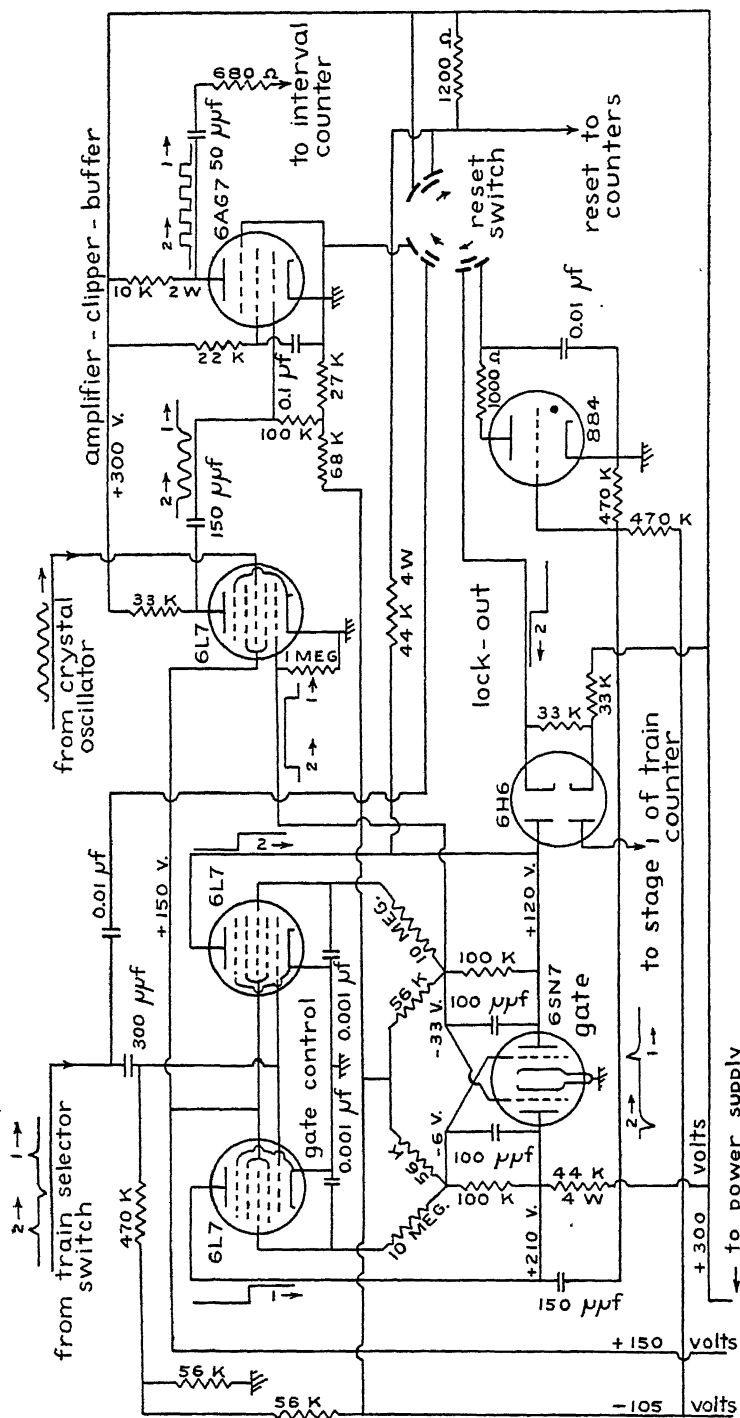


FIG. 6. Electronic switch, lockout and amplifier-clipper-buffer circuits. All resistors are $\frac{1}{2}$ w. unless otherwise specified.

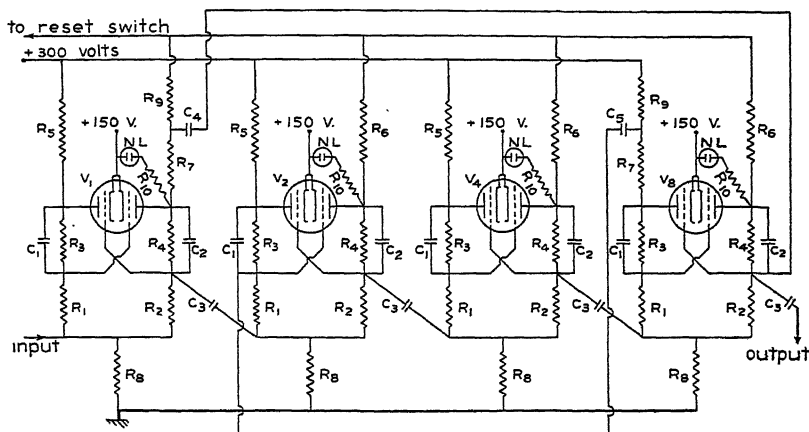


FIG. 7. Decade frequency scaling unit.

R_1, R_2 56,000 ohms
 R_3, R_4, R_8 100,000 ohms
 R_5, R_6 44,000 ohms
 R_7, R_9 22,000 ohms
 R_{10} 470,000 ohms

All resistors are $\frac{1}{2}$ w.

C_1, C_2 300 μ f.
 C_3 500 μ f.
 C_4 50 μ f.
 C_5 100 μ f.

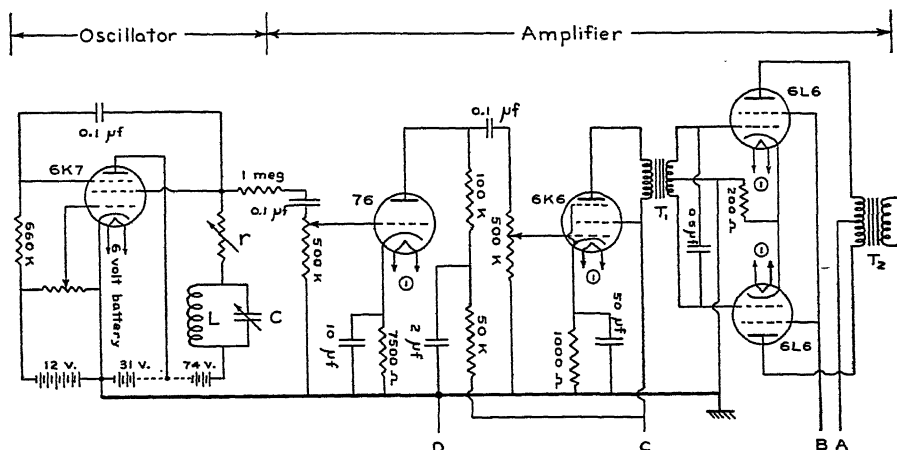


FIG. 8. Transistron oscillator and amplifier

L 10 h., 130 ohm, air core.
 C 0 to 10 μ f. variable condenser.
 r 0 to 3000 ohms.
 T_1 { P 11,000 ohms
 $S/2$ 690 ohms
 T_2 { P 5000 ohms
 S 5000 ohms
 A 420 v.
 B 360 v.
 C 280 v.
 D 0 v. } to power supply.

oscilloscope. The output of the transitron oscillator was connected to the horizontal plates of the oscilloscope and a static Lissajous figure was obtained by adjusting the frequency of the transitron to 220 c.p.s. This adjustment was repeated several times, and each time the frequency was measured, using a number of different train lengths. The maximum departure of any of these readings from 220.000 cycles per second was 0.009%, which is within the accuracy with which the Lissajous pattern could be set.

References

1. BAKER, G. T. J. Sci. Instruments, 25 : 194. June, 1948.
2. BRUNETTI, C. Proc. Inst. Radio Engrs. 25 : 1595. 1937.
3. BRUNETTI, C. Proc. Inst. Radio Engrs. 27 : 88. 1939.
4. CLARK, A. L. and KATZ, L. Can. J. Research, A, 16 : 183. 1938.
5. CLARK, A. L. and KATZ, L. Can. J. Research, A, 18 : 22. 1940.
6. CLARK, A. L. and KATZ, L. Can. J. Research, A, 19 : 111. 1941.
7. CLARK, A. L. and KATZ, L. Can. J. Research, A, 21 : 1. 1943.
8. ECCLES, W. H. and JORDAN, F. W. Radio Rev. 1 : 143. 1919.
9. PHELPS, B. E. Electronics, 18 : 110. July, 1945.
10. POTTER, J. T. Electronics, 17 : 110. June, 1944.
11. POTTER, J. T. Electronics, 17 : 358. June, 1944.
12. REGENER, V. H. Rev. Sci. Instruments, 17 : 180. 1946.

THE RESONANCE METHOD OF MEASURING THE RATIO OF THE SPECIFIC HEATS OF A GAS, C_p/C_v

VI. CARBON DIOXIDE, NITROUS OXIDE, AND METHANE

BY L. KATZ, W. F. LEVERTON, AND S. B. WOODS

Abstract

Carbon dioxide, nitrous oxide, and methane have been carefully purified and the variation of γ with pressure measured. The results when extrapolated to zero pressure give values of γ_0 which are in agreement with those obtained by spectroscopic methods. Agreement in each case is better than 0.10%.

Carbon Dioxide

The variation of γ , the ratio of the specific heats, with pressure was measured previously for carbon dioxide by this method (1). Upon extrapolation of the results to zero pressure it was found that the value of γ_0 was higher than that obtained by the spectroscopic method by 0.49% (3).

Since the probable error in the zero pressure value of γ by this method is less than 0.10%, it was felt that the large difference might have been due to the presence of impurities in the carbon dioxide.

For the present experiment carbon dioxide 99.5% pure was obtained from a commercial source and a careful purification undertaken. The impurities were air and water vapor. The gas was purified by a fractional distillation over liquid air, the first and last tenth being discarded at each stage. γ was measured for a sample which had been put through a three stage distillation. The zero pressure value was found to be 0.10% higher than the spectroscopic value. The results given in Table I were obtained using a sample of carbon dioxide which had been given a five stage distillation.

The $Pv-P$ data of Michels (7) used previously (1) was employed in calculating Δ and G . The constants of the apparatus were as follows.

Mass of piston = 95.448 gm.

Volume of enclosed gas = 34.053 cm.³

Effective area of end of piston = 7.9169 cm.²

Substitution of these in the equation for γ developed previously (5) yields

$$\gamma = 1.0102 \times 10^{-3} \frac{f_m^2}{P_0} \Delta \chi G \Gamma$$

where f_m is in cycles per second and P_0 is in standard atmospheres.

Manuscript received in original form September 14, 1948, and, as revised, January 26, 1949.

Contribution from the Department of Physics, University of Saskatchewan, Saskatoon, Sask.

TABLE I
CARBON DIOXIDE (29.9° C.)

Pressure, atm.	Resonance frequency, c.p.s.	Λ	G	χ	Γ	γ	$\gamma_{\text{equa.}}$	$\gamma - \gamma_{\text{equa.}}$ $\times 10^4$
1.2283	39.416	1.0008	1.0060	1.0004	1.0061	1.2948	1.2934	+14
1.7514	47.027	1.0011	1.0086	1.0001	1.0047	1.2942	1.2967	-25
2.1315	51.953	1.0014	1.0105	1.0001	1.0040	1.2998	1.2991	+7
3.6082	67.578	1.0023	1.0181	1.0001	1.0027	1.3084	1.3084	0
4.3076	73.849	1.0028	1.0219	1.0001	1.0024	1.3140	1.3128	+12
5.1330	80.537	1.0033	1.0260	1.0001	1.0021	1.3170	1.3180	-10
6.2058	88.513	1.0041	1.0320	1.0001	1.0019	1.3242	1.3247	-5
7.2744	95.852	1.0048	1.0381	1.0001	1.0017	1.3333	1.3315	+18
8.2250	101.766	1.0054	1.0434	1.0001	1.0015	1.3365	1.3374	-9

The results were fitted by the method of least squares, giving the equation

$$\gamma_{\text{equa.}} = 1.2857 + 6.29 \times 10^{-3}P. \quad (1)$$

The last column of Table I shows the differences between experimental values of γ and those calculated using Equation (1). The mean difference is 0.0011 or approximately 0.08%. Extrapolation of Equation (1) to zero pressure yields $\gamma_0 = 1.2857$. The spectroscopic method (4) yields $\gamma_0 = 1.2857$ at zero pressure and the same temperature, 29.9° C. The difference is 0.00%. The experimental results and the least squares equation are plotted in Fig. 1.

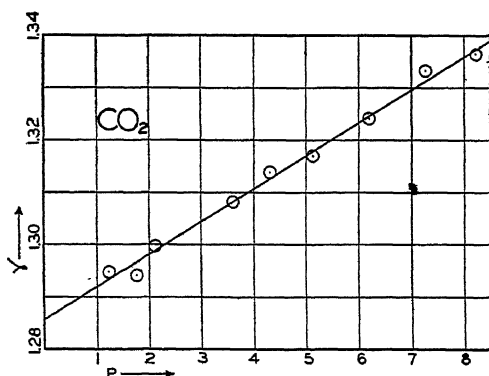


FIG. 1. Ratio of specific heats for carbon dioxide as a function of pressure, at 29.9° C.

Nitrous Oxide

Gamma has been determined previously for nitrous oxide (2) but at zero pressure the resulting value was 0.38% higher than that obtained by the spectroscopic method (3). A supply of nitrous oxide of 98 to 99% purity was obtained, the impurity being nitrogen. The gas was put through a five stage distillation similar to that employed with carbon dioxide. Table II shows the results obtained.

TABLE II
NITROUS OXIDE (25.3° C.)

Pressure, atm.	Resonance frequency, c.p.s.	Δ	G	χ	Γ	γ	$\gamma_{\text{equa.}}$	$\gamma - \gamma_{\text{equa.}}$ $\times 10^4$
1.4017	38.943	1.0007	1.0081	1.0002	1.0049	1.2795	1.2794	+ 1
1.6944	42.816	1.0009	1.0098	1.0002	1.0043	1.2811	1.2810	+ 1
1.8877	45.177	1.0010	1.0109	1.0002	1.0040	1.2813	1.2821	- 8
2.3101	49.986	1.0013	1.0134	1.0003	1.0033	1.2845	1.2848	- 3
2.6944	54.005	1.0015	1.0158	1.0002	1.0031	1.2884	1.2876	+ 8
2.9757	56.755	1.0016	1.0175	1.0002	1.0029	1.2906	1.2897	+ 9
3.6897	63.165	1.0025	1.0219	1.0001	1.0026	1.2954	1.2959	- 5
4.8102	72.156	1.0033	1.0290	1.0001	1.0022	1.3061	1.3077	-16
5.3356	76.118	1.0037	1.0325	1.0001	1.0020	1.3152	1.3141	+11

The constants of the apparatus were as follows:

Mass of piston = 114.361 gm.

Volume of enclosed gas = 32.808 cm.³

Effective area of end of piston = 7.9165 cm.²,

whence $\gamma = 1.1663 \times 10^{-3} \frac{f_m^2}{P_0} \Delta \chi G \Gamma$.

We used the same Pv - P data as used previously (2). The results were fitted by the method of least squares to the following second order equation

$$\gamma_{\text{equa.}} = 1.2744 + 2.25 \times 10^{-3}P + 9.73 \times 10^{-4}P^2. \quad (2)$$

The last column of the table shows the differences between experimental values of γ and those calculated using Equation (2). The mean difference is 0.0007 or 0.05%. Equation (2) yields a zero pressure value $\gamma_0 = 1.274$. The spectroscopic method (4) yields $\gamma_0 = 1.2733$ at the same temperature, 25.3° C. Our value differs from the spectroscopic value by 0.0011 or 0.09%. The experimental results and the least squares equation are plotted in Fig. 2.

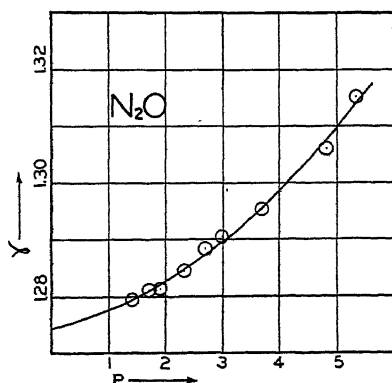


FIG. 2. Ratio of specific heats for nitrous oxide as a function of pressure, at 25.3° C.

Methane

Methane of 99% purity was obtained and was purified by the previously described five stage distillation over liquid air. The Pv - P data of Keyes and Burks (6) was used in calculating Λ and G . The apparatus constants were the same as for nitrous oxide. The results for methane are shown in Table III.

TABLE III
METHANE (25.1° C.)

Pressure, atm.	Resonance frequency, c.p.s.	Λ	G	χ	Γ	γ	$\gamma_{\text{equa.}}$	$\gamma - \gamma_{\text{equa.}}$ $\times 10^4$
1.5471	41.319	1.0003	1.0027	1.0003	1.0086	1.3023	1.3025	- 2
2.0435	47.517	1.0004	1.0036	1.0002	1.0070	1.3031	1.3028	+ 3
2.5402	52.973	1.0005	1.0045	1.0002	1.0059	1.3026	1.3033	- 7
3.2130	59.633	1.0006	1.0057	1.0002	1.0050	1.3056	1.3045	+11
3.6238	63.317	1.0007	1.0064	1.0002	1.0046	1.3056	1.3055	+ 1
3.9704	66.295	1.0008	1.0070	1.0001	1.0043	1.3068	1.3063	+ 5
4.4032	69.788	1.0008	1.0078	1.0002	1.0040	1.3066	1.3077	-11
4.8240	73.086	1.0009	1.0086	1.0001	1.0037	1.3086	1.3091	- 5
5.2965	76.646	1.0010	1.0094	1.0001	1.0034	1.3117	1.3109	+ 8

The experimental values of γ , at 25.1° C., were fitted by the method of least squares by the following equation:

$$\gamma_{\text{equa.}} = 1.3029 - 1.05 \times 10^{-3}P + 4.84 \times 10^{-4}P^2. \quad (3)$$

Table III also shows the differences between experimental values of γ and those calculated using Equation (3). The mean difference is 0.0006 or 0.05%. Equation (3) yields a zero pressure value $\gamma_0 = 1.3029$.

Using the value of C_{p0} obtained by Vold (8) by the spectroscopic method, the zero pressure value of γ at the same temperature (25.1° C.) is 1.303₀. These values differ by 0.0001 or 0.01%. The experimental results and the least squares equation are plotted in Fig. 3.

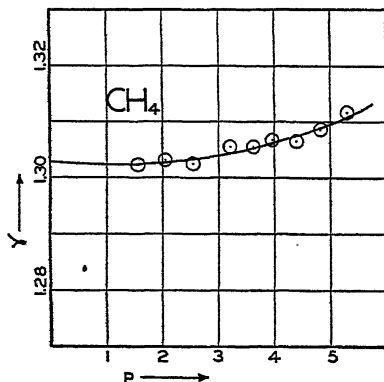


FIG. 3. Ratio of specific heats for methane as a function of pressure, at 25.1° C.

It is of interest to note that Vold sets an upper limit of 3% on the error in his value of C_{p_0} . An error of 3% in C_{p_0} introduces an error of 0.9% in γ_0 . The excellent agreement of our zero pressure value with that using Vold's results indicates that his values of C_{p_0} for methane are probably accurate to within a few tenths of one per cent.

Summary

Table IV gives a summary of results by the resonance method, together with results obtained by spectroscopic methods by various observers.

TABLE IV
SUMMARY OF RESULTS

Gas	Temp., ° C.	γ , Present work		γ_0 , Spectroscopic methods, 0 atm.	Diff. %
		1 atm.	0 atm.		
CO ₂	29.9	1.292 ₀	1.285 ₇	1.2857 (4)	0.00
N ₂ O	25.3	1.277 ₆	1.274 ₄	1.2733 (4)	+0.09
CH ₄	25.1	1.302 ₃	1.302 ₉	1.303 ₀ (8)	-0.01

References

1. CLARK, A. L. and KATZ, L. Can. J. Research, A, 18 : 22. 1940.
2. CLARK, A. L. and KATZ, L. Can. J. Research, A, 19 : 111. 1941.
3. CLARK, A. L. and KATZ, L. Can. J. Research, A, 21 : 1. 1943.
4. KASSEL, L. S. J. Am. Chem. Soc. 56 : 1838. 1934.
5. KATZ, L., WOODS, S. B., and LEVERTON, W. F. Can. J. Research, A, 27 : 27. 1949.
6. KEYES, F. G. and BURKS, H. G. J. Am. Chem. Soc. 49 : 1403. 1927.
7. MICHELS, A. and MICHELS, C. Proc. Roy. Soc. (London), A, 153 : 201. 1935.
8. VOLD, R. D. J. Am. Chem. Soc. 57 : 1192. 1935.

APPENDIX

Effect of Impurities

For a mixture of n gases, containing m_1, m_2, \dots, m_n moles of the different gases, the ratio of specific heats may be calculated as follows:

The heat absorbed by the mixture per degree centigrade rise in temperature at constant volume is given by

$$(DQ)_v = mC_{v \text{ mix}} = \sum_1^n m_j C_{v j}, \quad (1)$$

where $m = \sum_1^n m_j$. This equation assumes that there is no interaction between the molecules of the different gases.

Now, from thermodynamics,

$$C_{pi} - C_{vi} = T \left(\frac{\partial P}{\partial T} \right)_v \left(\frac{\partial V}{\partial T} \right)_P = R_i, \quad (2)$$

where R_i depends on the gas, temperature, and pressure, but is equal to the gas constant, R , at zero pressure.

Dividing each side by C_{vi}

$$\frac{C_{pi} - C_{vi}}{C_{vi}} = \gamma_i - 1 = \frac{R_i}{C_{vi}}, \quad (3)$$

or

$$C_{vi} = \frac{R_i}{\gamma_i - 1}.$$

Introducing this into Equation (1) we have

$$\frac{R_{mix}}{\gamma_{mix} - 1} = \sum_1^n \frac{r_i R_i}{\gamma_i - 1}, \quad (4)$$

where

$$r_i = \frac{m_i}{m}.$$

At zero pressure, $R_i = R_{mix} = R$

and

$$\gamma_{mix., 0} = 1 + \frac{1}{\sum_1^n \frac{r_i}{\gamma_i - 1}} \quad (5)$$

For a mixture of two components, where $r_1 \gg r_2$

$$\gamma_{mix., 0} = \gamma_1 + r_2 (\gamma_2 - \gamma_1) \left(\frac{\gamma_1 - 1}{\gamma_2 - 1} \right).$$

Change in γ of carbon dioxide caused by 1% by weight of various impurities:

Impurity	% change in γ
H ₂	+ 1.2
He	+ 1.3
A	+ 0.14
N ₂	+ 0.10
O ₂	+ 0.09
Air	+ 0.10

A RECORDING METER FOR AURORAL RADIATIONS¹

BY W. D. PENN AND B. W. CURRIE

Abstract

This paper describes a device that was developed to give a continuous record of the intensity of auroral radiations from the zenithal sky. Detection is by means of the multiplier phototube, R C A type 1P21. A null method of recording is used, the light flux reaching the phototube being kept to a constant value by moving a neutral, wedge filter in front of the phototube. A simple servo-mechanism is used for this purpose. A pen attached to the filter traces a record of the changes of auroral intensity on a clock-driven chart.

Introduction

The development of a convenient, mechanical device for recording the occurrence and intensity of auroras is a necessity, if progress is to be made in deducing reliable diurnal and annual variations of auroras and in detecting significant relations between auroral variations and magnetic, earth-current, and ionospheric disturbances. The visual observations, presently available, suffer from at least three faults that are inherent in using human instead of mechanical detectors and recorders. The first is a lack of continuity, since most observatories never have sufficient staff to keep a continuous watch on the night sky; the second arises from the inability of an observer to record more than a small fraction of the apparent auroral changes during active displays; and the third results from the lack of comparative standards of brightness and intensity, an observer having to depend on his previous experiences and his judgment in making estimates of these quantities.

Objective methods of recording auroral occurrence and intensity require the use of either photographic or photoelectric detectors. With photographic detectors the exposure times must be sufficiently long to make possible reliable measurements of the blackening of the emulsion. For the majority of displays, this condition requires exposures over periods that are long in comparison with the times for the more rapid changes in geomagnetic disturbance. However, the photographic method has been, and is, used to a limited extent (2, 3, 4), either the plate on a spectrograph being moved slowly parallel to the slit or a film being moved slowly past a narrow slit through which can pass the auroral radiations from a particular region of the sky. While photoelectric detectors respond almost instantaneously to changes of flux, the currents induced by the auroral radiations are so small that they require considerable amplification to operate a recorder. Until the development of multiplier phototubes, this meant the use of fairly involved electronic circuits that evidently could not be operated satisfactorily under the conditions usually

¹ Manuscript received November 8, 1948.

Contribution from the Physics Department, University of Saskatchewan, Saskatoon, Sask. This paper was presented at the General Assembly of the International Union of Geodesy and Geophysics at Oslo, Norway, August 19-28, 1948.

prevailing at high-latitude observatories. In any case, no systematic study of the records from such a device has appeared in auroral literature, although the use of the records has been mentioned (6).

Gartlein (1) has operated a photoelectric recorder, using a multiplier phototube, at Ithaca, New York State, for several years. This recorder apparently uses a rotating sector disk to pulse the radiations incident on the phototube, an alternating current amplifier, a rectifier, and a recorder. The writers have operated a photoelectric recorder, also using a multiplier phototube, at Saskatoon, Saskatchewan ($52^{\circ} 6' \text{ N.}$, $100^{\circ} 36' \text{ W.}$). It makes use of a null method of recording, the flux on the phototube being kept substantially constant by using a servo-mechanism to move a neutral wedge filter backward and forward in front of the phototube. The results to date indicate that a great deal of useful information concerning auroral intensities (the integrated effect of brightness over a particular region of the sky), can be secured by this device, or by modification of it, for correlation with various types of geomagnetic disturbance.

Details of the Recorder

One of the most sensitive photoelectric detectors of low light fluxes available is the tube referred to as R C A Type 1P21. It has an average current amplification factor of 1.2×10^6 for a power supply of 100 v. per dynode stage. This large amplification makes it particularly suitable for detecting the smallest auroral fluxes, since with it there is a minimum need for external amplifying units that not only add to the bulk of the recorder but increase the possibility of an unfavorable signal-to-noise ratio. However, it is subject to a fatigue in the later and higher-current stages that increases rapidly for increasing output currents above $10 \mu\text{a.}$ This is a matter of some concern in using this type of phototube in an auroral recorder, since the recorder should yield reliable values of light fluxes ranging from those of the twilight sky to those of the normal night-sky when covered with cloud. Assuming a brightness of 10^{-8} candles per cm.^2 for the night-sky, an effective reduction of this quantity by a factor of 10^{-2} by cloud, and a brightness of 10^{-5} candles per cm.^2 for the zenithal sky when the sun is 8° below the horizon, the maximum flux on the phototube amounts to 10^5 times the minimum flux.

Two methods may be used to control the output current at times of high light flux. One is to reduce the dynode voltage by the plate-cathode current of a control tube, the grid voltage of which is dependent on the current from the phototube (5), and the other is to reduce the light flux incident on the phototube by moving a wedge filter between the phototube and the sky. The latter method was adopted, since the changes of light flux could be conveniently recorded by attaching a pen to the filter and having it leave a trace on a clock-driven chart.

A simple servo-mechanism is used to move the filter. The circuit diagram for the recorder (including the servo-mechanism), is shown in Fig. 1. The voltage drop across a 1-megohm resistor (R_{13}) in the anode circuit of the

phototube, due to any low value of the light flux reaching the phototube, is balanced by the voltage drop across a variable resistor (R_4). These two voltages are applied to the grids of a balanced voltage amplifier (V_6 and V_7). The anodes of the tubes in the voltage amplifier are connected to the grids of a balanced power amplifier (V_4 and V_5). The currents from the tubes in the power amplifier flow in opposite directions through the split-field windings of a motor, so that the motor is motionless as long as the two currents are equal. A brass rod (53 threads per inch) is attached to the shaft of the motor, and carries a steel nut that is fastened to the filter. When the light flux reaching the phototube increases or decreases to a value where a voltage differential of about 0.25 v. from the preset condition is established, the motor rotates and moves the filter to a position that restores the initial balance.

A power supply (T_1 and V_1) delivers 120 ma. at 350 v. to the servo-mechanism, and also feeds a glow tube (V_3) through a resistor (R_3) to provide a ± 150 v. source. This source provides the voltage drop across R_4 and R_5 that is used in balancing the voltage drop across R_{13} . It also provides the voltage for the final stage of the phototube. Small variations of the power supplied by this unit do not affect the operation of the recorder.

A second power supply (T_2 and V_2), consisting of a 1500 v. transformer and a beam power tetrode gives the adjustable and stabilized voltages that are required for the first nine stages of the phototube. The cathode of V_2 is grounded, and the end of the secondary winding of T_2 in series with the plate circuit is at an output voltage of -720 to -1080 v., depending on the setting of a rheostat (R_{14}). A potential divider (R_1 , R_{14} , R_{15} and R_{16}) is connected between the output voltage and the aforementioned voltage of $+150$ v. A portion of this potential difference (across R_{14}) is applied to the grid of V_2 ; and the positive side of the 150 v. supply is connected to the screen of V_2 . If the output voltage changes, the portion of this change applied to the grid is of such a polarity as to cancel the variation in the output. This circuit gives a high degree of stabilization in the output voltage over a line voltage range of 83 to 135 v., a.c. The output voltage is applied to the dynodes of the phototube by means of a resistor chain (R_{17} to R_{25}), which is mounted on the base of the phototube.

The armature of the servo-motor operates on a current of about 1.5 amp. from a 6 v. supply. For convenience, a transformer giving a secondary voltage of about 6.3 v. and a copper oxide rectifier are used instead of a storage battery.

The wedge filter in use during the past year was made by exposing Process film in such a way that the resulting optical density across a 7 in. strip varied almost linearly from 0 to 3.5. However, suitable wedge filters having a somewhat larger density range are available commercially, and their purchase is recommended since a great number of trials is usually required before one with approximately linear characteristics can be made photographically.

The drum, which carries the paper past the pen, is driven by a small a-c. motor through a train of reducing gears so that the paper advances at the rate of about 4.5 in. per hr. A glazed paper (available commercially for recording galvanometers) about 11 in. wide is used. A satisfactory combination of pen and ink, for all weather conditions is still to be found. A satisfactory combination for active displays during cold weather gives a broad trace during periods of quiet aurora and warm weather. In addition to obscuring some of the finer detail in the auroral record, this broad trace smudges readily because of the time required for it to dry. So far, the nearest approach to a satisfactory pen is one made by drilling a hole of 0.013 in. diameter along the axis of a circular brass rod, bevelling the end of the rod with the hole until a tip about 0.03 in. diameter is formed, and then drilling out the other end to form an ink reservoir about 0.25 in. diameter. A fine wire of 0.012 in. diameter passes through the hole in the tip and rests on the paper when the pen is in use. The length of the hole partly determines the rate of flow of the ink. For the aforementioned dimensions a length of 0.25 in. gives the best results during warm weather. The type of ink that is used at the present time is one used for autographic meteorological instruments during cold weather.

Time marks are placed on the record at five-minute intervals by a second pen that is operated electromagnetically through the closing of a circuit by a master clock located in the laboratory. This clock is also used to start the recorder at a selected time each evening and to stop it the following morning.

Baffles with circular openings restrict the light flux to a cone with a half-angle of 22.5° . Ordinarily, the recorder is operated so that the axis of this cone passes through the zenith. A weatherproof box (28 by 19 by 23 in.) encloses the recorder, a circular glass plate in the top admitting the light flux.

Calibration marks are placed on the charts once each week by the unit that is shown diagrammatically in Fig. 2. This is placed over the window of the recorder. It excludes all light except that from a tungsten lamp that is operated at a known, constant voltage. A series of diffusing screens and diaphragms between the lamp and the recorder reduce the flux from the lamp to the same magnitude as that from the sky. A movable brass strip with a series of apertures of known diameters is used to admit different light fluxes to the phototube.

Experience with the Recorder

Experience with the recorder (intermittently during August and September, 1947, and almost continuously since then) indicates certain advantages and disadvantages of the recorder. With little or no moonlight or twilight and with clear skies, the duration of zenithal aurora per night can be determined with an estimated error of about five minutes, the time at which a rapid change of auroral intensity begins or ends can be determined to within 30 sec. of the actual time, and small changes of intensity that would certainly be ignored in visual observations are evident on the records. With increasing

moonlight or twilight, the durations of displays and the times at which large intensity changes occur become less certain, since the logarithmic response of the recorder gives a smaller displacement on the chart for an aurora of a given

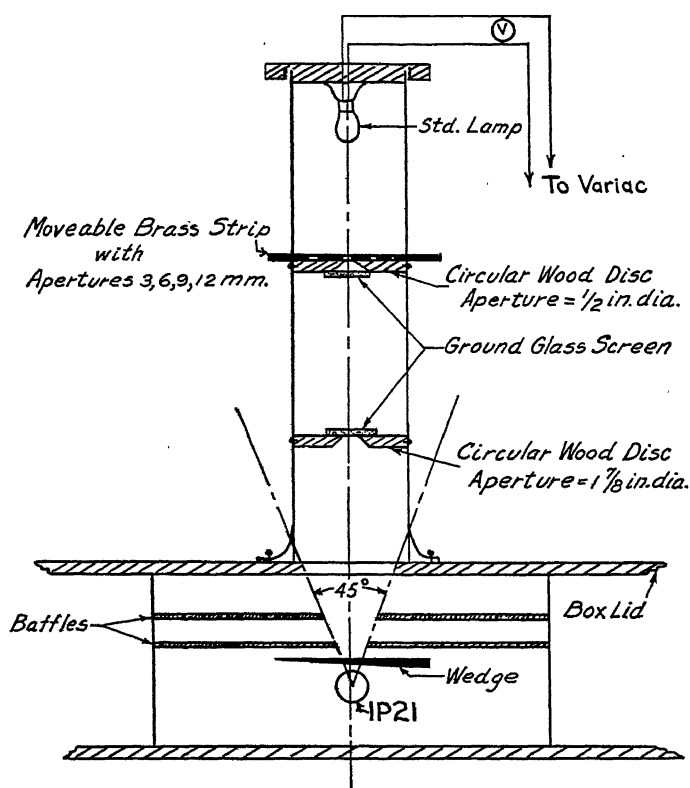


FIG. 2. A semidiagrammatic sketch of the unit used for placing calibration marks on the charts of the auroral recorder.

intensity when accompanied by moonlight or twilight than when the night is dark. However, the presence of all except faint aurora is evident as a superimposed variation on a regular trend in the trace due to the moonlight and twilight radiations. Broken cloud during periods of moonlight and twilight introduces an ambiguity into the record that cannot be settled with certainty. The direct effect of cloud is to reduce the recorded intensity. This can be readily detected by drawing a smooth curve on the chart for the intensity of the moonlight or twilight, if the sky had been clear. Unfortunately, light reaching the ground through breaks in the cloud cover is diffusively reflected back to the cloud and then to the recorder (especially with a snow cover), and gives a record that may be easily interpreted as one due to aurora. Reflection of the light from the city lamps by clouds also gives a record that is difficult to interpret.* Although the intensity of the aurora (in relative units)

* It has been suggested that cloud in the zenithal sky could be registered on the record by using a small searchlight to flash a beam upward at periodic intervals.

can be readily determined for any instant from the record, the average hourly intensity cannot be estimated as readily by inspection as on autographic records with a linear scale.

Figs. 3 and 4 show photographic reproductions of the auroral record for the night of March 14-15, 1948. This was a night with much quiet aurora in the zenithal sky, and with little cloud. The straight line that is drawn along the

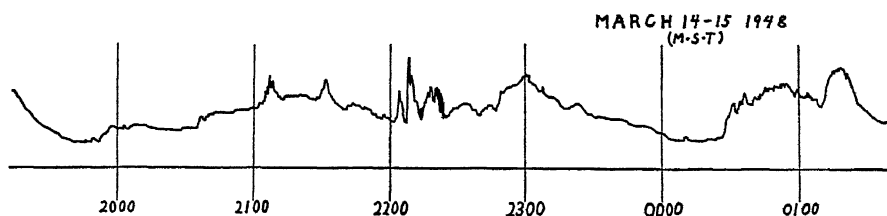


FIG. 3. A photographic reproduction of the auroral record for the evening hours of March 14-15, 1948. The heavy, horizontal line near the bottom of the record indicates the intensity of the radiations from a clear sky without aurora.

lower side of each record shows the position on the record corresponding to the light flux from the normal night sky. The upward trend in the record that starts at about 0400 hr. is due to the morning twilight. Superimposed on this part of the record is evidence of a very oscillatory type of aurora.

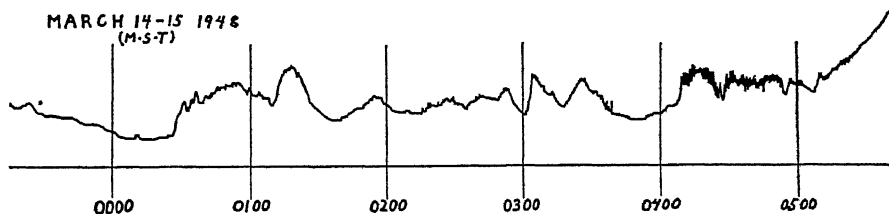


FIG. 4. A photographic reproduction of the auroral record for the morning hours of March 14-15, 1948.

Visual observations of aurora at Saskatoon indicate that this is a characteristic feature of aurora in this region just before sunrise. Pulses of auroral light travel in rapid succession upward to the zenith from the horizon toward the sun. While the time response of the recorder is too slow to record the full intensity of these pulses, it does indicate their occurrence. Some estimate of their intensity can be made by exposing the recorder to an intermittent source of illumination, and noting the frequency of illumination required to reduce the amplitude of the record to one-half of its value when the frequency of illumination is sufficiently slow for the maximum changes to be recorded.

Fig. 5 is a photographic reproduction of the auroral record for the night of May 14-15, 1948. The effects of twilight and some moonlight are evident in this record. The aurora on this occasion was more active than on March 14-15, probably owing to the presence of solar radiation in the upper atmosphere at this time of year.

Comparisons of the auroral records for four days of very active aurora at Saskatoon with the corresponding magnetic records from the Meanook Magnetic Observatory ($54^{\circ}37'N.$, $113^{\circ}20'W.$) showed remarkable similarities

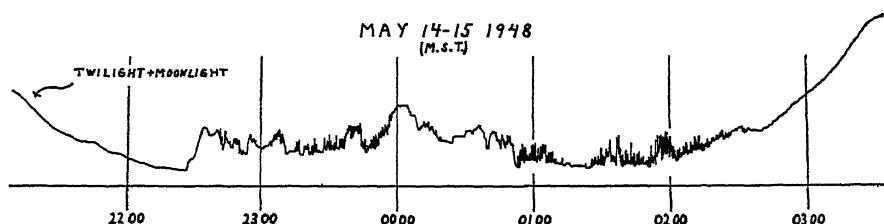


FIG. 5. A photographic reproduction of the auroral record for the night of May 14-15, 1948.

between the changes of auroral intensities and the variations of the H component and to a lesser extent of the Z component, although the two places are about 550 miles apart. However, both places have about the same geomagnetic latitude ($61.8^{\circ}N.$ for Meanook and $60.5^{\circ}N.$ for Saskatoon), so that the changes in the current systems responsible for the magnetic variations at Meanook must have been accompanied by corresponding time variations of auroral intensity at Saskatoon. Again, the intensity changes during auroral displays on successive nights are occasionally so similar as to leave little doubt that some features of an aurora are repeated on successive nights. Still another feature of the records for the past year is the high frequency of aurora in the morning hours, indicating that the diurnal maximum at Saskatoon may occur three to four hours after local midnight.

A detailed analysis of the records will appear in a later communication.

Acknowledgment

The development of this recorder and its operation was made possible by financial assistance from the National Research Council of Canada.

References

1. GARTLEIN, C. W. Rochester Eng. 24 : 82. 1945.
2. GARTLEIN, C. W. Document T124, Eighth Assembly, International Union of Geodesy and Geophysics. Oslo. 1948.
3. HARANG, L. Terr. Magn. Atm. Elec. 37 : 167. 1932.
4. HARANG, L. Terr. Magn. Atm. Elec. 51 : 353. 1946.
5. SWEET, M. H. J. Optical Soc. Am. 37 : 432. 1947.
6. VEGARD, L. Section on the aurora in Terrestrial magnetism and atmospheric electricity. Edited by J. A. Fleming. McGraw-Hill Book Company, Inc., New York. 1939.

DETERMINATION OF THE ELEMENTS OF METEOR PATHS FROM RADAR OBSERVATIONS¹

BY D. W. R. MCKINLEY AND PETER M. MILLMAN

Abstract

Methods of determining meteor velocities from single-station observations are discussed. Where three-station observations are available both the velocity and the elements of the meteor's path through the atmosphere can be computed in favorable cases. These methods are applied to a selected daytime meteor, recorded by the three radar stations at 17^h 59^m 48^s E.S.T., Aug. 4, 1948. The following elements of the meteor's path have been obtained from the radar data:—

Apparent geocentric velocity	35.0 ± 0.4 km. per sec.
True bearing of apparent radiant	074° ± 2°
Elevation of apparent radiant	2° ± 2°
Total radar path length	270 km.
Height above sea level	108–104 km.

These values lead to an orbit similar to one of the short-period comets, with these elements:—

Semi-major axis	a	2.66
Eccentricity	e	0.87
Angle node to perihelion	ω	294°9
Longitude of node	Ω	132°4
Inclination	i	33°6
Period	P	4.33 years

Introduction

It is now well established that the ionization produced by the passage of a meteor through the atmosphere at heights in the neighborhood of 100 km. above the earth can be detected by conventional radar equipment operating in the frequency range 3 to 200 Mc. per second. Assuming that the other parameters of the radar system remain constant it has been found that the meteor echo rates vary roughly as the square of the wave length. The durations of the echoes exhibit a similar dependence on the wave length. At first glance it would seem that the longer the wave length the better for the radar observation of meteors but several factors must be taken into consideration. If steerable directive antennas are to be used the shorter wave lengths are obviously preferable because the physical size of an array of given gain may be reasonable at 4 meters, say, but prohibitive at 40 meters. On the shorter wave lengths the echo is usually received only from a short portion of the meteor path in the immediate vicinity of the point where the meteor crosses the line of sight at right angles (17). This normal reflection law has been used by Hey and Stewart (5), Clegg (1), and McKinley and Millman (7) to determine the radiants of meteor showers by various techniques. On the

¹ Manuscript received January 27, 1949.

Contribution from the Radio and Electrical Engineering Division, National Research Laboratories, and from the Dominion Observatory, Ottawa, Canada. Issued as N.R.C. No. 1927, and Contributions from the Dominion Observatory, Vol. II, No. 5.

longer wave lengths a longer portion of the meteor path becomes visible on the radar display, subject to the limitation that detectable ionization is usually produced only within the *M*-region (7) extending from 80 km. to 110 km. above sea level. Another point worthy of consideration in the choice of an operating wave length is the interference to be encountered on the longer wave lengths from distant high-frequency transmitting stations. Daytime absorption of the radio wave in the upper atmosphere is more pronounced on the longer wave lengths.

Taking all these factors into account it was decided to use radio frequencies in the band 30 to 36 Mc. per second (10.0 to 8.3 meters) as a reasonable compromise. Three complete and independent radar stations were installed, at Ottawa, Arnprior, and Carleton Place, see Fig. 1. The Ottawa station

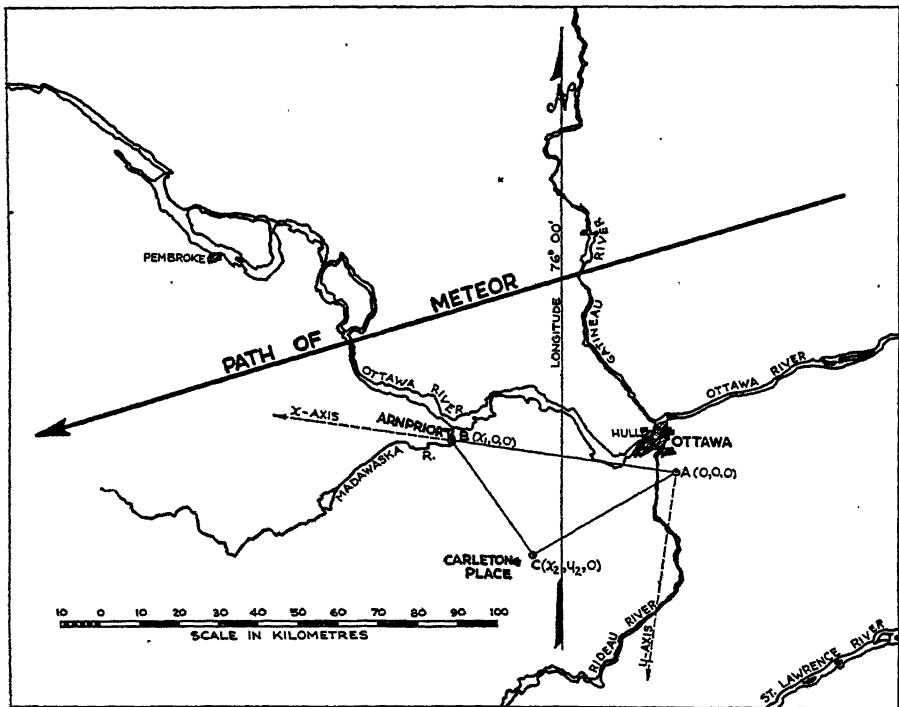


FIG. 1. Map showing positions of radar stations and path of meteor at 17^h 59^m 48^s E.S.T. Aug. 4th, 1948.

has been operated intermittently since August, 1947, and the Arnprior station was first put on the air in April, 1948. The Carleton Place station commenced operation about the first of August, 1948, and all three stations were run on a 24 hr. schedule for the annual Perseid shower during the first two weeks of August. The geographical co-ordinates, base lines between the three stations, and the essential electrical parameters are given in Table I.

TABLE I

	<i>A</i> -Ottawa	<i>B</i> -Arnprior	<i>C</i> -Carleton Place
Latitude N	45° 20' 32"	45° 24' 55"	45° 09' 20"
Longitude W	75° 36' 05"	76° 21' 38"	76° 05' 17"
Interstation distances, km.	<i>AB</i> = 57.44	<i>BC</i> = 35.94	<i>CA</i> = 41.20
Transmitter peak power, kw.	400	50	50
Pulse width, μ sec.	20	8	8
Receiver sensitivity, w.	2×10^{-14}	5×10^{-14}	5×10^{-14}
Radio-frequency, Mc./sec.	32.7	36.0	34.5
Antennas	Half-wave horizontal dipoles, mounted a quarter-wave above ground		
	Orientation N-S	Orientation NW-SE	Orientation NW-SE
Display	Range-time sweep, intensity-modulated by signal		

The range-time display is similar to the one conventionally used in ionospheric recording. A horizontal linear sweep, about 350 km. long, is displayed on a 5GP11 cathode ray tube. Twenty-kilometer negative marker pips are applied to the intensity-grid of the c.r.t. for range calibration. Seconds pulses received by radio at the three locations from station CHU operated by the Time Services of the Dominion Observatory (19) are fed through special circuits which produce positive pips on the intensity grid. These seconds pips are applied twice to the range sweep, near minimum and also near maximum range, so that alignment errors in the recording system can be eliminated. A special camera photographs the range sweep continuously on a 100 ft. roll of 35 mm. film which is moved at a constant speed past the open lens. Film speeds of $\frac{1}{2}$, $\frac{3}{4}$, 1, 2, and 4 in. per min. are available. The positive video output from the receiver is passed through a limiter circuit and applied to the intensity-grid of the cathode-ray tube.

Suppose that a target moving through space in a straight line with a constant velocity v is detected by the radar system. The echo on the range-time display will describe a hyperbola, defined by:

$$R^2 = R_0^2 + v^2 (t - t_0)^2, \quad (1)$$

where R is the range to the target at time t and R_0 is the minimum range to the straight line path of the target at time t_0 . In general, a meteor will produce detectable ionization only while traveling between the approximate height levels of 110 and 80 km., so that the possible ionized path length will depend on the inclination of the meteor's path to the tangent plane of the earth—that is, on the angle of elevation of the meteor radiant. A bright meteor traveling nearly tangentially to the earth's surface could thus produce an ionized path several hundred kilometers long, but a similar meteor arriving

from near the zenith would produce ionization over 10 to 30 km. only of its path. Whether or not all or a part of this ionized path is actually detected by the radar system depends on a number of conditions. A faint meteor can usually be detected only over a very short path length in the neighborhood of the R_0 point, and if this point on the path does not fall within the M -region no echo is seen. A bright meteor can be detected over a longer portion of its ionized path, even if this portion is located on the hyperbola at some distance from the R_0 point, on either the approaching or the receding branch. The picture is further complicated in many cases by the appearance of echoes definitely associated with the meteor, but delayed in time after the passage of the meteor. The various characteristic echoes and a theory to account for them are discussed in detail elsewhere, and a classification table (7, 9) has been drawn up to aid in describing the echo types seen on the range-time display. In this paper we shall consider only those echoes which appear to have a clearly defined component (h characteristic) moving with the meteor velocity. In the terminology of the classification table these will be the Ah , Dh , or Uh types, and the more complicated examples of these types, such as an $Ahbe3$ echo. Echoes falling in the Ab , Db , or Ub classes are not as reliable for velocity determination, as experience has shown that the leading-edge envelope of the echo curve on the range-time display often yields an equivalent velocity somewhat lower than the real velocity of the meteor. Af , Ae , Df , and De echoes are quite useless for meteor velocity determinations because the apparent velocity they exhibit is not directly related to the actual meteor velocity, but depends on rather complicated factors involving wind drifts and possible changes of the reflection points on the trail (5), rates of expansion and decay of the ionized cloud, and delays in the appearance of the echo from various parts of the trail. These delays are functions of the height of the trail and of the angle between the meteor path and the observer.

Determination of Meteor Velocities from Single-station Observations

The first determination of meteor velocities from radar data was made by Hey, Parsons, and Stewart (4) using their observations on 60 Mc. during the Giacobinid shower in 1946. They obtained a faint fast-moving echo (h characteristic in our classification) which was assumed to have the meteoric velocity. From 22 tracks a velocity of 22.9 ± 1.3 km. per sec. was found and this corresponded satisfactorily with the theoretical velocity of 23.7 km. per sec. as computed from the cometary orbit. The h characteristic echoes detected on the lower frequencies used in our work appear more frequently and extend over a considerably greater path length than those observed by Hey, Parsons, and Stewart. On this basis the potential accuracy of our velocity measurements might be expected to be better. Other factors enter the problem, of course, and will be considered later.

To illustrate the discussion, let us refer to Fig. 2, which shows a meteor echo that appeared as type Uhb at all three stations on Aug. 4, 1948, at $17^h 59^m 45-53^s$ E.S.T. As this meteor occurred during daylight no visual

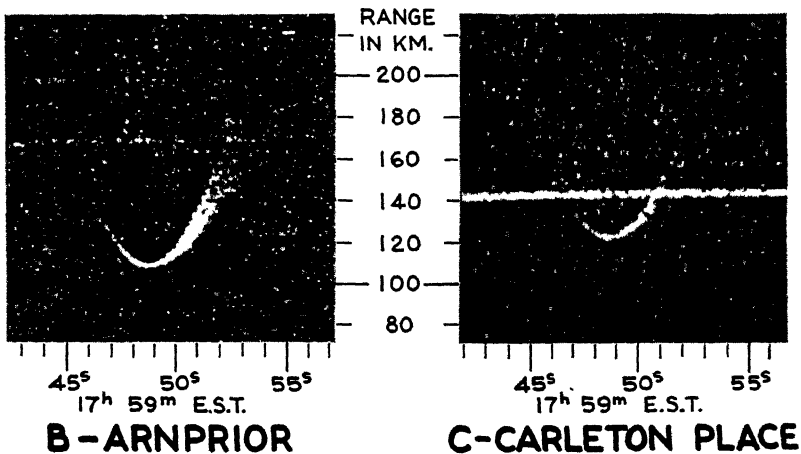
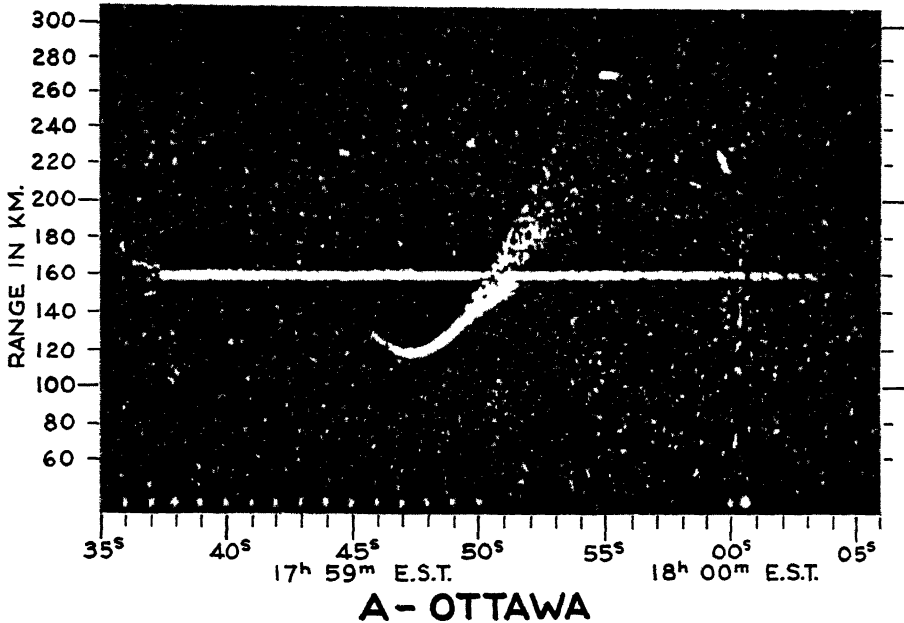


FIG. 2. Meteor echoes photographed at the three stations on Aug. 4th, 1948:—

- (a) A Uhb echo at 17^h 59^m 45-53^s. This is the echo that is considered in detail in this paper.
- (b) An F echo at 17^h 59^m 37^s, enduring for 27 sec. on the Ottawa record. This echo first appeared at a true height of 101 km. with bearing 197° and ground distance 120 km. from Ottawa. After 15 sec. the height of the echo was 94 km. and the apparent drift of the echo was about 20 km. in a southeast direction.
- (c) Visible on the Ottawa photograph are an F echo at 17^h 59^m 55^s, range 270 km., duration one second, and an Ah echo at 17^h 59^m 59^s, range 228 to 216 km. As these echoes did not appear at the other stations it was not possible to triangulate heights and positions.

or photographic observations were available. Various techniques for measuring the velocity of such an echo have been evolved and four of these methods are described below.

(i) *Curve-fitting Method*

It is possible to fit hyperbolic curves directly to an enlargement of any one of the Uh echoes of Fig. 2 and thus to determine by trial and error the best fit. This will give only an approximate value of the velocity because the range-time record suffers from several small distortions. For example, the range sweep is slightly nonlinear, so that the spacing of the 20-km. pips is not quite uniform; the sweep may have a slight bend due to stray steady magnetic fields; and the range axis may not be truly orthogonal to the time axis because of errors in lining up the c.r.t.-camera system. These irregularities can be eliminated by transferring the original echo curve point by point to a large sheet of standard graph paper. To do this the range intervals are first measured and then plotted to determine the range correction factor to be applied at any given range of the echo curve. Next, the time intervals are similarly measured and any necessary correction factors applied, though the time intervals are usually quite uniform. Any curvature in the c.r.t. sweep can be detected by momentarily brightening the sweep from time to time during the observations. This curved R axis must be used in reading points from the original photograph. Having transferred the echo curve to Cartesian co-ordinate paper, it becomes a simple matter to calculate and plot hyperbolae with the observational values of R_0 and t_0 and with various assumed values of v until the best fit is obtained with the observational curve. Probable upper and lower limits of velocity can be assigned by drawing curves which bracket the points of the observational curve. It may happen that the original curve deviates from a true hyperbola by more than the observational and measurement errors. When this occurs it is usually possible to explain the deviation in terms of the time delays associated with the angle of elongation of the meteor and height within the M -region, and small empirical corrections, deduced from known cases, can be applied with fair success.

(ii) $\dot{R}\dot{R}$ Method

In many cases of the Ah and Dh echo types, the echo segment of the hyperbola does not include the R_0 , t_0 point, so that the simple curve-fitting technique described above is difficult to apply. If the segment is long enough and sufficiently well delineated to allow the curvature to be accurately measured, it is possible to calculate the velocity, and at the same time to determine the R_0 , t_0 points with fair precision. Differentiating Equation (1) with respect to time, we have:

$$\dot{R}\dot{R} = v^2t - v^2t_0, \quad (2)$$

so that if $R\dot{R}$ is plotted against t we should obtain a straight line with slope v^2 . The values of \dot{R} may be obtained by precision measurements of the slope of the observational curve at selected points, either by graphical methods or by calculating differences. The time at which the line crosses the t -axis is the t_0 point. It is easier to fit a straight line to a set of points which are presumed to satisfy a linear relation than it is to fit a curve to the same observational data in hyperbolic form. In practice, the least squares method of determining the best straight line is used. Estimates are also made of probable error in v^2 due to the observational scatter, probable errors in measurement and reduction of the photograph, and probable errors in the range and time calibration.

(iii) *Three-Point Method*

Another method for the evaluation of v^2 involves substituting in Equation (1) three R, t values obtained from widely different parts of the observational curve, and solving the three equations simultaneously for v^2 . The algebra is straight-forward and yields for v^2 the formula:

$$v^2 = \frac{R_1^2 (t_3 - t_2) - R_2^2 (t_3 - t_1) + R_3^2 (t_2 - t_1)}{(t_2 - t_1) (t_3 - t_2) (t_3 - t_1)} \quad (3)$$

Uniform time intervals are usually selected so that this expression becomes simplified for practical computations. Needless to say, several sets of three-point values are used in calculating a mean v^2 . The t_0 point can also be computed from a similar formula.

(iv) *Parabolic Regression Method*

The curvilinear regression method of least squares (6) was also used in computing v . For this purpose ρ is written for R^2 in Equation (1) so that a parabolic relation should obtain between the observed values of ρ and t . The usual sets of normal equations are written down and solved. This method does use all the observational data simultaneously, but the calculations are rather tedious, and do not appear to lead to an answer that is any more trustworthy than that obtained by Methods (ii) or (iii).

The three types of errors that can affect the velocity determination are, in increasing order of importance, the basic errors in the range and time calibrations, the errors in measurement and reduction of the films, and the errors introduced by factors not under the control of the observer, such as the delays in echo appearance, and signal strength fluctuations.

The average timing error between consecutive seconds pulses is of the order of 0.02 sec. However, these pulses are supplied from a source with an integrated accuracy of 1 part in 10^6 or better so that if a number of seconds intervals are measured on the film, the basic error in timing can be reduced to the order of 0.001 sec., which is insignificant in the analysis. The intrinsic

accuracy of the 20 km. range markers is at present of the order of 0.1 km. over the working range of the display, and could be further improved if required. The effect of this range error on the single-station determination of v depends both on the value of v and on the mean range interval over which the echo is observed, but rarely contributes more than 0.1% to the error in v .

The sources of errors in measurement and reduction of the film have been discussed to some extent above. Careful application of all the scale correction factors involved is required to transfer the echo curve to large-scale co-ordinate paper. An inexperienced worker may introduce errors which affect the velocity by as much as 1 or 2%, but, with a skilled analyst, the reduction errors introduced at this stage are not significant in comparison with the larger errors to be considered below.

The greatest source of error lies in determining the real outline of the echo hyperbola—that is, in drawing on the photograph the thin line on which the measurements are made. The pulse width, the pulse rise time, the echo signal strength, and the probable delay times in the appearance of the echo at various parts of the path all have to be taken into consideration. When considering an Ah echo, the pulse width is immaterial, but the pulse rise time can cause small variations of the order of 0.3 km. in the apparent range measurements if the signal strength varies from barely detectable to saturation level. The density and width of the echo furnish a good indication of the signal strength up to the clipping level of the video limiter, and for higher signal strengths the length of the black shadow, due to the video overshoot, is a measure of signal strength. With these considerations in mind, a line can be drawn at or near the lower edge of the Ah echo. The Dh echoes are sometimes more difficult to treat. If the Dh echo is clean, i.e., with no trailing enduring part, the same technique is used as for the Ah types. More usually the Dh type has a reasonably well defined upper edge and a diffuse lower edge (b characteristic) so that the lower edge cannot be used. In these cases, the upper edge is used as the reference and the curve is drawn through points obtained by subtracting small distance intervals which are equal to or less than the pulse width in kilometers, depending on the signal strength and other factors mentioned above. In general, a Dh echo does not yield as reliable a velocity determination as the Ah or Uh types.

Determination of Meteor Paths from Three-station Observations

It will be apparent that in computing the meteor velocity from a range-time photograph made at a single station, the t_0 point is of little interest, except in the curve-fitting method. However, when computing the meteor path by triangulation from photographs made at three stations, it is essential to determine the three t_0 points with the greatest possible accuracy. The probable error of t_0 in Method (i) is of the order of 0.2 sec. or greater and the technique is applicable only to the Uh types. The probable error of t_0 in Methods (ii), (iii), and (iv) is of the order of 0.01 to 0.05 sec. when dealing with the Uh types, and of the order of 0.05 to 0.2 sec. in the Ah and Dh

cases, depending on the length and definition of the echo from the observed segment of the path. Accordingly, one or more of the latter three methods is used to determine the t_0 's at stations A , B , and C . The independent velocity determinations made at the three stations should agree within the respective probable errors, of course, and the data from all three stations are used in reaching a final weighted mean value of v . From Equation (1), using v and the t_0 values, the R_0 points at the three stations can now be calculated with considerably greater precision than is afforded by an inspection of the observational curves.

In computing the meteor path in space it is convenient to adopt Cartesian co-ordinates with the Ottawa station (A) at the origin, the Arnprior station (B) on the x -axis at $(x_1, 0, 0)$ and the Carleton Place station (C) at the point $(x_2, y_2, 0)$ in the x, y -plane through the three stations (see Fig. 1). If, at any given instant, the range of a target from Station A is R_A , from Station B is R_B , and from Station C is R_C , then the position of the target (x, y, z) is defined by the intersection of the spheres:

$$x^2 + y^2 + z^2 = R_A^2 \quad (4)$$

$$(x - x_1)^2 + y^2 + z^2 = R_B^2 \quad (5)$$

$$(x - x_2)^2 + (y - y_2)^2 + z^2 = R_C^2 \quad (6)$$

whence,

$$x = \frac{R_A^2 - R_B^2 + x_1^2}{2x_1} \quad (7)$$

$$y = \frac{R_A^2 - R_C^2 + x_2^2 + y_2^2}{2y_2} - x \frac{x_2}{y_2} \quad (8)$$

$$z = (R_A^2 - x^2 - y^2)^{\frac{1}{2}}. \quad (9)$$

By inserting various simultaneous values* of R_A , R_B , and R_C , each set of values being measured from the three observational curves at a selected instant in time, one can plot the meteor path in space. The points so obtained tend to be somewhat scattered because of small uncertainties in the determination of absolute time at the three stations. With present techniques these uncertainties are of the order of a few hundredths of a second.

A more satisfactory result can be achieved by using the data available from the velocity computations; namely, the mean value of v , the minimum ranges at the three stations, R_{0A} , R_{0B} , R_{0C} , and the corresponding times, t_{0A} , t_{0B} , t_{0C} . Equation (1) is then used to compute values of R_A , R_B , R_C at selected times. These sets of values are then inserted in Equations (7), (8), and (9), and a space plot of the meteor path is obtained. It can be shown that the x and y values computed in this particular manner will each be a linear function of time so that the horizontal projection of the path will be a straight line. This line will represent the best straight line that can be drawn through the x, y points that were obtained by direct triangulation. Owing to the arbitrary

sequence of Equations (7), (8), and (9) there will be a second-degree relation between z and t in general, though if the data were perfect the relation would become linear. In practice there will usually be a slight curvature of the computed path in the vertical plane, this curvature being attributable to small errors in v , R_{0A} , R_{0B} , R_{0C} , t_{0A} , t_{0B} , t_{0C} . It is possible to make small empirical adjustments to these parameters which will straighten out the space plot, but care should be taken that each correction is smaller than the probable error of the respective parameter. Because of the small intervals between the t_0 points the uncertainties in determining absolute time at the three stations tend to be more important than the errors in the other variables, so that any necessary adjustments are usually made to the t_0 parameters. However, this correction process should not be carried beyond the limitations of the observational data, as the effect on the orientation of the meteor path is not significant.

In practice the x and y co-ordinates are plotted on the ground plane map to show the projection of the meteor path, but the z co-ordinate is more conveniently plotted separately against time. The azimuth angle of the meteor path can be read directly from the map, and the elevation angle may be easily calculated from the z , t plot by making use of the velocity.

In the above discussion it has been assumed that the meteor path is theoretically a straight line. In general, the deviation of the observed path from a straight line owing to the earth's gravity (zenith attraction) and the rotation of the earth (diurnal aberration) will be measured in fractions of a degree, and is too small to be significant with the accuracy of measurement at present available. Where appreciable deceleration occurs, the meteor path will deviate from a straight line in the vertical plane but not in the x , y plane. Irregularities in the meteor path, such as those caused by explosions or bursts, may produce small deviations from linearity. Whipple (20) finds these are only very rarely as great as a third of a degree.

It might be remarked that meteor velocities can also be obtained by using a continuous-wave transmitter and measuring the Doppler whistles produced by the meteor echo (8). We have recently used this method, which yields accurate velocities from much shorter path lengths than those required for the radar method. We feel that a combination of techniques, using Doppler whistles for the velocities and three-station radar triangulation for the path positions, may greatly increase the number of meteors available for detailed path computations.

The Computation of a Meteor Path and Orbit

The $Uh\bar{b}$ meteor echo at $17^h 59^m 48^s$ Aug. 4th, 1948, shown in Fig. 2, is remarkable in the length of path visible by radar, and is a type rarely observed. During 2000 hr. of observations, about 50 such echoes displaying an ionized path well over 100 km. long have been photographed, and of this number only a dozen or so were obtained while all three stations were operating.

The reason for their rare occurrence is that the meteor must be traveling at a low angle to the horizontal plane and should be of a mass sufficient to ensure that it will not be completely vaporized for several seconds. The probability of a sporadic meteor which satisfies both these conditions occurring within range of the radar stations is very small. A strong meteor shower should increase the chances at the times of rising and setting of the shower radiant. Two striking photographs (9) of Lyrid meteor echoes were obtained on April 21, 1948, when the radiant was very low in the sky, though unfortunately only one station was operating at the time. The summer daytime showers (2), extending through May, June, and July also produced several such echoes, particularly when the radiants were setting. Several hundred meteor echo photographs are available which show from 50 to 100 km. path length, produced by meteors with higher radiants. The elements of the meteor paths calculated from these photographs have probable errors two or three times greater than the errors assigned to the exceptional low-angle cases.

As the preceding sections may have indicated, the work of reducing a three-station meteor echo is somewhat tedious and, therefore, will not be reproduced in detail. In the present case all four of the methods for measuring velocity were applied to the photographs and each yielded a velocity measurement agreeing with the others within the limits of the errors. The data for the RR method, for example, are plotted in Fig. 3 to show the dispersion of the points about the straight lines. The highest points on the Ottawa and Arnprior plots tend to show an upward curvature, and these are omitted in calculating the least squares lines, because they are derived from the less reliable parts of the original hyperbolae. The t_0 times for the three stations can be read immediately from Fig. 3 to an accuracy of the order of 0.03 second.

The smoothed path of the meteor was computed from the mean value of v and the R_0 and t_0 values, and it was noted that the horizontal projection of this path agreed well with the x, y points obtained by direct triangulation, the average deviation of the points being less than 2 km. Some apparent curvature in the z, t plot was reduced slightly by making small corrections to the t_0 times. The effect of this procedure on the horizontal plot was negligible. The x, y plot of the meteor path is shown in Fig. 1, and the z, t plot in Fig. 4. The solid portion of the straight line drawn through the points of Fig. 4 indicates the 160 km. of path length that was observed in common at all three stations, and the dotted extensions show the total path length as observed at the Ottawa station only. The apparent precision of the line in Fig. 4 is somewhat misleading, as the points are computed from smoothed data. The elevation of the radiant as deduced from this line is $+1^\circ$ but it would be safer to assume a mean elevation of $+2^\circ$ with a probable error of 2° , though this may be unnecessarily conservative. Entirely apart from the measurements made above it is possible to assign an upper limit of about 4° for the elevation solely on the assumption that the meteor fell 20 km. (the average effective thickness of the M -region) in its total recorded path length of 270 km.

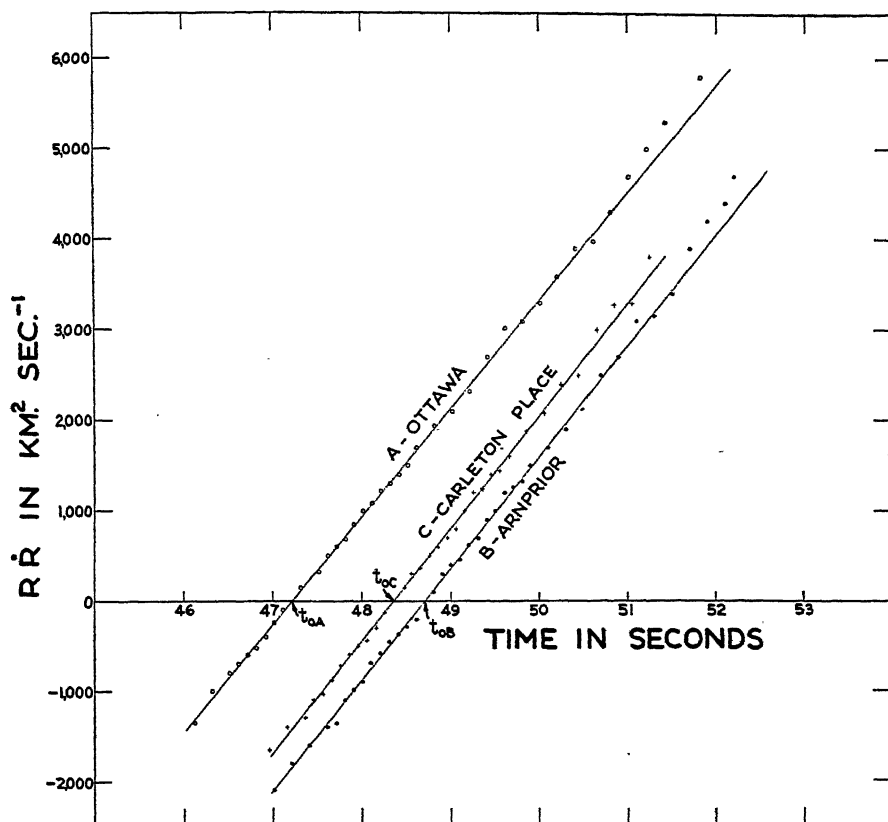


FIG. 3.

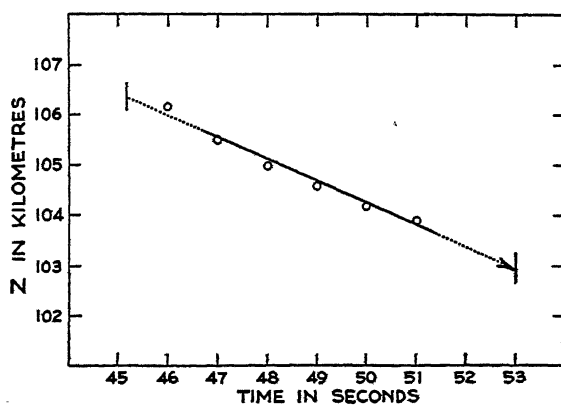


FIG. 4.

The radar data for this meteor are summarized in Table II.

It should be noted that the z values in Fig. 4 refer to heights above the co-ordinate plane through the three stations. True heights above sea level

TABLE II

	A-Ottawa	B-Arnprior	C-Carleton Place
R_0 , km.	117.8	108.6	122.1
t_0 , sec.	47.22	48.71	48.36
v , km./sec.	34.7 ± 0.6	35.3 ± 0.6	35.1 ± 0.6
Observed path length, km.	270	175	160
Apparent geocentric velocity		35.0 ± 0.4 km. per sec.	
Apparent radiant—true bearing		$074^\circ \pm 2^\circ$	
—elevation		$+2^\circ \pm 2^\circ$	
True height above sea level—beginning of path		108 km.	
—end of path		104 km.	

are obtained by correcting these values for the effects of the earth's curvature and the altitudes of the three stations. The height figures given in Table II refer to the beginning and end of the 270 km. path length observed at Ottawa.

The position of the apparent radiant determined above, when corrected for zenith attraction and diurnal aberration, gives a corrected radiant just one degree below the horizon at R.A. $324^\circ 7$, Dec. $+10^\circ 6$. This radiant position is within two degrees of the star ϵ Pegasi. An examination, by no means exhaustive, of various radiant lists (3, 10-16, 18) reveals nothing very striking in this region for the first week of August. Most of the radiants in this part of the sky are associated with the δ Aquarid shower and are located south of the equator rather than north. Radiant group No. 250 of Denning, radiants Nos. 1118, 1130, 1134, 1622, and 2225 of the American Meteor Society, and radiant No. 131 published by the Russian observers in Mirovédénie, 1925, are near ϵ Pegasi. These are all weak radiants represented by only four to seven meteors each. The meteor discussed in this paper may hence be considered to belong to the type generally classed as sporadic.

For the computation of the orbit about the sun it seemed advisable to take two possible positions of the apparent radiant, one at the observed elevation of 2° above the horizon, giving the meteor orbit, and the other at the maximum elevation that could be considered consistent with the radar data, i.e., 4° above the horizon. This second radiant position provides an alternative orbit which gives an indication of the order of magnitude of the changes in the elements resulting from a shift of the apparent radiant by two degrees. The computation of the two orbits was carried out by the Laplacian method, making use of the convenient summary of formulae published by Wylie (21).

The heliocentric velocity of the meteor was 37.6 km. per sec., well below the parabolic velocity for this date, 41.8 km. per sec. Both computed orbits are ellipses with eccentricities of 0.87 and aphelion points about the same distance from the sun as Jupiter's orbit. These orbits are therefore similar

to those of the short-period comets of Jupiter's family (22) but with somewhat higher eccentricities. The inclinations are near the upper limit for short-period meteor orbits determined up to the present. The orbital elements, for the equinox of date, are listed in Table III. The semi-major axes are given in

TABLE III

		Meteor orbit	Alternative orbit
Semi-major axis	a	2.66	2.98
Eccentricity	e	0.868	0.872
Angle node to perihelion	ω	294°9	290°8
Node	Ω	132°4	132°4
Inclination	i	33°6	34°8
Period, years	P	4.33	5.15

terms of the earth's mean distance from the sun. These orbits have been plotted in Fig. 5.

The changes in the elements resulting from the probable error in the observed velocity are, on the whole, smaller than those due to the uncertainties of radiant position. For example, if the observed velocity is assumed to be 34.6 km. per sec. we have $a = 2.49$, $e = 0.858$, $\omega = 294°6$, $i = 33°3$ and $P = 3.92$ years, giving an ellipse somewhat smaller than the plotted meteor orbit. The correction to the observed velocity for diurnal aberration was -0.3 km. per sec. for this meteor. This is less than the probable error in the observed velocity and was not included in the orbit computation.

The techniques here illustrated are applicable to individual echoes and hence should be particularly useful in examining specific meteors, either by day or by night, with a view to determining whether their orbits are hyperbolic or elliptical. This is an important consideration in any theory of the origin of meteors. While we have not yet made a detailed statistical study of meteor velocities it may be remarked that there has been no indication up to the present of hyperbolic orbits in the radar and Doppler data which we have accumulated.

Acknowledgments

It is a pleasure to record that three summer assistants, Dr. H. Kaufman, Mr. H. D. Griffiths, and Mr. R. L. Stauffer, carried out most of the computations of meteor velocity and three-station triangulation upon which this paper is based. Mr. E. L. R. Webb, with Mr. R. S. McClean as his assistant, supervised the design, construction, and operation of the radar equipment, while Mr. B. E. Bourne was responsible for many of the circuit details. It

would not have been possible to maintain the three radar stations on a 24 hr. watch for two weeks in August, 1948, without the enthusiastic co-operation of all personnel connected with the project.

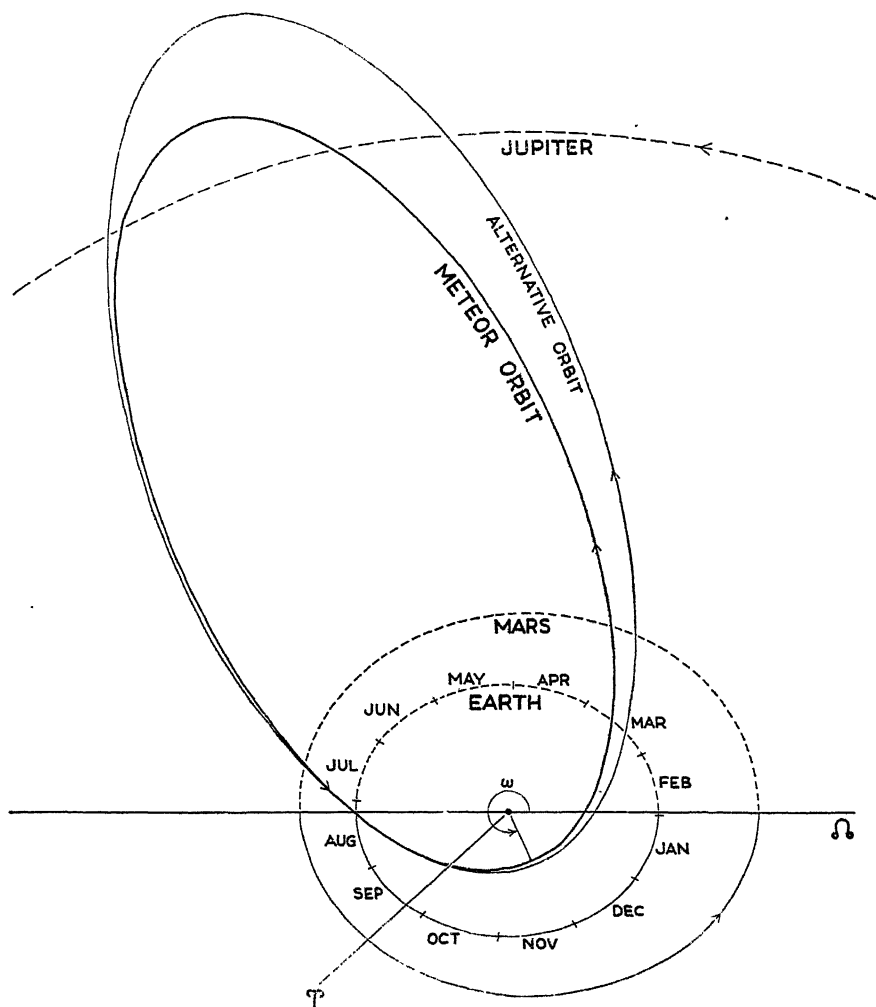


FIG. 5. *Computed meteor orbit.*

The Meteor Orbit, apparent radiant elevation + 2°, and the Alternative Orbit, apparent radiant elevation + 4°, have been plotted in the plane of the paper. The planetary orbits, inclined by approximately 34° to this plane, have been projected on to it.

References

1. CLEGG, J. A. *Phil. Mag.* (Ser. 7) 39 : 577. 1948.
2. CLEGG, J. A., HUGHES, V. A., and LOVELL, A. C. B. *Monthly Notices Roy. Astron. Soc.* 107: 369. 1947.
3. DENNING, W. F. *Mem. Roy. Astron. Soc.* 53: 203. 1899.

4. HEY, J. S., PARSONS, S. J., and STEWART, G. S. *Monthly Notices Roy. Astron. Soc.* 107: 176. 1947.
5. HEY, J. S. and STEWART, G. S. *Proc. Phys. Soc. (London)*, 59: 858. 1947.
6. HOEL, P. G. *Introduction to mathematical statistics*, pp. 89-90, 130-132, and 147-150. John Wiley & Sons, Inc., New York. 1947.
7. MCKINLEY, D. W. R. and MILLMAN, PETER M. *Proc. Inst. Radio Engrs.* 37: 364. 1949.
8. MANNING, L. A. *J. Applied Phys.* 19: 689. 1948.
9. MILLMAN, PETER M. and MCKINLEY, D. W. R. *J. Roy. Astron. Soc. Can.* 42: 121. 1948.
10. ÖPIK, ERNST. *Harvard Coll. Observ. Circ. No.* 388. 1934.
11. OLIVIER, C. P. *Trans. Am. Phil. Soc.* 22: 5. 1911.
12. OLIVIER, C. P. *Pub. Leander McCormick Observ.* 2: 131. 1914.
13. OLIVIER, C. P. *Pub. Leander McCormick Observ.* 2: 199. 1921.
14. OLIVIER, C. P. *Pub. Leander McCormick Observ.* 5: 1. 1929.
15. OLIVIER, C. P. *Popular Astron. Meteor Notes*, 1928-1947.
16. POKROVSKY, K. *Pub. Tartu Observ.* 25, No. 4: 77. 1923.
17. PRENTICE, J. P. M., LOVELL, A. C. B., and BANWELL, C. F. *Monthly Notices Roy. Astron. Soc.* 107: 155. 1947.
18. RUSSIAN AMATEUR SOCIETY FOR THE STUDY OF THE UNIVERSE, LENINGRAD, U.S.S.R., Section for the Observation of Meteors. *Mirovédenié, Astronomical Bulletin.* 1925-1930.
19. THOMSON, M. M. *J. Roy. Astron. Soc. Can.* 42: 105. 1948.
20. WHIPPLE, FRED L. *Proc. Am. Phil. Soc.* 91: 189. 1947.
21. WYLIE, C. C. *Popular Astron.* 47: 425. 1939.
22. YAMAMOTO, A. S. *Preliminary general catalogue of comets.* *Pub. Kwasan Observ.* 1: No. 4. 1936.

Canadian Journal of Research

Issued by THE NATIONAL RESEARCH COUNCIL OF CANADA

VOL. 27, SEC. A.

JULY, 1949

NUMBER 4

CONTRIBUTIONS TO THE THEORY OF WAVE GUIDES¹

BY W. Z. CHIEN², L. INFELD, J. R. POUNDER, A. F. STEVENSON,
AND J. L. SYNGE³

Abstract

Part I deals with the problem of determining the field due to a source of radiation inside a semi-infinite rectangular wave guide closed at one end by a plug, the current distribution in the source being regarded as known. Both the walls of the guide and the plug are treated as being perfectly conducting. Three different methods of solving the problem are given. The radiation resistance is then deduced from energy considerations. In particular, an expression for the radiation resistance of a linear antenna perpendicular to the wider face of the plug, fed at the point of entry, is derived, it being assumed that the antenna current is sinusoidal and that only the fundamental H -wave is transmitted by the guide.

In Part II, one of the methods of paper I is extended to the case of a guide of *arbitrary* cross section, and the general problem of the calculation of radiation resistance and reactance is discussed.

In Part III, a number of formulae for the radiation resistance of antennae of various shapes, with various assumed current distributions, in rectangular and circular guides, are given.

In Part IV, explicit calculations for the impedance of a linear antenna in a rectangular wave guide are given. Further numerical calculations relating to the same problem, from the point of view of matching and sensitivity, have been made by Messrs. Chien and Pounder, but are not reproduced here.

General Introduction

The four parts of this paper are based on four of the reports which were issued by the Special Committee on Applied Mathematics of the National Research Council, the authors of which were, at the time, members of the Department of Applied Mathematics of the University of Toronto. The four parts deal with rather closely related topics in the field of wave guide theory which are all of a certain mathematical interest.

They have been reproduced with only slight alterations from their original form, and no attempt has been made to refer to more recent work, although, so far as the authors are aware, most of the results contained herein have not hitherto been published. References are given at the end of each part separately. The figures and equations are also numbered separately for each part.

The authors wish to acknowledge the help received from the Field Station of the National Research Council.

¹ *Manuscript received October 29, 1948.*

Contribution from the Department of Mathematics, University of Toronto, Toronto, Ont.

² *Formerly of the University of Toronto.*

³ *Institute of Advanced Studies, Dublin.*

PART I. RADIATION FROM A SOURCE INSIDE A PERFECTLY CONDUCTING WAVE GUIDE OF RECTANGULAR SECTION

By L. INFELD, A. F. STEVENSON, AND J. L. SYNGE

1. Introduction

We consider a wave guide of rectangular section, extending to infinity in one direction and closed in the other direction by a plug. The guide and the plug are assumed to be perfect conductors.

A source of energy is placed inside the guide. First we take this source to be a dipole, arbitrary in position and direction. We find the field produced inside the guide by the dipole, particularly the field a long way down the guide. This gives the mean flux of energy at infinity in the guide. Since the walls and plug are perfectly conducting, no energy can pass into them or out of them, and so this flux of energy is the power output of the dipole. Dividing this output by the mean value of the square of the current in the dipole, we obtain the radiation resistance.

Once the field due to a dipole has been found, the field due to a finite antenna follows by integration. The power output of the antenna is obtained from the field a long way down the guide, and the radiation resistance of the antenna is given by dividing the output by the mean value of the square of the current entering the antenna. We thus find the resistance, but not the reactance. The Heaviside (or rational) system of units is used throughout, the final results being converted into ohms.

We have succeeded in solving our problem by three independent methods, all of them giving the same result. Since we do not know which of these methods will prove most useful in the calculation of reactance, we give all three of them here. The first two methods are included in the main body of the paper, the third in Appendix B.

These three different methods can be characterized as follows.

The first two methods are based on the idea of images. The first (Section 3) is the more intuitive one; it treats the dipoles as singularities throughout, and gives the field only at great distances from the lattice. The second (Section 4) is the more rigorous one; it gives the damped waves near the lattice as well as the field at great distances; it is characterized by a smoothing process which enables us to replace summations by integrations. Finally, the third method (Appendix B) avoids the use of images altogether (except for images in the end of the guide) and calculates the field not by means of the Hertzian vector, but directly from Maxwell's equations, assuming a known current distribution.

Our method is sufficiently general to cover any rectangular section for the guide and any form of antenna, assumed to be a very thin wire. Details are developed only for a guide which cuts off all radiation except the H_{10} wave;

for this case a general formula for radiation resistance is given, the antenna remaining arbitrary. In particular we take the antenna to be straight and perpendicular to the wider face of the guide, being fed at the point of entry. Then the radiation resistance is

$$(1.1) \quad R = \frac{60}{\pi} \frac{\lambda^2}{\gamma ab} \cos^2 \frac{\pi x_0}{a} \sin^2 \frac{2\pi \gamma z_0}{\lambda} \tan^2 \frac{\pi l}{\lambda} \text{ ohms,}$$

where a = longer edge of cross section in centimeters,

b = shorter edge of cross section in centimeters,

λ = wave length in centimeters (i.e., frequency = $3 \times 10^{10}/\lambda$ c.p.s.),

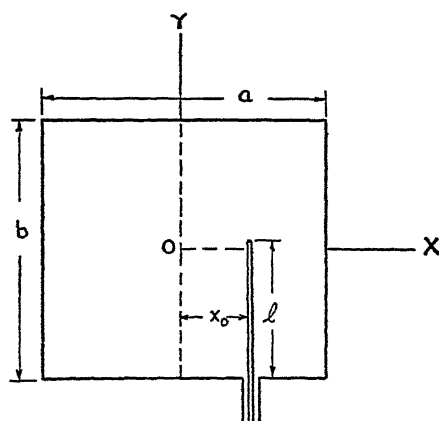
$$(1.2) \quad \gamma = \sqrt{1 - \frac{\lambda^2}{4a^2}},$$

l = length of antenna in centimeters,

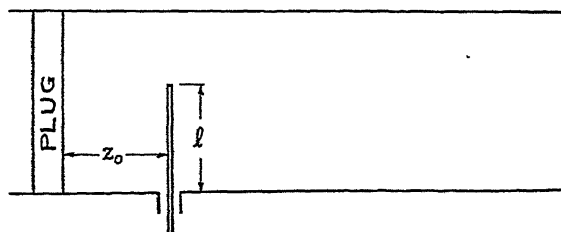
x_0 = distance of antenna from the central line of the wider face of the guide in centimeters,

z_0 = distance of antenna in front of plug in centimeters.

The arrangement is shown in Fig. 1.



CROSS SECTION OF GUIDE



LONGITUDINAL SECTION OF GUIDE

FIG. 1.

As a particular result, we place the antenna symmetrically ($x_0 = 0$) and take $l = \lambda/4$ and the following numerical values:

$$(1.3) \quad a = 5.5 \text{ cm.}, \quad b = 4.5 \text{ cm.}, \quad \lambda = 10 \text{ cm.};$$

then the resistance is

$$(1.4) \quad R = 185 \sin^2 (0.262 z_0) \text{ ohms.}$$

To match such a guide to a coaxial line with an impedance of 70 ohms we should take

$$(1.5) \quad \sin (0.262 z_0) = \sqrt{\frac{70}{185}} = 0.615, \quad z_0 = 2.53 \text{ cm.}, 9.46 \text{ cm.}, \dots$$

This gives the possible positions at which the plug should be set.

2. The Lattice of Dipoles

We use the method of images. This method is available only for the following sections:

- (i) Rectangle,
- (ii) Equilateral triangle,
- (iii) Isosceles right-angled triangle,
- (iv) 30° — 60° — 90° triangle.

The rectangular section is the simplest, and the only one of these sections actually employed; we shall confine our attention to it.

The image of a dipole with respect to a perfectly conducting plane is well known. It is found by taking the geometrical image, and then reversing direction. The dipole and its image give a field which satisfies the condition

$$(2.1) \quad \vec{E}_t = 0,$$

over the plane, \vec{E}_t being the tangential component of electric intensity.

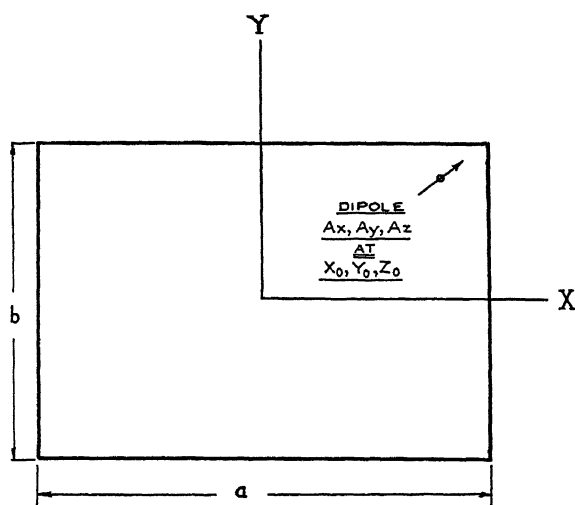


FIG. 2.

Let us first consider the case where the rectangular guide has no plug, so that it extends to infinity in both directions. Suppose that there is a dipole inside the guide. It is easy to find a doubly infinite system of images (all external to the guide) so that the lattice consisting of the dipole and its images gives a field satisfying the condition (2.1) over the walls of the guide. If we now add a plug, the condition (2.1) will be satisfied over it if we add to the above lattice its image in the plane of the plug.

Let us take the origin at the center of the plug (Fig. 2), the axes of x and y parallel to the edges of the rectangular section and the axis of z along the axis of the guide, pointing towards the open end. Let a and b be the lengths of the edges of the section of the guide.

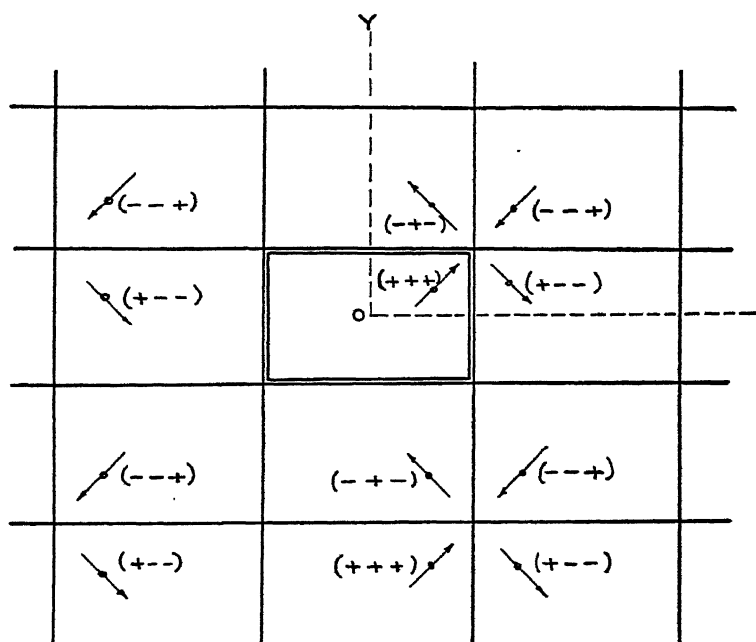


FIG. 3.

We place a dipole with components (A_x, A_y, A_z) at (x_0, y_0, z_0) , these components being complex in general. Fig. 3 shows part of the lattice in the plane $z = z_0$. The arrows are to be regarded as oblique to the plane of the paper and equally inclined to it. The signs indicate the components: thus

$$(+, +, +) \text{ means } (A_x, A_y, A_z),$$

$$(+, -, -) \text{ means } (A_x, -A_y, -A_z).$$

If we let μ and ν take all integer values, positive, zero, and negative, we may represent the components and positions of all the dipoles in the plane $z = z_0$ as follows:

$$(2.2) \quad \left\{ \begin{array}{ll} (A_x, A_y, A_z) & \text{at } (x_0 + 2\mu a, y_0 + 2\nu b, z_0), \\ (A_x, -A_y, -A_z) & \text{at } (-x_0 + (2\mu + 1)a, y_0 + 2\nu b, z_0), \\ (-A_x, A_y, -A_z) & \text{at } (x_0 + 2\mu a, -y_0 + (2\nu + 1)b, z_0), \\ (-A_x, -A_y, A_z) & \text{at } (-x_0 + (2\mu + 1)a, -y_0 + (2\nu + 1)b, z_0). \end{array} \right.$$

The images with respect to the plane of the plug are given by this table on changing the signs of A_x , A_y , and z_0 .

The lattice shown in (2.2) is a superposition of four *basic lattices*, in each of which all the dipoles are the same. The periods of all these basic lattices are $(2a, 2b)$. Instead of calculating at once the field due to the whole system of dipoles, we first calculate the field due to the basic lattice shown in the first line of (2.2). The fields of the other basic lattices then follow by simple substitutions; adding all four fields, we get the field due to the system (2.2). The field due to the plug is then easily obtained and added to the field already found.

The transformation by which we pass from the field of one basic lattice to that of another is given by the following table, read downwards:

	Basic lattice	Components	Base-point
(2.3) {	I	A_x, A_y, A_z	x_0, y_0, z_0
	II	$A_x, -A_y, -A_z$	$-x_0 + a, y_0, z_0$
	III	$-A_x, A_y, -A_z$	$x_0, -y_0 + b, z_0$
	IV	$-A_x, -A_y, A_z$	$-x_0 + a, -y_0 + b, z_0$

The co-ordinates of a general dipole in the basic lattice I are

$$(2.4) \quad x_{\mu\nu} = x_0 + 2\mu a, \quad y_{\mu\nu} = y_0 + 2\nu b, \quad z = z_0,$$

where μ, ν take all integer values, positive, zero, and negative.

Let λ be the wave length of the radiation (i.e., frequency = c/λ), and let $k = 2\pi/\lambda$. The time factor is e^{-ikct} . We shall use an accent on a symbol containing the time factor, and drop the accent when the time factor is omitted. As usual, physical quantities are to be found by taking the real parts of the complex expressions.

The Hertz vector at the point (x, y, z) due to a dipole \vec{A} at (x', y', z') is

$$(2.5) \quad \vec{\phi}' = \vec{\phi} e^{-ikct}, \quad \vec{\phi} = \frac{\vec{A}}{4\pi} \frac{e^{ikr}}{r},$$

where r is the distance between (x, y, z) and x', y', z' . Thus the Hertz vector due to the basic lattice I is

$$(2.6) \quad \vec{\phi} = \frac{\vec{A}}{4\pi} \sum_{\mu=-\infty}^{\infty} \sum_{\nu=-\infty}^{\infty} \frac{e^{ikr_{\mu\nu}}}{r_{\mu\nu}},$$

where $r_{\mu\nu}$ is the distance between (x, y, z) and $x_{\mu\nu}, y_{\mu\nu}, z_{\mu\nu}$.

3. The Field Due to a Basic Lattice: Discontinuous Method

The idea used here is based on the familiar theory of a diffraction grating. It is known that a finite lattice composed of oscillating dipoles sends out pencils of radiation in a discrete number of directions. The field far from the lattice and very near to the center of a pencil of radiation can be represented by a plane wave; the field outside these pencils of radiation is practically nonexistent. Without going into mathematical details we can foresee what will happen if the lattice becomes larger and larger. All the discrete pencils of radiation become wider and wider, finally covering the whole space. The regions where the radiation was practically nonexistent shrink to nothing. The final radiation at a point, arbitrary but far enough from the lattice, can be obtained by taking into account all the plane waves traveling in all the *admitted* directions, given by the geometrical structure of the lattice. This is the principal idea which we shall work out here mathematically.

Let us consider first a *patch*, that is a finite basic lattice, consisting of dipoles whose co-ordinates are given by (2.4), where

$$(3.1) \quad -M \leq \mu \leq M, \quad -N \leq \nu \leq N.$$

Let α, β, γ be the direction cosines of the line going through the center of a radiation pencil and x, y, z the co-ordinates along this line. Then, at distances great compared with the dimensions of the patch, we have, in the first approximation,

$$(3.2) \quad r_{\mu\nu} = r - 2\mu a\alpha - 2\nu b\beta,$$

r being the distance from the center of the patch; and the Hertz vector due to the patch is (to this approximation)

$$(3.3) \quad \vec{\phi}(M, N) = \frac{\vec{A}}{4\pi} \frac{e^{ikr}}{r} \left(\sum_{\mu=-M}^M e^{-2ik\mu\alpha} \right) \left(\sum_{\nu=-N}^N e^{-2ik\nu\beta} \right).$$

From (3.3) we obtain the possible direction cosines of the radiation pencils if M and N are large, which we shall assume throughout. These are:

$$(3.4) \quad \alpha = \alpha_m; \quad \beta = \beta_n; \quad \gamma = \gamma_{mn},$$

where

$$(3.5) \quad \alpha_m = \frac{m\pi}{ka}, \quad \beta_n = \frac{n\pi}{kb}, \quad \gamma_{mn} = \sqrt{1 - \frac{\pi^2}{k^2} \left(\frac{m^2}{a^2} + \frac{n^2}{b^2} \right)},$$

m and n being integers, positive, negative, or zero. Since γ must be real, the condition for m, n is

$$(3.6) \quad \frac{m^2}{a^2} + \frac{n^2}{b^2} < \frac{4}{\lambda^2},$$

the last inequality, together with (3.5), defining the directions of all the radiation pencils, or, in other words, all the (m, n) pencils. The Hertz vector along the center of the (m, n) pencil is

$$(3.7) \quad \vec{\phi}(M, N) = \frac{\vec{A}}{\pi} \frac{e^{ikr_{mn}}}{r_{mn}} MN.$$

This result is based on (3.2) which may be rewritten for the present choice of points of observation

$$(3.8) \quad \begin{aligned} r_{mn,\mu\nu} &= r_{mn} - 2\mu a\alpha_m - 2\nu b\beta_n \\ &= r_{mn} - \frac{2\mu m\pi}{k} - \frac{2\nu n\pi}{k}. \end{aligned}$$

The result as expressed in (3.7) is not very satisfactory since it contains M and N characterizing the dimensions of the patch. We can improve (3.7) by taking instead of (3.8) the rigorous formula

$$(3.9) \quad r_{mn,\mu\nu} = (r_{mn}^2 + 4\mu^2 a^2 + 4\nu^2 b^2 - 4r_{mn}\mu a\alpha_m - 4r_{mn}\nu b\beta_n)^{\frac{1}{2}}.$$

We see that (3.8) is the first approximation to (3.9), the second approximation being:

$$(3.10) \quad \begin{aligned} r_{mn,\mu\nu} &= r_{mn} - \frac{2\pi}{k} (\mu m + \nu n) \\ &+ \frac{2}{r_{mn}} \left[\mu^2 a^2 \left(1 - \frac{m^2 \pi^2}{a^2 k^2} \right) + \nu^2 b^2 \left(1 - \frac{n^2 \pi^2}{b^2 k^2} \right) - \frac{2\mu \nu m n \pi^2}{k^2} \right]. \end{aligned}$$

When this is substituted in (2.6), we get for the Hertz vector along the center of the pencil:

$$(3.11) \quad \begin{aligned} \vec{\phi}_{mn}(M, N) &= \frac{A}{4\pi} \frac{e^{ikr_{mn}}}{r_{mn}} \sum_{\mu=-M}^M \sum_{\nu=-N}^N \\ &\exp \left\{ \frac{2ik}{r_{mn}} \left[\mu^2 a^2 \left(1 - \frac{m^2 \pi^2}{a^2 k^2} \right) + \nu^2 b^2 \left(1 - \frac{n^2 \pi^2}{b^2 k^2} \right) - \frac{2\mu \nu m n \pi^2}{k^2} \right] \right\}, \end{aligned}$$

which is more rigorous than (3.7).

Let us now increase M and N to infinity, that is, we spread the pencil over the whole space. But in this case the pencils overlap and $\vec{\phi}_{M,N}(M, N \rightarrow \infty)$ ceases to represent the Hertz vector inside the broadening pencil. It will represent only the (m, n) contribution to the total $\vec{\phi}$, where

$$(3.12) \quad \vec{\phi} = \sum_{m=-m_0}^{m_0} \sum_{n=-n_0}^{n_0} \vec{\phi}_{mn}(M, N \rightarrow \infty),$$

M_0 and N_0 being the greatest integers satisfying (3.6).

We turn now toward the calculation of

$$(3.13) \quad \vec{\phi}_{mn} = \vec{\phi}_{mn}(M, N \rightarrow \infty),$$

by replacing the summation in (3.11) by an integration. This leads us to an integral of the type;

$$(3.14) \quad \int_{-\infty}^{\infty} \int_{-\infty}^{\infty} e^{i(c\xi^2 + d\eta^2 + 2g\xi\eta)} d\xi d\eta,$$

which can be brought by a rotation of the co-ordinate system into the form

$$(3.15) \quad \left(\int_{-\infty}^{\infty} e^{ic'\xi} d\xi \right) \left(\int_{-\infty}^{\infty} e^{id'\eta} d\eta \right) = 4(c'd')^{-\frac{1}{2}} \left[\sqrt{\frac{\pi}{8}} (1+i) \right]^2 = (c'd')^{-\frac{1}{2}} i\pi.$$

But

$$(3.16) \quad c'd' = cd - g^2.$$

Comparison with (3.11) gives:

$$(3.17) \quad c = 2ka^2 \left(1 - \frac{m^2\pi^2}{a^2k^2} \right), \quad d = 2kb^2 \left(1 - \frac{n^2\pi^2}{b^2k^2} \right),$$

$$g = -\frac{2mn\pi^2}{k}, \quad \xi = \frac{\mu}{\sqrt{r_{mn}}}, \quad \eta = \frac{\nu}{\sqrt{r_{mn}}}.$$

The result is:

$$(3.18) \quad \vec{\phi}_{mn} = \frac{i\vec{A}}{8kab r_{mn}} e^{ikr_{mn}},$$

where

$$(3.19) \quad r_{mn} = (x - x_0) \alpha_m + (y - y_0) \beta_n + (z - z_0) \gamma_{mn},$$

and (x, y, z) represents an arbitrary point in space. The plane wave as represented by (3.18) has no physical meaning. To find the Hertz vector at a point, arbitrary but far enough from the basic lattice, we must perform the summation indicated in (3.12). Remembering that, according to (3.5)

$$(3.20) \quad \alpha_{-m} = -\alpha_m, \quad \beta_{-n} = -\beta_n,$$

we have, because of (3.18), as our final result:

$$(3.21) \quad \vec{\phi} = \frac{i\vec{A}}{8kab} \left\{ e^{ik(z-z_0)} + 2 \sum_{m=1}^{m_0} \frac{1}{\gamma_{m0}} \cos k\alpha_m(x - x_0) e^{ik\gamma_{m0}(z-z_0)} \right.$$

$$+ 2 \sum_{n=1}^{n_0} \frac{1}{\gamma_{0n}} \cos k\beta_n(y - y_0) e^{ik\gamma_{0n}(z-z_0)}$$

$$+ 4 \sum_{m=1}^{m_0} \sum_{n=1}^{n_0} \frac{1}{\gamma_{mn}} \cos k\alpha_m(x - x_0) \cos k\beta_n(y - y_0) e^{ik\gamma_{mn}(z-z_0)} \left. \right\}$$

representing the Hertz vector due to the basic lattice I.

We can now find the Hertz vector of the lattices equivalent to that of the wave guide. We have to apply our formula (3.21) four times, changing the components of \vec{A} and x_0, y_0 , according to the table (2.3). In this way, we obtain the Hertz vector of the lattice in the plane $z = z_0$. The Hertz vector of the lattice in the plane $z = -z_0$ is obtained by changing z_0 into $-z_0$, and A_x, A_y into $-A_x, -A_y$ in this result. The final Hertz vector obtained in this way is a summation of the Hertz vector for *eight* properly chosen basic lattices. Denoting now by ϕ_x, ϕ_y, ϕ_z the components of this *resulting* Hertz vector we find because of (3.21) and (3.5):

$$(3.22) \quad \left\{ \begin{aligned} \phi_x &= \frac{2A_x}{kab} \left\{ \sum_{n=1}^{n_0} \frac{1}{\gamma_{0n}} \sin n\chi \sin n\chi_0 \sin(k\gamma_{0n}z_0) e^{ik\gamma_{0n}z} \right. \\ &\quad \left. + 2 \sum_{m=1}^{m_0} \sum_{n=1}^{n_0} \frac{1}{\gamma_{mn}} \cos m\psi \cos m\psi_0 \sin n\chi \sin n\chi_0 \right. \\ &\quad \left. \sin(k\gamma_{mn}z_0) e^{ik\gamma_{mn}z} \right\}, \\ \phi_y &= \frac{2A_y}{kab} \left\{ \sum_{m=1}^{m_0} \frac{1}{\gamma_{m0}} \sin m\psi \sin m\psi_0 \sin(k\gamma_{m0}z_0) e^{ik\gamma_{m0}z} \right. \\ &\quad \left. + 2 \sum_{m=1}^{m_0} \sum_{n=1}^{n_0} \frac{1}{\gamma_{mn}} \sin m\psi \sin m\psi_0 \cos n\chi \cos n\chi_0 \right. \\ &\quad \left. \sin(k\gamma_{mn}z_0) e^{ik\gamma_{mn}z} \right\}, \\ \phi_z &= \frac{4iA_z}{kab} \sum_{m=1}^{m_0} \sum_{n=1}^{n_0} \frac{1}{\gamma_{mn}} \sin m\psi \sin m\psi_0 \sin n\chi \sin n\chi_0 \\ &\quad \cos(k\gamma_{mn}z_0) e^{ik\gamma_{mn}z} \end{aligned} \right.$$

where

$$(3.23) \quad \left\{ \begin{aligned} \psi &= \frac{\pi x}{a} - \frac{\pi}{2}, & \psi_0 &= \frac{\pi x_0}{a} - \frac{\pi}{2}, \\ \chi &= \frac{\pi y}{b} - \frac{\pi}{2}, & \chi_0 &= \frac{\pi y_0}{b} - \frac{\pi}{2}. \end{aligned} \right.$$

Equations (3.22) represent the Hertz vector for great z inside the wave guide, i.e., for

$$-\frac{1}{2}a \leq x \leq \frac{1}{2}a, \quad -\frac{1}{2}b \leq y \leq \frac{1}{2}b.$$

4. The Field Due to a Basic Lattice: Continuous Method

Let us consider the basic lattice I in the plane $z = z_0$, as in (2.3). Instead of discrete dipoles, let us take a continuous distribution over the plane with density $\vec{\sigma}$, so that a dipole $\vec{\sigma} dx'dy'$ is associated with the element $dx'dy'$, where x' , y' are co-ordinates in the plane $z = z_0$. Let p be a large positive integer; consider the expression

$$(4.1) \quad \vec{\sigma} = \vec{A} \frac{K(p)}{ab} \cos^{2p} X' \cos^{2p} Y',$$

where $K(p)$ is a constant and

$$(4.2) \quad X' = \frac{1}{2}\pi(x' - x_0)/a, \quad Y' = \frac{1}{2}\pi(y' - y_0)/b.$$

It is evident that this density will be very small except in the immediate neighborhood of the positions of the dipoles in the discrete lattice; the larger we make p , the more closely does this continuous distribution approach the discrete distribution. We choose the constant $K(p)$ so that the total dipole

strength inside the period rectangle ($2a, 2b$) is the same in the continuous and discrete distributions, i.e., so that

$$(4.3) \quad \int \int \vec{\sigma} \, dx' \, dy' = \vec{A},$$

the ranges of the integral being

$$x_0 - a < x' < x_0 + a, \quad y_0 - b < y' < y_0 + b.$$

Since

$$\begin{aligned} \int_{x_0-a}^{x_0+a} \cos^{2p} X' \, dx' &= \frac{2a}{\pi} \int_{-\frac{1}{2}\pi}^{\frac{1}{2}\pi} \cos^{2p} X' \, dX' \\ &= 2a \frac{(2p)!}{2^{2p}(p!)^2}, \end{aligned}$$

we take

$$(4.4) \quad K(p) = \frac{2^{4p}(p!)^4}{4(2p!)^2}.$$

By Stirling's formula this is approximately $\pi p/4$, but it is actually more convenient to retain the exact value (4.4).

The Hertz vector for the basic lattice, smoothed out as described above, is

$$(4.5) \quad \vec{\phi} = \frac{1}{4\pi} \int \int \vec{\sigma} \, e^{ikr/r} \, dx' \, dy',$$

where r is the distance from the point (x', y', z_0) to the point of observation (x, y, z) . Let us drop a perpendicular from (x, y, z) on the plane $z = z_0$, and take polar co-ordinates (R, θ) relative to the foot of this perpendicular (Fig. 4). Then

$$(4.6) \quad x' = x + R \cos \theta, \quad y' = y + R \sin \theta,$$

and (4.5) gives

$$(4.7) \quad \vec{\phi} = \frac{\vec{A} K(p)}{4\pi ab} \int_0^\infty e^{ikr} r^{-1} R \, dR \int_0^{2\pi} \cos^{2p} X' \cos^{2p} Y' \, d\theta.$$

On substituting

$$\cos^{2p} X' = \frac{1}{2^{2p}} \sum_{m=-p}^p \binom{2p}{p+m} e^{2imX'},$$

and a similar expression for $\cos^{2p} Y'$, we have

$$\begin{aligned} (4.8) \quad & \int_0^{2\pi} \cos^{2p} X' \cos^{2p} Y' \, d\theta \\ &= \frac{1}{2^{4p}} \sum_{m=-p}^p \sum_{n=-p}^p \binom{2p}{p+m} \binom{2p}{p+n} e^{2i(mX' + nY')} \int_0^{2\pi} e^{i\pi R \left(\frac{m \cos \theta}{a} + \frac{n \sin \theta}{b} \right)} \, d\theta, \end{aligned}$$

where X, Y are given by (4.2) on removing all accents. Since for any real constants k_1, k_2 ,

$$(4.9) \quad \int_0^{2\pi} e^{i(k_1 \cos \theta + k_2 \sin \theta)} \, d\theta = 2\pi J_0(\sqrt{k_1^2 + k_2^2}),$$

where J_0 is the Bessel function of order zero, (4.7) reduces to

$$(4.10) \quad \vec{\phi} = \frac{\vec{A} K(p)}{2^{4p+1} ab} \sum_{m=-p}^p \sum_{n=-p}^p \binom{2p}{p+m} \binom{2p}{p+n} e^{2i(mX+nY)} I_{mn},$$

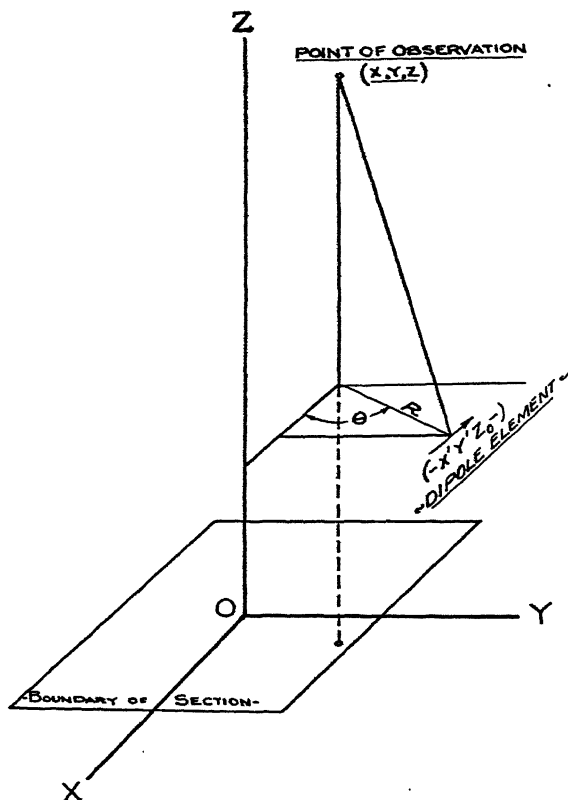


FIG. 4.

where

$$(4.11) \quad I_{mn} = \int_0^\infty e^{ikr} r^{-1} R J_0(C_{mn} R) dR,$$

$$(4.12) \quad C_{mn} = \pi \sqrt{m^2/a^2 + n^2/b^2}.$$

Now

$$R^2 = r^2 - (z - z_0)^2,$$

and so

$$(4.13) \quad I_{mn} = \int_{|z-z_0|}^\infty e^{ikr} J_0(C_{mn} \sqrt{r^2 - (z - z_0)^2}) dr.$$

This integral is evaluated in Appendix A; we find

$$(4.14) \quad I_{mn} = \frac{i}{k \gamma_{mn}} e^{ik \gamma_{mn} |z - z_0|},$$

where γ_{mn} is defined by

$$(4.15) \quad \begin{cases} k\gamma_{mn} = |\sqrt{k^2 - C_{mn}^2}| & \text{if } C_{mn} < k, \\ k\gamma_{mn} = i|\sqrt{k^2 - C_{mn}^2}| & \text{if } C_{mn} > k. \end{cases}$$

When we substitute this in (4.10) we get for the Hertz vector of the smoothed basic lattice I

$$(4.16) \quad \vec{\phi} = \frac{iA K(p)}{2^{4p+1}kab} \sum_{m=-p}^p \sum_{n=-p}^p \binom{2p}{p+m} \binom{2p}{p+n} \frac{1}{\gamma_{mn}} e^{ik[\alpha_m(x-x_0) + \beta_n(y-y_0) + \gamma_{mn}|z-z_0|]},$$

where

$$k\alpha_m = m\pi/a, \quad k\beta_n = n\pi/b.$$

If we go a long way down the guide, so that $z \rightarrow \infty$, only those terms in (4.16) survive for which γ_{mn} is real, i.e.,

$$(4.17) \quad C_{mn} < k,$$

or equivalently

$$(4.18) \quad \frac{m^2}{a^2} + \frac{n^2}{b^2} < \frac{4}{\lambda^2}.$$

This condition is the same as (3.6), and is in fact the cut-off condition given by the eigenvalue method for an empty guide. The condition limits the values of m and n to some finite ranges

$$-m_0 \leq m \leq m_0, \quad -n_0 \leq n \leq n_0.$$

Thus in calculating $\vec{\phi}$ from (4.16) we have only a finite number of terms. We now proceed to the limit $p \rightarrow \infty$ in order to pass from the smoothed basic lattice to the discrete basic lattice. Since, for fixed values of m and n ,

$$(4.19) \quad \lim_{p \rightarrow \infty} \frac{K(p)}{2^{4p}} \binom{2p}{p+m} \binom{2p}{p+n} = \lim_{p \rightarrow \infty} \frac{1}{4} \frac{(p!)^4}{(p+m)!(p-m)!(p+n)!(p-n)!} = \frac{1}{4},$$

we get for the Hertz vector of the discrete basic lattice I a long way down the guide

$$(4.20) \quad \vec{\phi} = \frac{iA}{8kab} \sum_{m=-m_0}^{m_0} \sum_{n=-n_0}^{n_0} \frac{1}{\gamma_{mn}} e^{ik[\alpha_m(x-x_0) + \beta_n(y-y_0) + \gamma_{mn}(z-z_0)]},$$

where

$$(4.21) \quad \gamma_{mn} = \sqrt{1 - \frac{C_{mn}^2}{k^2}} = \sqrt{1 - \frac{\lambda^2}{4} \left(\frac{m^2}{a^2} + \frac{n^2}{b^2} \right)}.$$

Equation (4.20) is the same as (3.21), and so the two methods lead to the same expression for the field at a great distance down the guide. From this point the argument proceeds in common.

However, before finally leaving the smoothed lattice, let us write down the Hertz vector at any point inside the guide. To do this, we have to superimpose on (4.16) the corresponding expressions for the other basic lattices in

(2.3), and then superimpose on the result the expression corresponding to the images with respect to the plane of the plug. A simple calculation gives

$$(4.22) \quad \vec{\phi} = \frac{iK(p)}{2^{4p+1}kab} \sum_{m=-p}^p \sum_{n=-p}^p \binom{2p}{p+m} \binom{2p}{p+n} \frac{1}{\gamma_{mn}} e^{ik(\alpha_m x + \beta_n y)} \\ [\vec{F}_{(mn)} e^{ik\gamma_{mn}[z-z_0]} + \vec{G}_{(mn)} e^{ik\gamma_{mn}[z+z_0]}],$$

where

$$(4.23) \quad \begin{cases} F_{(mn)x} = -G_{(mn)x} = A_x [e^{-ik\alpha_m x_0} + (-1)^m e^{ik\alpha_m x_0}] [e^{-ik\beta_n y_0} - (-1)^n e^{ik\beta_n y_0}], \\ F_{(mn)y} = -G_{(mn)y} = A_y [e^{-ik\alpha_m x_0} - (-1)^m e^{ik\alpha_m x_0}] [e^{-ik\beta_n y_0} + (-1)^n e^{ik\beta_n y_0}], \\ F_{(mn)z} = G_{(mn)z} = A_z [e^{-ik\alpha_m x_0} - (-1)^m e^{ik\alpha_m x_0}] [e^{-ik\beta_n y_0} - (-1)^n e^{ik\beta_n y_0}]. \end{cases}$$

5. The H_{10} Wave

Let us suppose that the dimensions of the guide and the frequency are such that

$$(5.1) \quad \frac{1}{a^2} < \frac{4}{\lambda^2} < \frac{1}{a^2} + \frac{1}{b^2}.$$

These conditions are satisfied for example by the numerical values given in (1.3). Then the condition (3.6) or (4.18) is satisfied only by

$$(5.2) \quad m = -1, 0, 1, \quad n = 0.$$

Putting $m_0 = 1$, $n_0 = 0$ in (3.22) and writing

$$(5.3) \quad \gamma = \gamma_{10} = \gamma_{-10} = \sqrt{1 - \frac{\lambda^2}{4a^2}},$$

we get for the Hertz vector a long way down the guide

$$(5.4) \quad \begin{cases} \phi_x = \phi_z = 0, \\ \phi_y = \frac{2A_y}{k\gamma ab} \cos \frac{\pi x_0}{a} \sin k\gamma z_0 \cos \frac{\pi x}{a} e^{ik\gamma z}. \end{cases}$$

The corresponding field is

$$(5.5) \quad \begin{cases} E_x = \frac{\partial^2 \phi_y}{\partial x \partial y} = 0, \\ E_y = \frac{\partial^2 \phi_y}{\partial y^2} + k^2 \phi_y \\ \quad = \frac{2kA_y}{\gamma ab} \cos \frac{\pi x_0}{a} \sin k\gamma z_0 \cos \frac{\pi x}{a} e^{ik\gamma z}, \\ E_z = \frac{\partial^2 \phi_y}{\partial z \partial y} = 0, \\ H_x = ik \frac{\partial \phi_y}{\partial z} = -\frac{2kA_y}{ab} \cos \frac{\pi x_0}{a} \sin k\gamma z_0 \cos \frac{\pi x}{a} e^{ik\gamma z}, \\ H_y = 0, \\ H_z = -ik \frac{\partial \phi_y}{\partial x} = \frac{2i\pi A_y}{\gamma a^2 b} \cos \frac{\pi x_0}{a} \sin k\gamma z_0 \sin \frac{\pi x}{a} e^{ik\gamma z}. \end{cases}$$

The time-mean of the flux of energy across a section of the guide is

$$(5.6) \quad F = \text{real part of } \frac{1}{2}c \int_{-\frac{1}{2}a}^{\frac{1}{2}a} \int_{-\frac{1}{2}b}^{\frac{1}{2}b} (E_x \bar{H}_y - E_y \bar{H}_x) dx dy \\ = \frac{k^2 c A_y \bar{A}_y}{\gamma ab} \cos^2 \frac{\pi x_0}{a} \sin^2 k \gamma z_0.$$

The transmitted wave is the H_{10} wave, as indeed we know otherwise by the eigenvalue method. It is the quantitative character of the present result that is new. We note that:

- (i) The radiation depends only on the component A_y of the dipole, i.e., on the component parallel to the shorter edge of the cross section.
- (ii) The radiation depends only on two (x_0, z_0) of the co-ordinates of the dipole.

A current $I' = I \exp(-ikct)$ flowing in an element $\vec{ds}_0 (dx_0, dy_0, dz_0)$ of wire with direction cosines L, M, N is equivalent to a dipole with components

$$(5.7) \quad A_x = \frac{iIL}{kc} ds_0, \quad A_y = \frac{iIM}{kc} ds_0, \quad A_z = \frac{iIN}{kc} ds_0.$$

If the current element belongs to an antenna in a rectangular wave guide with a plug, the field a long way down the guide is given by (5.5) when we substitute from (5.7).

If the antenna is very short (length l) compared with the wave length, and the current I is regarded as constant along it the output is by (5.6)

$$(5.8) \quad F = \frac{M^2 l^2 I \bar{I}}{c \gamma ab} \cos^2 \frac{\pi x_0}{a} \sin^2 k \gamma z_0.$$

Since the time-average of the square of the current is $\frac{1}{2} I \bar{I}$, the radiation resistance is

$$(5.9) \quad R = \frac{F}{\frac{1}{2} I \bar{I}} = \frac{2M^2 l^2}{c \gamma ab} \cos^2 \frac{\pi x_0}{a} \sin^2 k \gamma z_0$$

in Heaviside units. Since

$$(5.10) \quad 1 \text{ Heaviside unit of resistance} = 4\pi \times 9 \times 10^{11} \text{ ohms},$$

the radiation resistance of the short antenna is

$$(5.11) \quad R = 240\pi \frac{M^2 l^2}{\gamma ab} \cos^2 \frac{\pi x_0}{a} \sin^2 k \gamma z_0 \text{ ohms},$$

the lengths being measured in centimeters.

For a finite antenna the surviving parts of the field are by (5.5)

$$(5.12) \quad E_y = \frac{2iJ}{c \gamma ab} \cos \frac{\pi x}{a} e^{ik\gamma z}, \\ H_x = -\frac{2iJ}{cab} \cos \frac{\pi x}{a} e^{ik\gamma z}, \\ H_z = -\frac{2\pi J}{ck\gamma a^2 b} \sin \frac{\pi x}{a} e^{ik\gamma z},$$

where

$$(5.13) \quad J = \int I \cos \frac{\pi x_0}{a} \sin k\gamma z_0 dy_0,$$

the integral being taken along the antenna. Accordingly the output is

$$(5.14) \quad F = \frac{J\bar{J}}{c\gamma ab}.$$

If I_0 is the current entering the antenna, the radiation resistance is

$$(5.15) \quad R = \frac{F}{\frac{1}{2}I_0\bar{I}_0} = \frac{2J\bar{J}}{c\gamma ab I_0\bar{I}_0} \text{ Heaviside units} \\ = 240\pi \frac{1}{\gamma ab} \frac{J\bar{J}}{I_0\bar{I}_0} \text{ ohms.}$$

When this is calculated in any particular case the current I_0 cancels out, and the result depends only on the shape and position of the antenna and the point at which it is fed.

6. Straight Antenna Parallel to the Shorter Side of the Cross Section

When the condition (5.1) is satisfied, the only radiation transmitted by the guide is the H_{10} wave. Any form of antenna will transmit this wave, except an antenna lying entirely in a plane perpendicular to the y -axis. But it is only the component of current parallel to the y -axis that contributes to the radiation, and the simplest plan is to use a straight antenna parallel to the y -axis.

Let us consider the arrangement shown in Fig. 1, where the length of the antenna is l and it is fed at the point where it enters the guide. Let I_0 be the current entering; then according to the usual rule of sine-distribution the current along the antenna is

$$(6.1) \quad I = I_0 \frac{\sin k(l - \frac{1}{2}b - y_0)}{\sin kl}.$$

Then (5.13) gives

$$(6.2) \quad J = I_0 \cos \frac{\pi x_0}{a} \sin k\gamma z_0 \int_{-\frac{1}{2}b}^{l-\frac{1}{2}b} \frac{\sin k(l - \frac{1}{2}b - y_0)}{\sin kl} dy_0 \\ = I_0 \cos \frac{\pi x_0}{a} \sin k\gamma z_0 \frac{1}{k} \tan \frac{1}{2}kl,$$

and so by (5.15)

$$(6.3) \quad R = 240\pi \frac{1}{k^2\gamma ab} \cos^2 \frac{\pi x_0}{a} \sin^2 k\gamma z_0 \tan^2 \frac{1}{2}kl \text{ ohms} \\ = \frac{60}{\pi} \frac{\lambda^2}{\gamma ab} \cos^2 \frac{\pi x_0}{a} \sin^2 \frac{2\pi\gamma z_0}{\lambda} \tan^2 \frac{\pi l}{\lambda} \text{ ohms.}$$

Let us now place the antenna centrally, so that $x_0 = 0$, and at the same time put $l = \lambda/4$; we get

$$(6.4) \quad R = \frac{60}{\pi} \frac{\lambda^2}{\gamma_{ab}} \sin^2 \frac{2\pi\gamma_{z_0}}{\lambda} \text{ ohms.}$$

Finally we take the numerical values given in (1.3) and obtain (1.4); the matching condition (1.5) follows at once.

It is clear from (6.3) that there are three different ways of matching the radiation resistance of the antenna to the impedance of a given line:

- (i) By adjusting the position of the antenna relative to the central line, i.e., by changing x_0 ;
- (ii) By adjusting the position of the plug, i.e., by changing z_0 ;
- (iii) By adjusting the length of the antenna, i.e., by changing l .

Until such time as reactance has been calculated, it is not possible to decide which of these methods is the best.

Acknowledgment

We wish to thank Professors B. de F. Bayly and V. G. Smith of the Department of Electrical Engineering, University of Toronto, for useful advice during the accomplishment of this work.

APPENDIX A

We shall now evaluate the integral occurring in (4.13), namely

$$(A1) \quad I(\xi) = \int_{\xi} e^{ikr} J_0(C\sqrt{r^2 - \xi^2}) dr,$$

where ξ , k , C are real and positive.

Differentiation with respect to ξ gives

$$(A2) \quad \frac{dI}{d\xi} = -e^{ik\xi} - C\xi \int_{\xi}^{\infty} e^{ikr} \frac{J'_0(C\sqrt{r^2 - \xi^2})}{\sqrt{r^2 - \xi^2}} dr.$$

We integrate by parts, writing $\sqrt{r^2 - \xi^2} = R$;

$$(A3) \quad \begin{aligned} C \int_{\xi}^{\infty} e^{ikr} \frac{J'_0(CR)}{R} dr &= \int_{r=\xi}^{\infty} \frac{e^{ikr}}{r} J'_0(CR) d(CR) \\ &= \left[\frac{e^{ikr}}{r} J_0(CR) \right]_{\xi}^{\infty} - \int_{\xi}^{\infty} \frac{d}{dr} \left(\frac{e^{ikr}}{r} \right) J_0(CR) dr. \end{aligned}$$

The first term here is $-e^{ik\xi}/\xi$. Hence (A2) becomes

$$(A4) \quad \frac{1}{\xi} \frac{dI}{d\xi} = \int_{\xi}^{\infty} \frac{d}{dr} \left(\frac{e^{ikr}}{r} \right) J_0(CR) dr$$

Comparing this with (A1), we observe that the application of the operator

$$\frac{1}{\xi} \frac{d}{d\xi}$$

to the integral has the effect of inserting the operator

$$\frac{d}{dr} \frac{1}{r}$$

in front of the first part of the integrand. The fact that that part is actually e^{ikr} is not involved in the argument, except in so far as it secures convergence. Thus, applying the same operator to (A4), we get

$$(A5) \quad \frac{1}{\xi} \frac{d}{d\xi} \left(\frac{1}{\xi} \frac{dI}{d\xi} \right) = \int_{\xi}^{\infty} \frac{d}{dr} \left\{ \frac{1}{r} \frac{d}{dr} \left(\frac{e^{ikr}}{r} \right) \right\} J_0(CR) dr.$$

Let us now go back to (A1) and put, by virtue of the Bessel differential equation,

$$(A6) \quad J_0(CR) = -J_0''(CR) - J_0'(CR)/CR.$$

Thus

$$(A7) \quad I(\xi) = -C^{-1} \int_{r=\xi}^{\infty} e^{ikr} (R/r) J_0''(CR) d(CR) - C^{-1} \int_{\xi}^{\infty} e^{ikr} J_0(CR) / R dr.$$

On integrating the first integral by parts, we obtain

$$(A8) \quad \begin{aligned} I(\xi) &= C^{-1} \int_{\xi}^{\infty} \left\{ \frac{d}{dr} \left(e^{ikr} \frac{R}{r} \right) - \frac{e^{ikr}}{R} \right\} J_0'(CR) dr \\ &= C^{-1} \int_{\xi}^{\infty} e^{ikr} \left(\frac{ik}{r} - \frac{1}{r^2} \right) R J_0'(CR) dr \\ &= C^{-2} \int_{r=\xi}^{\infty} e^{ikr} \left(\frac{ik}{r^2} - \frac{1}{r^3} \right) R^2 J_0'(CR) d(CR), \end{aligned}$$

and further integration by parts gives

$$(A9) \quad C^2 I(\xi) = \int_{\xi}^{\infty} \frac{d}{dr} \left\{ e^{ikr} \left(-\frac{ik}{r^2} + \frac{1}{r^3} \right) (r^2 - \xi^2) \right\} J_0(CR) dr.$$

This integral splits into two parts. The first is

$$(A10) \quad \begin{aligned} &\int_{\xi}^{\infty} \frac{d}{dr} \left\{ e^{ikr} \left(-ik + \frac{1}{r} \right) \right\} J_0(CR) dr \\ &= k^2 \int_{\xi}^{\infty} e^{ikr} J_0(CR) dr + \int_{\xi}^{\infty} \frac{d}{dr} \left(\frac{e^{ikr}}{r} \right) J_0(CR) dr \\ &= k^2 I + \frac{1}{\xi} \frac{dI}{d\xi}, \end{aligned}$$

by (A1) and (A4). The second part of the integral is

$$\begin{aligned}
 (A11) \quad & -\zeta^2 \int_{\zeta}^{\infty} \frac{d}{dr} \left\{ e^{ikr} \left(-\frac{ik}{r^2} + \frac{1}{r^3} \right) \right\} J_0(Cr) dr \\
 & = \zeta^2 \int_{\zeta}^{\infty} \frac{d}{dr} \left\{ \frac{1}{r} \frac{d}{dr} \left(\frac{e^{ikr}}{r} \right) \right\} J_0(Cr) dr \\
 & = \zeta \frac{d}{d\zeta} \left(\frac{1}{\zeta} \frac{dI}{d\zeta} \right),
 \end{aligned}$$

by (A5). Thus (A9) becomes

$$(A12) \quad C^2 I = k^2 I + \frac{1}{\zeta} \frac{dI}{d\zeta} + \zeta \frac{d}{d\zeta} \left(\frac{1}{\zeta} \frac{dI}{d\zeta} \right),$$

or

$$(A13) \quad \frac{d^2 I}{d\zeta^2} + (k^2 - C^2) I = 0.$$

Hence

$$(A14) \quad I(\zeta) = A e^{i\zeta \sqrt{k^2 - C^2}} + B e^{-i\zeta \sqrt{k^2 - C^2}},$$

where A and B are independent of ζ . For definiteness, and without loss of generality, we interpret the radical in the following sense:

$$\begin{aligned}
 (A15) \quad & \sqrt{k^2 - C^2} = |\sqrt{k^2 - C^2}| \quad \text{if } k > C, \\
 & \sqrt{k^2 - C^2} = i |\sqrt{k^2 - C^2}| \quad \text{if } k < C.
 \end{aligned}$$

Now putting $\zeta = 0$ in (A1), we have a well known formula (Gray, Mathews, and MacRobert, Bessel Functions, p. 65)

$$\begin{aligned}
 (A16) \quad I_{\zeta=0} & = \int_0^{\infty} e^{ikr} J_0(Cr) dr \\
 & = \frac{i}{\sqrt{k^2 - C^2}},
 \end{aligned}$$

the radical being interpreted as in (A15). Also by (A4)

$$\begin{aligned}
 (A17) \quad \left(\frac{dI}{d\zeta} \right)_{\zeta=0} & = \lim_{\zeta \rightarrow 0} \zeta \int_{\zeta}^{\infty} \frac{d}{dr} \left(\frac{e^{ikr}}{r} \right) J_0(C\sqrt{r^2 - \zeta^2}) dr \\
 & = \lim_{\zeta \rightarrow 0} \zeta \int_{\zeta}^{\infty} \frac{d}{dr} \left(\frac{e^{ikr}}{r} \right) J_0(Cr) dr \\
 & = \lim_{\zeta \rightarrow 0} \zeta \left\{ -\frac{e^{ik\zeta}}{\zeta} J_0(C\zeta) - C \int_{\zeta}^{\infty} \frac{e^{ikr}}{r} J_0'(Cr) dr \right\}.
 \end{aligned}$$

Since the last integral has a finite limit for $\zeta \rightarrow 0$,
we get

$$(A18) \quad \left(\frac{dI}{d\zeta} \right)_{\zeta=0} = -1.$$

The values (A16), (A18) enable us to determine A and B in (A14). We obtain

$$(A19) \quad I(\zeta) = \int_{\zeta}^{\infty} e^{ikr} J_0(C\sqrt{r^2 - \zeta^2}) dr = \frac{i}{\sqrt{k^2 - C^2}} e^{i\zeta\sqrt{k^2 - C^2}}$$

the required result; the interpretation of the radicals on the right hand side is as in (A15), which agrees with (4.15).

We may remark that our result may be obtained formally by changing reals into imaginaries in a known formula; cf. Riemann-Weber, *Differentialgleichungen der Physik*, vol. 2(1927), p. 546. Such a procedure is not, of course, mathematically valid. We have not been able to find our result in the literature of Bessel functions.

APPENDIX B

The following treatment of the problem considered in this paper does not make use of the method of images, and offers interesting possibilities of generalization. In this, we find the steady-state solution corresponding to an assigned *volume* distribution of current throughout the wave guide, and deduce the field due to a current element (dipole) as a limiting case.

We use the same notation as before, except that it is now rather more convenient to take the origin at a corner of the plug-face than at its center. In Fig. 2, the origin must therefore be supposed transferred to the bottom left-hand corner, so that the equations of the faces of the guide are $x = 0$, $x = a$, $y = 0$, $y = b$.

Maxwell's equations for a volume current density \vec{j} may be written, in Heaviside units,

$$(B1) \quad \text{curl } \vec{E} = ik\vec{H}, \quad \text{curl } \vec{H} = -ik\vec{E} + \frac{1}{c} \vec{j}.$$

We shall, for the purposes of calculation, suppose that the wave guide extends to infinity in *both* directions along the z -axis, and eliminate the plug. We then assume that j_x , j_y are odd functions of z , and that j_z is an even function of z . It is then evident that the boundary condition (2.1) will be satisfied over the plug-face (as may be verified from the solution to be obtained).

We now make the following assumptions for the field components, which obviously satisfy the boundary conditions (2.1) on the faces of the guide:

$$\begin{aligned}
 E_x &= \sum_{m,n} A_{mn}^{(1)}(z) \cos(C_m x) \sin(D_n y), \\
 E_y &= \sum_{m,n} A_{mn}^{(2)}(z) \sin(C_m x) \cos(D_n y), \\
 E_z &= \sum_{m,n} A_{mn}^{(3)}(z) \sin(C_m x) \sin(D_n y), \\
 H_x &= \sum_{m,n} B_{mn}^{(1)}(z) \sin(C_m x) \cos(D_n y), \\
 H_y &= \sum_{m,n} B_{mn}^{(2)}(z) \cos(C_m x) \sin(D_n y), \\
 H_z &= \sum_{m,n} B_{mn}^{(3)}(z) \cos(C_m x) \cos(D_n y),
 \end{aligned}
 \tag{B2}$$

where $C_m = m\pi/a$, $D_n = n\pi/b$, the summations running from zero to infinity. For the components of \vec{j} we now assume

$$\begin{aligned}
 j_x &= \sum_{m,n} j_{mn}^{(1)}(z) \cos(C_m x) \sin(D_n y), \\
 j_y &= \sum_{m,n} j_{mn}^{(2)}(z) \sin(C_m x) \cos(D_n y), \\
 j_z &= \sum_{m,n} j_{mn}^{(3)}(z) \sin(C_m x) \sin(D_n y).
 \end{aligned}
 \tag{B3}$$

Substituting (B2) and (B3) in the Maxwell equations (B1), we have six linear equations of the first order to determine the six functions $A_{mn}^{(1)}(z), \dots, B_{mn}^{(3)}(z)$ in terms of the functions $j_{mn}^{(1)}, j_{mn}^{(2)}, j_{mn}^{(3)}$. The solution of these equations is facilitated by noting that from (B1) follows

$$(\nabla^2 + k^2) \vec{H} = -\frac{1}{c} \text{curl } \vec{j}.
 \tag{B4}$$

Taking say, the x -component of this equation, and using (B2), (B3), we find

$$\frac{d^2 B_{mn}^{(1)}}{dz^2} + u_{mn}^2 B_{mn}^{(1)} = \frac{1}{c} \left(\frac{dj_{mn}^{(2)}}{dz} - D_n j_{mn}^{(3)} \right),
 \tag{B5}$$

where

$$u_{mn}^2 = k^2 - C_m^2 - D_n^2.
 \tag{B6}$$

For definiteness, we suppose the positive root of (B6) is taken for u_{mn} if $u_{mn}^2 > 0$ and the positive-imaginary root if $u_{mn}^2 < 0$. The solution of (B5) which represents outgoing waves, or damped waves, for large positive or negative z is readily found, by the method of variation of constants, to be

$$B_{mn}^{(1)} = \frac{e^{iu_{mn}z}}{2icu_{mn}} \int_{-\infty}^z f_{mn}^{(1)}(z) dz + \frac{e^{-iu_{mn}z}}{2icu_{mn}} \int_z^{\infty} \bar{f}_{mn}^{(1)}(z) dz,
 \tag{B7}$$

where $f_{mn}^{(1)} = e^{-iu_{mn}z} (iu_{mn} j_{mn}^{(2)} - D_n j_{mn}^{(3)})$,

and the bar denotes, here and in what follows, the complex conjugate (the functions $j_{mn}^{(1,2,3)}$ being treated as *real*). This gives outgoing waves at infinity if u_{mn} is real, and damped waves if u_{mn} is positive imaginary.

In a similar manner, the y - and z -components of (B4) give us $B_{mn}^{(2)}$ and $B_{mn}^{(3)}$, and the second of (B1) then gives us $A_{mn}^{(1)}$, $A_{mn}^{(2)}$, $A_{mn}^{(3)}$. We thus find:

$$B_{mn}^{(\alpha)} = \frac{e^{iu_{mn}z}}{2icu_{mn}} \int_{-\infty}^z f_{mn}^{(\alpha)}(z) dz + \frac{e^{-iu_{mn}z}}{2icu_{mn}} \int_z^{\infty} \bar{f}_{mn}^{(\alpha)}(z) dz, \quad (\alpha = 2, 3),$$

$$(B8) \quad A_{mn}^{(\beta)} = \frac{e^{iu_{mn}z}}{2kcu_{mn}} \int_{-\infty}^z g_{mn}^{(\beta)}(z) dz + \frac{e^{-iu_{mn}z}}{2kcu_{mn}} \int_z^{\infty} \bar{g}_{mn}^{(\beta)}(z) dz - \frac{i}{kc} j_{mn}^{(3)} \delta_{\beta 3}$$

$$(\beta = 1, 2, 3; \delta_{\beta 3} = 0 \text{ unless } \beta = 3, \delta_{33} = 1),$$

where

$$f_{mn}^{(2)} = e^{-iu_{mn}z} (C_m j_{mn}^{(3)} - iu_{mn} j_{mn}^{(1)}),$$

$$f_{mn}^{(3)} = e^{-iu_{mn}z} (D_n j_{mn}^{(1)} - C_m j_{mn}^{(2)}),$$

$$g_{mn}^{(1)} = e^{-iu_{mn}z} [(C_m^2 - k^2) j_{mn}^{(1)} + C_m D_n j_{mn}^{(2)} - iC_m u_{mn} j_{mn}^{(3)}],$$

$$g_{mn}^{(2)} = e^{-iu_{mn}z} [C_m D_n j_{mn}^{(1)} + (D_n^2 - k^2) j_{mn}^{(2)} - iD_n u_{mn} j_{mn}^{(3)}],$$

$$g_{mn}^{(3)} = e^{-iu_{mn}z} [iC_m u_{mn} j_{mn}^{(1)} + iD_n u_{mn} j_{mn}^{(2)} + (u_{mn}^2 - k^2) j_{mn}^{(3)}].$$

In deriving (B7), (B8), it has been assumed that \vec{j} , and hence the functions $j_{mn}^{(1,2,3)}$, tends to zero at infinity sufficiently rapidly, and also that j_x , j_y , and hence $j_{mn}^{(1,2)}$, vanish for $z = 0$, so that these functions are continuous for $z = 0$. If this latter condition is not satisfied, other terms appear; but we can evidently suppose it satisfied, since we are going to proceed to the limiting case of a current element.

(B2), together with (B7) and (B8), now gives a solution of the equations (B1), as may be verified by direct substitution, and all conditions are satisfied.

Suppose now that the guide transmits only the H_{10} wave; then from (B6) we see that all the u_{mn} are pure imaginary except u_{10} . From what has been said above, it then follows that all the functions $A_{mn}^{(1)}, \dots, B_{mn}^{(3)}$ represent damped waves except those with $m = 1, n = 0$. Hence, from (B2), (B7), (B8), and since the $j_{mn}^{(\beta)} \rightarrow 0$ as $z \rightarrow \infty$, we find for the field, for z large and positive

$$E_y = \frac{-k}{2cu_{10}} e^{iu_{10}z} \int_{-\infty}^{\infty} j_{10}^{(2)} e^{-iu_{10}z} dz \cdot \sin \frac{\pi x}{a},$$

$$(B9) \quad H_x = -\frac{u_{10}}{k} E_y,$$

$$H_z = \frac{\pi i}{2acu_{10}} e^{iu_{10}z} \int_{-\infty}^{\infty} j_{10}^{(2)} e^{-iu_{10}z} dz \cdot \cos \frac{\pi x}{a},$$

$$E_x = E_z = H_y = 0.$$

This represents an H_{10} wave. From (B3) we have

$$(B10) \quad j_{10}^{(2)}(z) = \frac{2}{ab} \int_0^a dx \int_0^b dy \cdot j_y(x, y, z) \sin \frac{\pi x}{a}.$$

To obtain the field due to a current element of components ($ILds_0$, $IMds_0$, $INds_0$) situated at the point (x_0, y_0, z_0) , we now suppose that \vec{j} tends to zero everywhere except in the immediate neighborhood of the points (x_0, y_0, z_0) and $(x_0, y_0, -z_0)$. At these points \vec{j} is to tend to infinity in such a way that the total components of current in any small region surrounding (x_0, y_0, z_0) are ($ILds_0$, $IMds_0$, $INds_0$), and the total components of current in any small region surrounding $(x_0, y_0, -z_0)$ are $(-ILds_0, -IMds_0, +INds_0)$. The introduction of the singularity at $(x_0, y_0, -z_0)$ is, of course, necessary in order to preserve the odd or even character of the components of \vec{j} . This case can be represented symbolically in terms of δ -functions by putting, in our final results,

$$(B11) \quad \begin{cases} j_x = ILds_0 \delta(x - x_0) \delta(y - y_0) [\delta(z - z_0) - \delta(z + z_0)], \\ j_y = IMds_0 \delta(x - x_0) \delta(y - y_0) [\delta(z - z_0) - \delta(z + z_0)], \\ j_z = INds_0 \delta(x - x_0) \delta(y - y_0) [\delta(z - z_0) + \delta(z + z_0)]. \end{cases}$$

Using (B10), we then find, for this case,

$$(B12) \quad \int_{-\infty}^{\infty} j_{10}^{(2)} e^{-iu_{10}z} dz = \frac{-4i}{ab} \sin \frac{\pi x_0}{a} \sin (u_{10}z_0) IM ds_0.$$

Inserting this in (B9), and putting $u_{10} = \gamma k$, where γ is as defined in (5.3), we finally have for the field at a large distance down the guide

$$(B13) \quad \begin{cases} E_y = \frac{2iIMds_0}{\gamma abc} \sin \frac{\pi x_0}{a} \sin \gamma k z_0 \sin \frac{\pi x}{a} e^{i\gamma k z}, \\ H_x = -\gamma E_y, \\ H_z = \frac{2\pi IMds_0}{\gamma k a^2 bc} \sin \frac{\pi x_0}{a} \sin \gamma k z_0 \sin \frac{\pi x}{a} e^{i\gamma k z}. \end{cases}$$

Comparing with (5.5) and (5.7) and allowing for the change of origin, we see that this field is identical with that given by the method of images. The rest of the calculation now proceeds as before.

It may be remarked that use of (B11) in the general formulae (B2), (B7), (B8) gives the field at *any* point in the guide, expressed as a double Fourier series (except in the plane $z = z_0$, where the representation obviously fails).

PART II. A GENERAL METHOD FOR CALCULATING THE IMPEDANCE OF AN ANTENNA IN A WAVE GUIDE OF ARBITRARY CROSS SECTION

BY A. F. STEVENSON

1. Introduction

In this part, it is shown that the problem of finding the radiation resistance and reactance of an antenna of arbitrary shape in a wave guide of arbitrary cross section can be solved if the current distribution in the antenna is known, and if the eigenfunctions which determine the free propagation in the guide

can be found. In the case where only a single E - or H -wave is transmitted, a simple closed expression for the resistance results. The reactance, on the other hand, requires the summation of an infinite series, the calculation of which would be somewhat tedious, though quite feasible, in any given case. The reactance is discussed in Section 4. Incidentally, the field at any point in the guide is obtained in the course of the work.

The method used is a generalization of one of the three methods previously given for calculating the field due to a dipole in a rectangular wave guide in Part I. Its great advantage, as compared with previous special methods for rectangular and circular guides, is its generality and comparative simplicity.

In a recent report, Chu (2) has given formulae for the resistance of antennae in rectangular and circular guides in particular cases, and has stated that the method used is applicable to guides of any cross section. He gives no indication of the method, however, beyond stating that it involves the use of orthogonal functions. Actually, some of Chu's formulae are not correct.

2. Calculation of the Field

We consider a cylindrical wave guide closed by a plug, both guide and plug being perfectly conducting. We take origin in the plane of the plug-face, with the z -axis along the length of the guide (Fig. 1). We use Heaviside

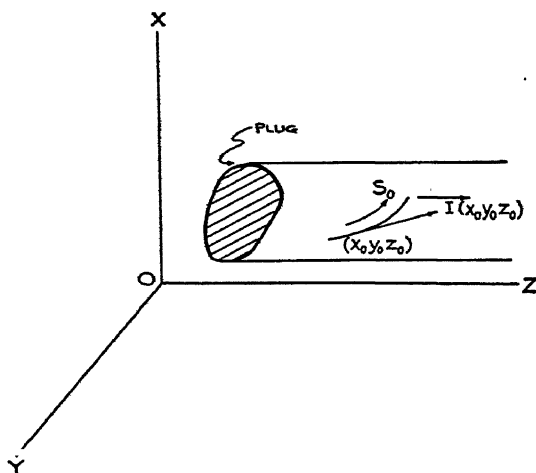


FIG. 1. Wave guide with antenna of arbitrary shape and current distribution.

units, and suppose a steady state in which all quantities vary with the time according to the factor $e^{-i\omega t}$, this factor being omitted (the electric field is thus the real part of $\vec{E}e^{-i\omega t}$, etc.).

We first recall the solutions which give the *free* propagation in a guide extending to infinity in both directions. For E -waves, we have to solve the eigenvalue problem

$$(1) \quad \left\{ \begin{array}{l} \frac{\partial^2 \psi}{\partial x^2} + \frac{\partial^2 \psi}{\partial y^2} + \mu^2 \psi = 0 \quad \text{inside } S, \\ \psi = 0 \quad \text{on } C, \end{array} \right.$$

where S denotes the interior of the cross section of the guide, and C denotes the boundary of S (Fig. 2). Let the eigenvalues of this problem, arranged

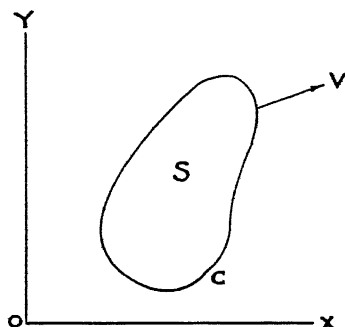


FIG. 2. Cross section of guide.

in ascending order of magnitude, and the corresponding orthogonal eigenfunctions, be

$$\mu = \mu_1, \mu_2, \dots,$$

$$\psi = \psi_1, \psi_2, \dots$$

We suppose the eigenfunctions normalized so that

$$\int_S \psi_n^2 dx dy = 1.$$

The case of degeneracy can be included by supposing that some of the μ 's may be equal. The field for an E_n -wave, propagated (or damped) in the positive z -direction, is then given, apart from an arbitrary constant factor, by

$$(2) \quad \begin{cases} E_x = f'_n(z) \frac{\partial \psi_n}{\partial x}, & E_y = f'_n(z) \frac{\partial \psi_n}{\partial y}, & E_z = \mu_n^2 f_n(z) \psi_n, \\ H_x = -ik f_n(z) \frac{\partial \psi_n}{\partial y}, & H_y = ik f_n(z) \frac{\partial \psi_n}{\partial x}, & H_z = 0, \end{cases}$$

where

$$k = \omega/c = 2\pi/\lambda, \quad f_n(z) = e^{iu_n z},$$

and

$$(2') \quad u_n = \sqrt{k^2 - \mu_n^2}.$$

In (2'), the positive square-root is to be taken if u_n is real (propagation), and the positive-imaginary if u_n is pure imaginary (damping).

For the H -waves, we have to solve the eigenvalue problem

$$(3) \quad \begin{cases} \frac{\partial^2 \Psi}{\partial x^2} + \frac{\partial^2 \Psi}{\partial y^2} + M^2 \Psi = 0 & \text{inside } S, \\ \frac{\partial \Psi}{\partial \nu} = 0 & \text{on } C, \end{cases}$$

where ν denotes the outward normal to C (Fig. 2). Let the eigenvalues, arranged in ascending order of magnitude, and corresponding eigenfunctions, be

$$M = M_1, M_2, \dots,$$

$$\Psi = \Psi_1, \Psi_2, \dots$$

As before, we suppose the eigenfunctions normalized so that

$$\int_S \Psi_n^2 dx dy = 1,$$

and degeneracy can be included as before. Then the field for an H -wave is given by

$$(4) \quad \begin{cases} E_x = ik F_n(z) \frac{\partial \Psi_n}{\partial y}, & E_y = -ik F_n(z) \frac{\partial \Psi_n}{\partial x}, & E_z = 0 \\ H_x = F'_n(z) \frac{\partial \Psi_n}{\partial x}, & H_y = F'_n(z) \frac{\partial \Psi_n}{\partial y}, & H_z = M_n^2 F_n(z) \Psi_n, \end{cases}$$

where

$$F_n(z) = e^{iU_n z},$$

and

$$(5) \quad U_n = \sqrt{k^2 - M_n^2},$$

the same convention as to the sign of the square root being used in (5) as in (2').

We now consider the problem of finding the field due to a current element in the wave guide. For this purpose, we suppose the guide extends to infinity in *both* directions, and eliminate the plug. We then suppose that there is an assigned volume distribution of current, of density \vec{j} , throughout the guide and find the field due to it. We then find the field due to a current element by proceeding to the limiting case where \vec{j} vanishes except at the element and its electrical image in the plug-face.

The Maxwell equations for the case considered are

$$(6) \quad ik \vec{H} = \text{curl } \vec{E}, \quad ik \vec{E} = -\text{curl } \vec{H} + \frac{1}{c} \vec{j}.$$

We suppose that \vec{j} is continuous and vanishes at infinity sufficiently rapidly. Bearing (2) and (4) in mind, we now assume for the field a superposition of E - and H -waves of the form

$$(7) \quad \begin{cases} E_x = \sum_n \left[a_n(z) \frac{\partial \psi_n}{\partial x} + ik A_n(z) \frac{\partial \Psi_n}{\partial y} \right], \\ E_y = \sum_n \left[a_n(z) \frac{\partial \psi_n}{\partial y} - ik A_n(z) \frac{\partial \Psi_n}{\partial x} \right], \\ E_z = \sum_n b_n(z) \psi_n, \\ H_x = \sum_n \left[-ik c_n(z) \frac{\partial \psi_n}{\partial y} + C_n(z) \frac{\partial \Psi_n}{\partial x} \right], \\ H_y = \sum_n \left[ik c_n(z) \frac{\partial \psi_n}{\partial x} + C_n(z) \frac{\partial \Psi_n}{\partial y} \right], \\ H_z = \sum_n D_n(z) \Psi_n, \end{cases}$$

where the summations run from 1 to ∞ , and where $a_n(z)$, ---, $D_n(z)$ are six functions to be determined. The field (7) satisfies the boundary conditions of the problem, and it can be proved that the most general such field can be expressed in this way.

For the components of \vec{j} , we assume analogously

$$(8) \quad \begin{cases} \frac{1}{c} j_x = \sum_n \left[p_n(z) \frac{\partial \psi_n}{\partial x} + ik q_n(z) \frac{\partial \Psi_n}{\partial y} \right], \\ \frac{1}{c} j_y = \sum_n \left[p_n(z) \frac{\partial \psi_n}{\partial y} - ik q_n(z) \frac{\partial \Psi_n}{\partial x} \right], \\ \frac{1}{c} j_z = \sum_n r_n(z) \psi_n. \end{cases}$$

We now note that by differentiating the first two of (8) with respect to x and y , and combining, and using the differential equations (1), (3) satisfied by the functions ψ_n , Ψ_n , we can replace (8) by

$$(8') \quad \begin{cases} \frac{1}{c} j_1 = - \sum_n \mu_n^2 p_n(z) \psi_n, \\ \frac{1}{c} j_2 = - ik \sum_n M_n^2 q_n(z) \Psi_n, \\ \frac{1}{c} j_z = \sum_n r_n(z) \psi_n, \end{cases}$$

where

$$j_1 = \frac{\partial j_x}{\partial x} + \frac{\partial j_y}{\partial y}, \quad j_2 = \frac{\partial j_z}{\partial y} - \frac{\partial j_y}{\partial x}.$$

We shall refer to (8') as the transform of (8). In a similar way (by differentiation and combination of the x - and y -component equations), we construct the transforms of (7) and (6).

We now substitute the transforms of (7) and (8) in the transform of (6). We then obtain six equations, in each of which only one of the sets of functions ψ_1, ψ_2, \dots or Ψ_1, Ψ_2, \dots occurs. We can then equate coefficients of each ψ_n or Ψ_n on both sides of the equations. We obtain in this manner three differential equations of the first order for the functions a_n, b_n, c_n and three for the functions A_n, C_n, D_n , the functions p_n, q_n, r_n being regarded as known. These differential equations are quite simple and are easily solved by the method of variation of constants, the arbitrary constants in the solution being determined so that only outgoing, or damped, waves exist at $z = \pm \infty$. We thus obtain

$$(9) \quad \begin{cases} a_n(z) = c'_n(z) - \frac{i}{k} p_n(z), \quad b_n(z) = \mu_n^2 c_n(z) - \frac{i}{k} r_n(z), \\ c_n(z) = \frac{e^{iu_n z}}{2k u_n} \int_{-\infty}^z e^{-iu_n z} (iu_n p_n - r_n) dz - \frac{e^{-iu_n z}}{2k u_n} \times \\ \quad \int_z^{\infty} e^{iu_n z} (iu_n p_n + r_n) dz, \\ A_n(z) = \frac{1}{M_n^2} D_n(z), \quad C_n(z) = \frac{1}{M_n^2} D'_n(z), \\ D_n(z) = -\frac{k M_n^2}{2U_n} e^{iU_n z} \int_{-\infty}^z e^{-iU_n z} q_n dz - \frac{k M_n^2}{2U_n} e^{-iU_n z} \int_z^{\infty} e^{iU_n z} q_n dz. \end{cases}$$

The constants u_n , U_n are those defined in (2'), (5) with the same convention as to the sign of the square root.

The functions p_n , q_n , r_n are found in terms of the components of \vec{j} by applying to (8') the usual process for determining the coefficients in expansions in orthogonal normalized functions. We thus have the field due to any continuous distribution of current \vec{j} . We pass to the case of a current element of strength $\vec{I}ds_0$ situated at the point (x_0, y_0, z_0) , in the presence of the plug, by putting, in accordance with the principle outlined previously,

$$(10) \quad \begin{cases} j_x = I_x ds_0 \delta(x - x_0) \delta(y - y_0) [\delta(z - z_0) - \delta(z + z_0)], \\ j_y = I_y ds_0 \delta(x - x_0) \delta(y - y_0) [\delta(z - z_0) - \delta(z + z_0)], \\ j_z = I_z ds_0 \delta(x - x_0) \delta(y - y_0) [\delta(z - z_0) + \delta(z + z_0)], \end{cases}$$

the notation of "delta-functions" being used. Finding first the functions p_n , q_n , r_n by means of (8'), substituting in (9), and then using (10), we thus find, for $z > 0$ and $z \neq z_0$,

$$(11) \quad \begin{cases} a_n(z) = \frac{i u_n}{k c \mu_n^2} P_n(x_0, y_0) f_1(u_n, z, z_0) - \frac{i}{k c} R_n(x_0, y_0) f_2(u_n, z, z_0), \\ b_n(z) = -\frac{i}{k c} P_n(x_0, y_0) f_3(u_n, z, z_0) - \frac{\mu_n^2}{k c u_n} R_n(x_0, y_0) f_4(u_n, z, z_0), \\ c_n(z) = \frac{1}{\mu_n^2} b_n(z), \\ A_n(z) = \frac{1}{c U_n M_n^2} Q_n(x_0, y_0) f_1(U_n, z, z_0), \\ C_n(z) = \frac{1}{c M_n^2} Q_n(x_0, y_0) f_3(U_n, z, z_0), \\ D_n(z) = M_n^2 A_n(z), \end{cases}$$

where

$$(12) \quad \begin{cases} P_n(x_0, y_0) = \left[I_x \frac{\partial \psi_n(x_0, y_0)}{\partial x_0} + I_y \frac{\partial \psi_n(x_0, y_0)}{\partial y_0} \right] ds_0, \\ Q_n(x_0, y_0) = \left[I_x \frac{\partial \Psi_n(x_0, y_0)}{\partial y_0} - I_y \frac{\partial \Psi_n(x_0, y_0)}{\partial x_0} \right] ds_0, \\ R_n(x_0, y_0) = I_z \psi_n(x_0, y_0) ds_0, \end{cases}$$

and

$$(13) \quad \begin{cases} f_1(u, z, z_0) = e^{i u z} \sin u z_0, z > z_0, \\ \quad \quad \quad = e^{i u z_0} \sin u z, z < z_0, \\ f_2(u, z, z_0) = e^{i u z} \cos u z_0, z > z_0, \\ \quad \quad \quad = i e^{i u z_0} \sin u z, z < z_0, \\ f_3(u, z, z_0) = i e^{i u z} \sin u z_0, z > z_0, \\ \quad \quad \quad = e^{i u z_0} \cos u z, z < z_0, \\ f_4(u, z, z_0) = e^{i u z} \cos u z_0, z > z_0, \\ \quad \quad \quad = e^{i u z_0} \cos u z, z < z_0. \end{cases}$$

Equations (7), (11), (12), (13) now give the field at any point in the guide due to a current element $\vec{I} ds_0$ at (x_0, y_0, z_0) in the presence of the plug. It will be observed that the functions f_2, f_3 are discontinuous at $z = z_0$. This is due to the nature of the field in the immediate neighborhood of the element; in the plane $z = z_0$, the series (7) are not valid in general. But this is of no practical consequence.

To find the field due to a thin antenna with a given distribution of current of linear density $\vec{I}(x_0, y_0, z_0)$ (Fig. 1), we have merely to write $\vec{I} = \vec{I}(x_0, y_0, z_0)$ and integrate the expressions for $a_n(z)$, ---, $D_n(z)$ given by (11), (12), (13) with respect to s_0 along the antenna, ds_0 being an element of length. We can draw the following two general conclusions:

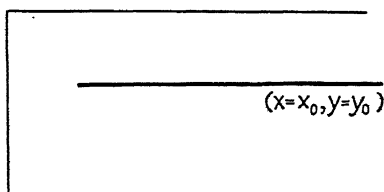


FIG. 3. Longitudinal antenna.

- (1) A longitudinal antenna (Fig. 3) can only generate E -waves, whereas a transverse antenna (Fig. 4) can generate both E - and H -waves. This fact is already doubtless well known to experimental workers.

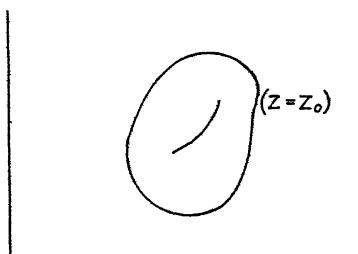


FIG. 4. Transverse antenna.

- (2) When a transverse antenna is used for generating an E_n -wave, the effect is a maximum, other things being equal, when the antenna coincides with one of the orthogonal trajectories of the curves $\psi_n = \text{constant}$. The effect is zero when the antenna coincides with one of the curves $\psi_n = \text{constant}$.
- (3) When a transverse antenna is used for generating an H_n -wave, the effect is a maximum when the antenna coincides with one of the curves $\Psi_n = \text{constant}$. The effect is zero when the antenna coincides with one of the orthogonal trajectories of the curves $\Psi_n = \text{constant}$.

3. The Formulae for Radiation Resistance

To find the resistance, we need merely calculate the mean flux of energy at $z = +\infty$ by Poynting's theorem, and equate this to the mean rate of working of the applied voltage. The method is sufficiently well known, and we omit the details of calculation. In considering the field at infinity, only a few terms (usually only one) of the infinite series in (7) survive, all the other terms being damped out. We consider the following two cases:

- (1) The dimensions of the guide (and manner of excitation) are such that only the E_n -wave is generated. We find

$$(14) \quad (R)_{\text{ohms}} = 120\pi\alpha_n \left| \frac{1}{k} \int \left(I_x \frac{\partial \psi_n}{\partial x} + I_y \frac{\partial \psi_n}{\partial y} \right) \sin(u_n z) ds - \frac{1}{\alpha_n} \int I_z \psi_n \cos(u_n z) ds \right|^2 \frac{1}{|I_0|^2},$$

where $\psi_n = \psi_n(x, y)$, I_0 is the current at the feeding point, and

$$\alpha_n = \frac{k u_n}{\mu_n^2} = \frac{u_n/k}{1 - (u_n/k)^2}.$$

We note that $u_n = 2\pi/\lambda'$, where λ' is the wave length *in the guide*, so that $u_n/k = \lambda/\lambda'$. The integral in (14) is extended over the length of the antenna (we have dropped the suffix 0). We recall that ψ_n is a *normalized* eigenfunction (for definition of μ_n , ψ_n see beginning of Section 2). If μ_n is a degenerate eigenvalue of (1), (14) must be replaced by the sum of such expressions for each independent and orthogonal eigenfunction ψ_n .

- (2) The dimensions of the guide (and manner of excitation) are such that only the H_n -wave is generated. We find

$$(15) \quad (R)_{\text{ohms}} = 120\pi\beta_n \left| \frac{1}{k} \int \left(I_x \frac{\partial \Psi_n}{\partial y} - I_y \frac{\partial \Psi_n}{\partial x} \right) \sin(U_n z) ds \right|^2 \frac{1}{|I_0|^2},$$

where

$$\beta_n = \frac{k^3}{U_n M_n^2} = \frac{k/U_n}{1 - (U_n/k)^2}.$$

The same remarks apply to the case of degeneracy as in (14). (For definition of M_n , U_n , Ψ_n see beginning of Section 2.)

We conclude that for a longitudinal antenna lying along the line $x = x_0$, $y = y_0$, and generating an E_n -wave, R varies as $[\psi_n(x_0, y_0)]^2$; while for a transverse antenna lying at a distance z_0 from the plug, and generating either an E_n - or an H_n -wave, R varies as $\sin^2 \frac{2\pi z_0}{\lambda'}$, where λ' is the wave length in the guide. These results are true, of course, for a guide of *any* cross section, and for any assumed current distribution.

4. Calculation of Reactance

The e.m.f. method of calculating reactance uses the formula (3)

$$(16) \quad R - iX = -\frac{1}{I_0^2} \int I(s)E(s)ds,*$$

where the integral is extended along the antenna, and $E(s)$ denotes the electric field along the surface of the antenna calculated for a current concentrated on the axis of the antenna. This procedure can be justified when the gap is along the length of the antenna, but it seems rather questionable to the writer whether it holds when the gap is *across* the antenna, as is usually the case in a wave guide (for the *resistance*, which can be calculated by means of the *distant* field, the procedure is less open to doubt). Assuming, however, that (16) holds, the reactance can evidently be calculated by means of the formulae in Section 2 giving the field. But as there will now be an infinite number of terms surviving in the series (7), the result will be expressed by means of an infinite series. Formula (16) assumes that the field is symmetrical about the axis of the antenna. This is evidently approximately the case if the radius of the antenna is small compared with its distance from the walls of the guide (except at the point of entry), and if it enters the guide normally (taking account of the image effect in the tangent plane). Otherwise an *average* of $E(s)$ over the cross section of the antenna must be used in (16).

We shall not give an explicit formula for reactance in the general case. Without detailed calculation, however, we can draw a rather interesting conclusion regarding the way the reactance of a transverse antenna, generating only an E_n - or H_n -wave, varies with the distance of the antenna from the plug, other factors being kept constant. Let the axis of the antenna be any curve lying in the plane $z = z_0$, and let us take the integral in (16) along a parallel curve lying in the plane $z = z_0 + r$, where r is the radius of the antenna. Then use of (7), (11), (13) shows that the integral in (16) is, in its dependence on z_0 , r , of the form

$$(17) \quad \sum_m [A_m e^{iu_m(2z_0+r)} + B_m e^{iu_m r} + C_m e^{iU_m(2z_0+r)} + D_m e^{iU_m r}],$$

where A_m, \dots, D_m are independent of z_0, r . In the first and third terms of the summand in (17), r can be neglected.

Suppose now, for definiteness, that only the E_n -wave is generated. Then u_n is real, but all the other u 's and *all* the U 's (except possibly those for which the corresponding coefficient A_m, \dots, D_m is zero) are pure imaginary. Then (17) can be written

$$(18) \quad A_n e^{2iu_n z_0} + \sum_{m \neq n} A_m e^{-2|u_m|z_0} + \sum_m C_m e^{-2|U_m|z_0} + D,$$

where A_n, \dots, D are independent of z_0 . The 2nd and 3rd terms in (18) will evidently be small compared with the other terms unless z_0 is small,

* Formula (16) is a little different from that given by Labus, but is more compact and is easily deducible from his formula. The negative sign appears here before iX on account of the time factor being taken as $e^{-i\omega t}$.

i.e., unless the antenna is near the plug (when the above method would, in any case, break down). Excluding this case, therefore, we see from (16) that X is approximately of the form

$$X = C_1 \cos(2u_n z_0 + \epsilon) + C_2,$$

where C_1 , C_2 , ϵ are independent of z_0 . An exactly similar result is obtained if only the H_n -wave is generated, with U_n in place of u_n .

Hence if the distance from the plug to the antenna varies, other factors being kept constant, the reactance should vary approximately sinusoidally (except near the plug), the period being half the wave length in the guide. This is the same behavior as in the case of the resistance (see end of Section 3), though the phase will of course be different. Some experiments of Chipman and Burr (1) support this conclusion for the case of a straight transverse antenna in a rectangular guide.

References

1. CHIPMAN, R. A. and BURR, A. C. Queen's University, Department of Physics. Rept. No. 2. Revised March 25, 1942.
2. CHU, L. J. Massachusetts Institute of Technology, Radiation Laboratory. Rept. No. 43-4.
3. LABUS, J. Hochfrequenztech. u. Elektroakust. 41 : 17. 1933.

PART III. THE RESISTANCES OF ANTENNAE OF VARIOUS SHAPES AND POSITIONS IN RECTANGULAR AND CIRCULAR WAVE GUIDES

BY W. Z. CHIEN

1. Introduction and Summary

The radiation resistance of an antenna inside a wave guide is defined as the ratio of the total power radiated to the mean square value of the feeding current. If the current distribution along the antenna is given, the first step is to calculate the field at the far end of the guide. When this has been done, the calculation of the total power radiated is just a straightforward integration.

In the following section, we give a list of formulae for the resistance of various antennae inside rectangular and circular wave guides. These formulae are divided into four general cases according to the cross section of the wave guide and the type of wave transmitted. For each general case, we have a general formula for the resistance in terms of integrals depending on the shape and position of the antenna and its current distribution. The general formula (1), quoted from Part I, gives the resistance of an arbitrary antenna in a rectangular wave guide transmitting the H_{10} wave only. The formulae (2), (3), (4) give the resistance of various antennae in circular wave guides. These formulae are calculated from the field distributions given by H. Buchholz (1). The purpose of keeping these general formulae in the list is that they offer a simple means of calculating those special cases missing in this list without knowing the actual field distribution. It should be noted that these formulae are but special forms of two more general formulae, which have been given by A. F. Stevenson in Part II.

2. Results

The Resistance of an Arbitrary Antenna in a Rectangular Wave Guide Transmitting only the H_{10} Wave

General formula:

$$(1) \quad R = \frac{240\pi\varphi^2}{ab\gamma} \text{ ohms,}$$

where

$$(1a) \quad \varphi = \int \frac{I}{I_0} \sin\left(\frac{2\pi}{\lambda} \gamma z_0\right) \cos\left(\frac{\pi}{a} x_0\right) dy_0 \text{ (taken along the antenna).}$$

The conditions for transmitting the H_{10} wave only in a rectangular wave guide are in general:

$$(1b) \quad \frac{1}{a} < \frac{2}{\lambda} < \frac{1}{b}, \quad \frac{1}{a} < \frac{2}{\lambda} < \frac{2}{a}.$$

The notation is as follows:

x, y, z = the rectangular co-ordinate system, origin at the center of the plug face,

a = the longer side of the guide along the x -axis.

b = the shorter side of the guide along the y -axis,

λ = the wave length,

$$\gamma = \sqrt{1 - \left(\frac{\lambda}{2a}\right)^2}, \quad \frac{2\pi}{\lambda} \gamma = \text{the phase constant of the } H_{10} \text{ wave.}$$

x_0, y_0, z_0 = the co-ordinates of a point on the antenna,

I = the current along the antenna,

I_0 = current at the feeding point of the antenna.

Special cases:

- 1a. A straight antenna of length l parallel to the y -axis, running from $y = -b/2$ to $y = l - b/2$ (Fig. 1). Assuming sinusoidal current distribution,

$$R = \frac{60\lambda^2}{\pi ab\gamma} \left[\cos\left(\frac{\pi}{a} x_0\right) \sin\left(\frac{2\pi\gamma}{\lambda} z_0\right) \tan\left(\frac{\pi l}{\lambda}\right) \right]^2 \text{ ohms,}$$

where x_0 = the off-center distance from the y -axis to the antenna,

z_0 = the distance from the plug to the antenna.

- 1b. The same antenna as in case 1a. Assuming uniform current distribution,

$$R = \frac{240l^2}{ab\gamma} \left[\cos\left(\frac{\pi}{a} x_0\right) \sin\left(\frac{2\pi\gamma}{\lambda} z_0\right) \right]^2 \text{ ohms.}$$

- 1c. A circular loop, the axis of which is parallel to the x -axis, radius r_0 , center at (x_0, y_0, z_0) (see Fig. 2).

Assuming uniform current distribution,

$$R = \frac{960\pi^3 r_0^2}{ab\gamma} \left[\cos\left(\frac{\pi}{a} x_0\right) \cos\left(\frac{2\pi\gamma}{\lambda} z_0\right) J_1\left(\frac{2\pi\gamma}{\lambda} r_0\right) \right]^2 \text{ ohms.}$$

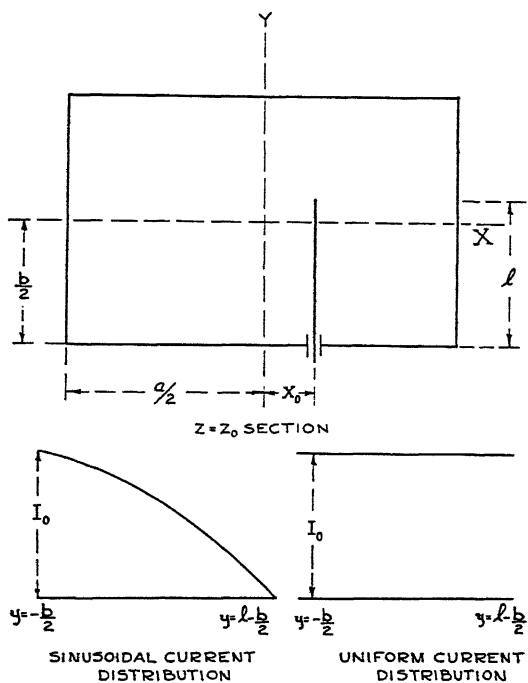


FIG. 1.

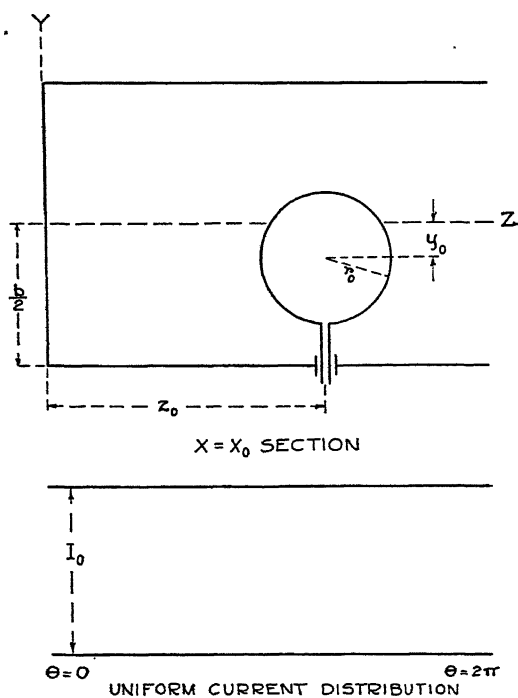


FIG. 2.

- 1d. A circular loop, the axis of which is parallel to the z -axis, radius r_0 , center at (x_0, y_0, z_0) (see Fig. 3).

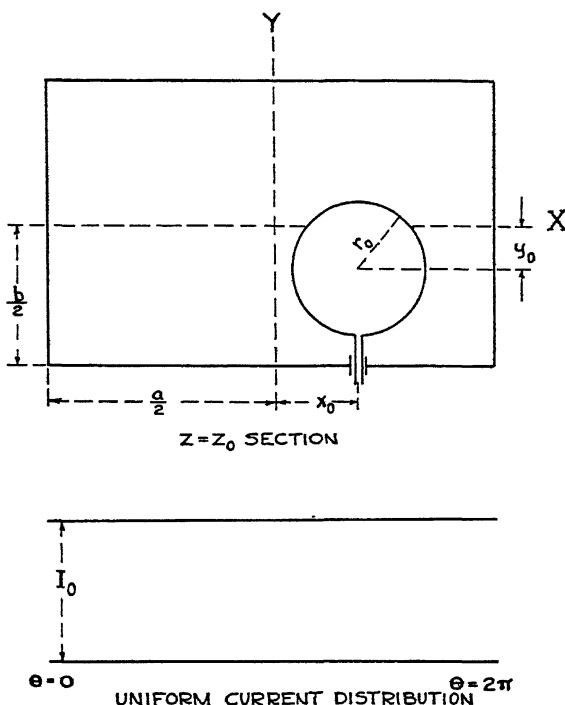


FIG. 3.

Assuming uniform current distribution,

$$R = \frac{960\pi^3 r_0^2}{ab\gamma} \left[\sin\left(\frac{\pi}{a} x_0\right) \sin\left(\frac{2\pi\gamma}{\lambda} z_0\right) J_1\left(\frac{\pi}{a} r_0\right) \right]^2 \text{ ohms.}$$

- 1e. An American antenna of circular shape in the yz plane, being divided into four sections, radius r_0 and center at (x_0, y_0, z_0) (see Fig. 4). Assuming sinusoidal current distribution in each section so that $\pi r_0 = \lambda$,

$$R = \frac{61440\pi r_0^2}{\gamma ab} \left[\cos\left(\frac{\pi}{a} x_0\right) \cos\left(\frac{2\pi}{\lambda} \gamma z_0\right) F(2\gamma) \right]^2 \text{ ohms,}$$

where

$$F(x) = \frac{d^2}{dx^2} \left(\frac{\sin^2 \frac{x}{2}}{x} \right), \pi r_0 = \lambda.$$

- 1f. An American antenna of the circular shape in the XY plane, being divided into four sections, radius r_0 and center at (x_0, y_0, z_0) (see Fig. 5). Assuming sinusoidal current distribution in each section so that $\pi r_0 = \lambda$,

$$R = \frac{61440\pi r_0^2}{ab\gamma} \left[\sin\left(\frac{\pi}{a} x_0\right) \sin\left(\frac{2\pi}{\lambda} \gamma z_0\right) F\left(\frac{\lambda}{a}\right) \right]^2 \text{ ohms.}$$

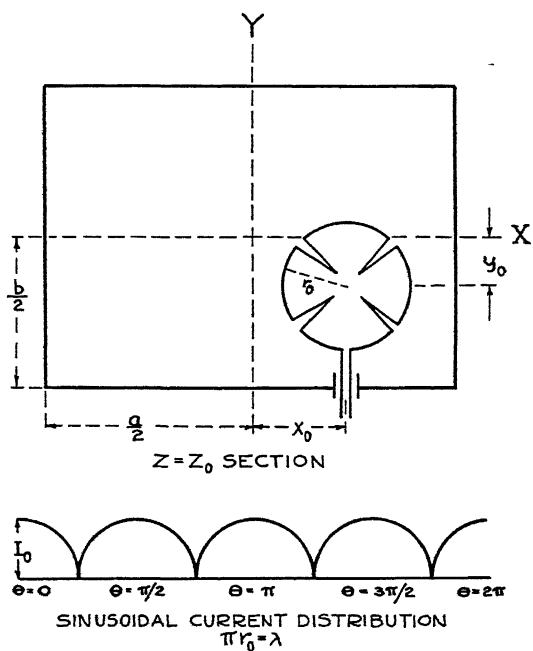


FIG. 4.

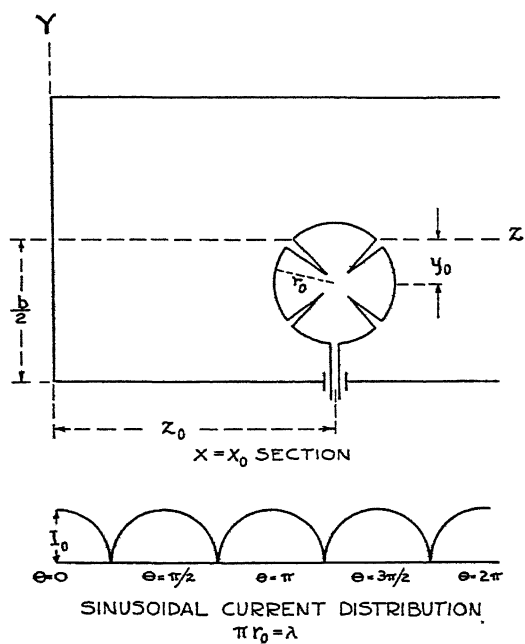


FIG. 5.

The resistance of an Antenna Parallel to the Axis in a Circular Wave Guide Transmitting the E_{01} Wave Only

General Formula:

$$(2) \quad R = \frac{30}{\pi^2 J_1^2(j_{01})} \frac{\lambda^2}{\gamma_{01} a^4} \left[\varphi_0 J_0 \left(j_{01} \frac{r_0}{a} \right) \right]^2 \text{ ohms,}$$

where

$$(2a) \quad \text{the numerical factor} = \frac{30}{\pi^2 J_1^2(j_{01})} = 11.28,$$

$$(2b) \quad \varphi_0 = \int \frac{I}{I_0} \cos \left(\frac{2\pi}{\lambda} \gamma_{01} z_0 \right) dz_0 \text{ (taken along the antenna).}$$

The conditions for transmitting the E_{01} wave only in a circular wave guide are:

(2c) antenna parallel to the axis,

$$(2d) \quad j_{01} = 2.405 < \frac{2\pi a}{\lambda} < 5.520 = j_{02}.$$

The notation is as follows:

a = radius of the wave guide,

$j_{01} = 2.405$ = the first root of $J_0(x)$,

$$\gamma_{01} = \sqrt{1 - \left(\frac{j_{01} \lambda}{2\pi a} \right)^2} = \sqrt{1 - \left(0.3827 \frac{\lambda}{a} \right)^2},$$

$\frac{2\pi}{\lambda} \gamma_{01}$ = the phase constant of the E_{01} wave,

r_0, z_0 = the co-ordinates of the antenna, r_0 = the off-center distance,

z_0 = the distance from the plug,

I = current along the antenna,

I_0 = current at the feeding point.

Special cases:

2a. A straight antenna of length l parallel to the z -axis, running from $z = 0$ to $z = l$. Assuming sinusoidal current distribution (Fig. 6),

$$R = \frac{308.0}{\gamma_{01}} \left\{ \frac{\sin \left[\frac{\pi l}{\lambda} (1 + \gamma_{01}) \right] \sin \left[\frac{\pi l}{\lambda} (1 - \gamma_{01}) \right]}{\sin \left(\frac{2\pi l}{\lambda} \right)} J_0 \left(j_{01} \frac{r_0}{a} \right) \right\}^2 \text{ ohms.}$$

$$\left[\frac{480}{[j_{01} J_1(j_{01})]^2} = 308.0. \right]$$

2b. The same antenna as in the case 2a. Assuming uniform current distribution,

$$R = 1.652 \frac{\lambda^4}{a^4 \gamma^3} \left[\sin \left(\frac{2\pi}{\lambda} \gamma_{01} l \right) J_0 \left(j_{01} \frac{r_0}{a} \right) \right]^2 \text{ ohms.}$$

$$\left[\frac{15}{2} \left[\frac{j_{01}}{\pi^2 J_1(j_{01})} \right]^2 = 1.652. \right]$$

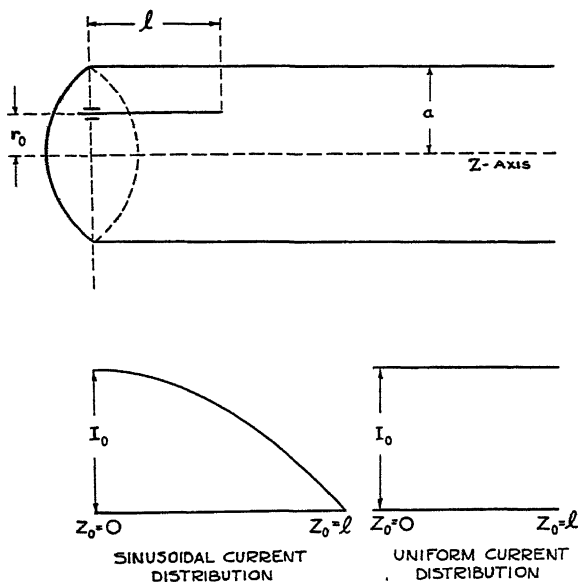


FIG. 6.

The Resistance of a Circular Loop Antenna Coaxially Placed in a Circular Wave Guide Transmitting the H_{01} Wave Only, Assuming Uniform Current Distribution (Fig. 7)

$$(3) \quad R = \frac{480\pi^2}{J_0^2(j'_{01})} \frac{r_0^2}{\gamma_{01}^2 a^2} \left[J_1 \left(\frac{r_0}{a} j'_{01} \right) \sin \left(\frac{2\pi}{\lambda} \gamma_{01} z_0 \right) \right]^2 \text{ ohms,}$$

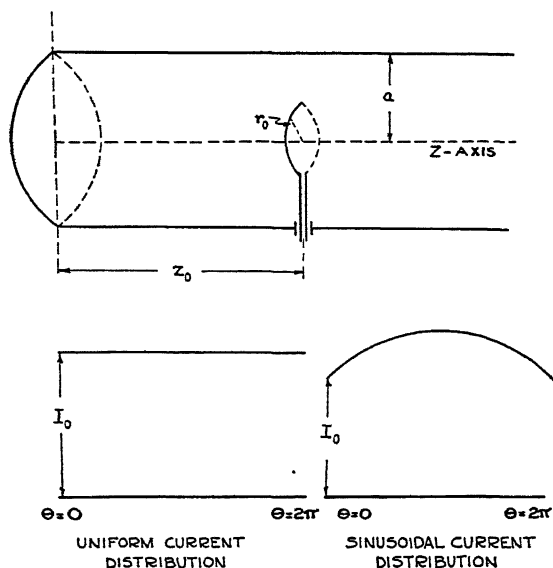


FIG. 7.

where the numerical factor is

$$(3a) \quad \frac{480\pi^2}{J_0^2(j'_{01})} = 2.921 \times 10^4.$$

The conditions for transmitting the H_{01} wave only in a circular waveguide are:

(3b) symmetrically placed loop antenna with uniform current distribution,

$$(3c) \quad j'_{01} = 3.832 < \frac{2\pi a}{\lambda} < 7.016 = j'_{02}.$$

The notation is as follows:

$$j'_{01} = 3.832 = \text{the first root of } J_0(x),$$

$$r_0 = \text{the radius of the loop,}$$

$$a = \text{the radius of the wave guide,}$$

$$\gamma'_{01} = \sqrt{1 - \left(\frac{\lambda j'_{01}}{2\pi a}\right)^2} = \sqrt{1 - \left(0.6098 \frac{\lambda}{a}\right)^2},$$

$$\frac{2\pi}{\lambda} \gamma'_{01} = \text{the phase constant of the } H_{01} \text{ wave.}$$

The Resistance of an Arbitrary Antenna in a Circular Wave Guide Transmitting the H_{11} Wave Only

General formula

$$(4) \quad R = \frac{240}{J_1^2(j'_{11}) (j_{11}^2 - 1)} \frac{1}{\gamma'_{11}} \left(\varphi_{1r} - \frac{j'_{11}}{a} \varphi_{1\theta} \right)^2 \text{ ohms,}$$

where

$$(4a) \quad \text{the numerical factor} = \frac{240}{J_1^2(j'_{11}) (j_{11}^2 - 1)} = 296.6,$$

$$(4b) \quad \varphi_{1r} = \int \frac{I}{I_0} J_1 \left(j'_{11} \frac{r_0}{a} \right) \cos \theta_0 \sin \left(\frac{2\pi}{\lambda} \gamma'_{11} z_0 \right) \frac{dr_0}{r_0} \text{ (taken along the antenna),}$$

$$(4c) \quad \varphi_{1\theta} = \int \frac{I}{I_0} J_1' \left(j'_{11} \frac{r_0}{a} \right) \sin \theta_0 \sin \left(\frac{2\pi}{\lambda} \gamma'_{11} z_0 \right) r_0 d\theta_0.$$

The conditions for transmitting the H_{11} wave only in a circular wave guide are:

(4d) for an antenna having a component in the axial direction:

$$j'_{11} = 1.841 < \frac{2\pi a}{\lambda} < 2.405 = j_{01},$$

(4e) for an antenna having no component in the axial direction:

$$j'_{11} = 1.841 < \frac{2\pi a}{\lambda} < 3.054 = j'_{21}.$$

The notation is as follows:

$$a = \text{the radius of the wave guide,}$$

$$r_0, \theta_0, z_0 = \text{the co-ordinates of a point on the antenna,}$$

$$j'_{11} = 1.841 = \text{the first root of } J'_1(x),$$

$$\gamma'_{11} = \sqrt{1 - \left(\frac{j'_{11}\lambda}{2\pi a}\right)^2} = \sqrt{1 - \left(0.2930 \frac{\lambda}{a}\right)^2},$$

$$\frac{2\pi}{\lambda} \gamma'_{11} = \text{the phase constant of the } H_{11} \text{ wave.}$$

Special cases:

- 4a. A straight antenna of length l placed along a diameter of the wave guide with one end at the surface of the guide. Assuming uniform current distribution (Fig. 8),

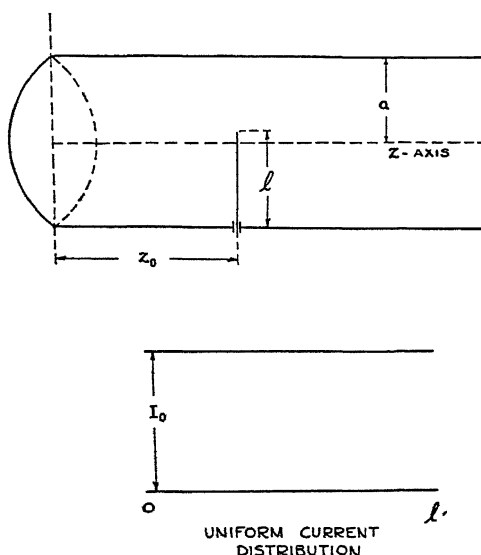


FIG. 8.

$$R = 296.6 \frac{1}{\gamma'_{11}} \left[\sin \frac{2\pi}{\lambda} \gamma'_{11} z_0 \right]^2 \left\{ B(j'_{11}) - B\left((a-l) \frac{j'_{11}}{a}\right) \right\}^2 \text{ ohms,}$$

where

$$B(x) = J'_0(x) + \int_0^x J_0(\alpha) d\alpha, \quad B(j'_{11}) = 1.382.$$

For the special case $l = 2a$: $R = 2259 \frac{1}{\gamma'_{11}} \left[\sin \left(\frac{2\pi}{\lambda} \gamma'_{11} z_0 \right) \right]^2 \text{ ohms.}$

- 4b. A circular loop of radius r_0 placed coaxially in the guide at a distance z_0 from the plug. Assuming sinusoidal current distribution (Fig. 7),

$$R = 1.588 \times 10^5 \frac{r_0^4}{a^2 \lambda^2 \gamma'_{11} \left(1 - \frac{4\pi^2}{\lambda^2} r_0^2 \right)^2} \times$$

$$\left[\sin \left(\frac{2\pi}{\lambda} \gamma'_{11} z_0 \right) \tan \left(\frac{2\pi^2}{\lambda} r_0 \right) J'_1 \left(j'_{11} \frac{r_0}{a} \right) \right]^2 \text{ ohms,}$$

where the numerical factor is

$$\frac{240 j_{11}^2}{(j_{11}^2 - 1) J_1^2(j_{11})} 16\pi^2 = 1.588 \times 10^5.$$

Reference

1. BUCHHOLZ, H. Ann. Physik, 39 : 81. 1941.

PART IV. THE IMPEDANCE OF A RECTANGULAR WAVE GUIDE WITH A THIN ANTENNA

By L. INFELD

WITH APPENDICES BY J. R. POUNDER AND A. F. STEVENSON

1. Introduction

A wave guide of rectangular section extends to infinity in one direction and is closed in the other direction by a plug. The guide and the plug are assumed to be perfect conductors.

A thin, cylindrical antenna is placed inside the guide. To make our argument simple, we place this antenna parallel to the plug and parallel to the two other (shorter) walls of the guide, midway between them. Fig. 1 shows the choice of our co-ordinate system. In it, the lower end of the antenna has the co-ordinates $(0, 0, 0)$ and the upper end has the co-ordinates $(0, l, 0)$ where l is the length of the antenna. The z -axis is perpendicular to the plug, and points toward the open end.

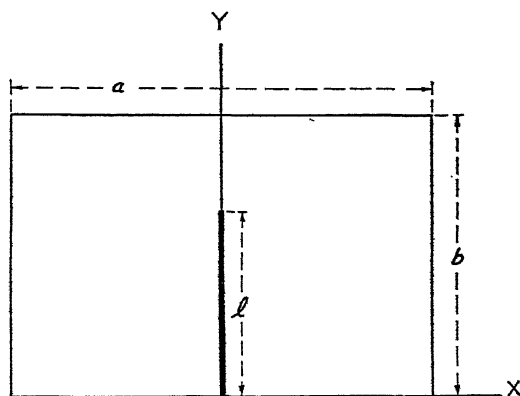


FIG. 1.

The parameters characterizing our problem are:

a, b , the dimensions of the guide,

$k = \frac{2\pi}{\lambda}$ (λ = wave length),

l = the length of the antenna,

ρ_0 = the radius of the antenna, (we assume $\rho_0 k \ll 1$),

z_0 = the distance between the plug and the antenna.

Our problem is to find the impedance of this wave guide under the assumption that the current distribution is sinusoidal. In this respect this paper is a continuation of Part I, in which the problem of the resistance of a rectangular wave guide was solved. However, the method of finding the impedance, and therefore both the resistance and the reactance, has turned out to be so simple that I intend to formulate this part independently, briefly repeating the reasoning concerning the images.

Our particular assumption about the position of the antenna is not essential. It would be easy to generalize our argument in this respect, as was done in Part I for the case of the resistance (see Appendix A). However, the assumption that the antenna is of cylindrical shape and that the current distribution is *given* is essential for our argument. Again, the assumption that the current distribution is sinusoidal is not necessary and the argument in the case of a constant current distribution and small antenna would be even simpler (see Appendix B).

Some of the results found here are valid for a wave guide of arbitrary shape as long as the antenna is parallel to the plug. This is shown by Stevenson in Appendix C. Especially the conclusions formulated in Section 8 are general and may be of interest to someone who does not care about the detailed calculations. Therefore, I tried to write Section 8 so that its contents may be understood without reading the previous parts.

2. The Lattice of Dipoles

We use the method of images. The image of a dipole with respect to a perfectly conducting plane is obtained by taking the geometrical image and then reversing the direction. The dipole and its image give a field satisfying the condition

$$(2.1) \quad \vec{E}_t = 0$$

over the plane, \vec{E}_t being the tangential component of the electric field.

Let us first consider the case where the rectangular wave guide has no plug, so that it extends to infinity in both directions. Suppose there is a dipole, inside the guide, placed along the y -axis. It is easy to find a doubly infinite system of images (all external to the guide) such that the lattice consisting of the dipole and its images gives a field satisfying the condition (2.1) over the walls of the guide. If we now add a plug, the condition (2.1) will be satisfied over it if we add to the above lattice its image in the plane of the plug.

We place a dipole with components $(0, A_y, 0)$ at $(0, y_0, 0)$. Fig. 2 shows part of the lattice in the plane $z = 0$.

If we let m and n take all integral values, positive, zero, and negative, we may represent the components and positions of all the dipoles in the plane $z = 0$ as follows:

$$(2.2) \quad \begin{array}{ll} (0, A_y, 0) & \text{at } (2ma, \pm y_0 + 2nb, 0) \quad \text{— two basic lattices,} \\ (0, -A_y, 0) & \text{at } (2m + 1)a, \pm y_0 + 2nb, 0 \text{— two basic lattices.} \end{array}$$

The images with respect to the plane of the plug are given by this table by changing the sign of A_y and replacing $z = 0$ by $z = -2z_0$. Thus we have eight "basic" lattices determining the field in the guide.

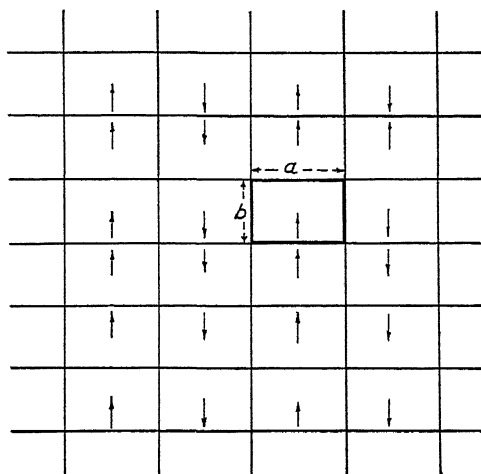


FIG. 2.

3. The Impedance of a Free Antenna

Before we return to our subject of the wave guide, we shall derive an expression for the impedance of a free antenna driven at the lower end. We assume the antenna to be as in Fig. 1, but we shall ignore the wave guide.

We shall now use Sommerfeld's formula (4), which allows us to write the Hertz vector (in Heaviside units) of a dipole at $(0, y_0, 0)$ in the form of an integral:*

$$(3.1) \quad \frac{A_y}{4\pi} \frac{e^{ikr}}{r} = \frac{iA_y}{8\pi} \int_{-\infty}^{+\infty} e^{i\alpha y} e^{-i\alpha y_0} H_0^{(1)}(\rho\sqrt{k^2 - \alpha^2}) d\alpha,$$

$$\rho^2 = x^2 + z^2, \quad r^2 = \rho^2 + (y - y_0)^2,$$

$$\sqrt{k^2 - \alpha^2} = \text{positive imaginary for } \alpha^2 > k^2,$$

$H_0^{(1)}$ = Hankel's function of the first kind and order zero.

We omit here and later the time-factor $e^{-i\omega t}$.

If we have, instead of a dipole, a finite antenna, then the Hertz vector of this antenna can be found by replacing A_y in (3.1) by

$$(3.2) \quad \frac{i}{kc} I_0 \frac{\sin k(l - y_0)}{\sin kl} dy_0,$$

and integrating over dy_0 from 0 to l . Here I_0 is the current at the driving point ($y_0 = 0$), and the expression (3.2) means the assumption of a sinusoidal current distribution.

* Our formula follows from Equation (3) on p. 416 in Watson's book by putting $\mu = -\frac{1}{2}$, $\nu = 0$.

It is convenient to introduce

$$(3.3) \quad f(\alpha) = \int_0^l e^{i\alpha\zeta} \sin k(l - \zeta) d\zeta \\ = \frac{1}{k \left(1 - \left(\frac{\alpha}{k} \right)^2 \right)} \left\{ e^{i\alpha l} - \cos kl - \frac{i\alpha}{k} \sin kl \right\}.$$

Using (3.3), we have for the Hertz vector Φ_y of the finite antenna:

$$(3.4) \quad \Phi_y = - \frac{I_0}{8\pi ck \sin kl} \int_{-\infty}^{\infty} f(\alpha) e^{i\alpha y} H_0^{(1)}(\rho \sqrt{k^2 - \alpha^2}) d\alpha.$$

The next step is to introduce the y -component of the electric field, the only one in which we are interested:

$$(3.5) \quad E_y = k^2 \Phi_y + \frac{\partial^2 \Phi_y}{\partial y^2} \\ = \frac{-I_0}{8\pi ck \sin kl} \int_{-\infty}^{\infty} (k^2 - \alpha^2) f(\alpha) e^{i\alpha y} H_0^{(1)}(\rho \sqrt{k^2 - \alpha^2}) d\alpha.$$

Our last step is to calculate the impedance (Z_{00}) of this free antenna by the e.m.f. method:

$$(3.6) \quad Z_{00} = - \frac{1}{I_0^2} \int_0^l E_y(\rho_0) I dy = - \frac{1}{I_0 \sin kl} \int_0^l E_y(\rho_0) \sin k(l - y) dy.$$

From (3.5), (3.6), (3.3), we obtain:

$$(3.7) \quad Z_{00} = \frac{1}{8\pi ck \sin^2 kl} \int_{-\infty}^{\infty} f(\alpha) \overline{f(\alpha)} (k^2 - \alpha^2) H_0^{(1)}(\rho_0 \sqrt{k^2 - \alpha^2}) d\alpha,$$

where $\overline{f(\alpha)}$ is the complex conjugate of $f(\alpha)$.

Equation (3.7) represents the impedance of a free antenna.

4. The Mutual Impedance of Two Antennae

Before we return to the wave guide we must solve the problem of the mutual impedance of two antennae.

Let us assume that the two antennae are parallel to each other and of the same length l . Let ρ be the distance between them. Then:

$$(4.1) \quad Z_{AB} = - \frac{1}{(I_0^{(A)})^2} \int_0^l E_y^{(B)}(\rho) I^{(A)} dy.$$

Here Z_{AB} is the contribution to the impedance of antenna (A) coming from antenna (B). The indices (A) and (B) denote the current and the field

belonging to antennae (*A*) and (*B*) respectively. Finally we may remark that our formula assumes $\rho_0 \ll \rho$ and therefore it is immaterial whether ρ means the distance between the axes of these antennae or between lines parallel to them and lying on their surfaces.

We shall now consider two cases:

Case a: Each point of antenna (*B*) is obtained from a point of antenna (*A*) by replacing

$$(4.2) \quad 0, y_0, 0 \quad \text{by} \quad a_0, y_0 + b_0, c_0,$$

a_0, b_0, c_0 , being constants.

The calculation of $Z_{AB}^{(a)}$ is very similar to that of Z_{00} . Where we had $y - y_0$ before, we shall now have $y - y_0 - b_0$. Secondly, where we had ρ_0 before, we shall now have

$$(4.3) \quad \rho = \sqrt{a_0^2 + c_0^2}.$$

Thus, instead of (3.7), we now have:

$$(4.4) \quad Z_{AB}^{(a)} = \frac{1}{8\pi ck \sin^2 kl} \int_{-\infty}^{+\infty} e^{-i\alpha b_0} f(\alpha) \overline{f(\alpha)} (k^2 - \alpha^2) H_0^{(1)}(\rho \sqrt{k^2 - \alpha^2}) d\alpha.$$

Case b: Each point of antenna (*B*) is obtained from a point of antenna (*A*) by replacing

$$0, y_0, 0 \quad \text{by} \quad a_0, -y_0 + b_0, c_0.$$

The calculation of $Z_{AB}^{(b)}$ will differ from that of $Z_{AB}^{(a)}$ in one respect: in the integration with respect to y_0 we shall have

$$(4.5) \quad \int_0^l e^{i\alpha y_0} \sin k(l - y_0) dy_0 = \overline{f(\alpha)},$$

instead of

$$\int_0^l e^{-i\alpha y_0} \sin k(l - y_0) dy_0 = f(\alpha)$$

as before.

Thus we have for $Z_{AB}^{(b)}$:

$$(4.6) \quad Z_{AB}^{(b)} = \frac{1}{8\pi ck \sin^2 kl} \int_{-\infty}^{+\infty} e^{-i\alpha b_0} (\overline{f(\alpha)})^2 (k^2 - \alpha^2) H_0^{(1)}(\rho \sqrt{k^2 - \alpha^2}) d\alpha.$$

Both results, (4.4) and (4.6), will be needed in our later argument.

5. The Impedance of a Wave Guide

We summarize the result of our previous section: The mutual impedance of two "parallel", identical antennae (case *a*) is:

$$(5.1) \quad Z_{AB}^{(a)} = \int_{-\infty}^{+\infty} e^{-i\alpha b_0} \varphi(\rho, \alpha) d\alpha.$$

The mutual impedance of two "antiparallel", identical antennae (case *b*) is:

$$(5.2) \quad Z_{AB}^{(b)} = \int_{-\infty}^{\infty} e^{-i\alpha b_0} \psi(\rho, \alpha) d\alpha.$$

Here we have, according to (4.4) and (4.6):

$$(5.3) \quad \begin{aligned} \varphi(\rho, \alpha) &= \frac{1}{8\pi c k \sin^2 kl} f(\alpha) \overline{f(\alpha)} (k^2 - \alpha^2) H_0^{(1)}(\rho \sqrt{k^2 - \alpha^2}), \\ \psi(\rho, \alpha) &= \frac{1}{8\pi c k \sin^2 kl} (\overline{f(\alpha)})^2 (k^2 - \alpha^2) H_0^{(1)}(\rho \sqrt{k^2 - \alpha^2}), \end{aligned}$$

and according to (3.3)

$$(5.4) \quad f(\alpha) = \frac{1}{k \left(1 - \left(\frac{\alpha}{k} \right)^2 \right)} \left\{ e^{-i\alpha l} - \cos kl + i \frac{\alpha}{k} \sin kl \right\}.$$

The self-impedance of an antenna is obtained from (5.1) by putting there:

$$(5.5) \quad b_0 = 0, \quad \rho = \rho_0.$$

Now we know that the impedance of a wave guide is equivalent to the impedance of an antenna surrounded by *eight* basic lattices. In (2.2) we wrote down the co-ordinates of the dipoles of four basic lattices. If the dipoles become finite antennae, the four antenna-lattices consist of "parallel" or "antiparallel" antennae. The remaining four lattices are opposite in direction and placed in the plane $z = -2z_0$. Thus we have, because of (5.1), (5.3), and (2.2) for the impedance of an antenna in a wave guide:

$$(5.6) \quad \begin{aligned} Z &= \sum_{m=-\infty}^{\infty} \sum_{n=-\infty}^{\infty} \int_{-\infty}^{\infty} e^{-i2n b \alpha} \left[\varphi(\rho_0 + 2ma, \alpha) + \psi(\rho_0 + 2ma, \alpha) \right. \\ &\quad - \varphi((2m+1)a, \alpha) - \psi((2m+1)a, \alpha) \\ &\quad - \varphi(\sqrt{(2ma)^2 + (2z_0)^2}, \alpha) - \psi(\sqrt{(2ma)^2 + (2z_0)^2}, \alpha) \\ &\quad \left. + \varphi(\sqrt{(2m+1)a^2 + (2z_0)^2}, \alpha) + \psi(\sqrt{(2m+1)a^2 + (2z_0)^2}, \alpha) \right] d\alpha. \end{aligned}$$

We have here, in square brackets, eight expressions, each corresponding to one of the basic lattices. The terms with ρ_0 , for $m = 0$, give the self-reactance, and in them ρ_0 must not be omitted. Otherwise, for $m \neq 0$, it is immaterial whether ρ_0 is omitted or not.

Our expression for the impedance, (5.6), though representing the solution of our problem, is too complicated to be used in actual calculations. Our aim is to change (5.6) in such a way that it will be applicable for practical purposes. We shall do it in detail for the first expression:

$$(5.7) \quad \sum_{m=-\infty}^{\infty} \sum_{n=-\infty}^{\infty} \int_{-\infty}^{+\infty} e^{-i2n b \alpha} \varphi(\rho_0 + 2ma, \alpha) d\alpha.$$

We introduce a new variable

$$\sigma = \frac{b}{\pi} \alpha.$$

Then instead of (5.7) we have

$$(5.8) \quad \frac{\pi}{b} \sum_{m=-\infty}^{\infty} \sum_{n=-\infty}^{\infty} \int_{-\infty}^{\infty} e^{-i2\pi n\sigma} \varphi \left(\rho_0 + 2ma, \frac{\pi}{b} \sigma \right) d\sigma.$$

We can now apply Poisson's formula (1), replacing (5.8) by

$$(5.9) \quad \frac{\pi}{b} \sum_{m=-\infty}^{\infty} \sum_{n=-\infty}^{\infty} \varphi \left(\rho_0 + 2ma, \frac{n\pi}{b} \right).$$

For $m \neq 0$, we have $\rho = \sqrt{4m^2a^2} = 2|m|a$. Therefore, the summation from $m = -\infty$ to $m = +\infty$ can be replaced by a summation from $m = 0$ to $m = \infty$. If we look back at (5.3), we see that $\varphi(-\alpha) = \varphi(\alpha)$; therefore $\varphi(-n) = \varphi(n)$. Again the summation from $n = -\infty$ to $n = \infty$ can be replaced by summation from 0 to ∞ . Thus (5.9) takes the form

$$(5.10) \quad \frac{\pi}{b} \sum_{m=0}^{\infty} \sum_{n=0}^{\infty} \delta_m \delta_n \varphi \left(\rho_0 + 2ma, \frac{n\pi}{b} \right),$$

where

$$\delta_s = 2 \text{ for } s \neq 0, \quad \delta_0 = 1.$$

We have to repeat the same reasoning for the remaining seven expressions in (5.6), each time using Poisson's formula. Having done this and having introduced for φ and ψ expressions (5.3) and (5.4), we obtain for the total impedance:

$$(5.11) \quad Z = \frac{1}{4bck \sin^2 kl} \sum_{m=0}^{\infty} \sum_{n=0}^{\infty} (-1)^m \delta_m \delta_n \frac{\left(\cos kl - \cos \frac{n\pi l}{b} \right)^2}{1 - \left(\frac{n\pi}{bk} \right)^2} \times \\ \left[H_0^{(1)} \left[\left(\rho_0 + ma \right) \sqrt{k^2 - \left(\frac{n\pi}{b} \right)^2} \right] \right. \\ \left. - H_0^{(1)} \left[\sqrt{\left((ma)^2 + (2z_0)^2 \right) \left(k^2 - \left(\frac{n\pi}{b} \right)^2 \right)} \right] \right].$$

This is the final result. If expressed in ohms, instead of Heaviside units, it must be multiplied by $120\pi c$.

6. Discussion of (5.11)

The great virtue of (5.11) is its quick convergence. Let us assume

$$(6.1) \quad \frac{\pi n}{bk} = \nu \gg 1, \quad mak = \mu \gg 1.$$

Then

$$(6.2) \quad |H_0^{(1)}(i\mu\nu)| \sim \frac{e^{-\mu\nu}}{\sqrt{\mu\nu}},$$

which shows that the evaluation of (5.11) will be comparatively easy to handle.

Let us imagine a point lattice (Fig. 3), where each point corresponds to one expression in the sum (5.11). Let us further assume that the dimensions of

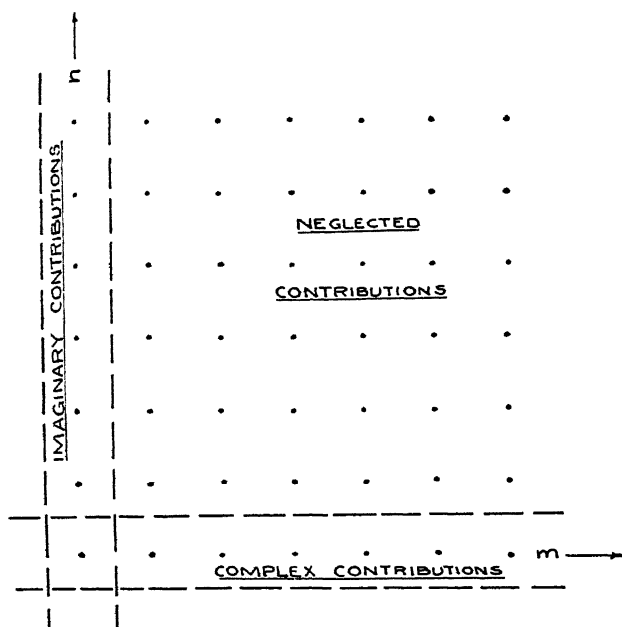


FIG. 3.

the wave guide are such that it lets through only the H_{01} wave, and that

$$(6.3) \quad \sqrt{1 - \left(\frac{\pi m}{ak}\right)^2} = \sqrt{1 - \left(\frac{\lambda m}{2a}\right)^2} \text{ is imaginary for } m = 2, 3, \dots, \text{ and real for } m = 1,$$

$$\sqrt{1 - \left(\frac{\pi n}{bk}\right)^2} = \sqrt{1 - \left(\frac{\lambda n}{2b}\right)^2} \text{ is imaginary for } n = 1, 2, \dots.$$

Because $H_0^{(n)}$ of an imaginary argument is imaginary, we see that the contribution to the impedance is purely imaginary if $n \geq 1$. Only the points along the m -axis give a complex contribution. Because of (6.2), the most important contribution will come from the points on the m - and n -axes. It was found that all others can be ignored in practical applications. Therefore, we shall now focus our attention upon the contributions to (5.11) from these points, which are as follows:

$$(a) \quad m = 0, \quad n = 0:$$

$$(6.4) \quad \frac{\tan^2 \frac{kl}{2}}{4bck} (H_0^{(n)}(\rho_0 k) - H_0^{(n)}(2z_0 k)),$$

(b) $m = 0, \quad n = 1, 2, \dots :$

$$(6.4) \text{ (Cont'd)} \quad \frac{1}{2bck \sin^2 kl} \sum_{n=1}^{\infty} \frac{\left(\cos kl - \cos \frac{\pi nl}{b}\right)^2}{1 - \left(\frac{\pi n}{bk}\right)^2} \left[H_0^{(1)}\left(\rho_0 k \sqrt{1 - \left(\frac{\pi n}{bk}\right)^2}\right) - H_0^{(1)}\left(2z_0 k \sqrt{1 - \left(\frac{\pi n}{bk}\right)^2}\right) \right],$$

(c) $n = 0, \quad m = 1, 2, \dots :$

$$\frac{\tan^2 kl/2}{2bck} \sum_{m=1}^{\infty} (-1)^m [H_0^{(1)}(mak) - H_0^{(1)}(k\sqrt{(ma)^2 + (2z_0)^2})].$$

As $H_0^{(1)}(x)$ behaves like $\log x$ for small x , the (a) part gives the logarithmic term which appears in all calculations of impedance. In the (b) part, we shall have to sum a few expressions only, if $\rho_0 k$ is of the order of, say, $1/10$. Finally (c), that is the summation along the m -axis, is very simple, although it does not converge exponentially. However, even (c) converges as $\sum \frac{e^{imx}}{m^{3/2}}$, since for great m we can write

$$(-1)^m (H_0^{(1)}(mak) - H_0^{(1)}(k\sqrt{(ma)^2 + (2z_0)^2})) \sim e^{-im\pi} \frac{2z_0^2}{mak} H_1^{(1)}(mak) \sim \frac{e^{im(\alpha k - \pi)}}{m^{3/2}}.$$

We shall see later how to deal with part (c) in actual calculations.

If we are looking for reactance only, we shall have to replace $H_0^{(1)}$ by iY_0 in (6.4) (a) and (c).

7. The Resistance

The resistance is the real part of (6.4) (a) and (c) for $\rho_0 \rightarrow 0$.

$$(7.1) \quad R = \frac{\tan^2 \frac{kl}{2}}{4bck} \sum_{m=-\infty}^{\infty} (J_0(mak) - J_0(k\sqrt{(ma)^2 + (2z_0)^2})) e^{i\pi m},$$

where R denotes the resistance.

We shall again use Poisson's formula, this time replacing summation by integration. Then we have:

$$(7.2) \quad R = \frac{\tan^2 \frac{kl}{2}}{4bck} \sum_{h=-\infty}^{\infty} \int_{-\infty}^{\infty} e^{-i2\pi(h-1/2)\alpha} [J_0(\alpha ak) - J_0(k\sqrt{(\alpha a)^2 + (2z_0)^2})] d\alpha.$$

We can replace the J_0 's by $H_0^{(1)}$'s and calculate R as the *real* part of

$$(7.3) \quad \frac{\tan^2 \frac{kl}{2}}{4bck} \sum_{h=-\infty}^{\infty} \int_{-\infty}^{\infty} e^{-i2\pi(h-1/2)\alpha} [H_0^{(1)}(\alpha ak) - H_0^{(1)}(k\sqrt{(\alpha a)^2 + (2z_0)^2})] d\alpha.$$

Now we can use Sommerfeld's formula (3.1) with

$$y_0 \rightarrow 2\pi(h - 1/2), \quad \rho \rightarrow iak, \quad y \rightarrow 0, \quad k \rightarrow \frac{2iz_0}{a}.$$

We have, according to this formula:

$$\begin{aligned} & \int_{-\infty}^{+\infty} e^{-i2\pi(h-1/2)\alpha} H_0^{(1)}(\alpha ak) d\alpha - \int_{-\infty}^{+\infty} e^{-i2\pi(h-1/2)\alpha} H_0^{(1)}(k\sqrt{(\alpha a)^2 + (2z_0)^2}) d\alpha \\ (7.5) \quad &= \frac{2}{i\sqrt{-(ak)^2 + 4\pi^2(h-1/2)^2}} - \frac{2e^{\frac{-2z_0}{a}\sqrt{-(ak)^2 + 4\pi^2(h-1/2)^2}}}{i\sqrt{-(ak)^2 + 4\pi^2(h-1/2)^2}}. \end{aligned}$$

We see that this expression will be real only if

$$(7.6) \quad h = 0 \quad \text{or} \quad h = 1.$$

In this case we have for the above integrals (for $h = 0$ and $h = 1$):

$$(7.7) \quad \frac{4}{ak\sqrt{1 - \left(\frac{\pi}{ak}\right)^2}} - \frac{4 \cos\left(2z_0 k \sqrt{1 - \left(\frac{\pi}{ak}\right)^2}\right)}{ak\sqrt{1 - \left(\frac{\pi}{ak}\right)^2}}.$$

The result is

$$(7.8) \quad R = \frac{2 \tan^2 \frac{kl}{2} \sin^2\left(z_0 k \sqrt{1 - \left(\frac{\pi}{ak}\right)^2}\right)}{abck^2 \sqrt{1 - \left(\frac{\pi}{ak}\right)^2}},$$

which is in perfect agreement with the result obtained in Part I.

8. The Impedance Circle

We shall present our reasoning here in the form of theorems, so that the reader interested in their formulation only can omit the proofs.

We assume the dimensions of the wave guide (a, b) and the wave length (λ) and the thickness of the antenna ($2\rho_0$) as known and kept constant. The characteristic impedance of the line (Z_0) is also known. Our problem is to find l_0 (the matching length of the antenna) and z_0 (the distance of the antenna from the plug) so that the resistance will be that of the line and the reactance will be zero. It is convenient to take as the unit of impedance that of the line (Z_0). In this unit our problem is to find l_0, z_0 , such that

$$(8.1) \quad R = 1, X = 0, \text{ where } Z = R - iX.$$

This we shall refer to as the *matching* problem.

Theorem I

The resistance can be expressed in the form

$$(8.2) \quad R = A(l) - A(l) \cos\left(\frac{4\pi}{\lambda} \gamma z_0\right),$$

where

$$(8.3) \quad \begin{cases} A(l) = \frac{30\lambda^2}{ab\pi\gamma Z_0} \tan^2\left(\frac{\pi l}{\lambda}\right), \\ \gamma = \sqrt{1 - \left(\frac{\lambda}{2a}\right)^2}. \end{cases}$$

The proof follows immediately from (7.8), if we assume that the impedance of the line (Z_0) is expressed in ohms.

Theorem II

If z_0 is *not* small compared with λ , then we can express the reactance in the form

$$(8.4) \quad X = A'(l) + A(l) \sin\left(\frac{4\pi}{\lambda} \gamma z_0\right), \text{ to a very good approximation,}$$

where $A'(l)$ is a certain complicated function given explicitly in the course of the proof. But—this is essential—neither A nor A' depends on z_0 .

Proof

The reactance X is the imaginary part of $-Z$. From (5.11) we see that $-Z$ can be split into two parts, one which does not depend on z_0 and the other which does. The part of Z which does not depend on z_0 is

$$(8.5) \quad \frac{30\pi}{Z_0 b k \sin^2 kl} \sum_{m=0}^{\infty} \sum_{n=0}^{\infty} (-1)^m \delta_m \delta_n \frac{\left(\cos \frac{n\pi l}{b} - \cos kl\right)^2}{1 - \left(\frac{n\pi}{bk}\right)^2} \times \\ H_0^{(1)} \left[(\rho_0 + ma) \sqrt{k^2 - \left(\frac{\pi n}{b}\right)^2} \right].$$

It was shown in Section 7 that the real part of this is A , as defined in (8.3). We shall therefore denote the expression (8.5) by

$$A - iA',$$

where A' is real. Thus we can write:

$$(8.6) \quad X = A' - \text{Im}(C),$$

$$(8.7) \quad C = \frac{30\pi}{Z_0 b k \sin^2 kl} \sum_{m=0}^{\infty} \sum_{n=0}^{\infty} (-1)^m \delta_m \delta_n \frac{\left(\cos kl - \cos \frac{n\pi l}{b}\right)^2}{1 - \left(\frac{n\pi}{bk}\right)^2} \times \\ H_0^{(1)} \left[k_n \sqrt{(ma)^2 + (2z_0)^2} \right],$$

where

$$k_n^2 = k^2 - \left(\frac{\pi n}{b}\right)^2.$$

Before, in Section 7, we calculated the *real* part of C . We shall now calculate in a very similar manner the imaginary part of C .

Using Poisson's formula (1) we can write for C

$$(8.8) \quad C = \frac{30\pi}{Z_0 b k \sin^2 kl} \sum_{n=0}^{\infty} \delta_n \frac{\left(\cos kl - \cos \frac{n\pi l}{b}\right)^2}{1 - \left(\frac{n\pi}{bk}\right)^2} \sum_{h=-\infty}^{\infty} \int_{-\infty}^{\infty} e^{-i2\pi(h-1/2)\alpha} \times \\ H_0^{(1)} \left[k_n \sqrt{(ma)^2 + (2z_0)^2} \right] d\alpha.$$

Now we proceed exactly as in Section 7, (7.4), (7.5), using Sommerfeld's formula (4). Therefore:

$$(8.9) \quad C = \frac{30\pi}{bkZ_0 \sin^2 kl} \sum_{n=0}^{\infty} \delta_n \frac{\left(\cos kl - \cos \frac{n\pi l}{b}\right)^2}{1 - \left(\frac{n\pi}{bk}\right)^2} \sum_{h=-\infty}^{\infty} \frac{2e^{-\frac{2z_0}{a} \sqrt{-(ak_n)^2 + 4\pi^2(h-1/2)^2}}}{i\sqrt{-(ak_n)^2 + 4\pi^2(h-1/2)^2}}.$$

For $n > 0$ the exponent of e is real and negative. If the antenna is not too near the plug, then the only contributions to C which have to be taken into account are those coming from $n = 0$:

$$(8.10) \quad C = \frac{60\pi \tan^2 \frac{kl}{2}}{bkZ_0} \sum_{h=-\infty}^{\infty} \frac{e^{-\frac{2z_0}{a} \sqrt{-(ak)^2 + 4\pi^2(h-1/2)^2}}}{i\sqrt{-(ak)^2 + 4\pi^2(h-1/2)^2}}.$$

For the same reason we can neglect all expressions in this sum with the exception of those for which

$$(8.11) \quad h = 0, \text{ or } h = 1.$$

Therefore:

$$(8.12) \quad \text{Im}(C) = -A \sin \left(\frac{4\pi\gamma z_0}{\lambda} \right),$$

and finally

$$(8.13) \quad X = A' + A \sin \left(\frac{4\pi\gamma z_0}{\lambda} \right),$$

which proves our theorem.

Theorem III

If we change z_0 and keep all other parameters (a , b , λ , ρ_0 , l) constant, then the points characterized by the corresponding pairs (R, X) lie on a circle, called the *impedance circle*. This circle is tangent to the X (reactance)-axis and the co-ordinates of its center are (A, A') .

This can easily be seen from (8.2) and (8.4). Indeed, eliminating z_0 from these equations, we have

$$(8.14) \quad (R - A)^2 + (X - A')^2 = A^2,$$

which proves our theorem. (See Fig. 4).

What is the physical significance of the symbols appearing in (8.14)? R and X are the resistance and reactance corresponding to given values of l and z_0 . As z_0 changes, the point (R, X) moves along the impedance circle. $2A$ is the

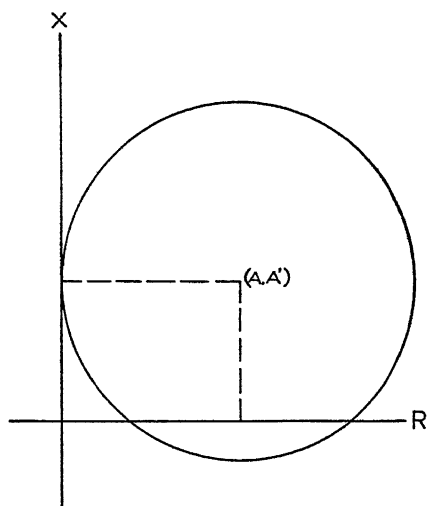


FIG. 4.

maximum resistance for a given l and variable z_0 . A' can be interpreted as the reactance at the point for which the resistance vanishes; indeed for

$$\frac{2\pi\gamma}{\lambda} z_0 = s\pi; \quad s = 1, 2, 3, \dots,$$

we have $R = 0$, $X = A'$.

9. The Matching Problem

We can now turn toward the solution of the matching problem. We have to find a circle, and a point on the circle, for which

$$(9.1) \quad R = 1, \quad X = 0.$$

Putting these values into (8.14) we have

$$(9.2) \quad A = \frac{A'^2}{2} + \frac{1}{2}.$$

Therefore the center of the impedance circle must lie on the parabola (9.2) for the matching problem to be solved (Fig. 5). The remaining problem is: how to find the right point on the parabola? Theoretically speaking, we ought to regard (9.2) as an equation for the determination of l_0 , as A and A' are known functions of l .

If we look at (9.2) we see that the difficulty is to find A' as a function of l , as the other expression, A , is very simple. But A' is a part of Z ; more explicitly the imaginary part of that part of $-Z$ which does not depend on z_0 . Let

us rewrite from (6.4) the part of $-Z$ in which we are interested, that is, the part which does not depend on z_0 . This is:

$$(9.3) \quad -A' = \left\{ \begin{aligned} & (a) \frac{30\pi \tan^2 \frac{kl}{2}}{bkZ_0} Y_0(\rho_0 k) \\ & + \\ & (b) \frac{60\pi}{ibkZ_0 \sin^2 kl} \sum_{n=1}^{\infty} \frac{\left(\cos kl - \cos \frac{\pi nl}{b} \right)^2}{1 - \left(\frac{\pi n}{bk} \right)^2} H_0^{(1)} \left(\rho_0 k \sqrt{1 - \left(\frac{\pi n}{bk} \right)^2} \right) \\ & + \\ & (c) \frac{60\pi \tan^2 \frac{kl}{2}}{bkZ_0} \sum_{m=1}^{\infty} (-1)^m Y_0(mak). \end{aligned} \right\}$$

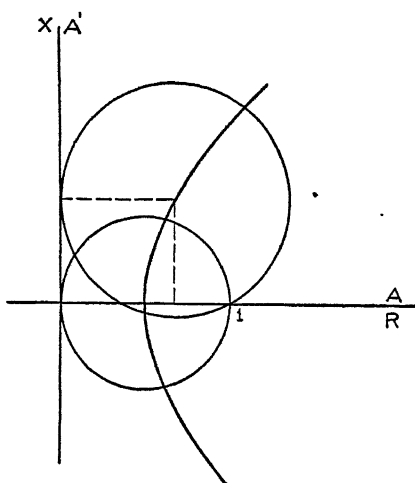


FIG. 5.

Thus we have here the explicit expression for A' which was used in all further calculations. In computing, the only difficulty encountered was to calculate (c):

$$(9.4) \quad \sum_{m=1}^{\infty} (-1)^m Y_0(mak),$$

which converges very slowly. This mathematical problem is treated elsewhere (2), where a table and graph of (9.4) is given.

To make our procedure clear we shall take the following special example:

$$(9.5) \quad \begin{aligned} a &= 7.213 \text{ cm.}, & b &= 3.404 \text{ cm.}, & \lambda &= 10.0 \text{ cm.}, \\ \rho_0 &= 0.397 \text{ cm.}, & Z_0 &= 80 \text{ ohms.} \end{aligned}$$

Then A' is a function of l only. Putting different values of l , we have $\frac{1}{2}(1 + A'(l)^2)$ as represented by Fig. 6. Next we draw A (which is much

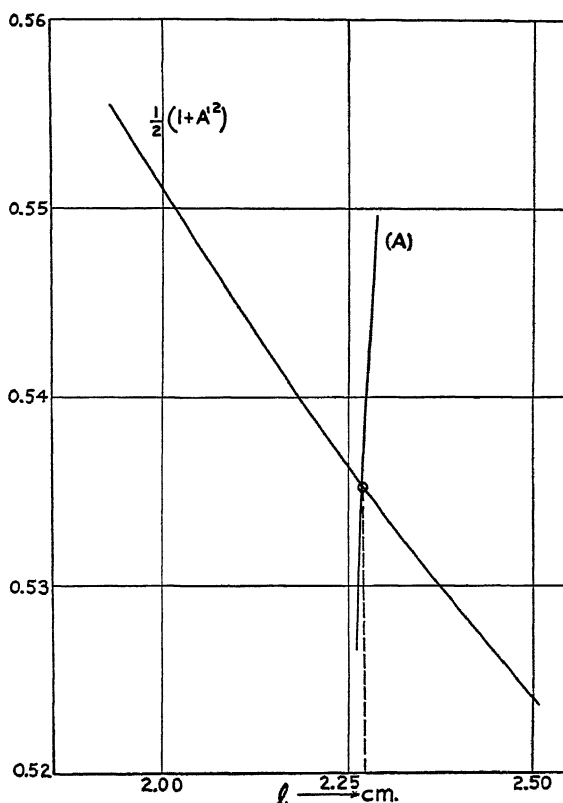


FIG. 6. A and $\frac{1}{2}(1 + A'^2)$ as functions of l . $\lambda = 10.0$ cm., $a = 7.213$ cm., $b = 3.404$ cm., $\rho = 0.397$ cm.

simpler) as a function of l . The intersection of these two curves has the co-ordinate l_0 , satisfying

$$(9.6) \quad \frac{1}{2}(1 + A'(l_0)^2) = A(l_0).$$

Once we have found l_0 , we can easily find the set of z_0 's from (8.2) and (8.3):

$$R = 1 = \frac{30\lambda^2}{ab\pi\gamma Z_0} \tan^2 \frac{\pi l_0}{\lambda} \left(1 - \cos \frac{4\pi\gamma Z_0}{\lambda}\right).$$

Thus the method allows us to find l_0, z_0 , for which $R = 1, X = 0$. In our particular case (9.5) we have

$$l_0 = 2.316; \quad z_0 = 9.839 \pm \frac{\lambda s}{2\gamma}; \quad s = 0, 1, 2, \dots$$

In this way l_0, z_0 were calculated for two wave guides, for different λ 's, ρ_0 's, Z_0 's. The calculations were made by Chien and Pounder. It proved that the omission of all the terms for which $m, n > 0$ was justified. In the expression (b) of (9.3) it was sufficient to take some six terms.

References

1. BOCHNER, S. Vorlesungen uber Fourierische Integrale, p. 33. Akademische Verlagsgesellschaft M.B.H., Leipzig. 1932.
2. INFELD, L., SMITH, V. G., and CHIEN, W. Z. J. Math. Phys. 26 : 22. 1947.
3. SCHELKUNOFF, S. A. Impedance of a transverse wire in a rectangular waveguide. Bell Telephone System, Lab. Rept. April, 1940.
4. WATSON, G. N. Theory of Bessel functions, pp. 415-416. Cambridge University Press 1922.

APPENDIX A

**Generalization of the Impedance Formula for an Unsymmetrical
Position of the Antenna Relative to the Sides of the Guide**

BY J. R. POUNDER

We assume now that the antenna is placed at a distance x_0 from the center of the guide (Fig. 7). Let us generalize the previous reasoning step by step. We have four lattices of dipoles in the plane $z = 0$,

$$(A1) \quad \begin{array}{ll} 0, A_y, 0 & \text{at } x_0 + 2ma, \pm y_0 + 2nb, 0 \\ 0, -A_y, 0 & \text{at } \overline{2m+1} a - x_0, \pm y_0 + 2nb, 0 \end{array}$$

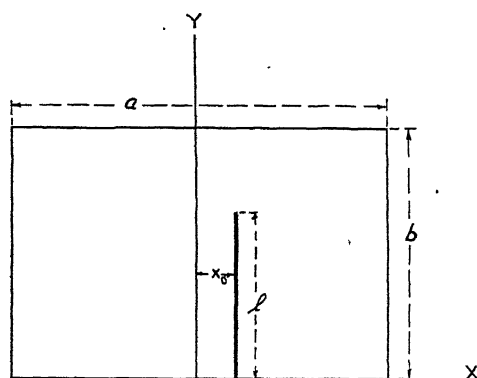


FIG. 7.

and four other lattices in the plane $z = -2z_0$ obtained by reflection in the plug and by changing A_y into $-A_y$. (Fig. 8)

The impedance of the antenna, corresponding to formula (5.6), is now by exactly the same method as before:

$$(A2) \quad \begin{aligned} Z = & \sum_{m=-\infty}^{\infty} \sum_{n=-\infty}^{\infty} \int_{-\infty}^{\infty} e^{-i2nb\alpha} d\alpha \left[\varphi(\rho_0 + 2ma, \alpha) + \psi(\rho_0 + 2ma, \alpha) \right. \\ & - \varphi(\rho_0 + \overline{2m+1} a - 2x_0, \alpha) - \psi(\rho_0 + \overline{2m+1} a - 2x_0, \alpha) \\ & - \varphi(\sqrt{(2ma)^2 + (2z_0)^2}, \alpha) - \psi(\sqrt{(2ma)^2 + (2z_0)^2}, \alpha) \\ & + \varphi(\sqrt{(\overline{2m+1} a - 2x_0)^2 + (2z_0)^2}, \alpha) \\ & \left. + \psi(\sqrt{(\overline{2m+1} a - 2x_0)^2 + (2z_0)^2}, \alpha) \right]. \end{aligned}$$

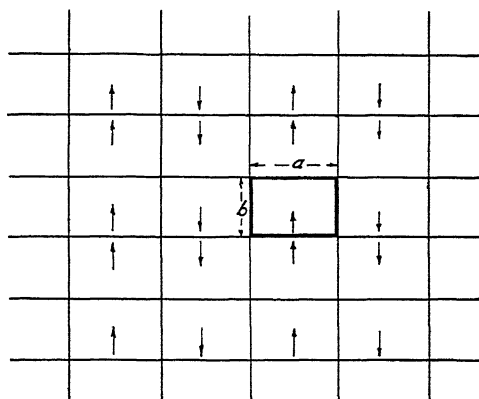


FIG. 8.

Again by the use of Poisson's formula (1) we obtain:

$$\begin{aligned}
 Z \text{ (in ohms)} &= \frac{30\pi}{bk \sin^2 kl} \sum_{n=-\infty}^{\infty} \sum_{m=-\infty}^{\infty} \frac{\left(\cos kl - \cos \frac{n\pi l}{b} \right)^2}{1 - \left(\frac{\pi n}{bk} \right)^2} \times \\
 &\quad \left\{ H_0^{(1)} \left[(\rho_0 + 2ma) \sqrt{k^2 - \left(\frac{\pi n}{b} \right)^2} \right] \right. \\
 &\quad - H_0^{(1)} \left[(\rho_0 + \overline{2m+1}a - 2x_0) \sqrt{k^2 - \left(\frac{\pi n}{b} \right)^2} \right] \\
 &\quad - H_0^{(1)} \left[\sqrt{((2ma)^2 + (2z_0)^2)} \left(k^2 - \left(\frac{\pi n}{b} \right)^2 \right) \right] \\
 &\quad \left. + H_0^{(1)} \left[\sqrt{((2m+1)a - 2x_0)^2 + (2z_0)^2} \left(k^2 - \left(\frac{\pi n}{b} \right)^2 \right) \right] \right\}.
 \end{aligned}
 \tag{A3}$$

As can be shown by computation very similar to that of Section 7, but somewhat more complicated, the real part of (A3) is:

$$R = 2A \cos^2 \left(\frac{\pi x_0}{a} \right) \sin^2 \left(\frac{2\pi \gamma z_0}{\lambda} \right) = 2B \sin^2 \left(\frac{2\pi \gamma z_0}{\lambda} \right),
 \tag{A5}$$

where A is defined by (8.3), and

$$B = A \cos^2 \frac{\pi x_0}{a}.
 \tag{A6}$$

This formula agrees with the corresponding one in Part I. It is obvious that for $x_0 = 0$ this expression for the resistance reduces to that given in (7.8).

It can be shown (with the same assumption as before, namely, that z_0 is not small compared with λ) that the reactance can be written:

$$X = B' + B \sin \frac{4\pi \gamma z_0}{\lambda}, \text{ where}
 \tag{A7}$$

$$(A8) \quad B - iB' = \frac{15\lambda}{Z_0 b \sin^2 kl} \sum_{n=0}^{\infty} \sum_{m=-\infty}^{\infty} \delta_n \frac{\left(\cos kl - \cos \frac{n\pi l}{b}\right)^2}{1 - \left(\frac{n\pi}{bk}\right)^2} \times \\ \cdot \left\{ H_0^{(1)} \left[(\rho_0 + 2ma)k \sqrt{1 - \left(\frac{n\pi}{bk}\right)^2} \right] \right. \\ \left. - H_0^{(1)} \left[(\rho_0 + \overline{2m+1}a - 2x_0)k \sqrt{1 - \left(\frac{n\pi}{bk}\right)^2} \right] \right\}.$$

Now (A5) can be written

$$(A9) \quad R = B \left(1 - \cos \frac{4\pi\gamma z_0}{\lambda} \right), \quad B = \frac{30\lambda^2}{ab\pi\gamma Z_0} \cos^2 \frac{\pi x_0}{a} \tan^2 \frac{kl}{2}.$$

It is evident from (A9) and (A7) that all that was said before about the impedance circle is true also in this more general case.

APPENDIX B

Antenna of Length $l = b$

By J. R. POUNDER

In the case in which the length of the antenna $= b$, one usually assumes uniform current distribution (see Fig. 9). The problem is not new, having been solved by Schelkunoff for a infinite guide without a plug (3). One of the two methods used by Schelkunoff seems to correspond to that presented in this paper.

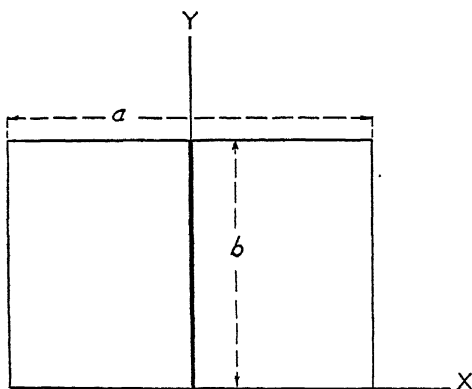


FIG. 9.

The same argument may be used here as before, or a slightly different treatment may be given which replaces the separate antenna-images by infinitely long antennae. The essential point of either method is that the double-sum is replaced by a simple summation. Here we shall outline the argument of the first method.

Because of the assumed uniform current distribution, we obtain instead of formula (3.3),

$$(B1) \quad f(\alpha) = \frac{1 - e^{-i\alpha b}}{i\alpha}.$$

By the same argument as before we arrive at formula (5.6), but the next step (the use of Poisson's formula) gives us an infinite series corresponding to (5.11) in which all terms involving $n \neq 0$ vanish. What remains is:

$$(B2) \quad \begin{aligned} Z = \frac{bk}{4c} \sum_{m=-\infty}^{\infty} \{ & H_0^{(1)} [(\rho_0 + 2ma)k] \\ & - H_0^{(1)} [(\overline{2m+1} a + \rho_0 - 2x_0)k] - H_0^{(1)} [k \sqrt{(2ma)^2 + (2z_0)^2}] \\ & + H_0^{(1)} [k \sqrt{(2m+1 a - 2x_0)^2 + (2z_0)^2}] \}. \end{aligned}$$

From this we can compute, just as before (using Poisson's and Sommerfeld's formulae), the resistance and the reactance. We obtain

$$(B3) \quad R = \frac{b}{ac\gamma} \cos^2 \frac{\pi x_0}{a} \left(1 - \cos \frac{4\pi\gamma z_0}{\lambda} \right), \quad \gamma = \sqrt{1 - \left(\frac{\lambda}{2a} \right)^2},$$

$$(B4) \quad \begin{aligned} X = \frac{b}{ac\gamma} \cos^2 \frac{\pi x_0}{a} \sin \frac{4\pi\gamma z_0}{\lambda} - Im \frac{bk}{4c} \sum_{m=-\infty}^{\infty} \{ & H_0^{(1)} [k(\rho_0 + 2ma)] \\ & - H_0^{(1)} [k(\overline{\rho_0 + 2m+1} a - 2x_0)] \}. \end{aligned}$$

If we consider only the special case in which $x_0 = 0$, and at the same time change from Heaviside units to ohms, these expressions become:

$$(B5) \quad R = \frac{120\pi b}{a\gamma} \left(1 - \cos \frac{4\pi\gamma z_0}{\lambda} \right) = Z_0 \left(D - D \cos \frac{4\pi\gamma z_0}{\lambda} \right),$$

$$(B6) \quad \begin{aligned} X &= \frac{120\pi b}{a\gamma} \sin \frac{4\pi\gamma z_0}{\lambda} - \frac{60\pi^2 b}{\lambda} \sum_{m=-\infty}^{\infty} (-1)^m Y_0(k(\rho_0 + ma)) \\ &= Z_0 \left(D' + D \sin \frac{4\pi\gamma z_0}{\lambda} \right), \end{aligned}$$

where Z_0 is the impedance of the line, and $D = \frac{120\pi b}{a\gamma Z_0}$.

Obviously, the theorems about the impedance circle hold as before.

The matching problem can be stated as before: How shall we make

$$(B7) \quad R = Z_0 \quad \text{and} \quad X = 0?$$

We eliminate z_0 as in Section 9, getting

$$(B8) \quad D'^2 + 1 = 2D.$$

We cannot now satisfy (B8) by choosing l , since l has been chosen as equal to b , but perhaps we can find some other parameter instead. Assuming a *given* wave guide, that is, given a , b , and λ , we may ask:

Having adjusted z_0 so that $R = Z_0$, can we adjust ρ_0 , the thickness of the antenna, so that $X = 0$, that is, so that (B8) is satisfied?

It turns out that it is quite easy to match the line by choosing ρ_0 . Here we shall give the matching conditions for the guide described in (9.5), that is,

$$\lambda = 10.0 \text{ cm.}, \quad a = 7.213 \text{ cm.}, \quad b = 3.404 \text{ cm.}$$

ρ_0 and z_0 , giving the matching conditions, are represented as functions of Z_0 by Fig. 10. As an example, imagine that $\rho_0 = 0.1985$ cm.; then we see from Fig. 10 that the matching requires $Z_0 = 60$ ohms and $z_0 = 6.15$ cm.

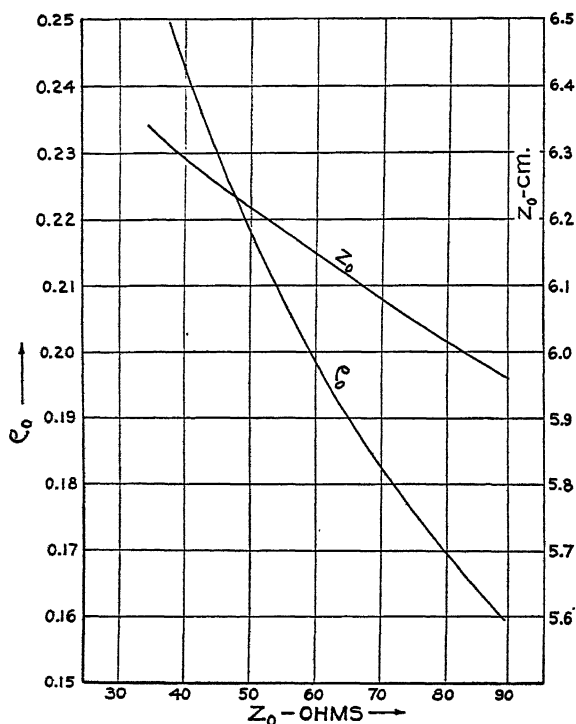


FIG. 10. ρ_0 and z_0 as functions of Z_0 . $\lambda = 10.0$ cm., $a = 7.213$ cm., $b = 3.404$ cm.

If experiment were to verify these results, it would mean that the current distribution is uniform.

APPENDIX C

Resistance and Reactance as Functions of Distance between Antenna and Plug for a Wave Guide of Arbitrary Cross Section

BY A. F. STEVENSON

The results (8.2) and (8.4) for resistance and reactance can be written

$$(C1) \quad R = A(1 - \cos 2uz_0),$$

$$(C2) \quad X = A' + A \sin 2uz_0,$$

where z_0 is the distance of the antenna from the plug, $u = 2\pi/\lambda'$, λ' being the wave length in the guide, and A, A' are independent of z_0 . We wish to point

out that the results (C1), (C2) hold for a wave guide of arbitrary cross section and an antenna of any shape which lies wholly in a plane distant z_0 from the plug, provided that the antenna is not too near the plug, and provided that the dimensions of the guide and manner of excitation are such that only a single E - or H -wave is transmitted. The current distribution in the antenna (provided it is independent of z_0) is immaterial.

In Part II, it was, in fact, shown that, under the conditions stated, R is proportional to $\sin^2 uz_0$, which is equivalent to (C1), but (C2) was only established in the less precise form

$$X = C_1 \cos(2uz_0 + \epsilon) + C_2.$$

The result (C2) follows easily, however, from (16) and (18) of Part II. For, disregarding unimportant terms, these give for the impedance in the case considered

$$(C3) \quad R - iX = Be^{2iuz_0} + C,$$

where B, C are (real or complex) constants independent of z_0 . Put

$$(C4) \quad B = B_1 + iB_2, \quad C = C_1 + iC_2.$$

Then equating the real parts of each side of (C3) we obtain

$$R = B_1 \cos 2uz_0 - B_2 \sin 2uz_0 + C_1.$$

Comparing this with (C1) (already established), we see that we must have

$$(C5) \quad C_1 = -B_1 = A, \quad B_2 = 0.$$

Substituting (C5), (C4) in (C3), and equating the imaginary parts of each side, we obtain

$$X = A \sin 2uz_0 - C_2,$$

which is equivalent to (C2). The result regarding the "impedance circle" follows as in Section 8.

VEILING GLARE IN AERIAL PHOTOGRAPHY¹

BY K. M. BAIRD²

Abstract

In this paper veiling glare is defined and its general aspects in aerial photography are discussed. Experimental results showing the effect of glare on the resolving power of a standard aerial film are presented in the form of graphs. A method of measurement is described and typical amounts encountered in widely used aerial cameras are given. From the results it is shown that veiling glare commonly causes a loss of photographic speed of as much as 100% where resolving power is the primary consideration. Recommendations are made for minimizing flare in cameras.

Introduction

Veiling glare is that scattered light which causes reduction of image contrast in an optical system. It may be conveniently expressed mathematically in different ways, depending on the particular aspect studied. For example, L. A. Jones (3) has used a "flare factor", defined as the ratio of the luminance scale of the scene to the luminance scale of the image. This factor, representing the compression of the luminance range caused by flare, was useful in studying tone reproduction. On the other hand, in the present paper, which is primarily concerned with resolving power, it has been found more convenient to use "per cent veiling glare", defined as the ratio of the amount of flare light in the image plane to the amount of pure image forming light, the ratio expressed as a per cent.

According to the definition given above, any light scattered outside the geometrical image, even that caused by diffraction or residual aberrations of the lens, might be called veiling glare; although the term is generally used only to describe light scattered over a relatively large area. The latter distinction is arbitrary and there is no sharp division either with respect to areas involved or effects on resolving power. Indeed, it is probable that the results given below could be used to predict in lines per millimeter the resolving power of a lens used in combination with Aero Super XX, if the energy distribution in the image formed by the lens were determined by use of the same film. Such a method is that used by Jones and Wolfe (4). The dependence of the amount of veiling glare found to be present on the area considered is discussed in the section on measurement of veiling glare.

In an exact study of the effect of veiling glare on the resolving power of film, the cause as well as the amount must be taken into account. This will be clear from a consideration of such typical causes as light scattered from the walls of the camera, reflections between lens surfaces, haze, etc. In the first example quoted, light that would not otherwise reach the image plane has been thrown on to the film, thereby increasing the illumination. In the second

¹ Manuscript received February 25, 1949.

² Contribution from the Division of Physics, National Research Council, Ottawa, Canada. Issued as N.R.C. No. 1952.

example, on the other hand, the veiling glare arises from the redistribution of what was originally image forming light, and the illumination of the film is not increased in general, although the shadow areas gain light at the expense of the highlights. Thus there are two general types of veiling glare, that which increases the amount of light reaching the film and that which does not. For convenience these will be designated "Type I" and "Type II", respectively. Haze does not clearly fall into one or other of these types but will be shown later to be more conveniently considered of Type II. The difference in effect of these two types will be considered in the next section.

Of the various causes of veiling glare those due to the camera or lens are usually easy to classify as one or the other of the above two types. In the case of haze the classification is a little more difficult since in considering the difference between conditions when haze does and does not exist the effect of decreased ground illumination caused by haze must be taken into account.

If it is assumed that an exposure meter is used as a guide to the camera aperture and shutter settings, it seems logical to consider the haze as veiling glare of Type II, i.e., it reduces contrast but does not greatly affect the average image luminance, since the meter reads the luminance of ground plus haze. Haze could be measured as a per cent veiling glare by determining the loss of contrast of objects that were of known contrasts on the ground. In this paper only measurements of veiling glare caused in the camera or lens are described.

Effect of Veiling Glare

The effects of the two types of veiling glare are indicated in Figs. 1 and 2 as a modification of the characteristic curve of the film. The characteristics

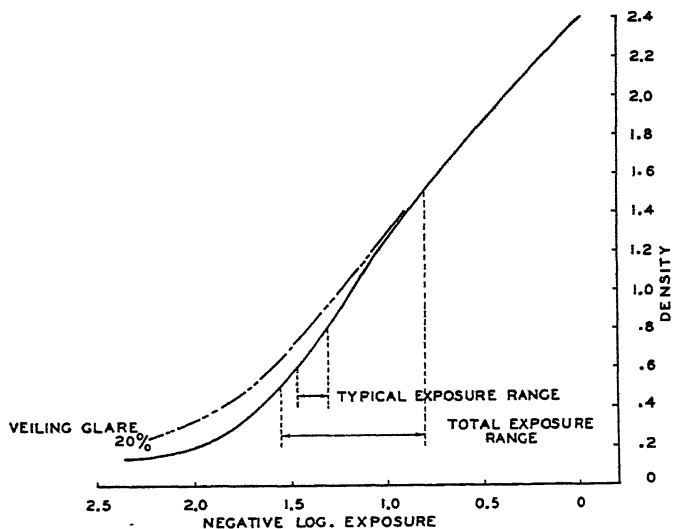


FIG. 1. Characteristic curve of Super XX Aero Film showing modification caused by 20% veiling glare in the case where glare consists entirely of added light. The range of typical exposures and the total exposure range are taken from a British report (5).

of the film itself are unchanged of course but the reproduction of tones under the given conditions of veiling glare is equivalent to that by a film having the modified characteristic curve under conditions of no glare. For the following

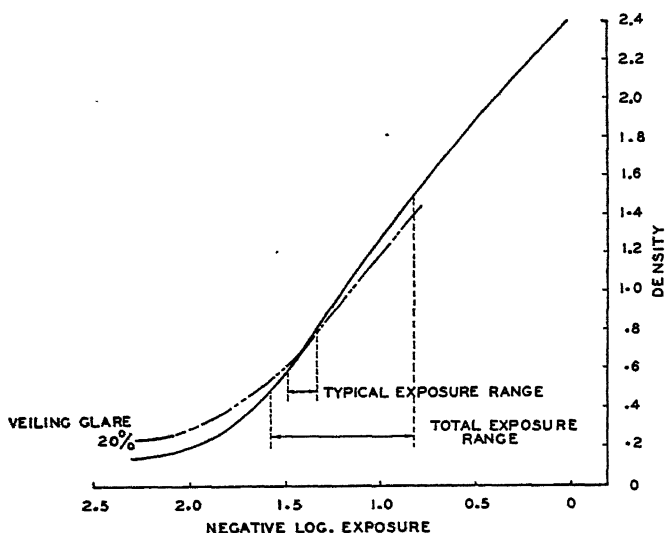


FIG. 2. Same as Fig. 1 except that the veiling glare arises from what was originally image forming light.

discussion it is convenient to define "object exposure" as the exposure that would result if the causes of veiling glare were absent, as distinguished from the "image exposure", which the film receives in the image plane. The corresponding terms "log object luminance ratio" and "log image luminance ratio" will also be used.

The broken lines of Figs. 1 and 2 are graphs of the densities on an Aero Super XX film, plotted as ordinates, that result from the log object exposures that are plotted on the abscissa. The solid lines of both figures are characteristic curves of Aero Super XX film and therefore identical. The broken line of Fig. 1 was obtained by finding the density that resulted from the object exposure plus 20% of the typical object exposure in aerial photography. This density was then plotted against the log object exposure. The densities on this curve are of course always greater than the Super XX densities owing to the added light, but the two curves approach each other asymptotically at large exposures.

The broken line of Fig. 2, which represents veiling glare of Type II, was obtained by finding the density that resulted from the object exposure less $1/6$ (i.e., $5/6$ of the object exposure) plus $1/6$ of the typical object exposure. It is clear that this corresponds to 20% veiling glare as it is defined above. This curve has the same shape as that of Type I but differs in that it crosses the Super XX curve at the typical log object exposure, namely -1.4 log meter candle seconds.

It should be understood that the log exposure values along the abscissa do not represent for the modified curves the actual log exposure on the film but rather the exposure that would result under conditions of no glare, i.e., they are log object exposures. The log image exposure corresponding to a given point on the modified curve is given by considering the point on the solid curve representing the same density as the given point.

It is pointed out that using 20% of the exposure at the middle of the typical exposure range as the added light is equivalent to assuming that the average exposure is the same as the typical exposure. This does not exactly represent conditions in an aerial photograph but it is felt that the inexactness does not affect the conclusions drawn except when there are unusually bright sources in the field of view.

The range of typical exposures and the total range of exposures shown in the figures were taken from a British report based on statistical findings in reconnaissance photography over Europe during the war (5).

The figures show that the two types of glare have different effects. In the case shown in Fig. 2, at the region of typical exposures, the glare reduces the optical contrast without affecting the exposure, with the result that the photographic contrast is reduced. In Fig. 1, on the other hand, the exposure is increased, resulting in the use of a different part of the Super XX curve. Since the slope of the curve is increasing, the loss of optical contrast tends to be compensated photographically in the lower part of the exposure range. It is noteworthy that in Fig. 1 the contrast on the film is actually increased at the toe of the curve although obviously the contrast of the optical image is always reduced by veiling glare. This is caused by the rapid change in slope at the toe of the true characteristic curve of the film. The effects on resolving power will be discussed in detail in a later section.

Determination of Effect on Resolving Power

The effect of various amounts of veiling glare on the resolving power of a camera-film combination was found by calculating the resulting change in contrast and making use of experimental curves relating resolving power to log exposure and contrast. A set of such curves for Super XX Aero Film processed in D-19b to a gamma of 1.34 is shown in Fig. 3.

These curves were obtained by printing sets of resolution charts on strips of film, the charts being illuminated through a calibrated optical step wedge. One of the films so obtained is reproduced in Fig. 4. Resolving power readings from such a film, together with the calibration of the wedge, gave one of the curves. (Each curve in Fig. 3 represents the average of several films.) The different curves were obtained by using charts of different contrasts. Processing was done with the accurate control that is usual in sensitometry. From the H and D curve, which also has been plotted in Fig. 3, it is seen that the range of typical densities recommended in the British paper (5), quoted above, lies in the region of maximum resolving power for a log luminance ratio of 0.2.

This value is given as the typical object contrast by the same report. In these curves and throughout this paper, contrast is expressed as the log of the luminance ratio of the two target areas. The log exposure is given for the brighter target area so that when the log exposure is such that the density resulting on the film is zero, the resolving power is also zero.

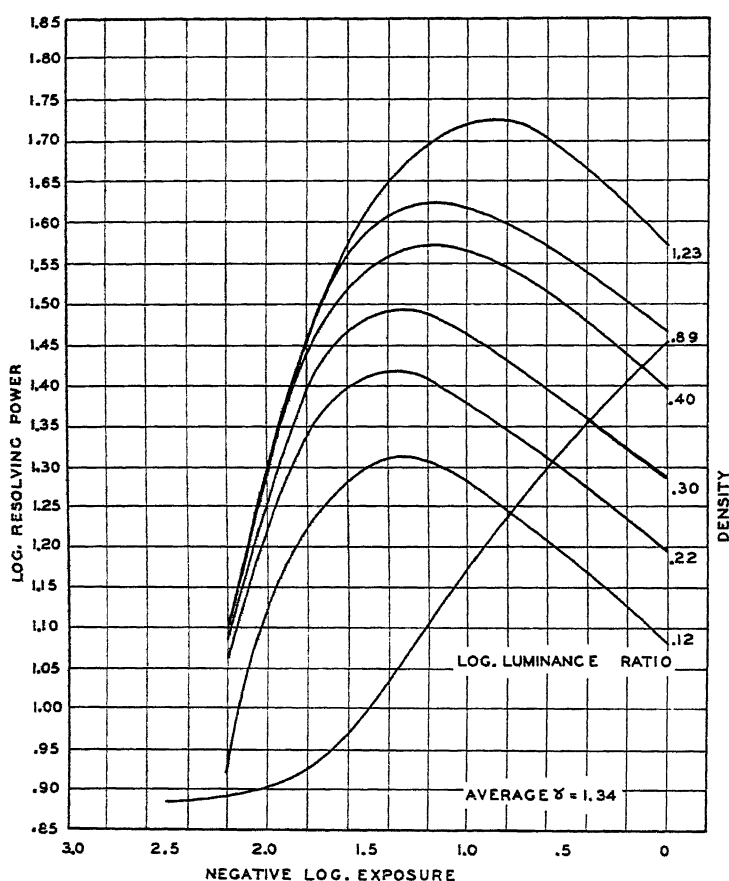


FIG. 3. Curves showing the variation of resolving power with log exposure for various log luminance ratios of the test target for Super XX Aero Film developed in D-19b. The densities along the right-hand side of the graph refer only to the H and D curve. The log resolving power values refer to the other curves.

The solid curves in Figs. 5, 6, and 7 were obtained from Fig. 3 by interpolation and have been plotted on a larger scale for convenience. These graphs show three variables, giving the resolving power for any log exposure or contrast in the range covered. Thus by calculating the change in log exposure and contrast caused by a given amount of veiling glare, the change in resolving power can be obtained. This has been done for values of 10, 20, and 40% veiling glare of Type I in Figs. 5, 6, and 7 respectively. The change in resolving power is indicated by the arrows and by the broken curves, which

PLATE I

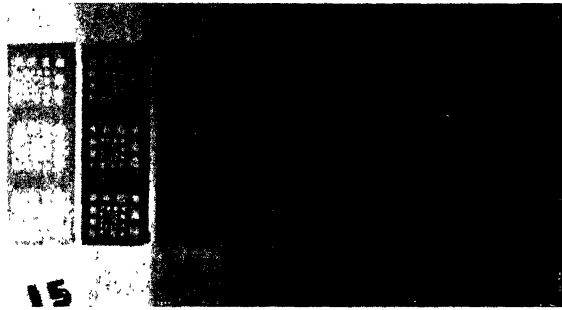


FIG. 4. A reproduction of one of the films used to obtain the curves in Fig. 3.



FIG. 9. Shows a picture taken in the tunnel in Fig. 8 for the determination of per cent veiling glare in an aerial camera. Note the grayness of the image of the black hole.

were obtained by calculating the modified log exposure and modified contrast for the given amounts of veiling glare. The modified log exposure was calculated by adding to the corresponding original exposure value a certain per cent of the typical exposure. By doing this for a given log exposure value and also for that value decreased by the log luminance ratio, two modified

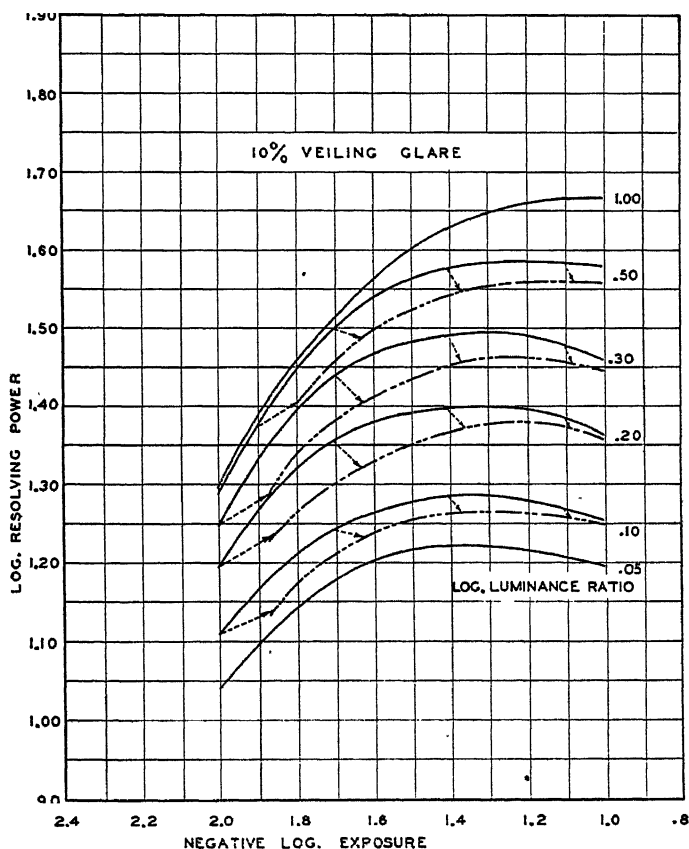


FIG. 5. Curves showing the effect of 10% veiling glare on the resolving power of Super XX Aero Film. The solid curves, obtained from Fig. 3, show the variation of resolving power with log exposure when there is no glare. The arrows show the change in position on the graph caused by 10% veiling glare. The broken curves show the modification of the film characteristic that results.

log exposure values were obtained, the difference of which gave the modified log luminance ratio contrast.

From the modified log exposure and contrast the resolving power is given by the appropriate point on the graphs. Corresponding points on curves without veiling glare (solid) and curves with veiling glare (broken) are represented by the tail and the head of an arrow respectively. Hence the change in resolving power due to a certain per cent veiling glare may be found by reading the head and tail of an arrow. For example log object exposure

$= -1.4$ and log object luminance ratio $= 0.2$ gives a log resolving power of 1.4 if there is no veiling glare. In the presence of 20% veiling glare of Type I this is changed to 1.35.

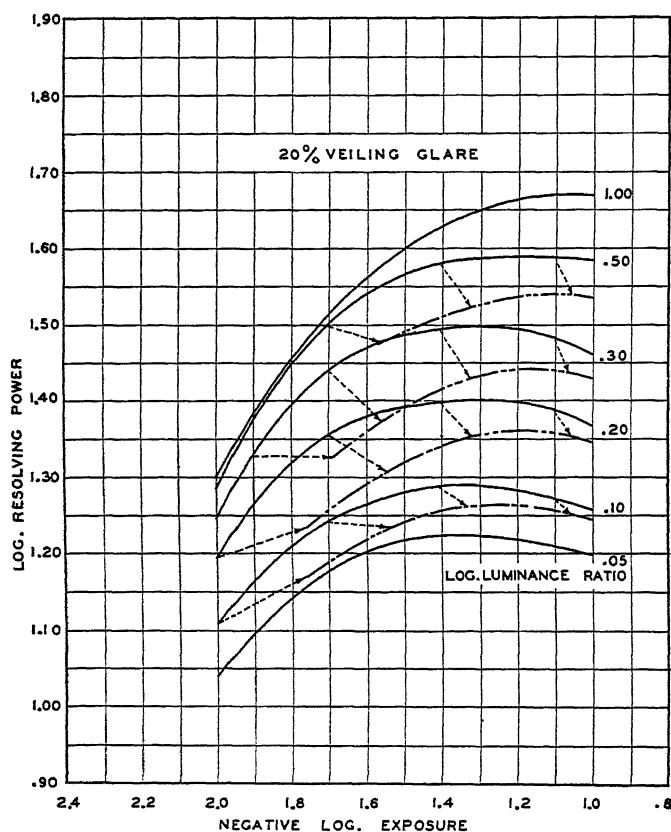


FIG. 6. Same as Fig. 5 for 20% veiling glare.

The effect of Type II veiling glare can also be obtained from the graphs. It can be shown that in this case the modified contrast is the same as for Type I but the modified log exposure is less than for the latter by an amount $\log(1 + V/100)$, where V signifies the per cent veiling glare. Thus for the point considered in the preceding example the modified log exposure is the same as the original (as would be expected at the middle of the typical exposure range) and the modified resolving power is therefore again about 1.35 (given by a point slightly above the broken curve).

The graphs show that Type II veiling glare caused greater loss of resolving power at low exposures but less loss at high exposures than Type I. However, as the above example shows, the difference is not great for the log exposure range of -1.3 to -1.5 , i.e., in the range of typical exposures in aerial photography. In fact the difference is not significant for the arguments in this

paper, and therefore the two types will not be considered separately hereafter. In any case, in practice both types exist simultaneously.

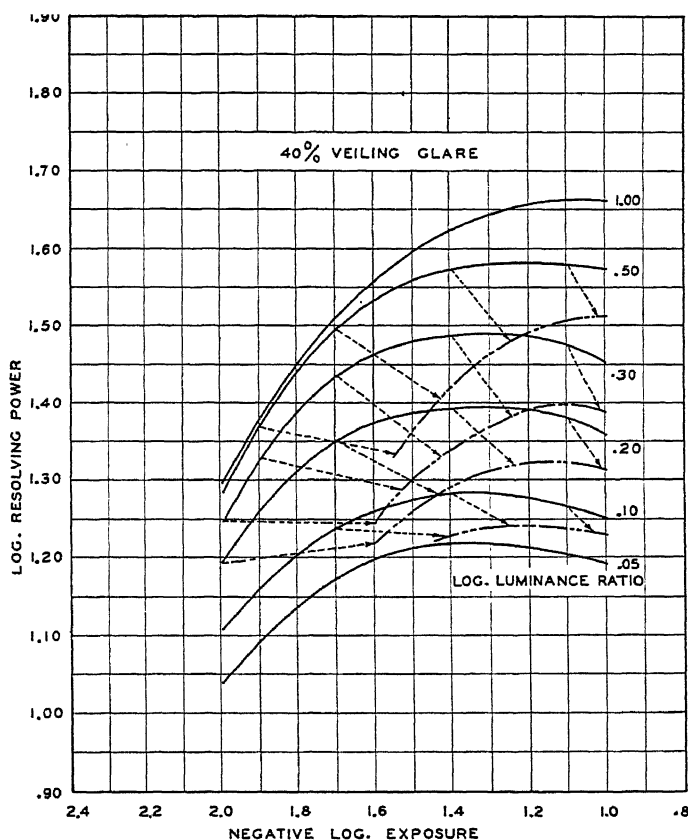


Fig. 7. Same as Fig. 5 for 40% veiling glare.

Discussion of Results

Considering a log luminance ratio of 0.20, Fig. 5 shows that 10% veiling glare changes the log resolving power by about -0.03 , i.e., a reduction of about 7%, in the typical exposure range. This amount is of the same order as the variation in lens-film resolving power from lens to lens in good quality survey lenses (2) and is therefore not serious. On the other hand 20 and 40% cause losses of about 12 and 20% respectively. The latter amounts are great enough to be undesirable but frequently occur in practice, as will be seen in the next section.

Instead of considering the effect of veiling glare as a loss of resolving power it may be thought to constitute a loss of camera speed. Thus if film speed is determined using the resolving power criterion suggested by L. E. Howlett (1), then the minimum acceptable exposure (i.e., that giving 90% of the maximum resolving power when the log luminance ratio is 0.20) is -1.70

for the film being considered, in the absence of veiling glare (see Fig. 6). To realize the same log resolving power (viz., 1.35) in the presence of 20% veiling glare on the other hand, the log exposure must be -1.35 . This is an increase in log exposure of 0.35 or an increase in the exposure of over 100%. As a result a camera equipped with an $f/5.5$ lens having 20% veiling glare would be effectively no faster in cases where resolving power is the prime consideration than one with an $f/8$ lens free from glare, assuming the same quality in other respects. While this admittedly may exaggerate the situation (for example if the minimum criterion had been 95% of the maximum, the loss in speed would have been infinite) it is felt nevertheless that the effect is more serious than is generally realized. To state the effect generally: for the useful range of exposures any resolving power obtainable in the presence of veiling glare can be achieved with less exposure if the glare is reduced. This effective increase of camera speed is more significant than gain of transmission if lens surfaces are coated to reduce reflection. An example is described in the section "Veiling Glare in Some Existing Cameras" that follows. Corresponding changes of photographic speed as determined by density criteria can be seen by considering Figs. 1 and 2.

It is interesting that for very low exposures 10 or 20% veiling glare increases the resolving power. It is this effect that is sometimes used in spectrographic work to detect very faint lines by deliberately fogging the photographic plate. However, over the range of exposures used in aerial photography the glare causes a loss of resolution.

Since the change of resolving power has been determined for the film alone, it might be argued that the results would not be valid for a lens-film combination. However it is felt that the conclusions would be the same in the latter case because the lens-film resolving power does not generally differ greatly from the resolving power of the film alone when fast relatively coarse grained film is used, as is the case in aerial photography.

Measurement of Veiling Glare

The amounts of veiling glare caused by inherent defects in camera-lens combinations have been determined for several widely used aerial cameras. The method of measurement was to photograph a field of view, which was of uniform luminance except for a black spot subtending an angle of about one degree, with the camera under test. A specially constructed tunnel shown diagrammatically in Fig. 8 was used to provide this field.

In the film plane of the camera a small calibrated optical step wedge was placed so that part of the bright field became exposed through it. An example of the pictures that resulted is reproduced in Fig. 9. After processing the film carefully, using brush development, suitable temperature control, etc., densities were read for the image of the steps of the printed wedge, the black spot, and the field. The characteristic curve of the film was plotted from the wedge densities and the log exposure difference between the images of the black spot

and the background obtained from the curve as indicated in Fig. 10. The antilog of the value obtained is the ratio: $\frac{\text{Glare}}{\text{Glare} + \text{Image light}}$. If this ratio is called R then the per cent veiling glare is given by: $\frac{R}{1 - R} \times 100$.

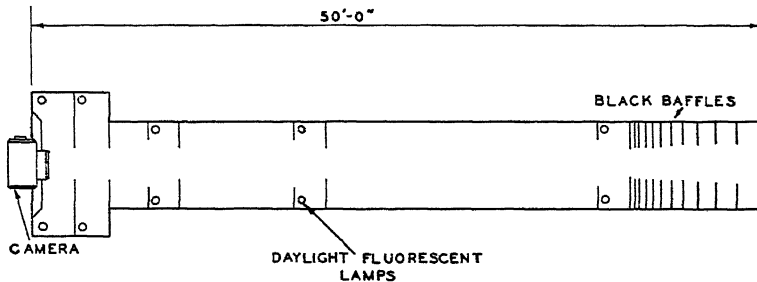


FIG. 8. Diagrammatic view of the tunnel used to measure veiling glare in aerial cameras. The sections of the tunnel containing the lights are painted white; the rest is black.

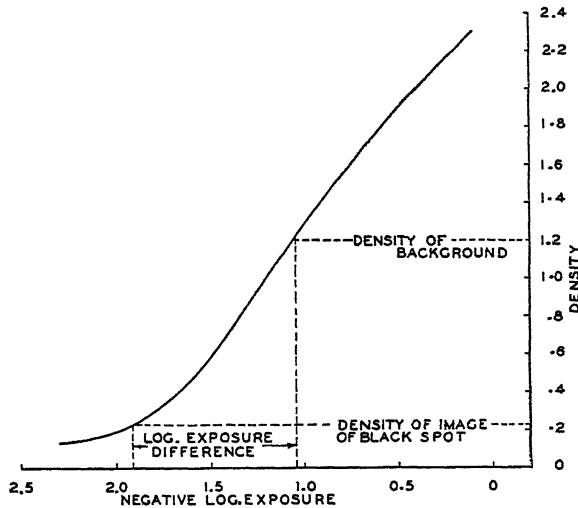


FIG. 10. Characteristic curve of the film shown in Fig. 9 plotted from the wedge included in the picture. The dotted lines indicate how the log exposure difference between the image of the black hole and the background is determined.

The value for "Glare + Image light" was measured in the immediate neighborhood of the point in the field where the veiling glare was being determined. This is in general different from a value averaged over the whole field of view because of vignetting, the cosine effect, variation over the field of the amount of flare, and so on. The choice of the former value is obviously the logical one in view of the method of determining effects on resolution discussed in the previous sections.

Recalling the discussion in the second paragraph of the introduction it is seen that, because the black spot used in the measurement described above

subtends about a degree, only light that is thrown at least a half degree from the edge of the geometrical image is included in the value obtained for the glare light. This is an arbitrary amount, and no attempt is made to justify it in this paper except to say that veiling glare has been used to describe only that light which is scattered over a "relatively large" area. In the case where secondary images are formed by reflection between lens surfaces it is clear that the scattered light may involve any area, as the secondary image may be very much out of focus or in focus and coincident with the primary image.

It is apparent that the method described above gives the per cent veiling glare that is effective when the camera is used in service because the color sensitivity, diffuseness of pickup of energy, etc., is identical in the test and in service use, provided the same kind of film is used. Conditions have necessarily been idealized in that a uniformly bright field of view has been used but this does not lead to serious error except in special circumstances, such as cases when the sun is in or nearly in the field of view, which cases must be considered separately.

The usual objections to photographic photometry such as reciprocity law failure, variation in processing, etc., are obviously not valid here because of the method used. Reproducibility of measurements has been found consistent with the practical considerations involved. For example, three separate tests on the axis of Camera *D* in Table I gave the values: 20, 25, 24% respectively.

Veiling Glare in Some Existing Cameras

The glare found in several widely used aerial cameras is shown in Table I. *A* and *B*, a short focal length reconnaissance camera and a survey camera respectively, are representative of cameras having fair correction. The cones are painted black inside and are large enough so that there is little tendency for light to be reflected specularly on to the film. Neither camera has coated

TABLE I

Camera	Veiling glare on axis, %	Veiling glare at edge of field, %
<i>A</i>	13	7½
<i>B</i>	22	8
<i>C</i>	35	11
<i>C'</i>	11	9
<i>D</i>	23	14
<i>E</i>	7	4

The identification of the cameras mentioned in the preceding table is as follows:

A is an F24 reconnaissance camera.

B is a Fairchild K 17b with a 6 in. Bausch & Lomb Metrogon lens.

C and *C'* represent a Williamson O.S.C. with a 6 in. Ross W.A. Survey lens.

D is a Fairchild F224 Cartographic camera with a Metrogon lens.

E is an F52 camera with a 36 in. F/6.3 N.R.C. Booth Telephoto lens.

lenses, but the curvatures of the lens surfaces of Camera *A* are not very steep. Camera *B* has steeply curved lenses, and coating the lenses would likely reduce the glare to a value close to that of Camera *A*. The results given in the preceding section indicate that these cameras have lost about 10% of their potential resolving power because of veiling glare. This amount is not serious although it would be worthwhile to reduce it, especially in Camera *B*.

Camera *C* is a recently designed aerial survey camera that is well baffled. The unusually high veiling glare was found to be caused by reflections from the lens surfaces, which are very steeply curved, with the result that reflections at large angles of incidence cause light to be thrown back into the camera. *C'* is the same camera after the lens was coated with antireflection films. The glare has been reduced to an unobjectionable amount.

Another recently designed survey camera with not much more than normal glare under normal conditions is Camera *D*. However, apparently in the interests of compactness, the cone was designed to fit the outside rays very closely, with a disregard for veiling glare, and no field limiting baffle was provided outside the lens. The result is slightly increased glare (especially at the edge of the field) under normal conditions, viz., when the field of view is of nearly uniform luminance. When very bright sources such as clouds or lakes with the sun reflected from them are imaged on the inside of the cone, serious glare results. From measurements on the camera and on aerial negatives showing lakes it was found that glare of over 35% could be expected frequently.

Camera *E* is a well designed long-focal-length reconnaissance type with relatively flat lens curves. Fig. 11 shows typical variation of glare with angle in the field.

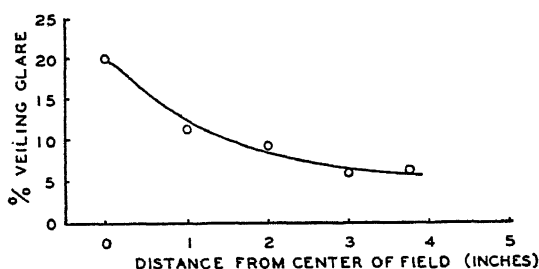


FIG. 11. Curve showing typical variation of veiling glare across the field of view of an aerial camera.

Conclusion

From the foregoing results it is seen that in an aerial camera in which reasonable care has been taken in design, veiling glare will be of the order of 10 to 15%, corresponding to a reduction in resolving power in the typical exposure range of about 10%. Whereas this amount is undesirable it is not serious and it is generally not practical to reduce it.

It is also evident however that lack of care in design might result in veiling glare of the order of 40%. This would cause a loss of resolving power of over 20% or an equivalent serious loss of speed.

To keep veiling glare at a minimum it is recommended that the lens surfaces be coated to reduce reflection if there are many elements or if the surfaces are steeply curved, as is usually the case with wide angle lenses. There should be a field limiting cone outside the lens. The lens tunnel should be large, well baffled, and blackened on the inside.

Whereas the experimental results given above are for aerial cameras and one photographic emulsion, the general conclusions apply to photography in general.

Acknowledgment

The author wishes to express his gratitude for the invaluable assistance of Dr. L. E. Howlett and P. A. Tate in this research.

References

1. HOWLETT, L. E. Can. J. Research, A, 24 : 1. 1946.
2. HOWLETT, L. E. Can. J. Research, A, 24 : 15. 1946.
3. JONES, L. A. and CONDIT, H. R. J. Optical Soc. Am. 31 : 638. 1941.
4. JONES, L. A. and WOLFE, R. N. J. Optical Soc. Am. 35 : 559. 1945.
5. ROYAL AIRCRAFT ESTABLISHMENT, Technical Note, No. 190 (Ph. 513/GCB/57). June, 1942.

RELATIVE YIELDS OF THE D-D REACTIONS AT LOW ENERGIES¹

BY T. P. PEPPER

Abstract

By the simultaneous detection of the p , T , and He^3 particles in a thin window proportional counter the concurrent nuclear reactions $\text{D}(d,p)\text{T}$ and $\text{D}(d,n)\text{He}^3$ have been investigated throughout the deuteron energy range 26 to 63 kev. The ratio of the yield of the reaction $\text{D}(d,p)\text{T}$ to that of the reaction $\text{D}(d,n)\text{He}^3$ was found to be 1.15 ± 0.15 throughout this energy range. There is some slight evidence for an increase in this ratio towards lower bombarding energies.

Introduction

The bombardment of deuterium with deuterons produces the concurrent nuclear reactions

and $\text{D}(d,p)\text{T} \quad Q = +4 \text{ Mev.}$

$\text{D}(d,n)\text{He}^3 \quad Q = +3.3 \text{ Mev.}$

which will be referred to collectively as the D-D reactions. Various aspects of these reactions have been reported in the literature. When the present work was done early in 1948, however, the literature contained no reference to the simultaneous measurement of the D-D reactions at *low* energies. In addition it appeared that no study of the yields had been made using *similar* methods of monitoring the two reactions, as, for example, the detection of the charged products from each reaction as herein described. The present work was undertaken to show that the yields from both reactions could readily be measured simultaneously and under identical conditions. This method could therefore provide a simple means of obtaining the ratio of the yields at low energies.

Reasons for the present experiment are suggested below. Measurement of the reactions $\text{D}(d,n)\text{He}^3$ by means of the He^3 particles would provide a useful standard of neutron emission. Obtaining the relative yields of the two D-D reactions would permit a neutron standard to be established from measurements of the yield of the more readily detectable protons and tritons. Knowledge of the ratio of the yields of the D-D reactions as a function of bombarding deuteron energy might prove useful in estimating the relative importance of the Coulomb and centrifugal barriers in the formation of the reaction products.

¹ Manuscript received March 10, 1949.

Contribution from the Nuclear Physics Branch, Chalk River Laboratory, Division of Atomic Energy Research of the National Research Council of Canada. Issued as N.R.C. No. 1956. This work was part of a thesis submitted to McGill University in partial fulfillment of the requirements for the degree of Doctor of Philosophy, October 1948.

Experimental Method

A small 50 kv. accelerator, designed and built by D. Roaf, employed a conventional 25 kv. voltage-doubler circuit. The ion source was a radio-frequency positive ion source designed and built by A. J. Bayly and A. G. Ward (1). The ion beam was employed without resolution. It consisted, as described by Ward and Bayly, of about 200 μ a. mixture of masses 1 to 6, the odd integral masses being due to hydrogen impurities in the deuterium. Approximately 50% of the total beam was atomic heavy hydrogen: the relative intensities of D^+ , DD^+ , and DDD^+ were 6, 2, and 1: the relative energies were E , $E/2$, and $E/3$. The yields at energy E were one to two orders of magnitude greater than those at $E/2$ or $E/3$. To a good approximation, therefore, the observed yields were due to the higher energy, more intense atomic deuteron beam. It is the energy of this beam that is quoted throughout. For extracting and focusing the ions two separate 0 to 10 kv. power supplies were available. Thus an ion had a maximum energy of 70 kev. The voltage was measured directly by observing the current through a 50 megohm chain of carbon resistors. Since the present method of determining the relative yields of the D-D reactions did not require precise determination of this voltage, the resistor chain was not calibrated for voltage or thermal variations.

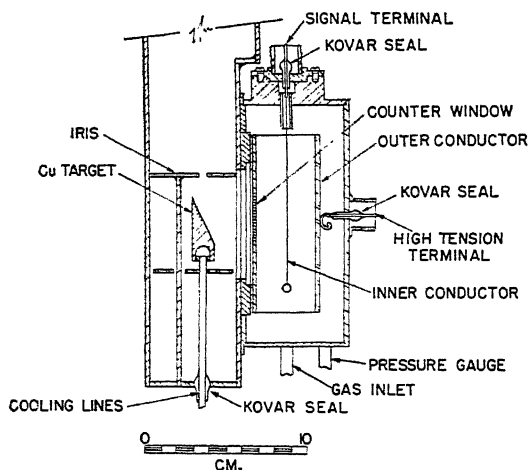


FIG. 1. Cross sectional view of a water-cooled copper target for condensing the deuterons and proportional counter for detecting protons, tritons, and He^3 particles.

Fig. 1 represents a cross-sectional view of target and cylindrical counter. The deuterium target was a condensation target, i.e., a water-cooled copper target onto which the impinging ions condensed, forming a deuterium layer that was then bombarded by succeeding deuterons in the beam. The resultant particles from the D-D reaction, i.e., 3 Mev. protons, 1 Mev. tritons, 2.4 Mev. neutrons, and 0.8 Mev. He^3 particles, penetrated a thin Formvar window and entered the sensitive volume of the proportional counter in a cone of semiangle 20° . This degree of collimation was effected by an array

of 0.040 in. holes drilled in a 0.1 in. steel plate, which supported the Formvar window. During the experiment, windows of 0.25 and 0.12 mgm. per cm.² were used. A thin layer of gold was sputtered onto the Formvar windows to render them conducting and to reduce the light entering the counter from the deuteron beam and target. The minimum path length in the counter for the charged particles was 3 cm. For most of the runs, methane was used as counter filling. The final series of runs was made, however, using *n*-octane vapor at room temperature (7). The counter was operated with a gas amplification of approximately 100. The ionization pulses were further amplified, sorted according to size, and counted.

Experimental Results

The experimental procedure was arranged, first, to identify the three groups of pulses observed on the pulse analyzer (8), and, second, to obtain the relative yields of the D-D reactions. The results are most readily presented by referring to representative pulse distributions observed.

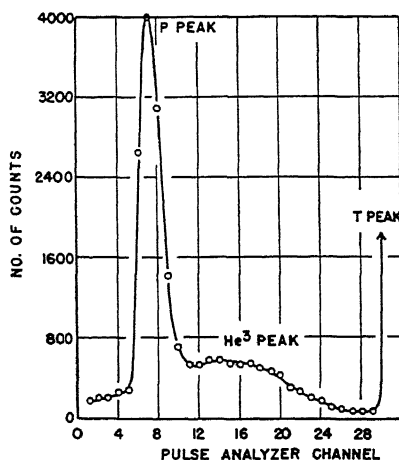


FIG. 2. Proton, triton, and He³ pulses from the D-D reactions. Methane-filled proportional counter at pressure of 30 cm. of mercury. Formvar window 0.25 mgm. per cm.² Energy = 39 kev.

Figs. 2, 3, and 4 show the three groups of pulses labelled as subsequently identified. In Fig. 2 (counter pressure, 30 cm. of mercury) the He³ peak is broad and spreads across the sharper, less energetic proton peak, while the triton peak falls entirely in Channel No. 30, the last channel, of the pulse analyzer. This channel counted all pulses above a certain size. By reducing the pressure in the counter the triton peak emerges as shown in Fig. 3 (counter pressure, 18 cm. of mercury) to become a well resolved peak while the He³ peak is somewhat sharpened and the proton peak has receded into the noise background of Channel No. 1. By still further reducing the pressure in the counter the relative positions of the triton and the He³ peaks were interchanged, as

expected (Fig. 4). At counter pressures of 1.9 cm. of mercury the He^3 peak became sharp and similar to the proton or triton peak.

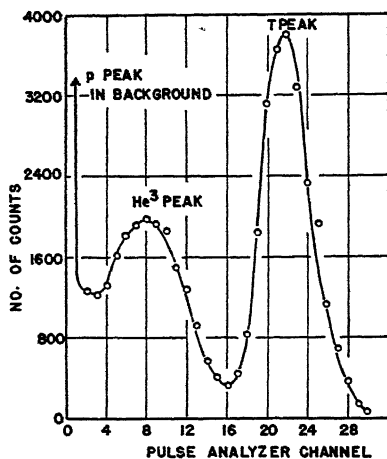


FIG. 3. He^3 and triton pulses from the D-D reactions. Methane-filled proportional counter at pressure of 18 cm. of mercury. Formvar window 0.25 mgm. per cm^2 . Energy = 60 kev.

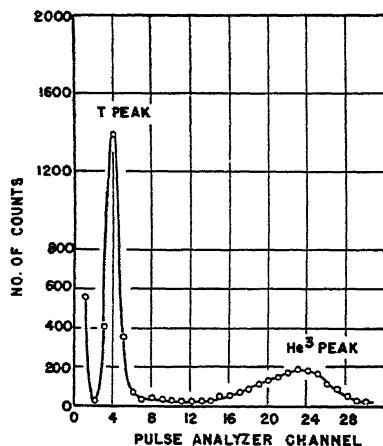


FIG. 4. Triton and He^3 pulses from the D-D reactions. Methane-filled proportional counter at pressure of 3.5 cm. of mercury. Formvar window 0.12 mgm. per cm^2 . Energy = 43 kev.

The ratio of the yields of the D-D reactions was obtained in three ways from the resolved proton, triton, and He^3 peaks. These are best illustrated with reference to Figs. 2 and 4.

Method A

For the counter filled with methane to a pressure of 30 cm. of mercury (Fig. 2) the triton pulses fell in Channel No. 30. By counting these pulses and the pulses associated with the combined proton and He^3 peaks, the ratio of the number of counts
$$\frac{T}{(p + \text{He}^3) - T}$$
 can be obtained. This is equivalent to the ratio T/He^3 .

Method B

Again from Fig. 2 the ratio p/He^3 can be obtained by direct interpolation of the He^3 peak beneath the p peak.

Method C

For the counter filled with methane to a pressure of 3.5 cm. of mercury the T and He^3 peaks were resolved as illustrated in Fig. 4. Upon an arbitrary assignment of those counts lying between the main portions of the T and He^3 peaks a straightforward deduction of the ratio T/He^3 is obtained. Two extreme cases were considered: the one apportioned the ambiguous counts so as to maximize the ratio T/He^3 , the other to minimize it. The largest spread encountered in all the cases considered was 14%. The consistent cleanness of the T peak and the characteristic straggling of the He^3 peak lead to an arbitrary weighting of 2 : 1 in favor of assigning the doubtful counts to the He^3 peak.

Ratios obtained by Methods A, B, and C are each treated as equivalent to the ratio of the yields of the reactions $\text{D}(d,p)\text{T}$ and $\text{D}(d,n)\text{He}^3$. Had the peaks been completely resolved from one another and any spurious background, all three methods would have given the same results. The three methods are presented and employed therefore to indicate the amount of uncertainty introduced by the imperfect resolution. Averaging of the results removes in large part the errors associated with any one of the methods outlined above.

Each method was applied at various deuteron energies from 26 to 63 kev. The ratios so obtained are presented in Table I.

TABLE I
MEASUREMENT OF YIELDS OF $\text{D}(d,p)\text{T}$ AND $\text{D}(d,n)\text{He}^3$

	<i>d</i> -energy kev.	Counter filling, in cm. Hg	Ratio of yields
Method A Ratio calculated $\frac{\text{T}}{(p + \text{He}^3) - \text{T}}$		CH_4	
	27	30	1.07
	39	30	1.06
	59	30	1.10
Method B Ratio calculated $\frac{p}{\text{He}^3}$	34	30	0.99
	40	30	1.07
	45	30	1.11
	51	30	1.12
	56	30	1.12
	62	30	1.12
Method C Ratio calculated $\frac{\text{T}}{\text{He}^3}$	27	3.4	1.35
	31	3.5	1.19
	44	3.5	1.20
	52	3.5	1.16
		C_8H_{18}	
	26	0.5 - 1.0	1.31
	61	0.5 - 1.0	1.28

Discussion of Results

Method *C* was applied to runs made using a window 0.12 mgm. per cm.², i.e., half the thickness of the one providing the data for Methods *A* and *B*. This was permitted by the lower pressure requirements of Method *C*. That the ratios obtained by Method *C* are some 8% higher than those obtained by Methods *A* and *B* may indicate selective absorption of the He³ particles by the window. The ratios 1.31 and 1.28 deduced using Method *C* at bombarding energies 26 and 61 kev. were obtained using *n*-octane vapor at room temperature. These ratios are in satisfactory agreement with those obtained using methane at about six times the pressure.

The possibility of selective absorption of the charged products by small irregularities in the surface of the target was considered but thought to be unlikely, as indicated by the following argument. To the deuteron beam the target depth was just that for the *energy* of the deuteron beam. This depth *l* was never greater than 63 kev. The target made an angle of approximately 30° with the deuteron beam. The particles entering the counter therefore penetrated a maximum target of $l \tan (30 \pm 20)^\circ$. For a perfectly smooth target only the shortest range particles (He³ of 4 mm. air equivalent) need be considered. The He³ particles, would, on their way to the counter, lose less than 100 kev. in the target. With the windows used this would broaden but not decrease the He³ peak. On the other hand, for a target with small metal spurs, the emitted particles might indeed be prevented from entering the counter. However, if such were the case for an appreciable fraction of the particles, those that did enter the counter would not form a defined peak. The fact that the He³ particles did produce such a peak, which with adequate reduction of the counter stopping power could be sharpened to resemble the *p* or T peak, is good evidence against serious loss of the He³ particles before entry into the counter. As a precautionary measure the copper target was always very highly polished with Hydro-Durexsil 700 paper and only in an up and down motion so that whatever grooves were formed would be in the plane containing the beam, the target, and the counter window.

The possibility that the measured ratio was altered by scattering of the emitted particles on their way to the counter was considered. Assuming the scattering to be of the same order of magnitude as that of deuterons on deuterium as reported by Blair *et al.* (2), the fraction of *p*, T, He³ particles scattered before entry into the counter was found to be negligible.

The D-D reaction products are known to be anisotropically distributed in the center of mass system of co-ordinates. Bretscher, French, and Seidl (4) have measured the angular distribution of protons for deuteron energies 20 to 80 kev. They found that the angular distribution could be represented by the relation $N_\theta = N_{90}(1 + A \cos^2 \theta)$, where N_θ is the proton flux proceeding at an angle θ to the deuteron beam and N_{90} is the flux proceeding perpendicularly to the beam. The quantity *A* is a function of the deuteron energy

and increases linearly from 0.25 at 20 kev. to 0.45 at 80 kev. The angular distribution of the neutrons has not been determined at these low energies. At higher energies, however, the angular distributions are similar for protons and neutrons (3). It is therefore unlikely that they differ radically at low energies. In the case of identical angular distribution functions for protons and neutrons the ratio of the fluxes at $\theta = 90^\circ$ can correctly be taken as the ratio of the total yields of the reactions $D(d,p)T$ and $D(d,n)He^3$. In the extreme case, that the neutron flux is isotropic for the energies considered, the error so introduced is only 6%. That the angular distribution of the neutrons is markedly more asymmetric than that of the protons is very unlikely. It is improbable therefore that the error introduced by the angular distribution is more than 2%.

From Table I it is seen that the ratio of the yields of the reaction $D(d,p)T$ and $D(d,n)He^3$ is 1.15 ± 0.15 throughout the energy range 26 to 63 kev. Assuming that the results obtained using the thinner window and Method C are the more reliable there is some slight evidence that the ratio increases toward lower deuteron energies.

Blair *et al.* (3) have found that throughout the energy range 1 to 3.5 Mev. the ratio of the cross sections of the reactions $D(d,p)T$ and $D(d,n)He^3$ is almost constant and equal to 0.9. The reaction $D(d,n)He^3$ was detected by means of the He^3 in a proportional counter, but owing to the high energy of the scattered deuterons the He^3 particles and protons were not monitored simultaneously but at different times using windows of different thickness. At the low deuteron energies of the present experiment, the scattered deuterons could not enter the counter, and hence the charged products could readily be detected together.

Coon and co-workers (5, 6) have investigated the D-D reaction throughout the energy range 100 to 300 kev. and have found that the ratio of the cross sections of the reactions $D(d,p)T$ and $D(d,n)He^3$ is 0.6 at 300 kev. and 1.0 at 130 kev. Their results indicate by extrapolation that at still lower energies the ratio exceeds unity. These results were obtained by detecting the protons in an ionization chamber at angles of 20° , 45° , and 90° to the deuteron beam and the neutrons in a surrounding manganese sulphate solution. The relative cross sections therefore required the use of a neutron standard, a complication not met when the reactions are detected entirely by the charged particles. The present results are consistent with those of Coon *et al.*, extrapolated to lower energies.

Acknowledgments

The author wishes to acknowledge with thanks the assistance of Mr. A. G. Ward for supervision of the work, Mr. G. C. Hanna for the designing of the electronic equipment, and Dr. B. W. Sargent for an encouraging interest in the work and aid in presenting the details of the experiment.

References

1. BAYLY, A. J. and WARD, A. G. Can. J. Research, A, 26 : 69. 1948.
2. BLAIR, J. M., FREIER, G., LAMPI, E., SLEATOR, W., JR., and WILLIAMS, J. H. Phys. Rev. 74 : 1594. 1948.
3. BLAIR, J. M., FREIER, G., LAMPI, E., SLEATOR, W., JR., and WILLIAMS, J. H. Phys. Rev. 74 : 1599. 1948.
4. BRETSCHER, E., FRENCH, A. P., and SEIDL, F. G. P. Phys. Rev. 73 : 815. 1948.
5. GRAVES, A. C., GRAVES, E. R., COON, J. H., and MANLEY, J. H. Phys. Rev. 70 : 101. 1946. *See also* M.D.D.C. 207.
6. MANLEY, H., COON, J. H., and GRAVES, E. R. Phys. Rev. 70 : 101. 1946. *See also* M.D.D.C. 206.
7. PEPPER, T. P. Rev. Sci. Instruments, 20 : 222. 1949.
8. WESTCOTT, C. H. and HANNA, G. C. Rev. Sci. Instruments 20 : 181. 1949.

THE SPECIFIC HEAT OF NAPALM*-GASOLINE GELS¹

BY G. O. LANGSTROTH² AND K. H. HART

Abstract

The heat capacities of gasoline, Napalm, and various Napalm-gasoline gels have been measured in the range -50°C. to 50°C. by the method of mixtures, using an ordinary type of Richard's adiabatic calorimeter. The specific heat in calories per gram per Centigrade degree at a temperature $T^{\circ}\text{C.}$ within this range is given to within 2% by the relation

$$S_T = 0.479 - 0.00054C + 0.00092T,$$

where C denotes the Napalm concentration in per cent by weight. Concentrations of 0% and 100% are included. These data supplement earlier results on thermal conductivity.

The thermal conductivity of Napalm-gasoline gels has been determined previously (2) over the temperature range -50° to 50°C. with Napalm concentrations from 0 to 10% by weight. Specific heat data for the same temperature range with Napalm concentrations from 0 to 100% are presented in this article.

Apparatus and Procedure

The determinations were made by the method of mixtures with the ordinary type of Richard's adiabatic calorimeter. The cylindrical brass calorimeter vessel (diameter, 2 in.; height, 4 in.) was mounted on an insulating support inside a water-tight brass jacket (diameter, 3 in.; height, $5\frac{1}{2}$ in.). The jacket was immersed in a motor-stirred water bath of 3 gal. capacity. Samples were introduced to the calorimeter vessel through a tube soldered to the top of the jacket and extending just above the bath level; normally the tube was closed with a cork. The calorimeter vessel was provided with a hinged top, which was opened or closed by a thread extending through the tube. The water in it was stirred manually by means of a small copper vane mounted on a plastic rod that passed through the top of the jacket.

A copper-constantan thermocouple, with one junction in contact with the calorimeter vessel and the other in the bath, was connected directly to the terminals of a galvanometer. A difference of 0.003°C. between the calorimeter and bath temperatures produced a deflection of 1 mm. Changes in bath temperature involved in maintaining adiabatic conditions while the sample and calorimeter contents attained equilibrium were read to 0.001°C. from a Philadelphia differential thermometer. Bath temperatures were read to 0.01°C. from a calibrated mercury thermometer.

Samples to be measured were placed in cylindrical containers of thin brass closed by screw caps with thin gaskets. The containers had a diameter of

¹ Manuscript received March 3, 1949.

Contribution from the Physics Department, University of Alberta, Edmonton, Alta.

² Present address: Experimental Station of the Defence Research Board of Canada, Suffield, Alta.

* Napalm is a commercial product consisting of a basic aluminum soap of naphthenic, oleic, and palmitic acids in the approximate ratio 1 : 1 : 2.

2 cm., a height of 7 cm., a volume of 20 cc., and a mass of 18 gm. The gasket weighed about 0.1 gm. No leakage was detected.

The bath used to bring the samples to the desired initial temperature before introduction to the calorimeter had a capacity of about 1 gal. It was similar to that used previously in conductivity measurements (2). The bath liquid was water for temperatures above, and methyl alcohol for those below, 0° C. Temperature constancy was maintained by the operation of a heating element with a toluene thermostat control working against a cooling tube containing acetone and carbon dioxide snow. Vertical brass tubes about 7 in. long and 1 in. in diameter with their tops just above the liquid level served as dry receptacles for the sample containers. The bath temperature was measured to 0.01° C. by potentiometric determination of the e.m.f. of a copper-constantan thermopile of three couples in series, calibrated at the steam, ice, and carbon dioxide snow points. It exhibited periodic fluctuations of 0.01° C. above 0° C., and of 0.05° C. below 0° C., but no drift occurred over periods of several hours.

Before insertion in the constant temperature bath, the sample containers were placed in shields designed to minimize heat losses or gains during the four second interval required for transfer from the bath to the calorimeter. A shield consisted of a brass tube just large enough to hold a container. It was closed permanently at the upper end and was corked at the lower. In transferring a sample from the bath to the calorimeter, the shield was held over the tube in the calorimeter jacket, the cork was removed, and the sample container was lowered into the calorimeter by means of a thread passing through the top of the shield.

A graded series of gels was prepared by mixing appropriate quantities of Napalm and gasoline with mechanical stirring for half an hour. The gasoline was supplied by the Research Council of Alberta. It had a tetraethyl lead content of 3.4 cc. per gal., and a specific gravity of 0.702. About 15 gm. of the gel to be examined was placed in a sample container and brought to the desired initial temperature by insertion for at least one hour in the constant temperature bath. The temperature attained by it was taken to be equal to the mean bath temperature over the latter part of this period. The temperature of the weighed mass of distilled water in the calorimeter vessel and also that of the calorimeter bath was so adjusted that the value attained after adding the sample was as nearly as possible 21.00° C. On transfer of the sample to the calorimeter, adiabatic conditions were achieved as nearly as possible by additions of warm or cold water to the calorimeter bath. On attainment of thermal equilibrium the temperature change of the bath, and so of the water in the calorimeter vessel, was determined from the initial and final readings of the differential thermometer. The final temperature was read to 0.01° C. from the bath thermometer. The heat capacity of the sample between its initial and final temperature was calculated in the usual way, the heat capacities of the calorimeter vessel, stirrer, and sample container being

taken into account. The heat capacity between the initial temperature and 21.00° C. was calculated from this value by application of a small correction.

From 100 to 140 gm. of water was used in the calorimeter vessel; its temperature never exceeded 24° C. nor fell below 18° C. Temperature changes caused by introduction of the sample were from 2° to 4° C. The specific heat of water was taken as 1.000 cal. per gm. per Centigrade degree. In view of the small departures from 21° C., use of this value introduced an error of less than 0.1%.

The heat capacity of the calorimeter vessel and stirrer was determined in tests in which 5 to 8 gm. of distilled water at 0° C. was added to 20 to 30 gm. of water in the vessel, with a resulting temperature drop of about 3° C. The mean value for the 21° C. region was 16.5 ± 0.2 cal. per °C. The heat capacity of each sample container was calculated from the masses and specific heats of brass and the gasket material. On the average these contributed respectively about 0.05 and 1.6 cal. per °C. to the heat capacity of the loaded container (9 to 10 cal. per °C.). The specific heat of the gasket was determined from measurements on sample containers filled with disks of the material. It was found to be 0.52 cal. per gm. per Centigrade degree. Since the gasket accounted for only about 0.5% of the heat capacity of the loaded containers, variations with temperature were not measured. The specific heat of commercial brass was determined from heat capacity measurements on a 150 gm. cylinder by the method described above. The data are given in Table I. The heat capacities H_{21}^{θ} between the initial temperature θ and 21.00° C. are described to better than 1% by the relation

$$H_{21}^{\theta} = -1.859 + 0.0885\theta + 0.000019\theta^2 \quad (1).$$

Consequently the specific heat S_T at T° C. is given in calories per gram per Centigrade degree by

$$S_T = 0.0885 + 0.000038T \quad (2)$$

over the temperature range of Table I.

TABLE I

OBSERVED HEAT CAPACITIES IN CALORIES PER GRAM BETWEEN θ AND 21.00° C. FOR A SAMPLE OF COMMERCIAL BRASS ROD, AND THE DEVIATIONS FROM THEM OF THE VALUES GIVEN BY EQUATION (1)

θ (°C.)	Cal./gm.	% Dev.	θ (°C.)	Cal./gm.	% Dev.
50.15	2.63	0.0	-21.27	-3.74	0.3
49.64	2.59	-0.4	-29.85	-4.49	0.2
40.18	1.72	0.6	-39.76	-5.33	-0.4
33.40	1.11	0.9	-49.53	-6.19	-0.2
0.00	-1.85	-0.5	-50.77	-6.32	0.3

In preliminary tests the bath temperature was maintained equal to that of the water in the calorimeter over periods of more than half an hour without detectable change in the reading of the differential thermometer. It follows

that heat exchange with the exterior and heat loss by evaporation were negligible over the period required for making a determination. Other tests showed that 100 rather vigorous strokes of the stirrer caused a temperature rise of only 0.005°C. in the water in the calorimeter. Since in making a determination only three or four gentle strokes were used on about three occasions during the course of heat exchange, the stirring was not sufficient to cause a detectable rise in temperature. As a check on over-all reliability, the average specific heat of copper was determined for the ranges 21° to 50°C. and 21° to 58°C. The mean of six determinations was $0.0932\text{ cal. per gm. per Centigrade degree,}$ in agreement with a value of $0.0930\text{ cal. per gm. per Centigrade degree}$ calculated from the results of Bronson *et al.* (1).

Results of Heat Capacity Measurements

Measured heat capacities between various initial temperatures θ and 21.00°C. are given in Table II for gasoline, Napalm, and gasoline-Napalm gels of four different concentrations.

TABLE II

OBSERVED HEAT CAPACITIES IN CALORIES PER GRAM BETWEEN θ AND 21.00°C. FOR GASOLINE, NAPALM, AND VARIOUS GASOLINE-NAPALM GELS, AND THE DEVIATIONS FROM THEM OF THE VALUES GIVEN BY EQUATION (4). PERCENTAGE NAPALM CONCENTRATIONS BY WEIGHT ARE GIVEN AT THE HEAD OF EACH PAIR OF COLUMNS.

$\theta, ^{\circ}\text{C.}$	0.0		5.0		7.5		10.0		12.5		100	
	Obs.	% Dev.	Obs.	% Dev.	Obs.	% Dev.	Obs.	% Dev.	Obs.	% Dev.	Obs.	% Dev.
50.15	15.09	-1.2	14.89	-0.5	14.87	-0.6	14.92	-0.7	14.77	-0.4	13.24	1.4
49.64	14.79	-0.8	—	—	—	—	—	—	—	—	—	—
44.61	12.05	-0.4	11.89	0.3	11.96	-0.2	11.91	0.3	11.74	0.9	10.72	0.7
40.18	9.84	-1.3	—	—	—	—	—	—	—	—	—	—
39.81	—	—	—	—	—	—	9.43	0.3	—	—	8.47	1.2
39.73	9.56	-0.9	9.38	0.4	9.20	2.3	—	—	9.40	-0.4	—	—
33.42	6.24	0.3	—	—	—	—	—	—	—	—	—	—
30.52	4.72	1.1	4.62	2.8	4.63	1.9	4.63	2.4	4.79	-1.7	4.38	-1.1
0.00	-10.47	-1.9	-10.07	1.4	-10.18	0.1	-10.10	0.5	-9.95	1.7	-9.03	0.4
-11.17	-15.66	-0.6	-15.41	0.4	-15.35	0.5	-15.47	-0.6	-15.30	0.2	-13.88	-0.9
-21.27	-20.22	0.2	-20.01	0.6	-20.19	-0.4	-20.03	0.0	-19.99	-0.2	-18.00	-0.5
-29.85	—	—	—	—	—	—	-23.89	-0.1	—	—	-21.54	-0.8
-31.26	-24.85	-0.2	-24.49	0.7	-24.65	-0.2	—	—	-24.40	0.2	—	—
-39.76	-28.59	-0.1	-28.32	0.2	-28.48	0.5	-28.28	-0.1	-28.23	-0.2	-25.25	0.0
-49.53	-32.85	0.1	-32.38	0.9	-32.53	0.2	-32.45	0.1	-32.36	0.1	-29.08	-0.3
-50.77	-33.62	-0.7	-33.06	0.5	-33.23	-0.3	-33.12	-0.3	-33.11	-0.5	-29.50	-0.1
Average	—	0.7	—	0.8	—	0.7	—	0.5	—	0.6	—	0.7

Discussion

An examination was made of two types of empirical relation to describe the heat capacity data of Table II. The one finally adopted was the power series

$$H_{21}^{\theta} = -P + Q\theta + R\theta^2, \quad (3)$$

where H_{21}^{θ} denotes the heat capacity in calories per gram between the initial temperature θ and 21.00°C. , and P , Q , and R are constants. The values of the constants were first determined by fitting the equation by the method of least squares to the data independently for each Napalm concentration, including 0% and 100%. Plots of P , Q , and R against the Napalm concentration C then showed a linear relation between the first two and C , but no detectable dependence on C of the small constant R . The equations of the lines in the P and Q plots were substituted for P and Q in Equation (3) to express explicitly the dependence of H_{21}^{θ} on Napalm concentration. The value of R was taken to be the mean value for the entire data. On this basis Equation (3) became

$$H_{21}^{\theta} = -10.27 + 0.012C + (0.479 - 0.00054C)\theta + 0.00046\theta^2. \quad (4)$$

The values of H_{21}^{θ} calculated from Equation (4) showed an average deviation of 0.7% from the 69 observed values, as may be seen from Table II. The maximum deviation was 2.8%. There were three deviations greater than 2%, and 11 between 1% and 2%. Two of the former, and four of the latter were associated with data for the initial temperature closest to 21.00°C. , and for these the experimental error is expected to be greatest; the average deviation for the $\theta = 30.52^{\circ}$ data was 1.8%. Equation (4) satisfies the requirement that H_{21}^{θ} should effectively vanish when $\theta = 21.00^{\circ}\text{C.}$ Calculated values of H_{21}^{θ} for the concentrations in the order given in Table II are 0.03, -0.01, -0.02, 0.00, 0.00, and 0.06 cal. per gm.

It follows from Equation (4) that the specific heat S_T in calories per gram per Centigrade degree at any temperature $T^{\circ}\text{C.}$ between 50° and -50°C. and any Napalm concentration C in per cent by weight, is given by

$$S_T = 0.479 - 0.00054C + 0.00092T. \quad (5)$$

This relation is considered to be good to about 2%. Although no data were obtained between $C = 12.5\%$ and $C = 100\%$, there is no reason to expect serious errors from interpolation for this region.

References

1. BRONSON, H. L., CHISHOLM, H. M., and DOCKERTY, S. M. *Can. J. Research, A*, 8 : 282. 1933.
2. LANGSTROTH, G. O. and ZEILER, F. *Can. J. Research, A*, 26 : 50. 1948.

THE NUCLEAR MOMENTS OF P^{31}

BY M. F. CRAWFORD AND J. LEVINSON²

Abstract

Hyperfine structures have been observed in the $3s4s\ ^3S_1 - 3s4p\ ^3P_{0,1,2}^0$ transitions of P IV with a 21 ft. concave grating and in the $4s\ ^2S_{1/2} - 4p\ ^2P_{1/2}^0$ transition of P III with a transmission echelon. The half-widths of the lines, excited in an electrodeless discharge, were reduced by mixing neon with the phosphorus vapor and by using a condenser of small capacity. Their intensities were increased by discharging the condenser through the exciting coil nine times per half-cycle by means of a rotating spark gap. The structures of the P IV lines confirm $I = 1/2$ and show that μ , the nuclear magnetic moment, is positive. $\mu = 1.15 \pm 0.05$ n.m. and $\mu = 1.11 \pm 0.1$ n.m. are obtained from the P IV and P III structures, respectively.

Introduction

The nuclear magnetic moments of nearly all the nuclei lighter than Yt with odd atomic number and odd mass number are known. P^{31} is one exception. Its spin, $I = \frac{1}{2}$, has been determined from alternating intensities in the band spectrum of diatomic phosphorus vapor (1, 10). Its magnetic moment has been investigated by Tolansky (14): he found no resolvable hyperfine structure in any of the 13 lines of the second spectrum of phosphorus studied by him, and concluded that the nuclear gyromagnetic ratio, g , is anomalously small. However, these lines of P II would have very narrow structures even for a g -value corresponding to a magnetic moment of the order of one nuclear magneton (3).

The fourth spectrum of phosphorus is more favorable for a determination of the magnetic moment. The transitions $3s4s\ ^3S_1 - 3s4p\ ^3P_{0,1,2}^0$ in P IV (2, 13) should have hyperfine structures of the order of seven times larger than the widest structure in the lines studied by Tolansky. Accordingly these transitions were investigated. An electrodeless discharge was used to excite the fourth spectrum, and the effects of source conditions on the half-widths of the lines were studied. The reduction effected in the half-widths made it possible to resolve hyperfine structures and determine the magnetic moment.

Experimental

The light source was an electrodeless discharge in a mixture of phosphorus vapor and neon in a quartz tube 75 cm. long and 2.5 cm. in diameter. The discharge was observed through a plane window at one end. An exciting coil 50 cm. long was wound tightly on mica wrapped around the central portion of the tube. Neon was circulated through the discharge tube. The construction and operation of the circulating and purifying system are described

¹ Manuscript received February 5, 1949.

Contribution from the Department of Physics, University of Toronto, Toronto, Ontario.

² Holder of a Fellowship under the National Research Council of Canada, 1946-1947. Now at the Research Laboratory of Electronics, Massachusetts Institute of Technology, Cambridge, Massachusetts.

in the book by Tolansky (15). Freedom from hydrogen and mercury in the discharge tube is essential since both appreciably quench the higher spectra of phosphorus.

A schematic diagram of the exciting circuit is shown in Fig. 1. The oil condensers, C , combined in series as shown, had a capacity of $0.002 \mu\text{f}$. The exciting coil, D , consisted of 118 turns of 1.5 mm. copper wire, and had an

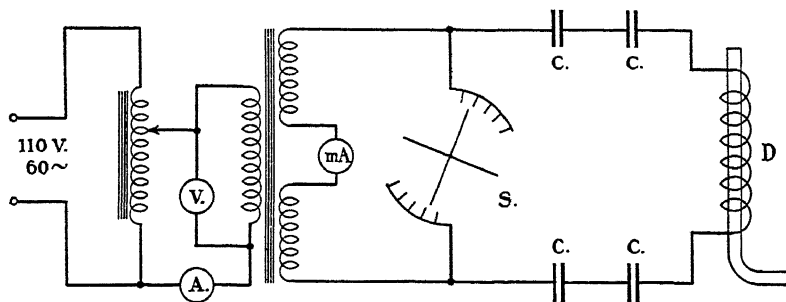


FIG. 1. *Exciting circuit.*

inductance of $27.5 \mu\text{h}$. It was found empirically that smaller values of the capacity resulted in sharper lines, but reduced the intensity appreciably. In order to use small capacity without loss of intensity, the method of multiple discharge per half-cycle was adopted. The condensers were discharged through the coil by the rotating spark-gap, S , which was synchronous with the applied voltage. The number of discharges per half-cycle was determined by the number of fixed terminals per quadrant, and as many as nine were used. With the above value of the capacity the condensers charged up to approximately the same potential before each discharge. The charging current was supplied by a 1.5 kva., 220 : 75,000-v. transformer. Its input was controlled by a 1.5 kva. autotransformer and was adjusted to give a sparking voltage of approximately 20,000 v.

The best compromise between intensity and half-width for P IV lines was obtained with the electrical conditions described above and a pressure of 1 mm. of neon. Since the discharge tube was operated at room temperature, the partial pressure of the phosphorus vapor was that of yellow phosphorus at room temperature. The effects of source conditions were not investigated in sufficient detail to warrant much speculation on the mechanism of the excitation process. However, the empirical results indicate that the line widths of the higher spectra depend more upon the velocities acquired by ions in the exciting field than upon other factors, and thus show that data relevant to the theory of discharges in gases at low pressure can be obtained from the study of line contours.

The spectrograph was a 21 ft. concave grating in a modified Eagle mounting with a plate holder 12 ft. long. It was in a constant temperature room separated from the source room except for a small opening through which the light entered. The 3350 \AA region was recorded in the fourth and fifth orders

simultaneously. In the fifth order, which is the more intense, the theoretical resolving power is 400,000.

Ilford Zenith plates were used and developed in Ilford metolhydroquinone developer. A Corning red-purple Corex filter was placed before the slit to reduce the background and the overlapping of orders. Although the plates were grainy, traces obtained with a Leeds and Northrup microphotometer were relatively smooth because a sufficiently long portion of the line was scanned to average out fluctuations. The separations, as well as the intensities of the hyperfine structure components, were determined from the traces.

An accurate calibration of the emulsion was obtained from the nonuniform intensity distribution along a spectral line due to the astigmatism of the concave grating, as first suggested by Dieke (5). Dieke's method is applicable only if the slit is uniformly illuminated and the grating is uniformly reflecting along the length of a ruling. Since these conditions were not fulfilled, his method was modified to incorporate the principle of the "Two-Line Method" described by Churchill (4). On a concave grating spectrogram the relative intensity distribution along the length of a spectral line is the same for all lines in a narrow spectral region. Thus the densities of two selected lines measured at equal distances from the centers of the lines represent a constant intensity ratio independent of the distance from the centers. By measuring corresponding densities at a number of distances from the centers of the lines the characteristic curve can be determined if the intensity ratio of the two lines is known. If the intensity ratio is not known, the characteristic curve can be plotted only on an arbitrary log I scale.

In this investigation the intensity ratio of the transitions $^3S_1 - ^3P_1^0$ (3364 Å) and $^3S_1 - ^3P_0^0$ (3371 Å) was used to determine the log I scale uniquely. This ratio was first measured using a characteristic curve obtained from a stepped-slit exposure on another plate of the same emulsion number, and was within 10% of the ratio 3:1 given by multiplet theory for LS coupling. This is the order of agreement expected when the standard is not on the same plate as the spectrum. Thus it was deemed justifiable to use the theoretical ratio 3:1 to determine the log I scale of the characteristic curve obtained by the Two Line Method. The intensity ratios for hyperfine structure components and for the lines of the fine-structure multiplet as determined with this calibration are consistent with theory to within 5% as shown in Fig. 2.

This consistency is appreciably better than that obtained with a stepped-slit calibration, particularly at low densities. This is not unexpected since the Two Line Method uses the lines themselves, and hence is independent of source fluctuations and variation of emulsion sensitivity over the plate. Further, the background corrections can be made with greater precision.

Results

The intensity contours of the three P IV lines studied are given by the heavy lines in Fig. 2, (a), (b), (c). They were obtained from the microphotometer

traces of the best plate. Traces of seven other plates showed no appreciable departure in form from those of the best plate. Relative intensities obtained from several of these plates agreed with those obtained from the best plate to within 10%, and half-widths agreed to within 2%. In our judgment the contours obtained from the best plate are reliable to better than 5%, and are probably more accurate than a simple average of the contours obtained from all the plates.

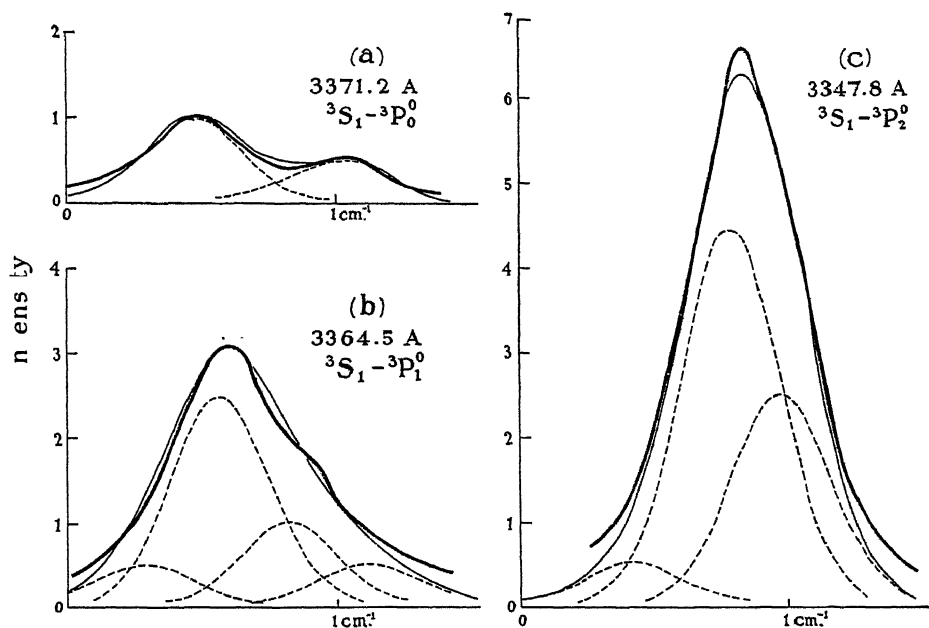


FIG. 2. Intensity contours

The dashed contours in Fig. 2 represent the theoretical hyperfine structure components, assumed to have a Gaussian distribution. They are based on the theoretical patterns shown in Fig. 3, (a), (b), (c). These patterns are drawn for $I = \frac{1}{2}$ and a positive nuclear magnetic moment. The relative intensities are shown in Fig. 3 by the heights of the lines representing the components and were obtained from the formulae of Hill (9). The hyperfine structure separations given in terms of g in Fig. 3 are calculated as described below. The theoretical line contours shown in Fig. 2 as light continuous lines are the sums of the dashed contours of the components. Only two experimentally derived data were used in plotting the theoretical contours: 0.44 cm^{-1} as the half-width of a component, deduced from 3348 Å ; and $0.54 (5) \text{ cm}^{-1}$ as the separation of the hyperfine structure states of 3S_1 , obtained from the measured separation of the peaks ($0.49 \pm 0.02 \text{ cm}^{-1}$) in 3371 Å by correcting for the small overlapping of the components. The intensity unit for both the theoretical and the experimental contours is the intensity of the stronger peak of 3371 Å .

The presence of just two hyperfine structure components in the pattern of 3371 Å with a measured intensity ratio of 1.98 proves uniquely that $I = \frac{1}{2}$, the value obtained by Ashley (1) and Jenkins (10) from the molecular spectrum.

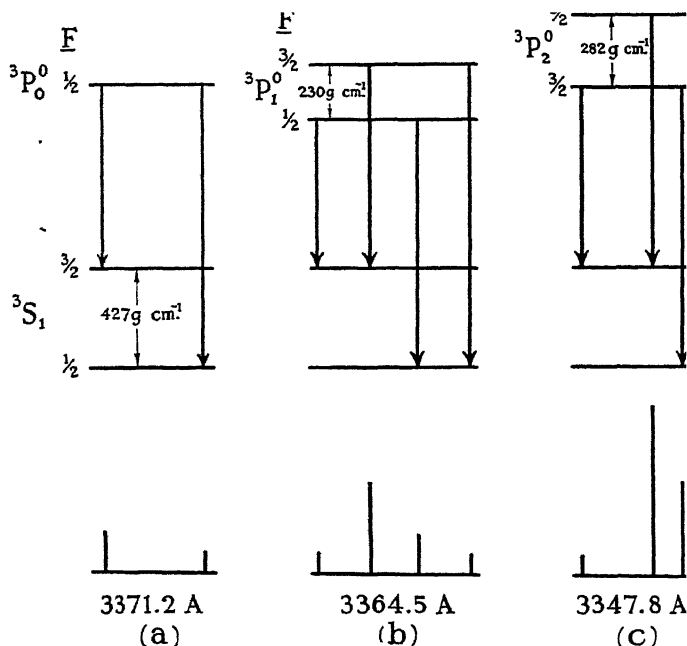


FIG. 3. Theoretical patterns.

The hyperfine structure splitting of the 3S_1 level for $I = \frac{1}{2}$ is given by (7, 8)

$$\Delta(^3S_1) = \frac{3}{2} \cdot \frac{1}{2} \cdot (a_{3s} + a_{4s}) \cdot K \text{ cm.}^{-1}; \quad (1)$$

where

K is a relativistic correction and has the value 1.02 for an s electron of phosphorus,

$$a_{ns} = \frac{8}{3} R\alpha^2 \frac{Z_i Z_0^2}{n_e^3} \cdot g \text{ cm.}^{-1}, \quad (2)$$

R is the Rydberg constant,

α is the Sommerfeld fine-structure constant,

Z_i is the inner effective nuclear charge and equals 15 for an s electron of phosphorus.

Z_0 is the outer effective nuclear charge,

n_e is the effective principal quantum number,

g is the ratio of the nuclear magnetic moment in Bohr magnetons to the nuclear angular momentum in Bohr units.

Thus,

$$a_{ns} = 232.8 \frac{Z_0^2 g}{n_e^3} \text{ cm.}^{-1} \quad (3)$$

The values of Z_0^2/n_e^3 are different for the two electrons of $3s4s\ ^3S_1$, and are not obtainable directly. Since the Rydberg formula for the term value gives only Z_0^2/n_e^2 , Z_0 or n_e must be determined explicitly for each electron. For the $3s$ electron Z_0^2/n_e^2 is evaluated by equating it to the term value, in Rydberg units, of the $3s4s$ configuration of P IV relative to the $4s$ configuration of P V. A value of n_e to be used with Z_0^2/n_e^2 is obtained as follows: n_e of the $3s$ electron of P V evaluated from Robinson's data (13), $T = 524,463\text{ cm.}^{-1}$ and $Z_0 = 5$, is 2.287. This is an approximate value of n_e for the $3s$ electron in the $3s4s$ configuration of P IV. It is true that $Z_0 = 5$ is too large for the $3s$ electron, by perhaps 10%, when the shielding by the $4s$ electron is taken into account; but the term value, $T = 524,463\text{ cm.}^{-1}$, taken from the P V analysis is also too large by 12% compared to the energy required to remove the $3s$ electron from the $3s4s$ configuration of P IV, namely $T = 460,384\text{ cm.}^{-1}$. These two errors tend to compensate. Since Z_0 probably is between 5 and 4.5, the value of n_e obtained in this manner should not be in error by more than $\pm 5\%$. Using $n_e = 2.287$ and $T = 460,384\text{ cm.}^{-1}$ for the $3s$ electron,

$$Z_0^2/n_e^3 = T/R \cdot n_e = 1.83_s . \quad (4)$$

Substituting this value in (3),

$$a_{3s} = 427\text{ g cm.}^{-1} . \quad (5)$$

For the $4s$ electron of the $3s4s$ configuration, Z_0 is taken as 4, then n_e is 3.061, as calculated from the term value, $187,423\text{ cm.}^{-1}$, of 3S_1 relative to $3s\ ^2S$ of P V. Thus from (3)

$$a_{4s} = 130\text{ g cm.}^{-1} . \quad (6)$$

Substitution of (5) and (6) in (1) gives

$$\Delta(^3S_1) = 425\text{ g cm.}^{-1} . \quad (7)$$

The experimentally determined value of $\Delta(^3S_1)$ is $0.54(5)\text{ cm.}^{-1}$, and the hyperfine structure is normal. Thus by Equation (7), $g = +0.00128$. However, Fermi and Segrè (6) have shown that if the quantum defects for an s -electron term sequence are not constant the right hand side of Equation (3) must be multiplied by a correction factor. From Robinson's data for the ns terms of P III and P V and for the $3sns$ terms of P IV the correction factor for the $3s$ electron is 1.016 and for the $4s$ electron 1.025. These corrections increase the coefficient of g in Equation (7) by 2%, and give $g = +0.00125 \pm 0.00005$. The nuclear magnetic moment, μ , in nuclear magnetons then is $+1.15 \pm 0.05\text{ n.m.}$

The separations of the levels of the $3s4p$ configuration are consistent with Houston's equations and show that the coupling departs somewhat from LS . The wave function for the triplet level with $J = 1$, designated as $\{^3P_1^0\}$, can be expressed as a linear combination of the triplet and singlet wave functions in pure LS coupling, designated as $[^3P_1^0]$ and $[^1P_1^0]$ respectively. Using Robinson's term values (13),

$$\{^3P_1^0\} = 0.994 [^3P_1^0] - 0.106 [^1P_1^0]. \quad (8)$$

Equation (8) shows that the departure from LS coupling is small, and that the 3:1 intensity ratio assumed for the two lines used to calibrate the emulsion is valid to within 1%. However, the departure is significant in the calculation of the hyperfine structure splitting of the $^3P_1^0$ level.

For this calculation (3) it is necessary to express the wave function as a linear combination of the jj wave functions of the two levels with $J = 1$. Designating these as $[1/2, 1/2]$ and $[1/2, 3/2]$, to indicate their origin in the jj subgroups,

$$\{^3P_1^0\} = 0.873 [1/2, 1/2] + 0.488 [1/2, 3/2]. \quad (9)$$

The coefficients in Equation (9) when substituted in the formulae of Breit and Wills (3) for intermediate coupling give the following relation for the splitting of the $^3P_1^0$ level:

$$\Delta(^3P_1^0) = \frac{3}{2}(0.327 a_{3s} + 1.09 a_{4p}), \quad (10)$$

where

$$a_{3s} = 427 \text{ g cm.}^{-1} \text{ from Equation (5),}$$

$$a_{4p} = \frac{\Delta\nu g}{(l + \frac{1}{2})Z_i} = 10.6 \text{ g cm.}^{-1}.$$

$$\Delta\nu = 207 \text{ cm.}^{-1}, \text{ the separation between the } J = 0 \text{ and } J = 2 \text{ levels,}$$

$$Z_i = 13, \text{ obtained from } \Delta\nu \text{ by the spin doublet formula,}$$

$$l = 1.$$

Relativistic corrections are included in the numerical coefficients of Equation (10). Thus, $\Delta(^3P_1^0) = 228 \text{ g cm.}^{-1} = 228 \times 0.00128 \text{ cm.}^{-1} = 0.29 \text{ cm.}^{-1}$, using the uncorrected value of g obtained from the 3S_1 splitting.

An experimental value of $\Delta(^3P_1^0)$ was obtained by comparing the observed contour of 3364 Å with the contours predicted using $\Delta(^3S_1) = 0.54(5) \text{ cm.}^{-1}$ and a series of values of $\Delta(^3P_1^0)$. The comparison gave a fairly unique value, $\Delta(^3P_1^0) = 0.27 \pm 0.04 \text{ cm.}^{-1}$. The contour plotted using this value, which is 0.02 cm.^{-1} smaller than the calculated splitting, matched the observed contour very well, including the hump on the high-wave-number side. This is evident from Figs. 3, (b), 2, (b); a small decrease in the splitting of $^3P_1^0$ increases the separation of the two central components and produces a hump on the side of the contour. However, the difference between the calculated and the experimental value of $\Delta(^3P_1^0)$ is within the assigned error which takes into consideration both the precision of the matching and the 4% error in the value of $\Delta(^3S_1)$ used in the analysis of the contour. Although this error is relatively large because of the incomplete resolution, the contour is compatible only with $I = \frac{1}{2}$. A similar analysis of the contour of 3348 Å gave $\Delta(^3P_2^0) = 0.39 \pm 0.11 \text{ cm.}^{-1}$. By calculation (3), $\Delta(^3P_2^0) = 282 \text{ g cm.}^{-1} = 0.36 \text{ cm.}^{-1}$. Thus, the hyperfine structures of these two lines, as well as that of 3371 Å, are consistent with $I = 1/2$ and $\mu = +1.15 \pm 0.05 \text{ n.m.}$

The third spectrum of phosphorus was also investigated with a transmission echelon. The transition $4s^2S_{3/2} - 4p^2P_{3/2}^0$ (4246 Å) (11, 13) was resolved into

two components with a separation of $0.11 \pm 0.01 \text{ cm.}^{-1}$. However, only one good spectrogram was obtained before two plates of the echelon became "uncontacted." The resolved structure on this spectrogram gave $\Delta(4s^2S_{3/2}) = 0.12 \pm 0.01 \text{ cm.}^{-1} = K \cdot a_{4s}$. Thus by Equation (3) with a Fermi-Segrè correction factor of 1.026, $\mu = +1.11 \pm 0.1 \text{ n.m.}$

During the writing of this report a letter was published by Pound (12) in which he gave $\pm 1.1314 \pm 0.0013 \text{ n.m.}$ as the nuclear magnetic moment of P^{31} obtained by the magnetic resonance method. Our values agree with his within the error set by us on the basis of experimental accuracy alone. In addition our results show that the nuclear magnetic moment is positive and confirm $I = 1/2$.

References

1. ASHLEY, MURIEL F. Phys. Rev. 44 : 919. 1933.
2. BOWEN, I. S. Phys. Rev. 39 : 8. 1932.
3. BREIT, G. and WILLS, L. A. Phys. Rev. 44 : 470. 1933.
4. CHURCHILL, J. R. Ind. Eng. Chem., Anal. Ed. 16 : 653. 1944.
5. DIEKE, G. H. J. Optical Soc. Am. 23 : 274. 1933.
6. FERMI, E. and SEGRÈ, E. Z. Physik, 82 : 729. 1933.
7. GOUDSMIT, S. Phys. Rev. 43 : 636. 1933.
8. GOUDSMIT, S. and BACHER, R. F. 34 : 1501. 1929.
9. HILL, E. L. Proc. Natl. Acad. Sci. U.S. 15 : 779. 1929.
10. JENKINS, F. A. Phys. Rev. 47 : 783. 1935.
11. MILLIKAN, R. A. and BOWEN, I. S. Phys. Rev. 25 : 600. 1925.
12. POUND, R. V. Phys. Rev. 73 : 1112. 1948.
13. ROBINSON, H. A. Phys. Rev. 51 : 726. 1937.
14. TOLANSKY, S. Z. Physik, 74 : 336. 1932.
15. TOLANSKY, S. High resolution spectroscopy. Methuen & Co. Ltd., London. 1947.

THE GAMMA RAYS OF RADIUM (B + C)¹

BY K. C. MANN AND M. J. OZEROFF

Abstract

An experiment has been performed to verify the gamma-ray energy spectrum of Radium (B + C) as reported by Latyshev and associates. The spectrum was obtained by measuring the energies of photoelectrons ejected from a thin lead radiator by means of a thin-lens magnetic beta-ray spectrometer. The spectrum obtained failed to reveal the presence of transitions other than those reported by C. D. Ellis. Comparative results are presented.

Introduction

The gamma rays of RaB and RaC have been reported in detail by Ellis and coworkers (5) from measurements of the energies of internal conversion electrons and of photoelectrons ejected from high atomic number materials. Later, Latyshev and his associates (1, 2, 8, 9, 10) measured the energy distribution of positrons formed in the process of internal pair production as well as internal conversion electron energies. They were able to report the detection and measurement of all the gamma rays found by Ellis above $2 m_0c^2$ (1.02 Mev.) plus 10 new gamma rays, the comparative intensities of the latter being high enough for reasonably easy detection. It is strange that these gamma rays were not found by Ellis, in spite of the extreme care which characterized his work, and for this reason it seemed advisable to investigate again the gamma-ray spectrum of radium in an effort to eliminate these uncertainties.

Apparatus and Method

The source used in this investigation was a silver "needle" containing 10 mc. of radium in equilibrium with its disintegration products. Gamma rays from this source were studied in a thin-lens magnetic beta-ray spectrometer of the type described by Deutsch, Elliott, and Evans (3). For this purpose the gamma rays were allowed to eject into the spectrometer photoelectrons from a thin lead foil 50 mgm. per cm.² in thickness. The momentum distribution of the photoelectrons was measured by varying the focusing current through the spectrometer's lens coil. For detection of electrons, a bell-type Geiger-Müller counter was used with a mica window 4 mgm. per cm.² thick.

The spectrometer was calibrated using the well known F-line of Thorium B. The momentum corresponding to this conversion line has been accurately determined (4, 11) and is

$$H\rho = 1385.6 \text{ gauss-cm.}$$

The thorium source was prepared by precipitation as a sulphide from a thorium nitrate solution on a thin backing of mica. When used in the spectrometer

¹ Manuscript received March 15, 1949.

Contribution from the Department of Physics, University of British Columbia, Vancouver, B.C.

the conversion line was quite sharp and gave a calibration constant for the spectrometer of 486.0 gauss-cm. per ampere.

Observations of photoelectron peaks indicate that the resolution of the spectrometer, $\frac{\Delta(H\rho)}{H\rho}$, is 4% at half-peak intensity.

Results

Fig. 1 shows the curve obtained with the spectrometer, using the radium source. The solid curve is the composite curve of photoelectron peaks and Compton electron background, the latter arising from a brass absorber used to eliminate all primary beta rays. The dotted curve represents the Compton electrons alone, taken with lead radiator foil removed.

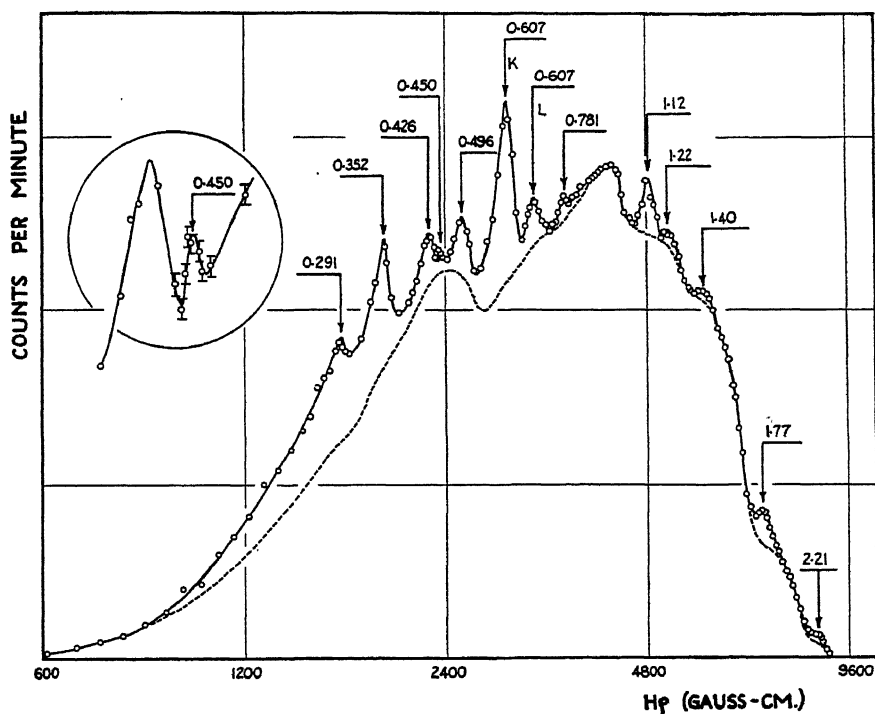


FIG. 1. The gamma ray spectrum of Radium (B + C).

The values of the energies in Mev. assigned to each photoelectron peak are the gamma-ray energies, calculated as the sum of the photoelectron energy plus the shell binding energy of lead. All peaks, with one exception, were assumed to be due to photoelectrons ejected from the *K*-shell, since this is most probable. For these, the *K*-shell binding energy used was 0.088 Mev. (taken from X-ray absorption limits (7)). In the one exception, a smaller peak following the 0.607 Mev. gamma ray was found to be 72 kv. more energetic and so was identified as an *L*-shell peak of the same gamma ray.

Table I compares the energies and relative intensities of the gamma rays found in this investigation with those reported by Ellis and coworkers, and by Latyshev. The relative intensities have been calculated on a basis of peak height above background corrected for variation of photoelectric cross section, using published curves (6).

TABLE I

Lines marked "i.c." denote internal conversion measurements.

Lines marked "p.e." denote photoelectric measurements.

Lines marked "i.p." denote internal pair measurements.

Ellis and coworkers	Latyshev and coworkers		Present investigation	
Gamma-ray energy, Mev.	Gamma-ray energy, Mev.	Relative intensity	Gamma-ray energy, Mev.	Relative intensity
0.0529 i.c.				
0.2406 i.c.				
0.2571 i.c.				
0.2937 i.c.			0.291	*
0.3499 i.c.			0.352	*
0.4260 p.e.			0.426	9
			0.450	4
0.4980 p.e.			0.496	14
0.6067 i.c.	0.606 i.c.		0.607	74
0.766 i.c.	0.766 i.c.		0.781	13
0.933 i.c.	0.933 i.c.			
	1.11 i.p.			
1.120 i.c.	1.120 i.c.		1.12	9
	1.21 i.p.	23		24
1.238 i.c.	1.234 i.c.			
1.379 i.c.	1.370 i.c.			
	1.39 i.p.	49	1.40	23
1.414 i.c.	1.414 i.c.			
	1.52 i.p.	29		
	1.62 i.p.	22		
	1.69 i.p.	17		
	1.75 i.p.	100	1.77	100
1.761 i.c.	1.761 i.c.			
	1.82 i.p.	17		
	2.09 i.p.	15		
2.193 i.c.	2.20 i.p. + i.c.	41	2.21	25
	2.40 i.p.	21	2.40	*

* Not estimated.

The 2.40 Mev. gamma ray reported in this paper does not appear as a photoelectron peak. It was assumed that a weak gamma ray must be responsible for the Compton recoil electron distribution of the upper energy end of the curve. Choosing the end point of this distribution by inspection to be 2.14 Mev., the gamma-ray energy responsible can easily be shown to be 2.40 Mev., with an uncertainty of the order of $\pm 3\%$.

As used in this investigation, the spectrometer is somewhat insensitive to gamma rays of energy less than 0.250 Mev. because of the long electron path with its attendant scattering and the relatively thick counter window and lead

radiator foil. Hence the low energy rays reported by Ellis did not appear here. In addition, conversion coefficients strongly affect the comparison of results. For example, the 1.414 Mev. transition is known to be almost completely converted and, as a result, it does not appear at all in our measurements.

One faint peak from a 0.450 Mev. gamma ray was found which has not been reported previously. Its intensity is so low that it is certainly near the limit of detection of the spectrometer.

An inspection of the comparative results indicates a radium gamma-ray spectrum along the Ellis pattern. Little evidence of the extra gamma rays reported by Latyshev and coworkers was found. However, all photoelectron peaks above 1 Mev. are relatively weak compared to the admittedly high Compton background and it is possible that the latter may have masked the missing lines.

Techniques are now being developed in this laboratory in an attempt to reduce the Compton background, which if successful should increase the sensitivity of the spectrometer to low intensity gamma rays. The authors hope to be able to make a further report of this research in the near future.

Acknowledgments

This investigation was made possible by a Grant-in-aid of Research from the National Research Council of Canada to one of us (K.C.M.). The junior author (M.J.O.) is indebted to the National Research Council for the award of a Studentship. In addition, grateful acknowledgment is made to the British Columbia Cancer Research Institute for the use of the radium source used here, and to the Consolidated Mining and Smelting Co. of Trail, B.C., for a gift of lead used for protective baffles.

References

1. ALECHANOV, A. and LATYSHEV, G. D. *Compt. rend. acad. sci. U.R.S.S.* 20 : 429. 1948.
2. CONSTANTINOV, A. A. and LATYSHEV, G. D. *J. Phys. U.S.S.R.*, 5 : 249. 1941.
3. DEUTSCH, M., ELLIOTT, L. G., and EVANS, R. *Rev. Sci. Instruments*, 15 : 7. 1944.
4. ELLIS, C. D. *Proc. Roy. Soc. (London)*, A, 138 : 318. 1932.
5. ELLIS, C. D. *Proc. Roy. Soc. (London)*, A, 143 : 350. 1934.
6. GOODMAN, C. *The science and engineering of nuclear power.* Addison-Wesley Press Inc., Cambridge, Mass. 1947.
7. *HANDBOOK OF CHEMISTRY AND PHYSICS*, 30th ed., p. 2013. Chemical Rubber Publishing Co., Cleveland, Ohio. 1948.
8. KULCHITSKY, L. A. and LATYSHEV, C. D. *J. Phys. U.S.S.R.* 4 : 515. 1941.
9. LATYSHEV, G. D. *Revs. Modern Phys.* 19 : 132. 1947.
10. LATYSHEV, G. D., KOMPANEETZ, A. F., BORISOV, N. P., and GUCAK, J. H. *J. Phys. U.S.S.R.* 3 : 251. 1940.
11. WANG, K. C. *Z. Physik*, 87 : 633. 1934.

Canadian Journal of Research

Issued by THE NATIONAL RESEARCH COUNCIL OF CANADA

VOL. 27, SEC. A.

SEPTEMBER, 1949

NUMBER 5

WAVE LENGTHS, EQUIVALENT WIDTHS, AND LINE PROFILES IN THE SPECTRUM OF THE STAR H.D. 190073¹

BY C. S. BEALS AND MIRIAM S. BURLAND

Abstract

With the aid of long exposures (18 and 25 hr. respectively) the spectrum of H.D. 190073 in the ordinary region has been photographed with dispersions of 7.3 to 15.2 Å per mm. The resulting spectrograms revealed approximately 100 stellar lines not observed with single-prism dispersion as well as indicating more clearly the structure of a number of complex line profiles. Wave lengths, identifications, and equivalent widths are listed for all observed lines, and a number of the more interesting line profiles are illustrated. The interpretation of line profiles is discussed and it is pointed out that the presence of asymmetrical hydrogen lines is an indication of a shell of relatively small diameter.

Introduction

The spectrum of the emission line star H.D. 190073 (α 1900 19^h 58.^m1, δ 1900 + 5° 28' mag. 7.9 AOe) is, in a number of respects, unique in the sky because of the peculiar character of its emission and absorption lines. Studies of its spectral characteristics have been made by Merrill (6), Beals (2, 3) and Struve and Swings (8).

The spectrum is characterized by emission lines due to hydrogen, neutral sodium, and ionized metals such as CaII, FeII, TiII, etc. A number of the lines have a P Cygni character and in the case of hydrogen the line profiles exhibit definite variability. The forms of the lines due to CaII in this spectrum are unusually intricate and complex, while H.D. 190073 is one of the few stars that exhibit well marked emission due to neutral sodium.

In spite of the fact that the star has been studied by several investigators and that a number of efforts have been made to work out detailed explanations of a number of its unusual features, its spectrum remains a puzzle that in the main has not been solved. The present study was undertaken with the hope of making a worth while contribution to our knowledge of this spectrum by investigating it with higher dispersion than had hitherto been employed.

The Observations

The spectrograms and microphotometer tracings on which this study is based were secured by one of the authors (Beals) at the Dominion Astrophysical Observatory at Victoria, B.C., before his transfer to Ottawa.

¹ Manuscript received May 10, 1949.

Vol. 2. No. 4. Contributions from the Dominion Observatory. Published by permission of the Director, Mines, Forests and Scientific Services Branch, Department of Mines and Resources, Ottawa, Canada.

Previous studies of the star at Victoria were made with single-prism dispersion in the ordinary region and three prisms in the visible. The values of spectrographic dispersions used in these earlier studies, as well as in the present work, are given in Table I. Seventeen spectra were secured in all, four in the visible λ 5500–6700 and thirteen in the ordinary photographic region λ 3850–5000.

TABLE I

Dispersing system	Camera focal length, cm.	Symbol	Dispersion, Å/mm.	
			λ 3933	λ 4340
I-Prism	96	IL	14.6	22.1
	71	IM	19.9	30.3
	42	IS	33.5	50.8
II-Prism	96	IIL	7.3	11.0
	71	IIM	10.0	15.2
III-Prism	71	IIIM	λ 5875	λ 6563
			34.5	46.0

A careful examination of the best of the single-prism spectrograms gave indication of many faint narrow lines of an intensity close to the limit of visibility, and there seemed reason to believe that studies with higher dispersion might well reveal many more lines. It also appeared probable that increased dispersion would yield additional information regarding the peculiar emission and absorption line profiles due to CaII and hydrogen as well as those of other atoms. The exposure time required to secure a IIL single-prism spectrogram of dispersion 22 Å per mm. at H_γ , well exposed in the region of λ 3933, was approximately six hours. For a star of the declination of H.D. 190073 this represents an all night exposure and it was clear that several nights would be required in order to secure good plates with the higher dispersion given by two prisms. Some risks of failure are involved in such long exposures and they are of course very prodigal of observing time but it was considered that the importance of the problem warranted the attempt.

An exposure was accordingly begun on the night of July 23, 1946, and continued through three nights including July 25. The total exposure was 17 hr. and 41 min. The long focus (96 cm.) camera was used with two prisms and this combination gives a dispersion of 7.3 Å per mm. at λ 3933 and 11.0 Å per mm. at H_γ . The temperature of the spectrograph was maintained at a uniform level by means of a thermostat. Some trouble was experienced on one night owing to a sudden drastic rise in the outside temperature, but it was found possible to exercise the necessary control by the use of a damp sheet covering the spectrograph and bags of dry ice symmetrically distributed about the spectrograph frame. The plateholders were firmly clamped into place so that at the end of a night's work it was possible to replace the dark

slide without jarring the plate. Suitably spaced exposures of the iron arc were made on each night, and while the images of the iron lines on the plates showed evidence of a certain amount of flexure at right angles to the dispersion, the lines were of good definition and there was little evidence that temperature or flexure effects had seriously interfered with the purity of the spectrum.

The star spectrum was of a good density in the region of λ 3968– λ 4500 and many fine metallic lines were clearly visible. In the region of the K line (λ 3933), however, the exposure was weak and it was decided to make another exposure of longer duration using a camera of shorter focal length (71 cm.) in the hope of getting adequate exposures at the bottoms of the very strong H and K lines of CaII. The second exposure was begun on August 6 and continued through August 9 with a total exposure time of 24 hr., 56 min. The result was a plate beautifully exposed in the H and K region and well usable throughout the entire range λ 3896– λ 4600. Illustrations of the spectra are shown in Plate I.

The present paper contains information on wave lengths, identifications, and line intensities from the two-prism spectrograms described above, as well as from a number of earlier single-prism plates of comparable quality but smaller dispersion.

Wave Length Measurements

For the determination of wave length, both direct micrometer measures of the plates as well as microphotometer tracings were used. The tracings were made on the Victoria microphotometer (1) and were of $\times 100$ magnification. Each tracing had superimposed upon it a record of both sets of iron comparison lines in addition to the star spectrum. The measurement of the tracings for wave length was carried out on a small micrometer machine specially designed for this purpose and loaned to the writers by the Dominion Astrophysicist, Dr. J. A. Pearce. The character of the machine is illustrated in Plate II. The motion of the tracing is governed by the rotation of a precision roller with a micrometer head on one end, and the accuracy with which the position of a line of the star or comparison spectrum can be read is 0.2 mm. on the tracing, corresponding to 0.002 mm. on the plate. While this may not look like extreme precision, since plate settings can be made to 0.0005 mm., it may be pointed out that settings on the tracings can be repeated with greater consistency than on the plates and the over-all accuracy is probably about the same. The advantage of the use of both methods is that it helps to eliminate spurious lines, while for the numerous peculiar line profiles in the spectrum of H.D. 190073 the part of the line involved in the setting is more definitely known when it is seen on a microphotometer tracing. In forming means, equal weight was given to measures of plates and tracings and in general the agreement between the two types of measurements was good.

In the reduction of the measures and the computation of wave lengths the ordinary Hartmann formula for prismatic dispersion was used in conjunction with correction curves derived from the iron comparison lines. Since the

radial velocity of the star is not large and since it is impossible to be certain that such line displacements as occur are not due to motions in the star's atmosphere, the wave lengths are published without correction for velocity effects other than that of the earth's motion. The intrinsic motion of the star and any Doppler effects within its atmosphere are therefore contained in the wave lengths of Table II.

When the list of wave lengths from the two high-dispersion plates was completed, it was compared with an earlier list derived from four single-prism plates by Beals. As might be expected there were some discrepancies and a very careful line by line comparison was made not only between the one- and two-prism plates, but between the corresponding tracings as well. It was found that in some instances lines that appeared as single on the one-prism plates were actually of multiple character when observed with the higher dispersion. Some lines of definitely spurious character were eliminated and it was found that on the larger dispersion plates there were recorded an additional 100 lines that did not appear on the single-prism spectrograms.

Identification of Lines

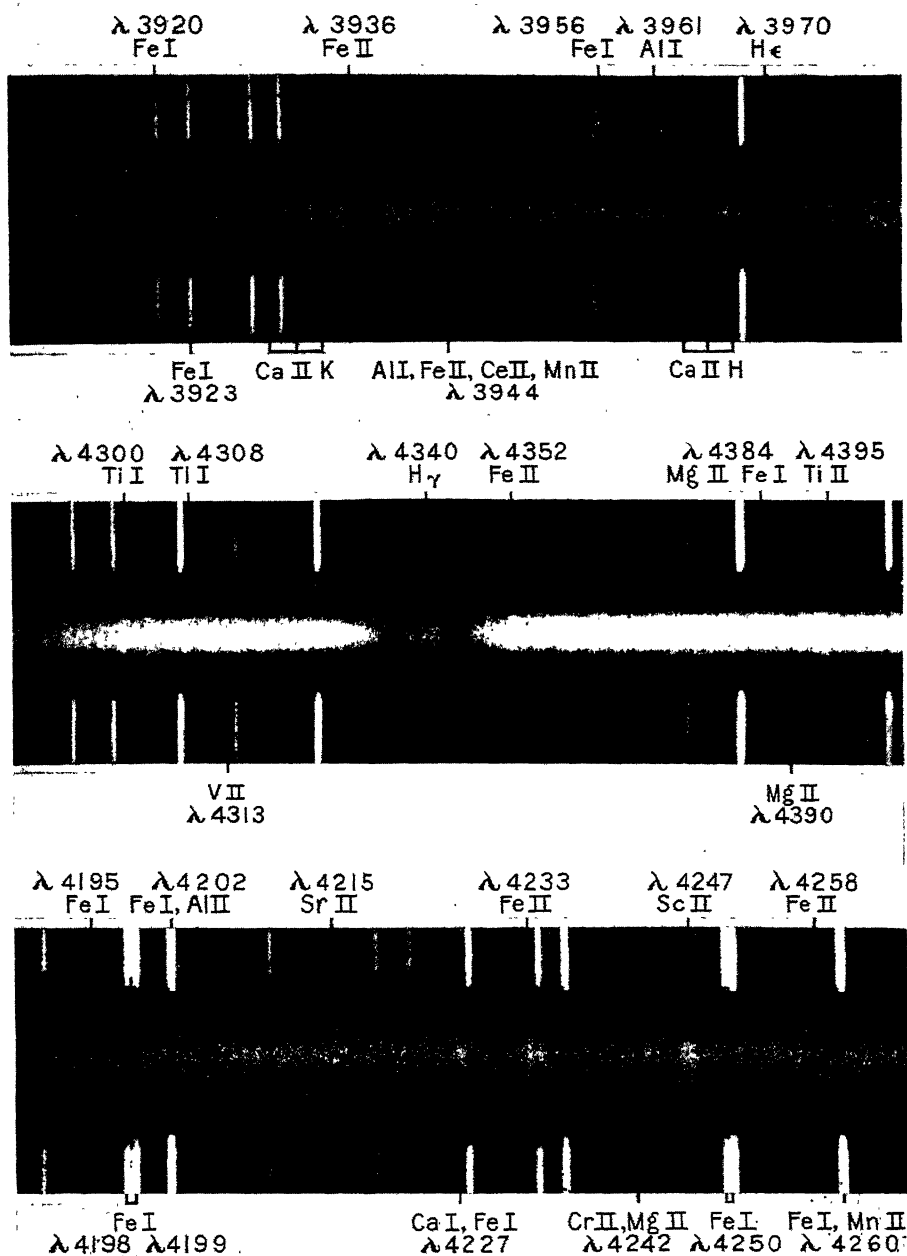
For the identification of lines, main reliance was placed on Mrs. Moore-Sitterly's New Table of Multiplets (7) although much initial labor was saved by consulting Wyse's (9) list of wave lengths in the spectrum of α Cygni.

A study of Table II indicates that, apart from the Balmer series of hydrogen, all the identifications suggested for the wave lengths of H.D. 190073 are lines of neutral and singly ionized metals. Apart from the CaII doublet, which is a very conspicuous feature of the spectrum, ionized iron and titanium are responsible for the strongest emission lines. It was at first considered that FeI appeared in absorption only, but as will be mentioned later, most such lines are now believed to be composite, consisting of both emission and absorption. It will be noted that there are very few of the stellar lines for which there is a single unambiguous identification, the majority being blends of several components.

Equivalent Widths

The plates on which the stellar spectrograms were made were all calibrated with the aid of a rapidly rotating step sector (100 r.p.s.) placed in front of the slit of a calibrating spectrograph.

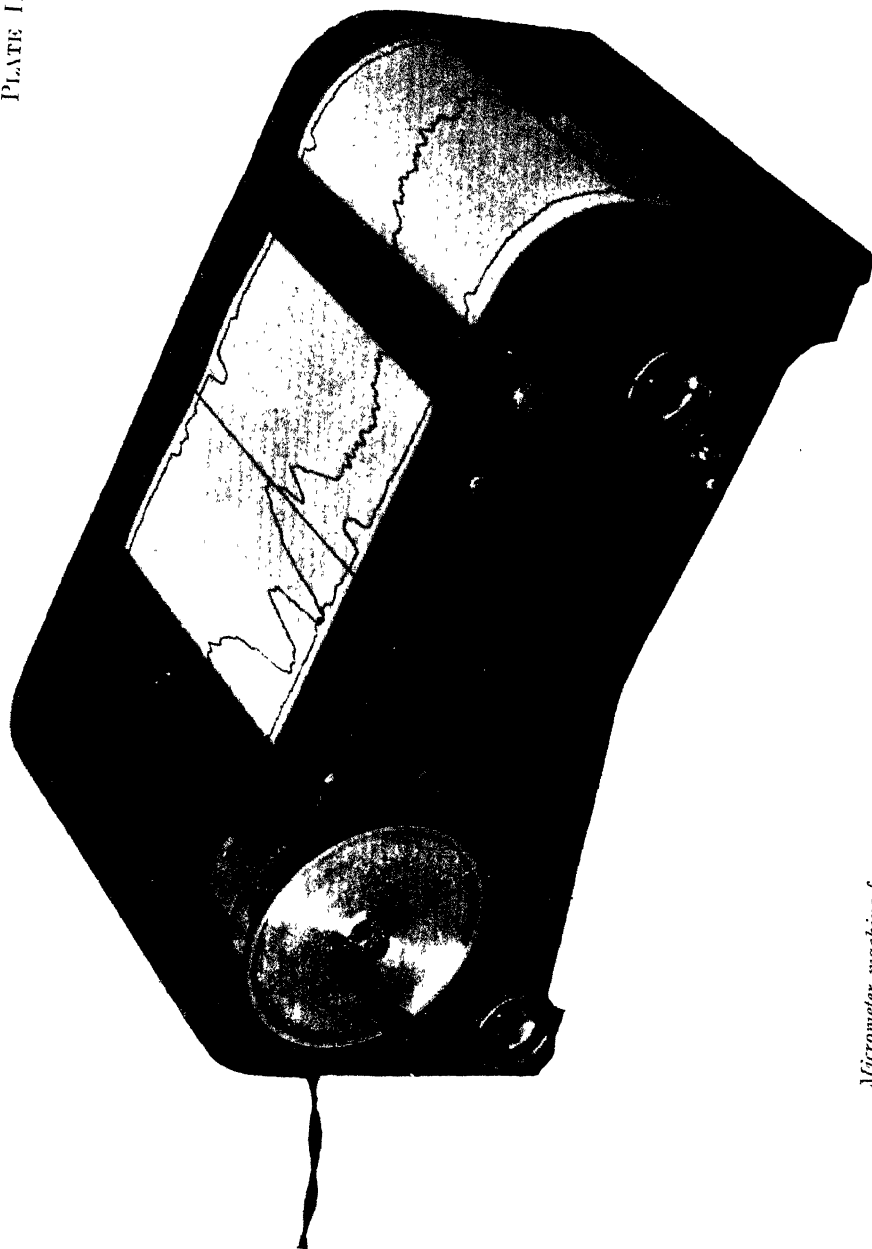
For the measurements of intensity the microphotometer tracings were transformed into true graphs of intensity with the aid of the Victoria intensitometer, which has been previously described (5). The equivalent widths of the lines were determined with the aid of a planimeter, the results being expressed both in angstrom units and in displacement in kilometers per second. Since the spectrum is known to be variable, a complete treatment of the subject of line intensities would involve separate values for each date. Actually



Spectra of H.D. 190073.

The two upper sections of the spectrum are from the II M plate. The lower one is of II L dispersion.

PLATE II



Micrometer machine for measurement of tracings. In the machine may be seen a tracing of the line λ 3968 of CaII with accompanying iron comparison spectrum.

in most cases the variations are small and it is considered that a table of mean values of intensity is the only practicable way of treating the data at the present time.

In view of the complex character of most of the emission lines, it is necessary to consider a number of the actual profiles in order to make clear the significance of the values given in the table. This has been done in Figs. 1 to 4 in which a variety of different types of profiles are shown. It is necessary to mention that no correction has been made for the distortions produced by the finite resolving power of the spectrograph.

For profiles where the absorption and emission components are clearly separated there is little ambiguity as to the significance of the values of equivalent width given in Table II. Even for the very complex lines of CaII the two displaced absorption components are well separated, and while there is undoubtedly some overlapping the general indication of intensity given by the integration of the area under the continuous spectrum is quite clear. A considerable number of the emission lines of this star, however, have absorption components directly superimposed upon the emission, as for example the FeII line λ 4233 of Fig. 1. The number of lines exhibiting these characteristics is very much greater on spectrograms of high dispersion. Many wave lengths that appeared to be pure absorption or pure emission when observed with single-prism dispersion are clearly a combination of the two when seen on two-prism plates. In particular, it is interesting to record that the lines of FeI which were first thought to be pure absorption are now definitely seen to have weak emission wings as shown in Fig. 1. It seems quite possible in fact that all the lines in the spectrum if observed with sufficient dispersion and contrast would display a composite character.

Profiles of the general character of the complex lines of Fig. 1 are sufficiently indicated in Table II by the fact that the same wave length is associated with both absorption and emission components. In this connection, the wave lengths λ 3933.70 CaII, λ 4045.78 FeI, and λ 4233.23 FeII may be quoted. The tabular value of equivalent width for the absorption is obtained by integrating the area included between the reconstructed emission profile and the line indicating the absorption, the result being divided by the mean ordinate of the top of the emission profile to reduce it to the continuous spectrum (See Fig. 1). The emission intensity is derived by simply integrating the area of the reconstructed emission profile. It should be clearly understood that equivalent widths derived in this way are of limited application and serve only as a general indication of the relative intensity of line components. Complete line profiles will be required for a detailed discussion of the interpretation of the observations.

Numerical Data

Table II, in which all numerical data are listed, consists of nine columns as follows. Column 1 contains the adopted wave lengths in angstroms of all lines measured in the spectrum. In Columns 2 and 3 the wave lengths as

H.D. 190073. July 23-25, 1946.

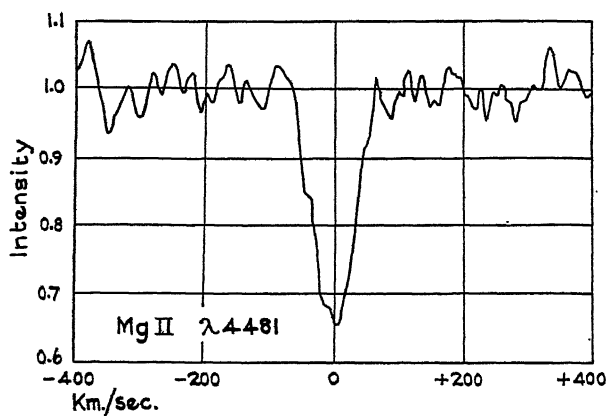
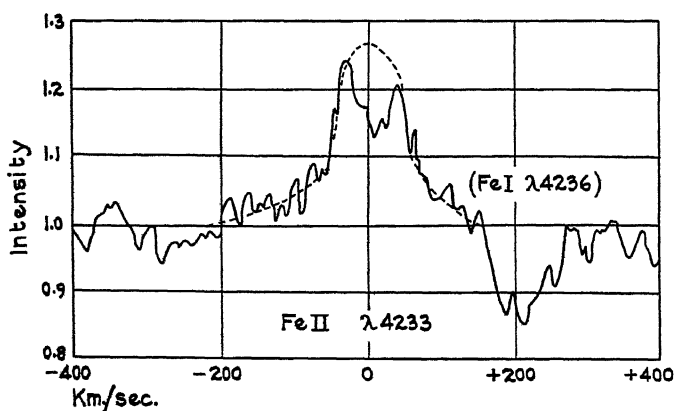
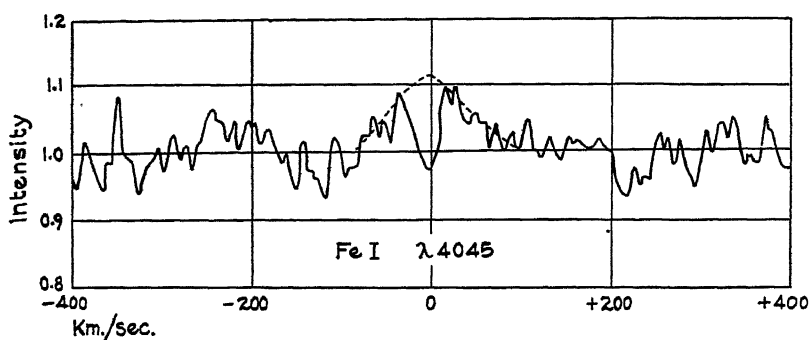


FIG. 1. Intensity profiles of lines in the spectrum of H.D. 190073. Dispersions as follows: $\lambda 4045$, 8.0 Å per mm.; $\lambda 4233$, 10.0 Å per mm.; $\lambda 4481$, 13.0 Å per mm.

derived from one and two-prism plates are compared. Column 4 gives the type of the line, A indicating absorption and E, emission. Columns 5 and 6 give the equivalent width first in angstrom units and then in velocity units of kilometers per second. The last three columns, Nos. 7, 8, and 9, are concerned with identification and give, respectively, the laboratory wave length of the line, the observed laboratory intensity, and the atom with which it is associated. In a few instances where the line has not been observed in the laboratory the symbol \odot indicates that it has been observed in the solar spectrum.

TABLE II

WAVE LENGTHS, INTENSITIES, AND IDENTIFICATIONS OF LINES IN
THE SPECTRUM OF H.D. 190073

Adopted wave length	Wave length, 1-prism	Wave length, 2-prism	Type	E.W., Å	E.W., km./sec.	Identification		
3849.90	49.90	—	A	0.09	7.2	3849.97 49.76	(40) (3)	FeI VII
3853.88	53.88	—	A	0.07	5.3	3853.72	(10n)	TiI
3856.10	56.10	—	A	0.17	12.9	3856.07 56.16 56.02	(3) (1) (8)	NII AII SiII
3862.59	62.59	—	A	0.10	7.5	3862.59	(6)	SiII
3863.92	63.92	—	A	0.05	3.9	3863.95	(1)	FeII
3865.36	65.36	—	A	0.10	7.9	3865.53	(30)	FeI
3867.04	67.04	—	A	0.07	5.7	3867.22	(7)	FeI
3872.63	72.63	—	A	0.09	7.1	3872.62 72.50	(60) (60)	GdII? FeI
3877.77	77.77	—	A	0.15	11.5	3877.59 78.02	(2n) (60)	TiI FeI
3878.38	78.38	—	A	—	—	3878.58	(100r)	FeI
3896.60	—	96.60	A	—	—	3896.53	(10)	ZrI
3900.76	00.76	—	E	0.29	22.0	3900.51	(10)	ZrI
3903.00	02.92	03.04	A	0.07	5.7	3902.92 02.95	(50) (20)	CrI FeI
3905.63	05.65	05.62	A	0.15	11.8	3905.66 05.64 05.53	(25) (100)	FeI** CrII SiI
3906.53	06.53	—	A	—	—	3906.48	(8)	FeI
3912.92	12.85	12.96	E	0.07	5.6	3912.89 12.98	(4) (5)	VI NiI
3913.47	—	13.47	A	0.04	3.3	3913.46	(60)	TiII

** Predicted.

TABLE II—*Continued*WAVE LENGTHS, INTENSITIES, AND IDENTIFICATIONS OF LINES IN
THE SPECTRUM OF H.D. 190073—*Continued*

Adopted wave length	Wave length, 1-prism	Wave length, 2-prism	Type	E.W., Å	E.W., km./sec.	Identification		
3913.89	13.82	13.93	E	0.06	4.4	3913.64	(4)	FeI
3914.44	—	14.44	A	0.06	4.7	3914.48	(2)	FeII
3916.41	16.21	16.51	A	0.08	6.0	3916.24 16.48	(25) (200)	CrI TmI
3918.56	18.60	18.53	A	0.07	5.3	3918.64 18.58	(6) (○)	FeI FeI
3920.20	20.16	20.22	A	0.04	3.4	3920.26	(20r)	FeI
3922.94	22.88	22.96	A	0.05	4.0	3922.91	(25R)	FeI
3926.04	—	26.04	A	0.04	3.2	3925.95	(6)	FeI
3927.94	—	27.94	A	0.06	4.8	3927.92	(30R)	FeI
3929.41	29.36	29.43	A	1.22	93.4	3933.66		CaII*K
3931.36	31.29	31.38	A	0.73	56.0	3933.66		CaII*K
3933.70	33.63	33.72	{E A}	1.11 0.93	84.6 70.6	}3933.66 (400R) CaII K		
3935.96	35.99	35.95	A	0.07	5.2	3935.94 35.96	(6) (30)	FeII CoI
3938.32	38.40	38.28	A	0.07	5.2	3938.29 38.40	(2) (0)	FeII MgI
3944.02	43.97	44.03	A	0.09	7.0	3944.01 43.83 43.89 43.86	(10R) (100)	AlI FeII CeII MnII
3945.29	45.16	45.32	A	0.03	2.0	3945.12 45.21 45.33 45.50	(4) (15) (9)	FeI FeII** CoI CrI
3947.52	47.76	47.39	A	0.06	4.5	3947.39 47.77 47.30	(1) (40) (10)	FeI TiI OI
3955.62	—	55.62	A	0.01	1.0	3955.77	(○)	FeI
3956.72	56.63	56.76	A	0.11	8.1	3956.68 56.46	(12) (9)	FeI FeI
3961.63	—	61.63	A	0.05	3.8	3961.52	(10R)	AlI
3964.29	64.16	64.33	A	0.84	63.6	3968.47		CaII*H
3966.17	66.11	66.18	A	0.47	35.7	3968.47		CaII*H

* *Displaced calcium line.*** *Predicted.*

TABLE II—*Continued*WAVE LENGTHS, INTENSITIES, AND IDENTIFICATIONS OF LINES IN
THE SPECTRUM OF H.D. 190073—*Continued*

Adopted wave length	Wave length, 1-prism	Wave length, 2-prism	Type	E.W., Å	E.W., km./sec.	Identification	
3968.56	68.55	68.56	$\left\{ \begin{array}{l} E \\ A \end{array} \right.$	$\left\{ \begin{array}{l} 1.06 \\ 0.58 \end{array} \right.$	$\left\{ \begin{array}{l} 80.4 \\ 44.0 \end{array} \right.$	} 3968.47 (350R)	CaII H
			A	10.37	782.7		He†
3981.95	82.31	81.77	A	0.04	2.8	3981.78 (7) 82.48 (30)	FeI TiI
3984.00	83.89	84.03	A	0.05	4.0	3983.96 (10) 83.83 (⊙) 83.91 (100)	FeI FeI CrI
3986.63	86.45	86.68	A	0.04	3.1	3986.40 (2)	MnI
3987.32	87.32	—	A	0.05	3.8	3987.46 (2)	MnI
3997.42	97.30	97.48	A	0.06	4.6	3997.39 (15)	FeI
3998.06		98.06	A	0.03	2.2	3998.05 (10)	FeI
4002.40	02.48	02.35	A	0.07	5.4	4002.66 (1) 02.55 (3) 02.47 (9n)	FeI FeII TiI
4003.02		03.02	A	0.05	3.9	4003.33 (25)	CrII
4005.18	05.24	05.14	A	0.06	4.4	4005.25 (25)	FeI
4005.86	—	05.86	A	0.04	2.8	4005.71 (800)	VII
4012.45	12.42	12.45	A	0.10	7.1	4012.49 (20) 12.47 (1)	CrI FeII
4014.55	14.48	14.57	A	0.04	3.2	4014.53 (10) 14.67 (10) 14.49 (5)	FeI CrI ScII
4015.51	—	15.51	A	0.02	1.8	4015.50 (1)	NiII
4017.25	17.25	—	A	0.03	2.5	4017.27 (1) 17.29 (15n)	CII VII
4021.94	—	21.94	A	0.04	2.8	4021.87 (12)	FeI
4023.37	23.26	23.40	A	0.03	1.9	4023.39 (600)	VII
4024.60	24.78	24.56	A	0.07	5.1	4024.55 (5) 24.74 (6n)	FeII FeI
4025.14	—	25.14	A	0.04	2.8	4025.14 (2) 25.11 (3)	TiII NiI
4028.34	28.29	28.35	A	0.05	4.0	4028.33 (7)	TiII

† Broad underlying hydrogen line.

TABLE II—*Continued*WAVE LENGTHS, INTENSITIES, AND IDENTIFICATIONS OF LINES IN
THE SPECTRUM OF H.D. 190073—*Continued*

Adopted wave length	Wave length, 1-prism	Wave length, 2-prism	Type	E.W., Å	E.W., km./sec.	Identification	
4029.64	—	29.64	A	0.03	2.1	4029.64 (P) 29.64 (3n)	TiII FeI
4030.62	30.68	30.60	A	0.07	4.9	4030.76 (200R) 30.50 (6) 30.51 (25n)	MnI FeI TiI
4032.96	32.88	32.98	A	0.05	4.0	4033.07 (150R) 32.95 (3)	MnI FeII
4034.52	—	34.52	A	0.04	3.2	4034.49 (100R)	MnI
4035.67	35.63	35.68	A	0.05	3.9	4035.63 (400) 35.54 (8) 35.73 (15)	VII CoI MnI
4044.11	44.11	—	A	0.03	1.9	4044.14 (8R)	KI
4045.78	46.04	45.72	{E A}	0.12 0.06	8.6 4.6	4045.82 (60r) 46.07 (○) 46.19 (3)	FeI FeI CrI
4048.87	48.97	48.84	A	0.05	4.0	4048.83 (3) 48.76 (15)	FeII MnI
4051.96	52.07	51.93	A	0.05	3.4	4051.92 (2) 51.97 (12)	FeI CrII
4053.88	53.95	53.86	A	0.08	6.1	4053.82 (1) 53.81 (3)	FeI TiII
4057.47	57.40	57.48	A	0.06	4.4	4057.36 (2) 57.35 (2) 57.50 (5n)	FeI NiI MgI
4060.14	—	60.14	A	0.01	1.0	4060.26 (20)	TiI
4062.01	61.69	62.17	A	0.02	1.3	4061.79 (1) 61.77 62.22 (60)	FeII CrII CeII
4063.53	63.44	63.55	{E. A}	0.06 0.06	4.6 4.8	4063.60 (45)	FeI
4064.50	—	64.50	A	0.01	0.9	4064.35 (1) 64.58 (300)	TiII SmII
4065.06	—	65.06	A	0.04	2.7	4065.07 (100)	VII
4067.01	67.14	66.98	A	0.07	5.0	4066.98 (6) 67.05 (3) 67.28 (4)	FeI NiII FeI
4067.98	—	67.98	A	0.03	1.9	4067.98 (8n)	FeI
4070.80	—	70.80	A	0.04	3.0	4070.77 (5n)	FeI

TABLE II—*Continued*WAVE LENGTHS, INTENSITIES, AND IDENTIFICATIONS OF LINES IN
THE SPECTRUM OF H.D. 190073—*Continued*

Adopted wave length	Wave length, 1-prism	Wave length, 2-prism	Type	E.W., Å	E.W., km./sec.	Identification	
4071.77	71.68	71.82	{E A	0.08 0.06	5.6 4.4	} 4071.74 (40) 71.54 (8)	FeI VI
4073.62	—	73.62	A	0.01	1.0		
4076.62	76.56	76.64	A	0.05	3.4	4076.64 (8n) 76.50 (1)	FeI FeI
4077.73	—	77.73	A	0.03	2.4	4077.71 (400r)	SrII
4083.61	—	83.61	A	0.02	1.4	4083.55 (1) 83.58 (100)	FeI SmII
4101.93	01.99	01.92	{E A	0.52 0.17	37.9 12.7	} 4101.74	H _δ *
		A		12.50	913.2		
4110.41	—	10.41	A	0.03	2.3	4110.38 (60)	CeII
4118.62	—	18.62	A	0.05	3.4	4118.55 (15)	FeI
4122.65	22.55	22.67	A	0.05	3.7	4122.64 (4) 22.52 (4)	FeII FeI
4128.08	28.11	28.07	A	0.16	11.4	4128.05 (8)	SiII
4130.93	30.90	30.94	A	0.14	9.8	4130.88 (10)	SiII
4132.12	32.11	32.12	A	0.09	6.2	4132.06 (25) 32.16 (4)	FeI CoI
4134.63	34.57	34.64	A	0.04	3.0	4134.68 (12) 34.72 (30)	FeI KII
4136.69	36.80	36.63	A	0.04	2.6	4136.51 (1)	FeI
4143.67	43.58	43.69	A	0.08	5.9	4143.42 (15) 43.87 (30) 43.76 (2)	FeI FeI HeI
4145.86	—	45.86	A	0.04	3.2	4145.77 (25)	CrII
4147.18	—	47.18	A	0.03	2.1	4147.34 (○)	FeI
4149.27	—	49.27	{E A	0.13 0.07	9.4 5.2	} 4149.37 (5n)	FeI
4153.95	54.19	53.89	A	0.07	5.0		
						4153.82 (25) 53.91 (10n)	CrI FeI
4154.75	—	54.75	A	0.07	4.9	4154.50 (12) 54.86 (2)	FeI TiI

* Emission component of hydrogen line.

† Broad underlying hydrogen line.

TABLE II—*Continued*WAVE LENGTHS, INTENSITIES, AND IDENTIFICATIONS OF LINES IN
THE SPECTRUM OF H.D. 190073—*Continued*

Adopted wave length	Wave length, 1-prism	Wave length, 2-prism	Type	E.W., Å	E.W., km./sec.	Identification		
4156.81	—	56.81	{E A	0.08 0.07	5.8 5.0	}4156.80	(12)	FeI
4161.66	—	61.66	A	0.03	1.9			
4163.65	—	63.65	{E A	0.12 0.06	8.9 4.6	}4163.64	(40)	TiII FeI
4167.30	67.28	67.30	A	0.08	5.4	4167.26	(10n)	MgI
						67.27	(10n)	MgI
4171.94	71.99	71.92	A	0.05	3.8	4171.90	(30)	TiII
						71.90	(2)	FeI
4173.48	—	73.48	{E A	0.07 0.06	4.7 4.2	}4173.45	(8)	FeII
4175.55	—	75.55	A	0.06	4.2	4175.64	(10)	FeI
4176.58	—	76.58	A	0.02	1.4	4176.57	(7n)	FeI
4177.75	—	77.75	{E A	0.16 0.07	11.5 5.1	}4177.70		FeII
4178.85	—	78.85	A	0.02	1.2	4178.86	(8)	FeII
4181.83	—	81.83	A	0.03	2.5	4181.76	(15)	FeI
4184.35	84.01	84.51	A	0.06	4.4	4184.22	(1)	FeI
4186.16	—	86.16	A	0.02	1.4	4186.12	(25)	TiI
						86.24	(30)	KII
4187.19	87.40	87.19	A	0.04	3.2	4187.04	(20)	FeI
						87.25	(4)	CoI
4187.86		87.86	A	0.07 0.06	5.2 4.4	4187.80	(20)	FeI
4191.21	91.33	91.21	A	0.03	1.8	4191.27	(25)	CrI
			A	0.04	2.8			
4191.57		91.57	A	0.04	2.6	4191.44	(15)	FeI
						91.56	(10)	VI
4195.58	—	95.58	A	0.03	2.4	4195.62	(3)	FeI
4196.96	—	96.96	{E A	0.03 0.01	2.4 1.0	}4197.10	(☉)	FeI
4198.33	98.61	98.33	A	0.07	5.0	4198.31	(20)	FeI
			A	0.10	7.4			
4199.15		99.15	A	0.07	5.3	4199.10	(20)	FeI
4200.65	—	00.65	{E A	0.10 0.07	7.1 4.8	}4200.75	(6)	TiI
4202.01	01.99	02.02	A	0.08	5.5	4202.03	(30)	FeI
						02.40	(2)	Al II

TABLE II—*Continued*WAVE LENGTHS, INTENSITIES, AND IDENTIFICATIONS OF LINES IN
THE SPECTRUM OF H.D. 190073—*Continued*

Adopted wave length	Wave length, 1-prism	Wave length, 2-prism	Type	E.W., Å	E.W., km./sec.	Identification		
4209.79	—	09.79	A	0.07	5.2	4209.76 (15) 09.86 (20)	CrI VI	
4210.41	—	10.41	A	0.08	5.6	4210.35 (15)	FeI	
4215.58	—	15.58	A	0.04	2.8	4215.52 (300r)	SrII	
4216.60	—	16.60	E	0.05	3.7			
4219.41	19.40	19.41	A	0.04	2.6	4219.51 (2) 19.36 (12)	VI FeI	
4221.09	—	21.09	E	0.02	1.4			
4222.24	—	22.24	A	0.04	2.7	4222.22 (12)	FeI	
4223.08	—	23.08	A	0.01	0.9	4223.04 (5)	NI	
4224.82	24.73	24.87	A	0.05	3.4	4224.85 (20) 24.80 (5)	CrII TiI	
4226.53	26.52	26.53	{E A	0.11 0.02	8.1 1.4	4226.73 (500R) 26.43 (3)	CaI FeI	
4227.31	—	27.31	A	0.02	1.4	4227.43 (30)	FeI	
4228.26	—	28.26	{E A	0.02 0.02	1.3 1.2			
4233.23	33.25	33.23	{E A	0.48 0.06	34.3 4.2	4233.17 (11) 33.25 (10)	FeII CrII	
4235.93	35.77	35.97	A	0.10	7.1	4235.94 (25)	FeI	
4238.85	—	38.85	A	0.06	4.4	4238.82 (10n) 38.96 (35)	FeI CrI	
4242.46	—	42.46	A	0.06	4.5	4242.38 (30) 42.47 (4)	CrII MgII	
4246.92	47.01	46.90	{E A	0.33 0.04	23.0 2.5	4246.83 (100)	ScII	
4250.17	50.35	50.17	A	0.06	4.4	4250.12 (25)	FeI	
4250.80		50.80	A	0.05	3.7	4250.79 (25)	FeI	
4251.77	—	51.77	E	0.02	1.6	4251.77 (2n)	TiI	
4252.68	—	52.68	A	0.05	3.2	4252.62 (100)	CrII	
4254.39	—	54.39	A	0.02	1.2	4254.35 (1000R)	CrI	
4256.23	—	56.23	A	0.02	1.4	4256.21 (3)	FeI	
4258.13	—	58.13	A	0.12	8.4	4258.16 (3)	FeII	

TABLE II—*Continued*WAVE LENGTHS, INTENSITIES, AND IDENTIFICATIONS OF LINES IN
THE SPECTRUM OF H.D. 190073—*Continued*

Adopted wave length	Wave length, 1-prism	Wave length, 2-prism	Type	E.W., Å	E.W., km./sec.	Identification		
4260.46	60.40	60.47	A	0.09	6.6	4260.48 60.47	(35)	FeI MnII**
4261.24	—	61.24	E	0.02	1.2	4261.35	(25)	CrI
4261.92	61.93	61.92	A	0.05	3.8	4261.92	(20)	CrII
4271.58	71.52	71.60	A	0.09	6.1	4271.65 71.55	(☉) (12)	FeI VI
4273.32	—	73.32	A	0.03	2.0	4273.32 73.31	(3) (2)	FeII TiI
4275.53	—	75.53	A	0.04	2.9	4275.57	(30)	CrII
4282.25	—	82.25	A	0.05	3.6	4282.41	(12)	FeI
4284.20	—	84.20	A	0.05	3.8	4284.21	(20)	CrII
4287.96	—	87.96	A	0.05	3.6	4287.89	(2)	TiII
4290.75	—	90.75	E	0.12	8.6			
4292.36	92.23	92.42	{E A	0.17 0.08	12.0 5.7	4292.29	(1)	FeI
4294.15	—	94.15	{E A	0.17 0.07	12.2 5.2	4294.10	(40)	TiII
4296.52	—	96.52	A	0.06	4.2	4296.57	(6)	FeII
4297.85	—	97.85	A	0.04	2.6	4297.74	(30)	CrI
4299.13	98.80	99.21	A	0.06	4.2	4298.66 99.23	(40) (15)	TiI TiI
4299.71	—	99.71	E	—	—	4300.05 299.72	(60) (20)	TiII CrI
4300.53	00.55	00.53	{E A	0.25 0.06	17.7 4.3	4300.57	(50)	TiI
4303.78	03.77	03.78	E	0.05	3.7			
4305.61	05.49	05.64	A	0.04	2.9	4305.46 05.72	(3) (10)	FeI ScII
4306.23	—	06.23	E	0.03	2.4			
4307.32	—	07.32	E	0.03	2.4			
4307.84	—	07.84	{E A	0.22 0.11	15.2 7.4	4307.90 07.91	(40) (35)	TiII FeI
4308.53	—	08.53	E	0.07	5.0	4308.51	(2)	TiI
4313.55	—	13.55	E	0.05	3.2	4313.30	(2)	VII

** Predicted.

TABLE II—*Continued*WAVE LENGTHS, INTENSITIES, AND IDENTIFICATIONS OF LINES IN
THE SPECTRUM OF H.D. 190073—*Continued*

Adopted wave length	Wave length, 1-prism	Wave length, 2-prism	Type	E.W., Å	E.W., km./sec.	Identification		
4314.19	—	14.19	A	0.03	2.0	4314.08 14.29	(60) (4)	ScII FeII
4315.14	—	15.14	A	0.01	0.7	4315.09	(10)	FeI
4316.84	—	16.84	A	0.03	2.1	4316.81	(1)	TiII
4319.98	—	19.98	{E A	0.02 0.02	1.6 1.5	}4320.36	(1)	FeI
4320.98	—	20.98	A	0.05	3.3			
						4320.74 20.96	(50) (1)	ScII TiII
4336.75	—	36.75	A	0.09	6.5	4340.47		H _γ *
4338.86	—	38.86	A	0.26	17.9	4340.47		H _γ *
4340.58	—	40.58	{E A	1.73 0.32	119.8 22.2	}4340.47		H _γ †
			A	13.39	924.7			
						4340.47		H _γ ‡
4351.84	51.74	51.86	{E A	0.34 0.04	23.1 2.9	}4351.76	(9)	FeII
4357.48	—	57.48	A	0.03	2.0			
						4357.57 57.52	(4) (15)	FeII CrI
4367.90	68.01	{67.90	A	0.08	5.8	}4367.91	(2)	FeI
4369.66		{69.66	A	0.06** 0.08	4.4** 5.6			
						4369.61 69.68	(5n)	FeII TiI
4375.32	—	75.32	E	0.07	4.9	4375.33	(30)	CrI
4384.62	—	84.62	{E A	0.42 0.16	28.5 10.8	}4384.64 84.13	(8) (C?)	MgII FeI
4386.01	85.92	86.06	E	0.06	4.2			
4386.90	—	86.90	{E A	0.63 0.07	43.3 5.1	}4386.86	(10)	TiII
4388.93	—	88.93	A	0.18	12.1			
4390.71	90.66	90.72	A	0.14	9.4	4389.12		VII
4394.69	94.86	{94.69	E	0.38 0.08	25.7 5.6	}4395.03	(60)	TiII
4395.20		{95.29	{E A					
4404.81	—	04.81	{E A	0.15 0.06	10.2 4.2	}4404.75	(30)	FeI

* Displaced hydrogen line.

† Emission component of hydrogen line.

‡ Broad underlying hydrogen line.

** Single prism observations.

TABLE II—*Continued*WAVE LENGTHS, INTENSITIES, AND IDENTIFICATIONS OF LINES IN
THE SPECTRUM OF H.D. 190073—*Continued*

Adopted wave length	Wave length, 1-prism	Wave length, 2-prism	Type	E.W., Å	E.W., km./sec.	Identification		
4415.31	—	15.31	A	0.06	4.3	4415.12	(20)	FeI
4416.40	16.66	16.27	E	0.10	6.8			
4422.08	—	22.08	A	0.05	3.7	4421.95	(1)	TiII
4434.02	—	34.02	A	0.09	6.4	4433.99	(8)	MgII
4443.40		43.40	E					
4443.92	43.87	43.93	{E A	0.33 0.04	22.2 2.4	4443.80	(50)	TiII
4455.02	54.67	55.19	A	0.07	4.6	4455.26 54.78	(3) (80)	FeII CaI
4468.69	68.60	68.71	{E A	0.43 0.05	28.9 3.5	4468.49	(50)	TiII
4476.20	—	76.20	A	0.03	2.2	4476.08	(4)	FeI
4481.36	81.26	81.38	A	0.42	27.9	4481.33 81.13	(100) (100)	MgII MgII
4488.05	88.05	—	A	0.08	5.1	4488.05	(30)	CrI
4501.55	01.33	01.61	E	0.38	25.4	4501.27	(40)	TiII
4508.62	08.27	08.70	E	0.24	16.1	4508.28	(8)	FeII
4515.55	15.58	15.53	E	0.18	12.0	4515.34	(7)	FeII
4522.52	22.37	22.56	{E A	0.45 0.06	30.0 3.9	4522.63	(9)	FeII
4534.13	33.57	34.27	{E A	0.26 0.04	17.3 2.8	4534.17	(2)	FeII
4549.95	49.83	49.98	{E A	0.54 0.10	35.3 6.8	4549.62	(60n)	TiII
4556.29	55.45	56.71	E	0.31	20.7	4556.76	(4)	VII
4559.36	—	59.36	E	0.11	7.4			
4564.10	63.65	64.21	E	0.21	14.0	4563.76	(30)	TiII
4572.29	72.24	72.31	{E A	0.44 0.06	28.7 3.7	4571.97	(50n)	TiII
4584.21	83.84	84.30	{E A	0.65 0.15	42.4 10.0	4583.83	(11)	FeII
4703.01	03.01	—	A	—	—	4702.98 02.98 02.99		MgI MgI MgI

TABLE II—*Concluded*WAVE LENGTHS, INTENSITIES, AND IDENTIFICATIONS OF LINES IN
THE SPECTRUM OF H.D. 190073—*Concluded*

Adopted wave length	Wave length, 1-prism	Wave length, 2-prism	Type	E.W., Å	E.W., km./sec.	Identification	
4857.27	57.27	—	A	0.14	8.7	4861.33	H β *
4860.75	60.75	—	E	3.09	190.5	4861.33	H β †
			A	10.44	644.0	4861.33	H β ‡
4920.08	20.08	—	A	0.12	7.1		
4923.79	23.79	—	{E A	{1.14 0.18	{69.3 11.0	}4923.92 (12)	FeII

* *Displaced hydrogen line.*† *Emission component of hydrogen line.*‡ *Broad underlying hydrogen line.*

Line Profiles

The increased resolving power afforded by two prisms has revealed additional detail in the line profiles and has made it possible to clarify a number of points that were formerly uncertain. One such matter concerns the relative intensities of the central reversals appearing in the emission components of the H and K lines of CaII. Struve and Swings (8), on the basis of relatively low dispersion, had suggested that the central reversal of the H line was abnormally weak relative to that of K and indeed there seemed some doubt as to whether the H absorption was present at all on their plates. From this they concluded that the reversal at H was affected by the broad hydrogen absorption and therefore arose in a low level in the stellar atmosphere.

Profiles of both the H and K lines of calcium from the two-prism plates are shown in Fig. 2. From this illustration it will be seen that the absorption in the normal position of CaII H is relatively conspicuous. It is difficult to arrive at a reliable estimate of the intensity of the line since this depends upon assumptions as to the form of the undistorted emission. However, on the basis of the reconstruction shown by the broken lines of Fig. 2, the equivalent widths of K and H are 71 km. per sec. and 44 km. per sec., while the central intensities are 0.29 and 0.50 respectively, with excellent agreement between the two high-dispersion plates. It would thus appear that these absorption features for H and K stand in normal relationship to one another and the intensity data are not inconsistent with an origin of this absorption in the outer envelope of the star.

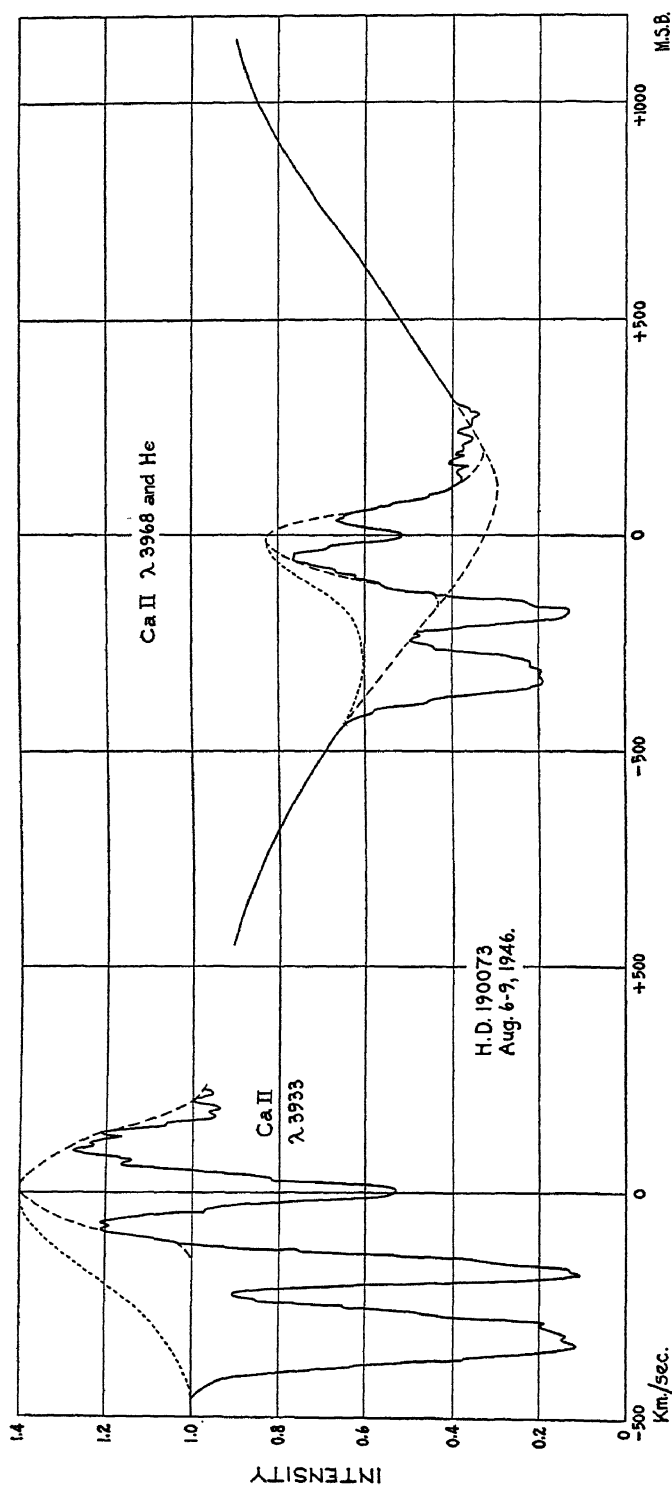


FIG. 2. Profiles of Ca II lines. The dotted lines correspond to alternative suggestions for reconstructing the undistorted emission.

An interesting aspect of the CaII lines is the fact that the more displaced component of the two P Cygni absorption features is approximately twice the width of its companion. The structure shown in the bottom of the wider component appears to be real and it would be interesting to see whether it is variable. Unfortunately one of our high-dispersion plates was too weak to record detail in the bottom of this very strong line. The additional structure shown on the violet emission wing of the H line of calcium as well as the unsymmetrical character of this line is possibly a consequence of blending with the weak P Cygni line of hydrogen which is superimposed on the broad H ϵ absorption.

It will be further noted that the maximum between the two strong displaced absorption lines approaches very close to the continuous spectrum for K and the wing of the hydrogen profile for H. The question thus arises as to whether, if still higher dispersion were used, this maximum might not have a central intensity greater than that of the continuous spectrum. This consideration, together with others already advanced in connection with a suggested explanation of the hydrogen line profiles of the star M.W.C. 374 (4), raises the question as to whether a quite different reconstruction of the emission profile than that shown by the heavy dotted lines in Fig. 2 may not give a clearer picture of the emitting envelope. In view of the great strength of the displaced absorption lines, it seems reasonable to suppose that the envelope emits in these wave lengths also and that the emission may have been suppressed by strong absorption. If this is the case, then the reconstructed emission profile would be markedly unsymmetrical as shown by the fine dotted lines of Fig. 2. Such asymmetry could arise as a consequence of occultation by the star's disk of that part of the envelope having the largest velocity of recession, and if this is the correct explanation then the conclusion follows that the diameter of the emitting envelope does not greatly exceed that of the central star.

Similar considerations may apply in connection with the lines of hydrogen. Profiles of H γ for the two high-dispersion plates are shown in Fig. 3. The difference in character between these two profiles clearly indicates the variable character of the spectrum. For the plate taken on July 23-25, 1946, there are two displaced absorption lines which are similar as regards displacement with the corresponding features of CaII although their relative intensities are quite different. On the plate of Aug. 6-9, 1946, only one displaced line definitely appears. Both profiles, however, exhibit a clearly marked asymmetry about the normal position, the extension to the violet being much greater than that to the red. Again, as for CaII, this appears most readily explicable in terms of occultation by the star's disk and again an envelope of relatively small dimensions is suggested.

Reference has already been made to the line profiles of FeI and FeII in connection with the discussion of equivalent widths. The central reversals shown by these and other lines represent possibly the most significant single feature of this remarkable spectrum. It is interesting to note that the metallic

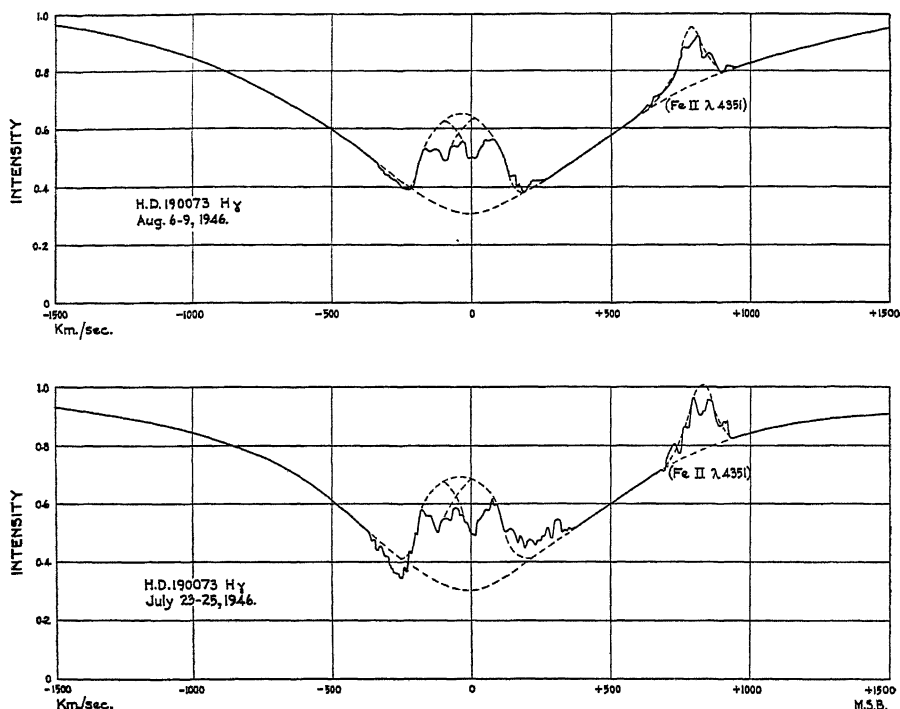


FIG. 3. Profiles of H_γ on different dates. Of special interest is the unsymmetrical character of the emission profile and the evidence of variability in the spectrum.

lines in the less refrangible region of the spectrum to the red of $\lambda 4400$ no longer show evidence of reversal and this is attributed to insufficient resolving power.

The profiles of the D lines of sodium are shown as pure emission lines in Fig. 4 as observed with three-prism dispersion of 34.5 \AA per mm. It would

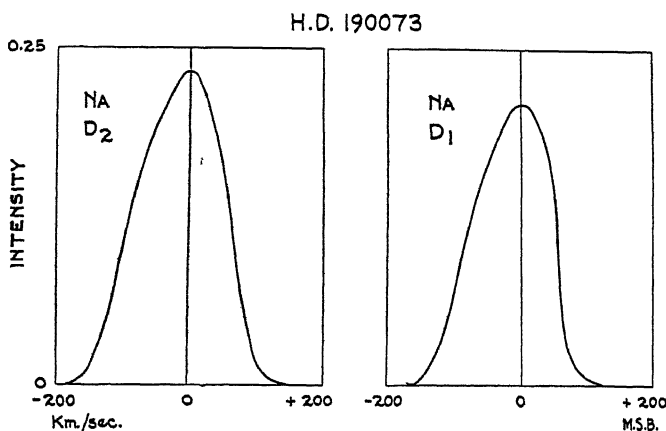


FIG. 4. Sodium emission line profiles. The dispersion of 34.5 \AA per mm. is insufficient to indicate whether or not these profiles are of complex structure.

be well worth while for any observatory with sufficiently powerful equipment to examine these lines with high dispersion (say 10 Å per mm.) to see whether they share the feature of central reversal with other metallic lines.

The only really strong line in the spectrum which shows no clear evidence of complexity on our plates is MgII λ 4481. A profile of this line is shown in Fig. 1 and it is seen to be a strong narrow absorption feature in no way differing in appearance from the same line in many normal stellar spectra. It is worth recording that there are several other emission line stars including H.D. 51480 and H.D. 45910 in which the MgII line also appears as pure absorption.

Conclusion

Apart from the addition of many new wave lengths and identifications to the known spectrum of H.D. 190073 the most important result of the present study is to be found in the clearer delineation of line profiles which makes possible a new approach to the question of interpretation.

The problem of the relative size of shell and envelope for an emission line star is a difficult one and in relatively few cases is a definitive answer possible. For the line H γ in both high-dispersion plates the asymmetrical character of the emission profile appears to be beyond question and its interpretation in terms of an envelope of small size reasonably probable. The writers believe that this evidence supersedes the previous suggestion by Beals (2, 3) that the central absorption takes place in an envelope many times the diameter of the star and the criticism of this earlier interpretation by Struve and Swings (8) must now be regarded as valid.

While uncertainty still exists as to the part of the stellar envelope where the central absorption originates, absorption data on the H and K calcium line profiles are no longer inconsistent with an origin in the outer layers of the envelope. In this connection, it may be noted that evidence of strong absorption appears in the relatively intense hydrogen emission lines H β and H α (3), and it is clearly easier to attribute minima in such strong emission lines to absorption in an outer layer than in a layer deep in the star's atmosphere.

From the point of view of interpretation the most difficult feature of the spectrum is still the peculiar nature of the profiles associated with CaII. It was at first thought that the form of these lines was unique among stellar spectra but recent investigations have shown that this is not the case. The data of this paper indicate that the lines of hydrogen in H.D. 190073 show similar characteristics although the relative intensities of components are quite different. Double, displaced absorption has been observed on a number of occasions in the hydrogen lines of H.D. 45910 as well as other stars. Such profiles are, however, always of a variable character such as could be associated with temporary detached shells.

No great theoretical difficulty attaches to the explanation of such complex lines if it be assumed that they are associated with temporary nova-like shells. Among observed novae many complexities of this type are known and have

been explained on the basis of separate absorbing and emitting media moving independently of one another. For a permanent envelope the explanation is more difficult. A formal interpretation in terms of acceleration and subsequent deceleration of atoms within the envelope under conditions of dynamical equilibrium has been presented by Beals (2, 3). Such an explanation has considerable flexibility in accounting for the observed phenomena but so far the physical mechanism producing the accelerations is obscure. Whether the relatively complicated shell structure postulated by a theory of this general character can be shown to have a valid physical basis remains to be seen, but until some other explanation is forthcoming it would appear that the most promising line of approach to the problem of these complex line profiles is to be found in a study of the forces responsible for the radial motions of atoms ejected from the star.

References

1. BEALS, C. S. Monthly Notices Roy. Astron. Soc. 96 : 730. 1936.
2. BEALS, C. S. J. Roy. Astron. Soc. Can. 34 : 169. 1940.
3. BEALS, C. S. J. Roy. Astron. Soc. Can. 36 : 145, 201. 1942.
4. BEALS, C. S. J. Roy. Astron. Soc. Can. 37 : 241. 1943.
5. BEALS, C. S. J. Roy. Astron. Soc. Can. 38 : 65. 1944.
6. MERRILL, PAUL W. Astrophys. J. 77 : 51. 1933.
7. MOORE, CHARLOTTE E. Contribs. Princeton Univ. Observ. No. 20. 1945.
8. STRUVE, OTTO and SWINGS, P. Astrophys. J. 96 : 475. 1942.
9. WYSE, A. B. Lick Observ. Bull. No. 492, p. 129. 1938.

DESIGN OF GRID IONIZATION CHAMBERS¹

By O. BUNEMANN,² T. E. CRANSHAW,³ AND J. A. HARVEY⁴

Abstract

Conformal representation theory is applied to a grid ionization chamber having plane parallel electrodes to give formulas useful in design. Expressions are obtained for the inefficiency of grid shielding of the electron collector, the spread of pulse size caused by the induced effect of positive ions, and the proportion of electrons collected by the grid. The theory was verified by experiment. The width of the polonium α -particle line at half-maximum was reduced to 50 kev. or about 1% of the energy by the use of a suitable grid and operating voltages. The corresponding standard deviation from all causes was 22 kev., made up of 2 kev. resulting from induced effect of positive ions, about 17 kev. from noise in the amplifier, and 14 kev. from straggling of ionization, thickness of source, and other effects. The spread caused by positive ions can therefore be almost completely eliminated by a grid.

Introduction

Many experimenters have used the number of ion pairs produced in the track of a charged particle in a gas filled ionization chamber to indicate the initial energy of the particle. The simplest chamber contains two plane parallel electrodes with an electrostatic field applied between them; that is, a high voltage electrode, and a collecting electrode that is connected to a suitable amplifier with a high resistance to ground. When an ionizing particle spends its energy in the gas between the electrodes the ions are collected and a pulse is fed to the amplifier. The rise time of this pulse depends on the orientation of the track in the chamber and the mobility of the components of the ionization, and its decay on the time constant of the capacity and leak resistance of the collecting electrode. This decay is usually arranged to be very long, and a short time constant later in the amplifier determines the output pulse duration. While this is frequently required to be short, the short time constant must be made about 10 times longer than the rise time. This condition is necessary to prevent the variation in rise time due to different track orientations from affecting the output pulse amplitude.

To permit the use of a fast amplifier by speeding up the rate of rise it is necessary first to use as a filling a gas that does not form negative ions by electron attachment, e.g., argon. The negative component of ionization then travels to the collector entirely as electrons, which have a high mobility. However the positive ions, which have a mobility less by a factor of about 1000,

¹ *Manuscript received May 28, 1949.*

Contribution from the Nuclear Physics and Theoretical Physics Branches, Division of Atomic Energy, National Research Council of Canada, Chalk River, Ontario. Issued as N.R.C. No. 1986. This work first appeared in Report CRP-247, dated May 1, 1946, of the National Research Council of Canada.

² *United Kingdom Staff; now at the Atomic Energy Research Establishment, Harwell, England.*

³ *United Kingdom Staff; now at the Cavendish Laboratory, Cambridge University, Cambridge, England.*

⁴ *Now at the Massachusetts Institute of Technology, Cambridge, Mass., U.S.A.*

induce a charge on the collector of the opposite sign. The potential of the collector will rise rapidly, as the electrons are collected, to an intermediate value given by the collected charge minus the induced charge divided by the capacity, and then rise slowly as the positive ions are removed, to the full potential. The induced charge depends on the orientation of the track in the chamber. If the induction effect of the positive ions can be eliminated the collector will attain its final potential immediately the electrons are collected.

The use of a grid to screen the electron-collecting electrode from the effect of the positive ions was suggested by O. R. Frisch (4). In such a three-electrode chamber the electron pulses are nearly proportional to the ionization in the tracks. The pulse consists of a rapid rise of the order of $1 \mu\text{sec.}$, and a fall determined as before. These fast pulses are more easily amplified linearly than those from a two-electrode chamber. A band width can be chosen that is more suitable for reducing the noise level, eliminating microphonics, increasing the permissible counting rate, and decreasing the building up of small background pulses. It is desirable to screen the collecting electrode as effectively as possible and at the same time to avoid the collection of electrons by the screening grid.

The present paper contains a theoretical and experimental study with the purpose of selecting a suitable grid and the proper operating voltages on the electrodes. The success of the arrangement is finally appraised by measuring the "line width" obtainable using a thin α -particle source.

Theoretical Analysis

(a) Preliminary Statement

A grid, G , shown in Fig. 1, is placed in front of the electron-collecting plate P to shield it from fields induced by the positive charges created at Q in the region A to G by ionization of a particle. It is convenient to define the electric field as the *positive* gradient of the potential, with the positive direction of the lines of force accordingly in the direction followed by electrons.

The efficiency of the grid shielding is measured by the extent to which the charge induced on P , or the number of lines per unit area ending there, E_P , is independent of the field E_Q . We define

$$\sigma = \frac{dE_P}{dE_Q}, \quad \text{for } V_P - V_G = \text{constant}, \quad (1)$$

as the "inefficiency" of the grid, and calculate it as a function of the two geometrical ratios r/d and p/d (Fig. 1). The results are shown by Equation (14) and Fig. 3. The charge induced at P by a unit charge created at Q is then calculated in terms of σ and the distances AQ and AG (Equation (15)).

The proportion of electrons collected by the plate is roughly equal to the proportion of lines that by-pass the grid, as electrons diffuse along the lines of force at the pressures prevailing in an ionization chamber. (This was an initial assumption and is justified by the experimental work.) This proportion

is calculated in terms of the grid geometry and potentials (Fig. 4), and conditions are derived for which all the lines by-pass the grid (Equations (21) and (23)).

(b) General Method

For the purpose of calculation it is convenient to replace the grid by a fictitious conducting wall of thickness t held at a potential V'_G that differs from V_G by an amount ΔV depending on E_Q and E_P and the grid geometry (see lower part of Fig. 1).

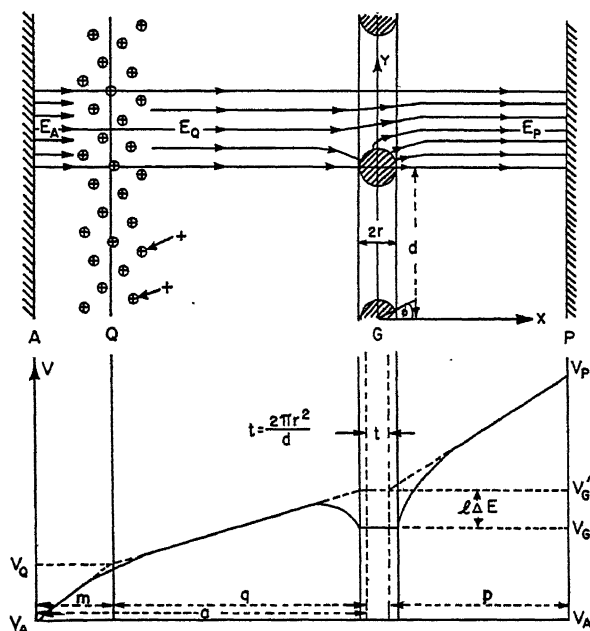


FIG. 1. Field (upper) and potential (lower) in grid ionization chamber. Positive ions and electrons at Q are produced near the cathode A by α -particles. A grid G of parallel wires shields the electron collector P from induced effect of the positive ions.

To calculate t , ΔV , the stagnation points (in the hydrodynamical sense), and numbers of lines, conformal representation theory is used (5). The number of lines passing between the x -axis and a general point in the x - y plane is denoted by U , the potential by V , and an analytic function of $z = x + iy$ is constructed to form the complex quantity $W = U + iV$. The grid wires are simulated by line charges and line dipoles placed along their axes. Nonuniformity of the field is neglected at P and Q . This assumption is permissible when their distances from the grid exceed the pitch of the grid wires.

(c) Line Charges Induced in Grid Wires

E_Q lines per unit area arrive at the grid, and E_P lines per unit area leave it. Hence $\Delta E = E_P - E_Q$ lines arise from unit area of grid or $(\Delta E)d$ lines from

a unit length of each wire, implying a line charge density of $(\Delta E)d/4\pi$ units. The complex potential function associated with unit line charge is $2i \log z$, but to represent the array of line charges producing a field periodic in y the function $\sinh \pi z/d$ must be used as argument of the logarithm in place of z . Now the equipotentials derived from the transformation

$$W = 2i \log \sinh \frac{\pi z}{d} \quad (2)$$

are approximately circular in the vicinity of $z = 0, \pm id, \pm 2id$, etc., and the mean value of the potential around an exact circle of radius r (the wire radius) is $2 \log \frac{\pi r}{d}$. Hence the complex potential

$$W_L = \frac{\Delta E}{2\pi} di \left(\log \sinh \frac{\pi z}{d} - \log \frac{\pi r}{d} \right) \quad (3)$$

takes account of the line charges induced in the wires when the grid is at zero potential. For large positive and negative x the potential is given approximately by

$$V_L = \frac{\Delta E}{2} \left(|x| - \frac{d}{\pi} \log \frac{2\pi r}{d} \right) + O(e^{-2\pi|x|/d}). \quad (4)$$

The deviations from uniformity in the field are therefore small even when $|x|$ is of the same magnitude as d .

(d) Line Dipoles Induced in Grid Wires

A uniform field E induces a dipole of intensity $\frac{1}{2}Er^2$ at the center of a cylindrical conductor of radius r . It is reasonable to expect that the dipoles induced in the grid wires have the intensity $\frac{1}{2}\bar{E}r^2$, where $\bar{E} = (E_P + E_Q)/2$ is the mean of the distant fields on the two sides of the grid.

The complex potential function for line dipoles of unit strength, one at each wire position and all orientated in the x direction, is the derivative with respect to z of the unit line-charge function, i.e., $2i(\pi/d) \coth \pi z/d$. In accordance with our expectation, we use as a trial function

$$W_D = -\bar{E}r^2 i(\pi/d) \coth \pi z/d, \quad (5)$$

and show that when combined with the potential function representing the mean field, viz.,

$$W_E = i\bar{E}z, \quad (6)$$

it yields $|z| = r$ as zero equipotential. Neglecting terms of order r^3 ,

$$W_D + W_E = i\bar{E} \left(z - \frac{r^2}{z} \right) = -2\bar{E}r \sin \phi, \quad (7)$$

which is real as required. (The angle ϕ is measured from the x -axis.) Similarly $|z \pm nid| = r$ for $n = 1, 2, \dots$ can be shown to be zero equipotentials.

(e) Complete Potential Function

The combination

$$W = iV_G + W_L + W_D + W_E \quad (8)$$

makes $|z| = r$, $|z \pm nid| = r$ equipotentials with $V = V_G$, and therefore satisfies conditions at the grid. It also yields correct values E_P and E_Q for the field at large positive and negative values of x . The function W yields

$$V = V_G + l(\Delta E) + E_P(x - \frac{1}{2}t) \quad (9)$$

and

$$V = V_G + l(\Delta E) + E_Q(x + \frac{1}{2}t) \quad (10)$$

for large positive and negative values of x respectively. In Equations (9) and (10)

$$l = \frac{d}{2\pi} (\frac{1}{4}\rho^2 - \log \rho), \quad (11)$$

$$t = \frac{d}{2\pi} \rho^2 = \rho r, \quad (12)$$

and

$$\rho = \frac{2\pi r}{d}. \quad (13)$$

More exact analysis reveals additional even powers of ρ in the formulas for l and t , beginning with

$$-\frac{7}{288} \left(\frac{d}{2\pi} \right) \rho^4 \quad \text{and} \quad -\frac{1}{12} \left(\frac{d}{2\pi} \right) \rho^4 \quad \text{respectively.}$$

These terms enter when, in order to make the equipotentials at the wires more nearly circular, quadrupoles are considered. The ratio l/d is plotted as a function of r/d in Fig. 2.

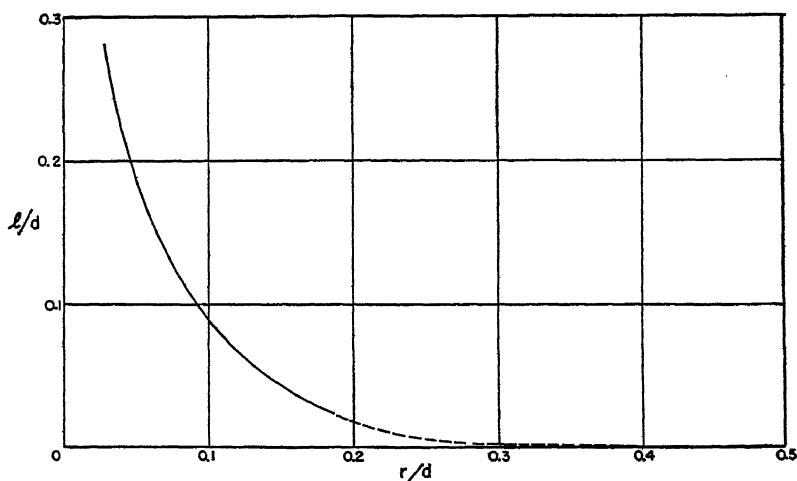


FIG. 2. Curve of l/d as a function of r/d , which is convenient for calculating the inefficiency τ of a grid.

(f) *Inefficiency of Shielding*

The inefficiency σ can be obtained by differentiating the relation

$$V_P - V_G = pE_P + l(\Delta E) = (p + l)E_P - lE_Q = \text{constant},$$

giving

$$\sigma = \frac{dE_P}{dE_Q} = \frac{l}{p + l} \approx \frac{d}{2\pi p} \log \left(\frac{d}{2\pi r} \right). \quad (14)$$

Curves of constant σ are shown in Fig. 3. It is seen that σ can be made small and the grid efficient either by choosing a grid-to-collector distance

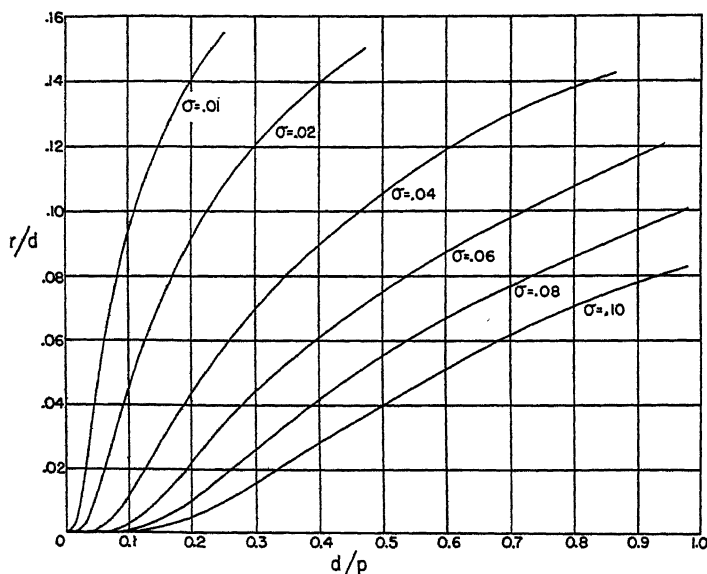


FIG. 3. Curves of constant inefficiencies σ of grids.

large compared to the pitch or by choosing the wire radius comparable to the pitch. It will be seen later that the second alternative is inadmissible (Equation (23)).

(g) *Charge Induced at P by Charge Created at Q*

From Fig. 1

$$\begin{aligned} V_G - V_A &= mE_A + qE_Q - l(\Delta E) \\ &= mE_A + (q + l)E_Q - lE_P = \text{constant}. \end{aligned}$$

Therefore

$$mdE_A + (q + l)dE_Q - ldE_P = 0,$$

which with the relation

$$dE_P = \sigma dE_Q,$$

yields

$$\begin{aligned} \frac{\text{charge induced at } P}{\text{charge created at } Q} &= - \frac{dE_P}{d(E_A - E_Q)} \\ &= \frac{\sigma m}{a + l(1 - \sigma)} \approx \sigma \frac{\overline{AQ}}{\overline{AG}}. \end{aligned} \quad (15)$$

(h) *Fraction of Lines Intercepted by Grid*

The real part U of the function W can be used to determine the number of lines leaving Q that are intercepted by the grid. On the grid wire where $|z| = r$ we obtain

$$U = -\phi(\Delta E) \frac{d}{2\pi} - 2\bar{E}r \sin \phi. \quad (16)$$

The stagnation points (5, p. 108), i.e., the points on the circumference where lines cease to enter and instead leave the grid, occur where U is stationary,

$$\text{i.e.,} \quad \frac{\partial U}{\partial \phi} = 0.$$

Therefore

$$\cos \phi = -\frac{(\Delta E)}{2\bar{E}} \frac{d}{2\pi r} = -\frac{(\Delta E)}{2\rho\bar{E}}. \quad (17)$$

The number of lines collected by each wire from the field E_q is given by the difference of U between the two solutions of (17) going via $\phi = \pi$. This difference is

$$\begin{aligned} \Delta U &= 4\bar{E}r |\sin \phi| - 2|\pi - \phi| (\Delta E) \frac{d}{2\pi} \\ &= 4\bar{E}r \sqrt{1 - \left(\frac{\Delta E}{2\bar{E}\rho}\right)^2} - 2(\Delta E) \frac{d}{2\pi} \cos^{-1} \left(\frac{\Delta E}{2\bar{E}\rho}\right). \end{aligned} \quad (18)$$

The number of lines collected by unit area of the grid is $\Delta U/d$, and the ratio between this and E_q represents the grid loss λ :

$$\lambda = \frac{\Delta U}{E_q d} = \frac{E_P - E_q}{\pi E_q} \left\{ \sqrt{\left(\frac{E_P + E_q}{E_P - E_q} \rho\right)^2} - 1 - \cos^{-1} \left(\frac{E_P - E_q}{E_P + E_q} \frac{1}{\rho}\right) \right\}. \quad (19)$$

The proportion of lines that end on the collector rather than the grid, $1 - \lambda$, is plotted as a function of E_P/E_q for three values of ρ in Fig. 4 over the range where the square root and the inverse cosine are real, viz.,

$$\frac{1 - \rho}{1 + \rho} < \frac{E_P}{E_q} < \frac{1 + \rho}{1 - \rho}. \quad (20)$$

The ends of the interval correspond to the conditions where the stagnation points unite and slip off the wires in the direction of the weaker field. For

$$\frac{E_P}{E_q} > \frac{1 + \rho}{1 - \rho} \quad (21)$$

all lines by-pass the grid, and $1 - \lambda = 1$. For

$$\frac{E_P}{E_q} < \frac{1 - \rho}{1 + \rho} \quad (22)$$

all of the balance between E_q and E_P is collected by the grid,

$$\lambda = \frac{E_q - E_P}{E_q} \quad \text{and} \quad 1 - \lambda = \frac{E_P}{E_q}.$$

Since V'_G differs from V_G , E_P/E_Q is not strictly proportional to the grid-plate potential difference for fixed $V_G - V_A$. Deviations from proportionality are of the order of σ . In particular zero grid-collector potential difference corresponds to $E_P/E_Q = \sigma$. The origin must be shifted to the right by an amount σ in Fig. 4 if the abscissa is to become a more accurate measure of the grid-collector potential difference (broken line).

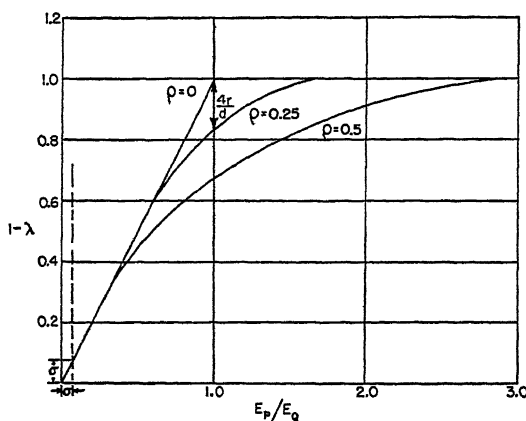


FIG. 4. Fraction of lines from cathode that end on electron collector is plotted against the field ratio E_P/E_Q . The origin must be shifted by σ if $(V_P - V_G)/p$ is used for E_P . ($\rho = 2\pi r/d$).

(i) Condition on Potential Differences for Zero Grid Interception

Condition (21) applies when all lines by-pass the grid. If this condition is satisfied in the absence of positive charge at Q , then it will certainly be satisfied in the presence of such charge. Hence a sufficient condition on V_A , V_P , and V_G can be derived on the assumption that there is no charge at Q . Substitution for E_P and E_Q then gives the condition:

$$\frac{V_P - V_G}{V_G - V_A} \geq \frac{p + \rho p + 2l\rho}{a - ap - 2l\rho}. \quad (23)$$

This must be balanced against the condition that σ (or l/p) should be small for efficient shielding (Equation (14)).

Experimental Investigation

An experimental investigation was undertaken to test the main results from the theoretical analysis and to indicate what lower limit in width of an α -particle line might be realized in practice.

(a) Ionization Chamber

The ionization chamber consisted of two parallel plates, 10 cm. square and about 6 cm. apart, mounted on insulators inside a cylindrical vessel. The

gas was argon, usually at a pressure of 3 atm. A grid of parallel wires could be mounted 1.43 or 0.67 cm. in front of the collector. Two grids were tested; one consisted of No. 38 copper wires 0.20 cm. apart, and the other of No. 36 copper wires 0.091 cm. apart. A negative potential of 1200 v. was applied to the cathode, which produced an adequate field between the electrodes for electron collection.

Sources of α -particles were made by evaporating a solution of polonium 210 on gold foils. The source, covered by a collimator consisting of $\frac{1}{8}$ in. holes in a $\frac{1}{32}$ in. aluminum sheet, was placed against the cathode. Without the collimator the distribution of pulse sizes was not symmetrical about the maximum and had a tail on the low energy side. This distortion is attributed to α -particles that had traveled approximately in the plane of the source and lost energy in irregularities in the source or in the backing foil before being scattered into the gas.

The electronic equipment for the measurement of pulse size has been described (1). The ionization pulses at the collector were fed into an amplifier designed for low noise and high stability of gain and then into a cutoff amplifier that subtracted a predetermined voltage and amplified the remainder. The output pulses were electronically sorted into groups according to height by a pulse analyzer (3). In this way the "line" containing the pulse heights could be expanded to show its shape and thereby to yield quantitative information on width at half-maximum or alternatively on the standard deviation from the mean.

(b) Collection of Electrons by the Grid

The first point considered was the possible collection of electrons by the grid. This is undesirable for two reasons. (1) The pulse size and the signal-to-noise ratio would be reduced. (2) The fraction of electrons collected might depend somewhat on the track orientation, and thus an additional cause of spread might enter.

Fig. 4 shows the fraction of lines from the cathode which by-pass the grid and end on the collecting electrode. If the electrons diffuse along the lines of force these relations also give the fractions of charge reaching the collecting electrode. Fig. 5 shows two curves of observed pulse size plotted against the ratio of the fields on the two sides of the grid. Figs. 4 and 5 are in good agreement, particularly at the upper end. For this region the field lines are nearly straight in the chamber. For very low potential difference between grid and collector the field lines have considerable curvature, and agreement is not as good. The pulses are larger than those calculated; this suggests that electrons slip off the field lines and reach the collector. The intercept for zero potential difference between grid and collector is greater than σ . It is seen

in Fig. 5 that a voltage can be chosen for the grid at which it does not collect electrons. The chamber is ordinarily operated under this condition.

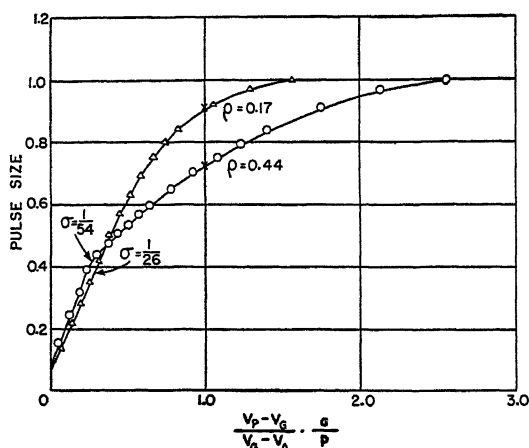


FIG. 5. Observed pulse size, indicating fraction of electrons reaching the collector, is plotted against $\frac{V_P - V_G}{V_G - V_A} \cdot \frac{a}{p}$ (Grids Nos. 2 and 3). The two points marked by crosses were calculated from theory.

(c) Spread of Pulse Size

Table I and Fig. 6 show the results of a typical run with polonium α -particles. The distribution of pulses from a signal generator is included. The distribution of the α -particle pulses is approximately Gaussian having a standard deviation s_1 . Five causes of spread may be noted: (1) thickness of source

TABLE I
PULSE DISTRIBUTIONS FOR α -PARTICLES AND ARTIFICIAL SIGNALS

Pulse analyzer channel No.	α -particles, counts	Artificial pulses, counts
1	0	—
2	2	—
3	2	—
4	2	—
5	4	—
6	4	—
7	8	—
8	8	—
9	8	—
10	10	2
11	20	10
12	48	96
13	64	158
14	116	162
15	124	66
16	116	20
17	48	—
18	14	—
19	2	—

material, (2) straggling of ionization, (3) variation of rise time of the electron pulses, (4) noise of the amplifier, and (5) induced effect of positive ions, as described in the introduction. The last item will be referred to as spread

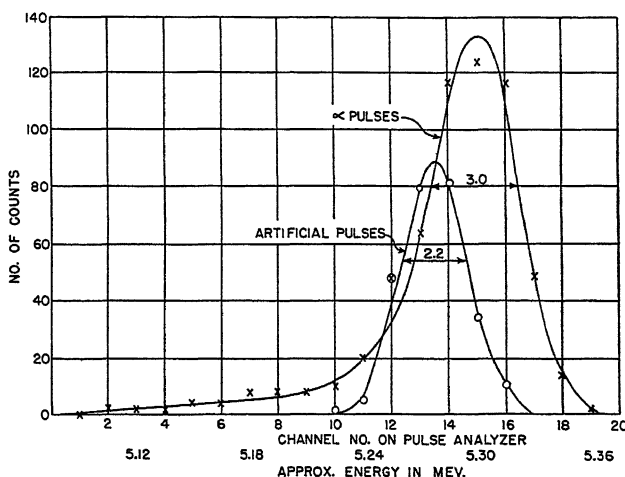


FIG. 6. Typical distributions of pulse sizes for polonium α -particles and artificial pulses (Grid No. 1). One channel spacing on pulse analyzer is equal to 15 kev.

caused by the chamber. The observed standard deviation s_1 is assumed to be associated with the separate standard deviations s_s , s_i , s_r , s_n , and s_c from the above causes respectively by the formula:

$$s_1 = \sqrt{s_s^2 + s_i^2 + s_r^2 + s_n^2 + s_c^2}.$$

In the present experiments s_s , s_i , and s_r always occur together, while s_n can be obtained by using artificial pulses. It is intended to compare the values of s_c obtained from measurements with the various grids with the theory.

(d) Spread of Pulse Size Due to Chamber

The distribution of pulse size will be examined, the effect of orientation of the α -particle track being taken into account. Noting that the induced effect of the positive ions depends on the first power of m (Equation (15)), the idea of center of ionization may be introduced (similar to center of mass in mechanics). The effective range \bar{R} , measured from the source of the α -particle to the center of ionization in the track, is evaluated from the Bragg curve for a single polonium α -particle. The perpendicular distance from the center of ionization to the cathode may be taken as the value of m .

The centers of ionization possess a distribution of m 's for a point source of α -particles at O in Fig. 7, without a collimator, having limits zero and \bar{R} . If N α -particles are emitted isotropically, the number making angles between θ and $\theta + d\theta$ with the normal is

$$\frac{2\pi N \bar{R}^2 \sin \theta d\theta}{4\pi \bar{R}^2} = \frac{N}{2} \sin \theta d\theta = \frac{N dm}{2\bar{R}}.$$

Thus, the distribution of m 's is rectangular (extending from $m = 0$ to $m = \bar{R}$), giving a similar distribution of pulse sizes. The maximum pulse size is that for which $m = 0$ and the minimum is that for which $m = \bar{R}$. In the absence of a

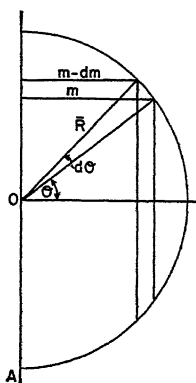


FIG. 7. Source at point O emits α -particles of effective range \bar{R} measured from O to centers of ionization in tracks.

grid the fractional width of the pulse distribution is equal to $\bar{R}/(\text{separation of electrodes})$. Fig. 8 shows pulse distributions observed without a grid. The

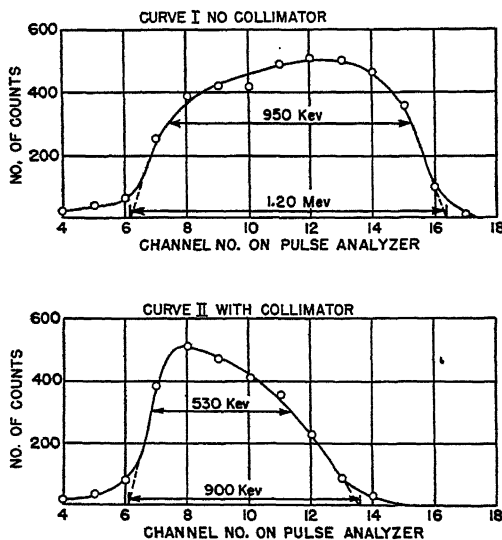


FIG. 8. Observed distributions of α -particle pulses in ionization chamber without a grid. Separation of electrodes was 5.9 cm. Argon pressure was 2 atm. Effect of collimator is shown.

effective range \bar{R} was calculated to be 1.15 cm. in argon at 2 atm., and the separation of electrodes was 5.9 cm. Thus the expected width of the pulse distribution of polonium α -particles without a collimator is $\frac{1.15}{5.9} \times 5.30$ Mev. = 1.0 Mev., in fair agreement with that observed (Curve I, Fig. 8).

When a collimator is used the distribution of pulse size is changed, as shown in Fig. 8. The collimator cuts off the largest pulses, which must come from the tracks making small angles with the cathode, since the induced effect of the positive ions is least for these tracks. The width at 60.7% of the maximum is reduced by the factor $950/530 = 1.8$. The calculated reduction is about 2.5. Since neither distribution is Gaussian, the first being rectangular, and the second nearly triangular, the exact value chosen for the effect of the collimator is rather arbitrary. The standard deviation when the collimator is present is about $\frac{1}{2}$ (530) kev. This may be related to the energy 5.30 Mev. of the polonium α -particle as follows:

$$\text{Standard deviation} = \frac{1}{2} \left(\frac{\bar{R}}{5.9f} \right) 5300 \text{ kev.} = \frac{1}{2} (530) \text{ kev.,}$$

where f is the collimator factor. Using $\bar{R} = 1.15$ cm. it is found that $f = 2.0$. It will be seen later that with a good grid shielding the collector the spread due to the chamber is not as large as other spreads. Therefore the distribution of pulse size with a spread due only to the chamber may be assumed Gaussian, and the collimator factor 2.0 carried over into the corresponding standard deviation.

(e) Shielding by the Grid

The standard deviation of a pulse distribution was estimated by three methods (6, pp. 134-153). (1) The width of the peak was measured at 60.7% of the maximum. (2) The mean square deviation was obtained from the histogram and Sheppard's correction applied. (3) An ogive plot, such as shown in Fig. 9, was used. The last method appeared most reliable. For

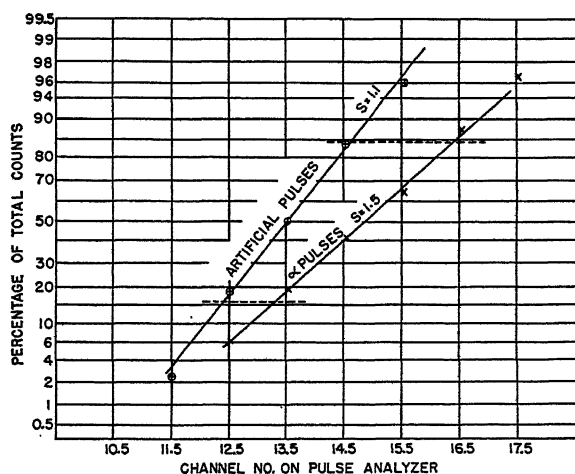


FIG. 9: Ogive plot for estimating standard deviation of a pulse distribution. Standard deviation is half of number of channels between intersections at dotted lines.

the data in Table I the standard deviations are 1.5 and 1.1 channel widths of the pulse analyzer respectively for the α -particles and artificial pulses.

Table II summarizes the experimental results for four different grid arrangements. The inefficiencies σ were calculated from Equation (14). The standard deviations are the averages of five determinations in each case. The small variations in s_n observed for the different experimental arrangements are in approximate agreement with the expected effects of changing the capacity of the chamber.

TABLE II
STANDARD DEVIATIONS IN PULSE DISTRIBUTIONS

s_1 = standard deviation for α -particle pulses

s_2 = standard deviation for artificial pulses

1 channel spacing = 15 kev.

Grid No.	$\sigma \times 10^3$	s_1 , channels	s_2 , channels	$\sqrt{s_1^2 - s_2^2}$, channels	$\sqrt{s_1^2 - s_2^2}$, kev.
1	8.73	1.42	1.08	0.92	13.8
2	18.5	1.66	1.25	1.09	16.4
3	38.3	1.65	1.05	1.27	19.1
4	78.4	1.74	1.10	1.35	20.2
4a	78.4	2.40	1.10	2.13	32.0

Grid No. 1: $r = 6.35 \times 10^{-3}$ cm., $d = 0.091$ cm., $p = 1.43$ cm., $AG = 4.49$ cm., $\bar{R} = 0.77$ cm. (argon at 3 atm. pressure).

Grid No. 2: $r = 6.35 \times 10^{-3}$ cm., $d = 0.091$ cm., $p = 0.67$ cm., $AG = 4.93$ cm., $\bar{R} = 0.77$ cm.

Grid No. 3: $r = 5.34 \times 10^{-3}$ cm. (wire coated with Aquadag), $d = 0.20$ cm., $p = 1.43$ cm., $AG = 4.49$ cm., $\bar{R} = 0.77$ cm.

Grid No. 4: $r = 5.34 \times 10^{-3}$ cm., $d = 0.20$ cm., $p = 0.67$ cm., $AG = 4.93$ cm., $\bar{R} = 0.77$ cm.

Grid No. 4a: same as No. 4 except that $\bar{R} = 1.15$ cm. in argon at 2 atm. pressure.

For the α -particle pulses

$$s_1 = \sqrt{s_s^2 + s_i^2 + s_r^2 + s_n^2 + s_c^2},$$

and for the artificial pulses

$$s_2 = \sqrt{s_n^2}.$$

Therefore

$$\sqrt{s_1^2 - s_2^2} = \sqrt{s_s^2 + s_i^2 + s_r^2 + s_c^2}.$$

The squares of the standard deviations s_s , s_i , and s_r , caused by the thickness of the source, straggling of ionization, and variations in rise time, should form an approximately constant quantity, independent of the grid. The standard deviation s_c caused by the chamber is expected to be

$$s_c = \frac{\sigma \bar{R}}{2f(a + l(1 - \sigma))} 5300 \text{ kev.} = \eta \times 5300 \text{ kev.}$$

from Equation (15) and the effect of the collimator. Owing to the finite extent of the electrodes and the proximity of the wall of the surrounding vessel one might expect s_c to be merely proportional to this expression. Although the constant of proportionality turned out to be approximately unity, at first proportionality but not equality was assumed. The measured quantities $\sqrt{s_1^2 - s_2^2}$ given in Table II were set equal to $\sqrt{a + b\eta^2}$. The best values of the parameters a and b , assumed to be constants, were obtained by the method of least squares, with the following result:

$$\sqrt{a} = \sqrt{s_s^2 + s_t^2 + s_r^2} = 14.3 \text{ kev.}$$

and

$$\sqrt{b} = 6030 \text{ kev.}$$

Table III shows that a satisfactory fit of all experimental data was obtained. The predicted shielding by the grid is verified, as shown by $\sqrt{b} = 6030 \text{ kev.}$ being approximately equal to the expected 5300 kev. or alternatively by the agreement of Columns 5 and 6. The discrepancy involves f directly, which is difficult to estimate owing to the asymmetry of the pulse distribution, as pointed out above.

TABLE III
STANDARD DEVIATIONS CAUSED BY CHAMBER

Grid No.	$\eta \times 10^4$	$\sqrt{s_1^2 - s_2^2}$, kev. (observed)	$\sqrt{s_s^2 + s_t^2 + s_r^2 + s_c^2}$, kev. (least squares)	s_c , kev. (least squares)	$\eta \times 5300 \text{ kev.}$ (theory)
1	3.74	13.8	14.5	2.2	2.0
2	7.19	16.4	15.0	4.3	3.8
3	16.25	19.1	17.3	9.8	8.6
4	30.3	20.2	23.2	18.3	16.1
4a	45.3	32.0	30.8	27.3	24.0

The following consideration shows that the standard deviation s_r is relatively small. This cause of spread in pulse size is the variation in electron collection times due to different orientations of the tracks of the α -particles. The band width of the amplifier used was defined by the usual two time constants of smoothing and differentiation, which were adjusted to be 5 and 50 $\mu\text{sec.}$ respectively. The collection time is not known with certainty, but a rough measurement was made by decreasing the time constants of the amplifier to 1 and 10 $\mu\text{sec.}$ There was no appreciable drop in pulse amplitude, which indicates a collection time of about 1 $\mu\text{sec.}$ With time constants of 5 and 50 $\mu\text{sec.}$ a variation in collection time between zero and 2 $\mu\text{sec.}$ would introduce a *total* spread of only 4 kev., which is much smaller than the spreads introduced by source thickness and ionization straggling.

(f) Limitations on Standard Deviations

The standard deviation from all causes on the pulse distribution of polonium α -particles was found to be as low as 22 kev. when a suitable grid was placed

in front of the electron collector. The corresponding width of the line at half-maximum was 50 kev. or about 1% of the energy of the polonium α -particle. The standard deviation caused by the induced effect of the positive ions was found to be as low as 2 kev. when a carefully designed grid was used to shield the collector. This cause of spread is now negligible, and further decrease in line width can be effected only by attention to other causes.

Through the use of artificial pulses the standard deviation caused by noise in the head amplifier was found to be about 17 kev. With existing tubes not much improvement can be expected here. The standard deviation caused by thickness of source, straggling of ionization, and variations in rise time of the pulses was 14 kev. From Fano's theory (2) an estimate of the standard deviation caused by straggling of ionization is about 8 kev. With the best conditions an over-all standard deviation of about 18 kev. may perhaps be attained. This corresponds to a width of 45 kev. at half-maximum for the polonium α -particle line.

Acknowledgments

We wish to thank Dr. B. W. Sargent and Mr. G. C. Hanna for their assistance and criticisms in preparing this paper for publication.

References

1. CRANSHAW, T. E. and HARVEY, J. A. Can. J. Research, A, 26 : 243. 1948.
2. FANO, U. Phys. Rev. 72 : 26. 1947.
3. FREUNDLICH, H. F., HINCKS, E. P., and OZEROFF, W. J. Rev. Sci. Instruments, 18 : 90. 1947.
4. FRISCH, O. R. Unpublished report, BR-49. Isotope analysis of uranium samples by means of their α -ray groups. British Atomic Energy Project.
5. SHOTKEY, W. (Part IIA) and POHLHAUSEN, K. (Part IIB). Theory of functions as applied to engineering problems. Edited by R. Rothe, F. Ollendorff, and K. Pohlhausen. Technology Press, Massachusetts Institute of Technology, Cambridge, Mass., U.S.A.
6. YULE, G. U. and KENDALL, M. G. An introduction to the theory of statistics. Charles Griffin & Co. Ltd., London, England. 1940.

Canadian Journal of Research

Issued by THE NATIONAL RESEARCH COUNCIL OF CANADA

VOL. 27, SEC. A.

NOVEMBER, 1949

NUMBER 6

PERMEABILITY STUDIES

IV. SURFACE AREA MEASUREMENTS OF ZINC OXIDE AND POTASSIUM CHLORIDE POWDERS¹

BY J. C. ARNELL

Abstract

The use of the modified Kozeny equation for the measurement of the specific surfaces of fine powders has been extended to include a number of standard zinc oxides and a sample of potassium chloride. The specific surfaces of the zinc oxides had been measured by 10 other methods, and the data are included for comparison. Comparative low temperature adsorption data for the potassium chloride are also given. Satisfactory agreement with other methods was found.

Introduction

In several papers published within the past three years (1, 2, 3, 7), a method has been discussed for the determination of the specific surface of very fine powders by gas-permeability methods. This method depends on the use of a modified Kozeny equation, which contains an additional term to correct for 'slip'. This equation has been found to be of the greatest use in the form:

$$G = \frac{Ah \epsilon^2 \rho_1}{kLS_v(1 - \epsilon)} \left[\frac{\epsilon \rho_{H_2O} \bar{P}}{\eta S_v(1 - \epsilon)} + \frac{8}{3} \sqrt{\frac{2R_0T}{\pi M}} \delta k_0 \right], \quad (1)$$

where G = rate of gas flow in grams per second,

A = cross-sectional area of the bed in square centimeters,

h = pressure head in centimeters of mercury,

ϵ = volume of pore space per unit volume (porosity),

$\rho_1 = \rho/P$ = density of the gas at unit pressure,

k = Kozeny's constant, which is approximately equal to 5,

L = length of the bed in centimeters,

S_v = specific surface of the powder in square centimeters per cubic centimeter,

¹ Manuscript received July 8, 1949.

Contribution from the Defence Research Chemical Laboratories, Ottawa, Canada. Also issued as D.R.C.L. Report No. 32.

ρ_{Hg} = density of mercury in grams per cubic centimeter,

g = acceleration due to gravity in centimeters per second per second,

$\bar{P} = (p_1 + p_2)/2$ = mean pressure in centimeters of mercury,

η = viscosity of the gas in poises,

R_0 = gas constant,

T = absolute temperature,

M = molecular weight of the gas,

δ = variable factor, having a value of approximately 0.9, and

k_0 = shape factor, whose value generally lies between 2 and 3 (5).

This equation has been tested against the data obtained from the flow of air through beds of finely ground quartz, inorganic pigment powders, and carbon blacks, and found to give values for the surface areas that showed good agreement with the values obtained by the use of other methods.

In this paper, the method has been applied to four samples of zinc oxide supplied by the New Jersey Zinc Company (of Pa.), Palmerton, Pennsylvania, U.S.A. About 15 years ago these samples were set aside for use in particle size investigations and their surface areas have been measured by many different methods in the intervening years. It was therefore of great interest to compare the results given by Equation (1) with the previous data.

Apparatus and Technique

The apparatus used for measuring the air flow through the different beds of zinc oxide has been described in detail in a previous paper in this series (2). The air flow through a bed of powder was measured at five different mean pressures, which were approximately 20, 30, 40, 50, and 65 cm. of mercury. The mass flows were then plotted against the corresponding mean pressures and the equation of the resultant straight line determined for each bed. These equations had the form:

$$G = B\bar{P} + C. \quad (2)$$

The specific surface was then calculated in two different ways. In the first method, the slope of the line, B , was equated to the first term on the right-hand side of Equation (1), which is equivalent to the original Kozeny equation, and in the second method, the intercept, C , was equated to the pressure independent term of the modified equation.

Experimental Results

The specific surfaces were calculated by the two methods from the data obtained on four beds of each sample of zinc oxide. The experimental results

are listed in Table I, together with the porosities of the beds calculated using a zinc oxide density of 5.67 (4). The areas in square meters per gram have been calculated by dividing the specific surface by the density and are also included for comparison.

TABLE I
SURFACE AREAS OF ZINC OXIDE POWDERS

Sample	Porosity	Specific surface, m ² /cc.	
		Slope (B)	Intercept (C)
Kadox Black Label-15 F1601	0.698	38.9	47.9
	0.660	43.0	45.2
	0.706	50.9	43.6
	0.695	46.4	40.8
		44.8	44.4
		7.9 m ² /gm.	7.8 m ² /gm.
XX Red-72 K1602	0.647	36.0	37.0
	0.630	33.8	33.9
	0.578	29.7	34.9
	0.617	38.1	39.1
		34.4	36.2
		6.1 m ² /gm.	6.4 m ² /gm.
XX Red-78 G1603	0.569	16.4	15.5
	0.557	15.0	14.3
	0.570	16.3	16.2
	0.536	16.6	16.6
		16.1	15.7
		2.8 m ² /gm.	2.8 m ² /gm.
Reheated Superfine KH 1604	0.458	3.6	4.0
	0.432	4.3	5.0
	0.424	3.7	4.2
	0.468	3.7	3.8
		3.9	4.3
		0.6 ₉ m ² /gm.	0.7 ₆ m ² /gm.

In addition to the above work, the specific surface of a sample of potassium chloride was measured by this method. The details of the preparation of the sample and the low temperature adsorption data have been published elsewhere (10). In brief, the sample was prepared by atomizing a solution of potassium chloride and collecting the resulting aerosol electrostatically. The experimental results are listed in Table II, together with the BET surface areas determined from low temperature adsorption isotherms (8).

TABLE II
SURFACE AREA OF FINELY DIVIDED POTASSIUM CHLORIDE

Permeability method	Specific surface, m ² /cc.	
Porosity	Slope (B)	Intercept (C)
0.481	4.1 ₂	4.0 ₈
0.473	4.0 ₁	4.0 ₅
0.471	3.5 ₄	3.5 ₂
	3.8 ₉	3.8 ₈
	1.9 ₆ m ² /gm.	1.9 ₆ m ² /gm.

Low temperature adsorption method (BET) (after Keenan)

Gas	Surface area, m ² /gm.			
	83° K.	84° K.	85° K.	90° K.
Nitrogen	—	2.19	2.21	2.21
Argon	2.83	—	2.92	2.79
Oxygen	—	—	2.76	2.63

Discussion

Through the kindness of Dr. C. E. Barnett of the New Jersey Zinc Company, the following table (Table III) summarizing all the surface area data obtained with the zinc oxide samples was made available for inclusion here.

Some of these data have been published previously (6, 8, 9), but much of it is new. The sedimentation results were measured by A. E. Jacobsen of the National Lead Company, Titanium Pigments Division. The electron microscope, turbidimetric, and infrared transmission measurements were made by the New Jersey Zinc Company, while the air permeability data using the single Kozeny equation were obtained by both the New Jersey Zinc Company and the National Bureau of Standards, Washington.

In general the results from Equation (1) are in fair agreement with those obtained from liquid permeability measurements; this indicates that the modified Kozeny equation adequately compensates for the 'slip' that occurs with gas flow through beds of very fine powders. These results also agree reasonably well with the gas adsorption data. Some of the other methods have been known in general to give low values for the surface area, and this is borne out here. With the larger particles, as in KH 1604, much better agreement is obtained between methods, owing probably to such factors as the virtual disappearance of the 'slip' factor.

The data on the potassium chloride sample are included as another example of the satisfactory agreement between the surface area measurements obtained by low temperature gas adsorption and air permeability corrected for slip.

TABLE III
SURFACE AREAS OF ZINC OXIDE PIGMENTS USING DIFFERENT METHODS

	Light micro- scope	Electron micro- scope	Liquid adsorp- tion	Sedimen- tation	Permeability			Gas adsorp- tion	Dark field count	Turbidi- meter	Infra- red trans- mission
					Liquid	Air					
						Kozeny equa- tion	Equation (1) Table II				
Kadox Black Label-15 F-1601											
d_1	0.15	0.10	—	—	—	—	—	—	—	0.18	—
d_3	0.28	0.18	0.20	0.30	0.12	0.26	0.14	0.11	—	—	—
$S, m^2/gm.$	3.8	6.0	5.4	3.5	8.9	4.1	7.8	9.5	—	—	—
D	0.21	0.14	—	—	—	—	—	—	0.14	—	—
$N \times 10^{10}$	2042	—	—	—	—	—	—	—	7257	—	—
d_4	0.37	—	—	—	—	—	—	—	—	—	0.27 0.34
XX Red-72 K-1602											
d_1	0.19	0.12	—	—	—	—	—	—	—	0.23	—
d_3	0.34	0.23	0.25	0.37	0.15	0.32	0.17	0.12	—	—	—
$S, m^2/gm.$	3.1	4.6	4.3	2.9	7.2	3.3	6.2	8.8	—	—	—
D	0.25	0.15	—	—	—	—	—	—	0.16	—	—
$N \times 10^{10}$	1139	—	—	—	—	—	—	—	4200	—	—
d_4	0.42	—	—	—	—	—	—	—	—	—	0.44
XX Red-78 G-1603											
d_1	0.30	0.25	—	—	—	—	—	—	—	0.36	—
d_3	0.79	0.48	0.56	0.76	0.25	$\begin{cases} 0.62 \\ 0.62 \end{cases}$	0.38	0.27	—	—	—
$S, m^2/gm.$	1.3	2.2	1.9	1.4	4.3	NBS-1.7 NJZ-1.7	2.8	3.9	—	—	—
D	0.49	0.35	—	—	—	—	—	—	0.26	—	—
$N \times 10^{10}$	153	—	—	—	—	—	—	—	1076	—	—
d_4	1.1	—	—	—	—	—	—	—	—	—	0.54
Reheated Superfine KH-1604											
d_1	1.0	—	—	—	—	—	—	—	—	—	—
d_3	1.9	—	5.3	2.1	1.25	1.63	1.5	1.61	—	—	—
$S, m^2/gm.$	0.6	—	0.2	0.5	0.85	0.65	0.71	0.66	—	—	—
D	1.4	—	—	—	—	—	—	—	0.82	—	—
$N \times 10^{10}$	6.6	—	—	—	—	—	—	—	32	—	—
d_4	2.2	—	—	—	—	—	—	—	—	—	—

NOTE: d_1 = average diameter ($\Sigma nd/\Sigma n$) in microns,
 d_3 = mean volume-surface diameter ($\Sigma nd^3/\Sigma nd^2$) in microns,
 S = surface area in square meters per gram,
 D = mean volume diameter ($\sqrt[3]{\Sigma nd^3/\Sigma n}$) in microns,
 N = number of particles per gram and given by $N = 1/\mu D^3$, where μ = specific gravity,
 d_4 = weight mean diameter ($\Sigma nd^4/\Sigma nd^3$) in microns.
NBS - National Bureau of Standards.
NJZ - New Jersey Zinc.

Acknowledgments

The author would like to express his thanks to Dr. C. E. Barnett and the New Jersey Zinc Company (of Pa.), Palmerton, Pennsylvania, for supplying the zinc oxide samples and their interest and help in making available the existing surface area data, and to Dr. A. G. Keenan of the National Research Council of Canada for supplying the potassium chloride sample.

References

1. ARNELL, J. C. *Can. J. Research, A*, 24 : 103. 1946.
2. ARNELL, J. C. *Can. J. Research, A*, 25 : 191. 1947.
3. ARNELL, J. C. and HENNEBERRY, G. O. *Can. J. Research, A*, 26 : 29. 1948.
4. BARNETT, C. E. Private communication.
5. CARMAN, P. C. *Trans. Inst. Chem. Engrs. (London)*, 15 : 150. 1937.
6. CARMAN, P. C. Symposium on new methods for particle size determination in the sub-sieve range, p. 24. *Am. Soc. Testing Materials*. 1941.
7. CARMAN, P. C. and ARNELL, J. C. *Can. J. Research, A*, 26 : 128. 1948.
8. EMMETT, P. H. Symposium on new methods for particle size determination in the sub-sieve range, p. 95. *Am. Soc. Testing Materials*. 1941.
9. EWING, W. W. *J. Am. Chem. Soc.* 61 : 1317. 1939.
10. KEENAN, A. G. In press.

THE SPECTRUM OF ATOMIC OXYGEN IN A HIGH CURRENT A-C. DISCHARGE¹

BY W. PETRIE, P. A. MONAGHAN,² P. A. DOLAN³

Abstract

The atomic oxygen spectrum has been produced in an a-c. discharge of current densities between 50 m.a. per cm² and 1.3 amp. per cm², and lines arising from the lower permitted levels of the atom are present in this spectrum. In view of the fact that the discharge is excited chiefly by electron collisions, and also that the aurora appears to be the result of collisional processes, the auroral spectrum should be examined carefully to determine whether or not these same permitted atomic oxygen lines are present.

Introduction

There is some doubt regarding the appearance of atomic oxygen lines in the auroral spectrum. A number of lines that originate from the lower levels of the atom fall in the near infrared, and this region of the auroral spectrum has not been too well resolved. Since $N\frac{1}{2}$ bands are features of the spectrum, evidently sufficient energy is available to populate the lower levels of the oxygen atom. There is much evidence that the auroral radiations are the result of collisional processes, and it seemed worthwhile to examine the spectrum of oxygen in an a-c. discharge in which the mechanism of excitation is chiefly electron collision. If lines from the lower levels of the oxygen atom are present, we might expect these same lines to appear in the auroral spectrum. Discharge spectra of oxygen have been studied by a number of workers including Frerichs (1), Hopfield (2), and Kvifte and Vegard (3). These spectra, however, only partially answer our question. Several of the lines in which we are interested are listed in the measures of Frerichs (1) and Kvifte and Vegard (3), but the former spectra are chiefly of the ionized oxygen atom, and those studied by Kvifte and Vegard (3) do not cover the spectral region in which a number of the lower level lines fall.

Description of the Apparatus

The discharge tube was 69 cm. long with an inside diameter of 1.4 cm., and the tube was surrounded with a water jacket of diameter 2.5 cm. The ends of the tube were flared out to 6 cm. diameter, and disk-shaped aluminum electrodes 12 cm. in diameter and 0.9 cm. thick were waxed to each end. A 1.4 cm. diameter hole was drilled through one electrode and a quartz window waxed to the outside, thus sealing the discharge chamber. In order to cool the ends of the tube and the electrodes during operation of the discharge, both electrodes were milled in radially to a distance of 2.5 cm. and made

¹ Manuscript received May 7, 1949.

Contribution from the Department of Physics, University of Saskatchewan, Saskatoon, Sask.

² Now with the Dept. of Mines and Resources.

³ Now attending the University of British Columbia.

waterproof by means of a rubber ring attached to the periphery. Inlet and outlet water cocks were attached to each electrode. The discharge chamber was evacuated by means of a rotary oil pump, and the discharge operated from a power supply that is rated at 2 kva. Two prism spectrographs were used to photograph the spectra, one a medium quartz Hilger instrument, and the other a spectrograph constructed in the Physics Shop at the University of Saskatchewan.

One liter of high purity oxygen was purchased from the Matheson Company of New Jersey, and a supply was also obtained by heating a flask containing potassium permanganate.

Discussion of the Spectra

A number of spectra were photographed in the region 3500 to 9000 angstroms, after the discharge tube had been flushed several times with the pure oxygen. A variety of voltages and currents were used, but the majority of the spectra were photographed when the discharge current density was around 50 m.a. per cm². The pressure was not measured, but was estimated to be several millimeters of mercury.

It is not our purpose to give a complete discussion of the spectra; in fact, the dispersion is too low for a careful analysis. However, we wish to point out that lines from the lower levels of the oxygen atom are certainly present in these spectra, as well as a few weak lines from singly ionized atoms.

It is worthwhile to compute the theoretical intensities of the low level lines if these are to be searched for in the auroral spectrum. The intensity of a spectral line from a source in thermodynamic equilibrium may be expressed in several ways. In terms of the Einstein transition coefficient the intensity of a spectral line is $I = N A h \nu$, where N is the number of atoms in the upper level from which the line arises, and A is the Einstein transition coefficient appropriate to the level involved. The intensity of a spectral line may also be expressed in the form $I = \frac{64\pi^4\nu^4}{3c^3} \frac{N}{\omega} [(a|P|b)]^2$, where ω is the statistical weight of the level from which the transition arises. This expression is similar to the one that gives the radiation from the classical oscillator, except for the factors ω and $[(a|P|b)]^2$; the latter is the square of the average electric moment for the levels involved. This factor is an integral involving wave functions and may be reduced to a product $\frac{e^2 a^2}{4l^2 - 1} s \rho^2$, where a is the radius of the first Bohr orbit, l is the larger of the initial or final values of the orbital quantum number of the "jumping electron" associated with the two electron configurations involved in the transition, s is the theoretical line strength, and ρ is the radial quantum integral, i.e., $\rho = \int R_{nl} R_{n'l'} r^3 dr$, where R_{nl} and $R_{n'l'}$ are the radial wave functions associated with the two electron configurations. Since we are dealing with the radiation from a source in thermodynamic equilibrium, the number of atoms in any level in terms of the

number in the ground level is expressed by the Boltzmann relation, i.e., $N = N_0 \frac{\omega}{\omega_0} e^{-\chi/kT}$, where N_0 is the number of atoms in the ground level, ω_0 is the statistical weight of the ground level, and χ the excitation potential of the level from which the transition arises. In these expressions, ν , c , e , h , k , and T have their usual meanings.

Then

$$I = NAh\nu = \frac{64\pi^4\nu^4}{3c^3} \frac{N_0}{\omega_0} e^{-\chi/kT} \frac{e^2 a^2}{4l^2 - 1} s\rho^2. \quad (1)$$

The calculation of ρ requires a knowledge of the radial wave functions. Slater (6) has shown how to obtain approximate hydrogenlike radial wave functions, and Menzel and Aller (4) have shown how to use these functions in the calculation of ρ . Using the Slater method, the integral for ρ becomes

$$\rho^2 = \left[\frac{2(Z - \sigma_1)}{n_1} \right]^{2n_1 + 1} \left[\frac{2(Z - \sigma_2)}{n_2} \right]^{2n_2 + 1} \frac{1}{\Gamma(2n_1)} \frac{1}{\Gamma(2n_2)} \left[\frac{\Gamma(n_1 + n_2 + 2)}{\left\{ \left(\frac{Z - \sigma_1}{n_1} \right) + \left(\frac{Z - \sigma_2}{n_2} \right) \right\}^{n_1 + n_2 + 2}} \right]^2. \quad (2)$$

In this formula Z is the atomic number, σ_1 and σ_2 are the screening constants for the two electron configurations involved in the transition, and n_1 and n_2 are the effective quantum numbers of the "jumping electron" in each electron configuration. The quantities σ and n are formed from the information given in Slater's paper. We have computed ρ values from Equation (2), and the results are given in Table I.

TABLE I
THEORETICAL OXYGEN LINE INTENSITIES

Transition	J'	J	λ	χ_a	s	l	ρ	I	M.I.T.
$2p^33s(^5S^0) - 2p^33p(^5P)$	2	3	7772	10.69	7.1	1	6	1.0	1.0
$2p^33s(^3S^0) - 2p^33p(^3P)$	1	2	8446	10.94	5.0	1	6	0.24	2.0
$2p^33p(^5P) - 2p^34s(^5S^0)$	3	2	11300	11.79	7.1	1	4.7	0.006	—
$2p^33p(^3P) - 2p^34s(^3S^0)$	2	1	13163	11.88	5.0	1	4.7	0.002	—
$2p^33p(^5P) - 2p^33d(^5D^0)$	3	4	9266	12.03	54.0	2	5.8	0.015	0.03
$2p^33p(^3P) - 2p^33d(^3D^0)$	2	3	7987	12.04	4.2	2	5.8	0.002	0.05
$2p^33s(^5S^0) - 2p^34p(^5P)$	2	3	3947	12.23	7.1	1	4.7	0.10	0.3
$2p^33s(^3S^0) - 2p^34p(^3P)$	1	2	4368	12.30	5.0	1	4.7	0.04	1.0
$2p^33p(^3P) - 2p^33s(^3S^0)$	2	3	7995	12.54	4.2	1	6	0.003	0.05
$2p^33p(^5P) - 2p^35s(^5S^0)$	3	2	6456	12.61	7.1	1	2.9	0.002	0.5
$2p^33p(^3P) - 2p^35s(^3S^0)$	2	1	7254	12.64	5.0	1	2.9	0.0008	0.015
$2p^33p(^5P) - 2p^36s(^5S^0)$	3	2	5437	12.96	7.1	1	2.4	0.0009	0.2

The method of obtaining the theoretical line strength s has been discussed by Petrie (5). Using Equation (1) the intensities of the lines arising from the lower permitted levels of the oxygen atom have been computed and are

listed in Table I, along with other relevant data. Only the strongest line in each multiplet is given. The intensity of the line $\lambda 7772$ which arises from the lowest excited permitted level is arbitrarily made unity, and the other intensities are in terms of the intensity of this line. This manner of expressing the intensities eliminates the necessity of including the constant factor $\frac{64\pi^4 N_0}{3c^3 \omega_0} e^2 a^2$. An explanation of Table I follows.

- Column 1. The electron configurations and terms from which the line arises. The configuration of lower energy is written first.
2. The J values of the two levels from which the line arises.
 3. The wave length of the line, in angstroms.
 4. The excitation potential in electron volts of the upper level involved in the production of the line.
 5. The theoretical line strength s .
 6. The l value of the "jumping electron" associated with each transition.
 7. The ρ values for each transition.
 8. The calculated line intensity.
 9. Intensities listed in the M.I.T. wave length tables. The intensities in Columns 7 and 8 are in terms of the intensity of the line $\lambda 7772$.

Concluding Remarks

All the lines listed in Table I in the region 3500 to 9000 angstroms appear in our spectra. Hence, a careful search should be made of the auroral spectrum to determine whether or not these same lines are present. Vegard (7) has listed the line $\lambda 4368$ as being present in the auroral spectrum. Unless there is something very strange about the excitation mechanism that operates in the upper atmosphere, other lines listed in Table I should be features of this spectrum. It is hoped that a new auroral spectrograph constructed at the University of Saskatchewan will settle the question of the appearance or non-appearance of these oxygen lines. It is not expected that the intensities of the oxygen lines in discharge spectra or in the auroral spectrum will agree exactly with the theoretical intensities that have been calculated. In discharge tubes and in the upper atmosphere there are departures from thermal equilibrium. Nevertheless, the theoretical intensities will be a useful guide when searching for these lines in the auroral spectrum.

Acknowledgments

The authors wish to thank Prof. E. L. Harrington for his generous assistance during the construction of the discharge tube. This investigation was supported by a grant from the National Research Council of Canada.

References

1. FRERICHs, R. Phys. Rev. 34 : 1239. 1929.
2. HOPFIELD, J. J. Phys. Rev. 37 : 160. 1931.
3. KVIFTE, G. and VEGARD, L. Geofys. Publikasjoner. Norske Videnskaps-Akad. Oslo, 17 : No. 1. 1947.
4. MENZEL, D. H. and ALLER, L. H. Astrophys. J. 94 : 436. 1941.
5. PETRIE, W. Can. J. Research, A, 25 : 293. 1947.
6. SLATER, J. C. Phys. Rev. 36 : 57. 1930.
7. VEGARD, L. Geofys. Publikasjoner. Norske Videnskaps-Akad. Oslo, 13 : No. 5. 1941.

DIELECTRIC PROPERTIES OF SOME ANIMAL TISSUES AT METER AND CENTIMETER WAVE LENGTHS¹

BY E. R. LAIRD AND K. FERGUSON

Abstract

Measurements have been made of the dielectric constant and the absorption coefficient of some animal tissues at λ 1.72 m. by the Drude-Cooledge method, and at λ 9.5 cm. and λ 3.2 cm. by the reflection with change of phase method as developed by von Hippel. The dielectric constant of beef fat changed from about 9.5 at λ 1.72 m. to 3.5 at λ 3.2 cm., that of bone remained about constant between 6.5 and 7, that of beef bone marrow was reduced from 20 to 3.7, and that of frog muscle from 135 to 35. The absorption coefficient increased from 0.026 to 0.79 per cm. for fat, from 0.0028 to 0.56 for bone, from 0.028 to 0.9 for bone marrow, and from 0.08 to between 5 and 6 for frog muscle in the same range. Uncertainties of measurement and variation between samples are in general large. The dielectric constant found for muscle at λ 1.72 cm. is higher than a value given by Osswald at λ 3 m.

Introduction

The work reported here was undertaken as part of a project, proposed by Dr. R. C. Dearle, to examine the biological effects of electromagnetic radiation of wave length less than 2 m. for possible clinical application. Relative heating effects in the special case of the use of condenser fields had already been studied, and McLennan and Burton (9, 10) had also examined this case theoretically, and given the relation connecting conductivity, dielectric constant, and frequency for optimum effect. Schereschewsky (13) made some measurements on dielectric constant at about 2 m. and Osswald (11) on both dielectric constant and conductivity of a number of animal tissues at 3 m. At shorter wave lengths the direct use of radiation becomes possible, and for this case also data on the dielectric constant and either the conductivity or absorption coefficient are desirable. Such measurements have now been made at wave lengths of approximately 1.72 m., 9.5 cm., and 3.2 cm. on muscle, fat, bone, and bone marrow. Some observations have also been made on liver and on water, and especially at λ 1.7 m. any appearance of nonheating effects was noted.

Method and Equipment

I. λ 1.72 m.

A consideration of the material to be used, and simplicity of construction, led to the choice of the Drude-Cooledge (5) method modified to suit present equipment. This method has been used in more recent years by Slätis (14) and found satisfactory for materials having an absorption index as high as 0.25. Its use has been criticized by Abadie (1) as unsatisfactory for highly absorbing substances, and a study showed that at times corrections should be made to the previously used formulae.

¹ Manuscript received June 28, 1949.

Contribution from the Department of Physics, The University of Western Ontario, London, Ont. This work was supported in part by the Ontario Cancer Treatment and Research Foundation.

The method uses a Lecher wire system, as in Fig. 1. B is a fixed bridge to which a copper-constantan thermocouple is attached. B' is a sliding bridge, and at A is a glass container with sealed-in platinum electrodes for holding

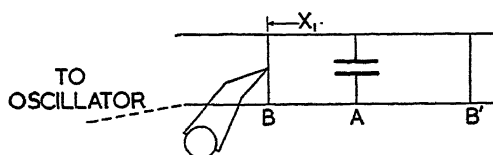


FIG. 1.

the materials to be used. The method of direct coupling to a lossy line from the continuous wave oscillator was tried, and seemed satisfactory. The bridge at B' is adjusted for a maximum response of the galvanometer, x_1 , x_2 , and the galvanometer deflection G_2 are measured, B' is again adjusted with the container removed, and the galvanometer deflection read, G_1 . The logarithmic decrement of the circuit without the container, δ , and the constants of the container-condenser, may be determined separately. From these data the dielectric constant and absorption coefficient of the material may be found.

Theory shows, see appendix, that when the conductivity of the material being tested is low, resonance occurs when

$$(1) \quad \cot \theta_1 + \cot \theta_2 = \omega CZ = \omega Z(C' + \epsilon C_0),$$

where $\theta_1 = \frac{2\pi x_1}{\lambda}$, $\theta_2 = \frac{2\pi x_2}{\lambda}$, Z is the characteristic impedance of the line,

and C is the capacity across it at A . Following Drude, one may put C equal to $C' + \epsilon C_0$, where C' is the capacity due to the wires external to the container, C_0 is the internal capacity with air as medium, and ϵ is the dielectric constant of the material being used.

The theory shows also that for low conductivity the index of absorption is given by

$$(2) \quad \frac{4\kappa}{1 - \kappa^2} = \frac{C' + \epsilon C_0}{\epsilon C_0} \cdot \frac{\delta}{\cot \theta_1 + \cot \theta_2} \left[(1 + \cot^2 \theta_1) \sqrt{\frac{G_1}{G_2}} - \frac{2}{\lambda} \left(\frac{x_1}{\sin^2 \theta_1} + \frac{x_2}{\sin^2 \theta_2} \right) \right]$$

The absorption coefficient 2α is $\frac{4\pi n \kappa}{\lambda}$.

The oscillator was an R.C.A.F. A.S.V. transmitter modified for continuous wave transmission. It was used at a frequency close to 175 Mc. per sec., and with constant voltage on the tube the output remained desirably constant.

The Lecher wires were of tinned copper 1.23 mm. diameter, centers 1.14 cm. apart. The sliding bridge B' was a silver disk 2.4 cm. diameter, with slots fitting closely over the Lecher wires, and could be held in position by the backing of a heavier brass bridge. The positions of the bridges and the

container were read either on a meter stick that could be laid for the purpose on supports close to the wires, or by means of a cathetometer fixed to be used horizontally at a distance of about 3 m. A correction was applied to the observed position of the thermocouple bridge B . Its effective position was taken to be at the distance $\lambda/2$ from the resonance position of the bridge B' when no container was present. $\lambda/2$ was taken as the distance between the first and second resonance settings of B' , and could also be checked by a frequency meter. The correction to the position of B varied between 0.1 and 0.5 cm. for different thermocouples. It will be noted that this correction assumes that the impedance of B' is negligible.

The galvanometer zero was taken as that reading obtained when a short was put across the Lecher wires at a distance $\lambda/4$ from the bridge B . In this case the impedance looking into the circuit tends to infinity, and the current through the thermocouple bridge is a minimum. The use of this reading as a galvanometer zero assumes that either there is no constant phase relation between this bridge current and the additional current flowing when the circuit is at resonance, or that they are about $\pi/2$ apart in phase. The high frequency resistance of the bridge was computed to be about 0.13 ohm, and an estimate of the inductive reactance was 8 ohms. The additional current flowing at resonance will be in phase with the voltage, so the assumption mentioned appears justified. Values of this order for the bridge impedance also account for the observed difference between the bridge position and what has been called its effective position.

Equation (2) assumes that there is the same voltage at B when each of the two maximum deflections is observed. An estimate of the change in admittance at B gave in the extreme case 10%. The oscillator was connected to the Lecher wire system through lossy cable as stated above. Some tests were made on the effect of altering the point of connection, and it was found to be negligible. However, in the case of muscle it was considered that G_1/G_2 might be small by 10%.

There was the further experimental source of error in obtaining G_2 owing to changes in room temperature. The thermocouple bridge was protected by a small mica jacket, and the second junction was in the shielded cable leading to the galvanometer, but the heavy Lecher wires were unprotected, and at times this caused great difficulty.

Equation (1) shows that for a constant value of ωZ there should be a linear relation between ϵ and the sum of the cotangents, $\cot \theta_1 + \cot \theta_2$. This was initially tested by measuring x_1 and x_2 at resonance with the materials air, benzene, ethyl ether, 50% acetone, and water in the container, and was found to hold. The constants of the container finally used were found from observations in which air, benzene, ethyl ether, and water were the standards, and the results were $C_0 = 0.0315$ and $C' = 0.075$ e.s.u. This container had an internal diameter of 5 mm. The ends of the platinum leads were hammered out to make plates about 3 mm. in diameter, and the tube wall was slightly

expanded at this point so that they were separated by 5 mm. Fig. 2 shows the general form. The logarithmic decrement was determined at intervals from a resonance curve, and was found to remain substantially constant at

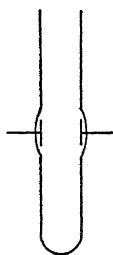


FIG. 2.

0.0070 ± 0.0001 . The breadth of the resonance curve at the second maximum was, within experimental error, double that at the first maximum; this indicated that the damping due to the bridges was relatively negligible. The computed value for a circuit of the given dimensions of copper is 0.0044, for one of tin 0.0112.

These constants, δ , C' , and C_0 , along with the observations on the test material, suffice to determine ϵ and κ in many cases. For materials of higher conductivity Equations (1) and (2) require correction terms that depend on R , the resistance of the test material in the container-condenser (see Equations (7), (8), and (10) of the Appendix). The value of R was estimated from the value of κ given by (2). This estimate was then used in the complete formulae. As the maximum correction was not more than 5%, a second approximation was not deemed necessary.

II. λ 9.5 cm. and λ 3.2 cm.

The method used at these two wave lengths was essentially that described by Roberts and von Hippel (12) and is indicated by the block diagram—Fig. 3.

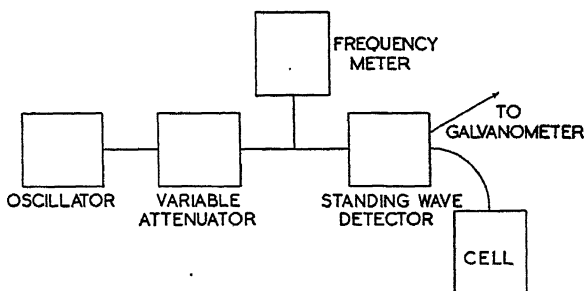


FIG. 3.

At λ 9.5 cm. the source was a Sutton tube, and was connected to a coaxial system. The cell had internal diameter 7 mm., the axis 2.94 mm., and was rather inconveniently small. At λ 3.2 cm. the source was a Shepard tube, and it fed into service size wave guide. The right angle bend was provided by a silver plated flexible piece of wave guide. In both cases the experiment consists in determining the depth d of the test material, the position of

the minimum on the slotted line, the ratio E_{\min}/E_{\max} of the field, and the frequency. Theory (L.C.) shows that

$$(3) \quad \frac{\tanh \gamma_2 d}{\gamma_2 d} = -j \frac{\lambda}{2\pi d} \frac{\frac{E_{\min}}{E_{\max}} - j \tan \frac{2\pi x_0}{\lambda}}{1 - j \frac{E_{\min}}{E_{\max}} \tan \frac{2\pi x_0}{\lambda}},$$

where $\gamma_2 = \alpha_2 + j\beta_2$ is the propagation factor in the test medium, x_0 is the distance of the first minimum from the boundary surface, and λ is the wave length in air in the coaxial, or in the wave guide. The real part of the dielectric constant,

$$(4) \quad \epsilon' = \frac{\lambda_0^2}{\lambda_c^2} + \frac{\lambda_0^2}{4\pi^2} (\beta^2 - \alpha^2),$$

where λ_c is the cutoff wave length for the wave guide, and is infinity for the coaxial, and λ_0 is the wave length in free space corresponding to the given frequency. The absorption coefficient for the coaxial is $2\alpha_2$; for the wave guide it is also approximately $2\alpha_2$, but the more accurate value is

$$2\alpha_2 \frac{\beta_2 \lambda_0}{2\pi n},$$

where

$$(5) \quad n^2 = \frac{1}{2}(\epsilon' + \sqrt{\epsilon'^2 + \epsilon''^2}) \quad \text{and} \quad \epsilon'' = \alpha_2 \beta_2 \frac{\lambda_0^2}{\pi^2}$$

Equation (3) is not directly solvable. If it is written in the form $\frac{\tanh \gamma_2 d}{\gamma_2 d} = X + jY$, where X and Y are obtained from the data, then when $\alpha_2 d$ is large, so that $\tanh \alpha d \doteq 1$, the left hand side becomes $\frac{1}{\alpha_2 d + j\beta_2 d}$, and

$$\alpha_2 = \frac{X}{(X^2 + Y^2)d}, \quad \beta_2 = \frac{-Y}{(X^2 + Y^2)d}$$

The value for β_2 obtained is fairly accurate, but since X is small in this case and could not be as accurately determined, this was not so good a procedure for obtaining the absorption coefficient. When $\alpha_2 d$ is small, so that $\tanh \alpha_2 d \doteq \alpha_2 d$, and $\alpha_2 d^2 \tan \beta_2 d \ll \beta_2 d$, Equation (3) approximates to

$$\frac{\tan \beta_2 d}{\beta_2 d} = X + \frac{Y}{X} \left(Y + \frac{\alpha_2}{\beta_2} \right)$$

$$\alpha_2 d = \frac{VR.d}{X(1 - \beta_2 d \tan \beta_2 d) - 1}$$

Tables giving $\frac{\tan x}{x}$ for values of x are available in N.D.R.C. Contract OEMsr-191, Report IX, and are very convenient. If necessary an assumed value for $\frac{\alpha_2}{\beta_2}$ may be used in getting $\frac{\tan \beta_2 d}{\beta_2 d}$, and a further approximation made.

For intermediate cases, and in general in the checking of the accuracy of the solution, the forms

$$X = \frac{\alpha_2 d \sinh 2\alpha_2 d + \beta_2 d \sin 2\beta_2 d}{(\alpha_2^2 d^2 + \beta_2^2 d^2) (\cosh 2\alpha_2 d + \cos 2\beta_2 d)}$$

$$Y = \frac{\alpha_2 d \sin 2\beta_2 d - \beta_2 d \sinh 2\alpha_2 d}{(\alpha_2^2 d^2 + \beta_2^2 d^2) (\cosh 2\alpha_2 d + \cos 2\beta_2 d)}$$

given by Cripwell and Sutherland (6) were found convenient.

The standing wave ratio E_{\min}/E_{\max} could be determined to within 1%. The greatest experimental error lay in the determination of d for substances that were neither solid nor fluid and that could not be shaped accurately. The method used was to measure with a depth gauge the total depth of the terminal cup, and the distance to the top of the material. In some cases a piece of mica 0.02 mm. thick was placed on top of the sample material to provide a more definite base for measurement, but if surface irregularities are present, the mica position gives a maximum value of the depth. The value of d is used not only directly in Equation (3), but indirectly in getting x_0 . This quantity is found from observations on the position of the minimum with the cup empty, X' , and with the test material in place, X'' . Then $x_0 = X'' - d - X'$. In the experiments at λ 9.5 cm., individual readings were made to 0.05 mm. In those at λ 3.2 cm. the X'' and X' could be measured to 0.01 or 0.02 mm., but the uncertainty in the value of d for the materials used was of the order of 0.1 mm. or more, and this introduced a large proportional error in x_0 in the observations with muscle. The first minimum observable in the λ 3.2 cm. set-up was six wave lengths from the base of the cup, and any slight change in frequency made an observable change in the readings X'' and X' . The frequency meter was read immediately before and after the other observations; under good conditions the change during a run was not more than 0.2 Mc. per sec.

In order to make observations on water at λ 9.5 cm. a portion of the cup was closed by a piece of polystyrene. This procedure might have improved the accuracy of the determination of d at λ 3.2 cm.

Results and Discussion

The results for muscle, fat, bone, bone marrow, and water at or near room temperature are shown in Table I. The power absorption coefficient is, as stated earlier, the same as the quantity commonly designated 2α , and is given in double nepers per centimeter. In all cases material designated as beef was from refrigerated supply; frog muscle, rabbit fat, and cat bone marrow were from freshly killed animals. A large number of samples of muscle were used. The spread in values obtained includes errors in measurement and real differences between the samples greater than the experimental error. Especially at λ 3.2 cm., these differences seemed to follow differences in the amount of fluid in the sample. In a general way the two constants were slightly higher for beef muscle than for frog, but the difference was not greater

TABLE I

Material	Dielectric constant			Absorption coefficient		
	1.72 m.	9.5 cm.	3.2 cm.	1.72 m.	9.5 cm.	3.2 cm.
Muscle						
Beef	147 \pm 11	54 \pm 6	37.5 \pm 4	0.087 \pm 0.011	1.54 \pm 0.14	5 - 7
Frog	135 \pm 4		34.5 \pm 4	0.079 \pm 0.005		5 - 6
Fat						
Beef	9.5 \pm 2.2	3.44 \pm 0.05	3.5 \pm 0.3	0.026 \pm 0.005	0.15 \pm 0.02	0.79 \pm 0.06
Rabbit	23 \pm 1			0.036		
Bone	6.6 \pm 1		6.86	0.0028		0.56
Bone marrow						
Beef	20.5 \pm 1.5		3.7 \pm 0.1	0.028		0.9 \pm 0.1
Cat	52			0.068		
Water		72	63 \pm 2	0.0038	0.91	5 - 6

than the difference between individual samples of one kind. A few observations were made on liver at λ 3.2 cm. The results lay within the range for muscle. The experimental uncertainty in the determination of the absorption coefficient of muscle at λ 3.2 cm. was very large. The data suggested that the absorption was slightly greater than that for water, but this is not certain. The fat used was free from noticeable amounts of blood. The effect of the presence of this was marked, as shown by the results with one sample of rabbit fat that was tested, with the note "much connective tissue, looks very bloody". The ϵ was 43, and the absorption coefficient 0.05, both much larger than the values given in the table. Similar effects on the values obtained for bone marrow were noted.

Some observations were made on the effect of temperature on the values of the constants for muscle and fat at λ 1.72 m. The dielectric constant increased about one unit per 1° C. for both frog and beef muscle. The data on the absorption coefficient are less clear, but indicate an increase of 0.005 per 10° C. For fat no change was observed greater than the experimental error for a rise of temperature of 10° C.

From a comparison of the results at different wave lengths, it is evident that there is a larger proportional increase in the absorption by muscle than by fat in going from λ 1.72 m. to the microwave region. This means a large increase in the relative heating of muscle in a radiation field, but at the same time a reduction in penetration. Although there is large uncertainty in the values given for the absorption coefficient, it is safe to say that at a depth of $2\frac{1}{2}$ mm. the intensity of radiation at wave length 3.2 cm. will be reduced to one-quarter of its value at the surface, or that three-quarters of the energy entering such a material will be absorbed in this layer. The reduction in the dielectric constant is more marked for muscle, and this is important, as the amount of reflection from a surface is thereby reduced. It may be noted

that values for bone marrow are very similar to those for fat, except for the dielectric constant at λ 1.72 cm. The dielectric constant of bone appears to change little over the range covered, but the absorption is much greater at λ 3.2 cm.

Table II shows some results reported by others on the dielectric constant and absorption coefficient of comparable material. The values of 2α attri-

TABLE II
VALUES OF ϵ AND 2α BY DIFFERENT OBSERVERS

	λ	Muscle		Fat		Bone marrow		Bone	
		ϵ	2α	ϵ	2α	ϵ	2α	ϵ	2α
Schereschewsky (13)	1.2 - 2.8 m.	77.6		13.6					
Osswald (11)	3 m.	71	0.26	12	0.039	7.3	0.028		
Authors	1.7 m.	148	0.09	9.5	0.026	20	0.028		
		135	0.08	23	9.036	52	0.068		
Dakin and Works (7)	10 cm.	62.6	1.48				$\lambda 3$	6.98	0.516
Authors	9.5 cm.	54	1.54				cm.	6.86	0.562

buted to Osswald have been computed from the values given by him for the conductivity σ from the relation $2\alpha = \frac{120\pi\sigma}{n}$. The present values are repeated for comparison. The differences are not greater than could be attributed to differences in the material used except in the case of muscle at λ 1.72 cm. Partly because of this difference, the theory of the method used was re-examined, and corrections were applied to the equations used by earlier investigators as indicated. Sources of error other than those discussed earlier, and in the appendix, have not suggested themselves. The error due to the effect of the current in the thermocouple bridge when the circuit is not in resonance has not lent itself to mathematical correction, and another method for the observation of resonance would be preferable.

There were some cases observed at λ 1.72 m. where the properties of muscle seemed to change more than could be attributed to heating, and later a long study was made on a variety of samples. The result showed that the earlier observations were due to a slight change in the experimental conditions, and no change in properties was found that could not be accounted for by the heating of the material.

The measurements on water were not made with special care, but for comparison sake, and are included because of the general importance of this medium. A review of data on water was given by Kner (8) in 1937. Some of the values that have appeared since then are given in Table III, together

TABLE III
VALUES FOR WATER BY DIFFERENT OBSERVERS

	λ	ϵ	2α		λ	ϵ	2α
Slevogt (15)	246 cm. 58.3 10.4	81 81 78.4	0.00167 0.030 0.81	Abadie (2)	11 cm. 3	78 65	0.7 8.2
Bäz (3)	9.35 2.8	77.5 66.7	0.91 9.8	Collie, Ritson and Hasted (4)	10	77.4	0.93
Authors	172 9.5 3.2	72 63	0.0038 0.91 5 - 6	Roberts and von Hippel (12)	6	77	1.9

with the values obtained with the equipment here. The values ascribed to Abadie were taken from a graph, and, since no two of those quoted have used the same form in stating results, these have been reduced as shown.

In general the data reported should give a fairly good estimate of the relative amount of energy that would be absorbed by different layers of such biological material if one knows the thickness and general composition. It does not appear to the authors that it would be of much value to try to improve on the measurements, because of such big differences in tissues of one type, and because in the microwave region absorption by individual ingredients is so masked by the strong absorption of water; on the other hand, similar measurements of the properties of the separate ingredients might produce interesting results.

Note

After this report was written, a note by T. S. England and N. A. Sharples on "Dielectric Properties of the Human Body in the Microwave Region of the Spectrum" appeared in *Nature* of March 26th. The results are given in the form of data on α and β as obtained from the propagation factor in the wave guide for a wave length 3.18 cm. Table IV shows their results and the present ones at λ 3.2 cm. for comparable material.

TABLE IV

Material	England and Sharples		Authors	
	α	β	α	β
Muscle	2.5 - 2.7	11.6 - 11.7	2.5 - 3.3	10.8 - 12.5
Fat	0.44 - 0.49	4.0	0.37 - 0.42	3.5 - 4.2
Bone	0.56	5.4	0.29 - 0.30	5.0
Bone marrow	0.79	5.1	0.33 - 0.51	3.5 - 3.7

On the whole the results suggest that animal tissue, even when from refrigeration, not frozen, has very much the same properties as the comparable human tissue. It was realized that the samples of bone used here had air-dried for several days, and this measurement has been repeated here with a fresh sample, giving $\alpha = 0.48$ $\beta = 5.4$. It was possible to add a measurement on samples of baby mice skin, and values of $\alpha = 2.4$ and 2.5 and of $\beta = 11.1$ and 13 were found, of the same order as those reported in *Nature*.

It was noted that this skin was less than 1 mm. thick, and that there are parts of the human body where the skin is thin, and to which the comment on the absorption in skin would not apply. It has been suggested elsewhere that a technique of irradiating a tissue for short intervals would avoid the undue heating of general tissue, if it should appear that any particular frequency has a desirable selective effect on some special ingredient.

Acknowledgments

We are greatly indebted to Dr. Helen Battle of the Department of Zoology for providing the prepared fresh material used, and for her unfailing kindness in giving information on biological questions. The work at λ 9.5 cm. and most of that at λ 1.72 m. was done during 1946-47 by the junior author on a grant from the Ontario Cancer Research Foundation, which has also supplied funds for some technical assistance and equipment. We wish to thank Dr. R. C. Dearle for the use of space and the facilities of the Department of Physics and for his interest in the progress of the research at a time when there were so many demands on both.

References

1. ABADIE, P. *Onde Elect.* 69 : 247. 1937.
2. ABADIE, P. *Trans. Faraday Soc.* 42A : 143. 1946.
3. BÄZ, G. *Physik. Z.* 40 : 394. 1939.
4. COLLIE, C. H., RITSON, D. M., and HASTED, J. B. *Trans. Faraday Soc.* 42A : 129. 1946.
5. COOLEGE, W. D. *Ann. Physik*, 69 : 125. 1899.
6. CRIPWELL, F. J. and SUTHERLAND, G. B. B. M. *Trans. Faraday Soc.* 42A : 149. 1946.
7. DAKIN, T. W. and WORKS, C. N. *J. Applied Phys.* 18 : 789. 1947.
8. KNER, H. W. *Phys. Rev.* 52 : 1054. 1937.
9. McLENNAN, J. C. and BURTON, A. C. *Can. J. Research*, 3 : 224. 1930.
10. McLENNAN, J. C. and BURTON, A. C. *Can. J. Research*, 5 : 550. 1931.
11. OSSWALD, K. *Hochfrequenztech. Elektroakust.* 49 : 40. 1937.
12. ROBERTS, S. and VON HIPPEL, A. *J. Applied Phys.* 17 : 610. 1946.
13. SCHERESCHESKY, J. W. *U.S. Pub. Health Service. Pub. Health Repts.* 48 : 844. 1933.
14. SLÄTIS, H. *Ann. Physik*, 36 : 397. 1939.
15. SLEVOGT, K. *Ann. Physik*, 36 : 141. 1939.

APPENDIX

The circuit as used at 1.7 m. was taken as equivalent to that in Fig. 4, where B' is a sliding bridge of zero impedance, and B a fixed bridge. At A

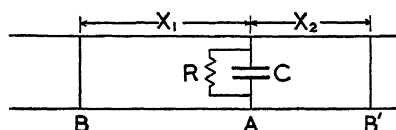


FIG. 4.

the impedance is composed of R , $\frac{1}{j\omega C}$, and $Z \tanh \gamma x_2$ in parallel, where Z is the characteristic line impedance, and $\gamma = \alpha + j\beta$ is the propagation constant. Using the value obtained thus as the terminal impedance of the section BA , the input impedance at B is found,

$$Z_B = Z \frac{1 + \tanh \gamma x_1 \left(\frac{Z}{R} + \coth \gamma x_2 + j\omega CZ_1 \right)}{\tanh \gamma x_1 + \frac{Z}{R} + \coth \gamma x_2 + j\omega CZ_1}.$$

If the effective P.D. across the line at B is constant, the mean square current flowing in the line at B , and hence the thermocouple response in B , will be proportional to

$$\left| \frac{Z}{Z_B} \right|^2 = U.$$

Neglecting terms beyond the first order in α ($\alpha \gg 4.1 \times 10^{-5} \text{ cm.}^{-1}$) one finds

$$(6) \quad U = \frac{(1 + \omega CZ_1 \cot \theta_1 - \cot \theta_1 \cot \theta_2)^2 + \frac{Z^2}{R^2} \cot^2 \theta_1 + \frac{2\alpha Z}{R} \left(\frac{x_1}{\sin^2 \theta_1} + \frac{x_2 \cot^2 \theta_1}{\sin^2 \theta_2} \right)}{(\cot \theta_1 + \cot \theta_2 - \omega CZ)^2 + \left(\frac{Z}{R} + \frac{\alpha x_1}{\sin^2 \theta_1} + \frac{\alpha x_2}{\sin^2 \theta_2} \right)^2},$$

where $\theta_1 = \beta x_1$, $\theta_2 = \beta x_2$. In this expression for U , x_2 or θ_2 is the only variable and the condition for a maximum may be found from $\frac{\delta U}{\delta x_2} = 0$.

Writing $\cot \theta_1 + \cot \theta_2 - \omega CZ = A$, this yields

$$\begin{aligned} \cot \theta_1 \left(A^2 - A \frac{1 + \cot^2 \theta_1}{\cot \theta_1} - \frac{Z^2}{R^2} \right) + A \frac{2\alpha Z}{R} \left[x_1 \left(\cot^2 \theta_1 - 1 \right) \right. \\ \left. + \cot \theta_1 \left(2x_2 \cot \theta_2 - \frac{1}{\beta} \right) \right] \\ - \frac{2\alpha Z}{R} \cot \theta_1 \left(\frac{x_1}{\sin^2 \theta_1} + \frac{x_2}{\sin^2 \theta_2} \right) - \frac{\alpha Z}{R} \left(1 + \cot^2 \theta_1 \right) \left(2x_2 \cot \theta_2 - \frac{1}{\beta} \right) = 0. \end{aligned}$$

In all cases met with, the coefficient of A in the second term is much less than that in the first term, and may be neglected. Dividing through by $\cot \theta_1$ one may then write

$$(7) \quad A^2 - A \frac{1 + \cot^2 \theta_1}{\cot \theta_1} - \Delta = 0,$$

where

$$\Delta = \frac{Z^2}{R^2} + \frac{2\alpha Z}{R} \left(\frac{x_1}{\sin^2 \theta_1} + \frac{x_2}{\sin^2 \theta_2} \right) + \frac{\alpha Z}{R} \left(\cot \theta_1 + \tan \theta_1 \right) \left(2x_2 \cot \theta_2 - \frac{1}{\beta} \right).$$

Since $\frac{1 + \cot^2 \theta_1}{\cot \theta_1} \ll 2$, and becomes infinite for $x_1 = \frac{\lambda}{4}$, while Δ is always small, < 0.02 in the present experiments except for muscle, where it may be as much as 0.2, the approximate solution of Equation (7) may be used,

$A = -\Delta \frac{\cot \theta_1}{1 + \cot^2 \theta_1}$, and except for materials of relatively high conductivity A may be put equal to zero. The equation

$$(8) \quad \omega CZ = \cot \theta_1 + \cot \theta_2 - A$$

yields the capacity C , and hence the dielectric constant.

To obtain an expression for the absorption index κ , returning to Equation (6) one has

$$U_{\max} = \frac{[1 + \cot \theta_1(\cot \theta_1 - A)]^2 + \frac{Z^2}{R^2} \cot^2 \theta_1 + \frac{2\alpha Z}{R} \left(\frac{x_1}{\sin^2 \theta_1} + \frac{x_2 \cot^2 \theta_1}{\sin^2 \theta_2} \right)}{\left(\frac{Z}{R} + \frac{\alpha x_1}{\sin^2 \theta_1} + \frac{\alpha x_2}{\sin^2 \theta_2} \right)^2 + A^2},$$

which for the case of no container present, $R = \infty$, $A = 0$ becomes

$$\left(\frac{2}{\alpha \lambda} \right)^2 = \left(\frac{2}{\delta} \right)^2.$$

In the numerator the last term is always negligible in comparison with the first, and in both numerator and denominator the second term is small in comparison with the first. Hence, if the maximum galvanometer deflections are called G_1 and G_2

$$(9) \quad \sqrt{\frac{G_1}{G_2}} = \frac{2}{\delta} \cdot \frac{\frac{Z}{R} + \frac{\alpha x_1}{\sin^2 \theta_1} + \frac{\alpha x_2}{\sin^2 \theta_2} + \frac{1}{2} A^2 / \left(\frac{Z}{R} + \frac{\alpha x_1}{\sin^2 \theta_1} + \frac{\alpha x_2}{\sin^2 \theta_2} \right)}{1 + \cot \theta_1(\cot \theta_1 - A) + \frac{1}{2} \frac{Z^2}{R^2} \cot^2 \theta_1 / [1 + \cot \theta_1(\cot \theta_1 - A)]}$$

$$= \frac{2}{\delta} \frac{\frac{Z}{R} + \frac{\alpha x_1}{\sin^2 \theta_1} + \frac{\alpha x_2}{\sin^2 \theta_2} + D_1}{1 + \cot^2 \theta_1 + D_2},$$

where D_1 and D_2 are small corrections.

From general electromagnetic theory $\sigma = \frac{n^2 \kappa}{30\lambda}$, and $\epsilon = n^2(1 - \kappa^2)$, where κ is the index of absorption defined by Drude; also $\frac{1}{R} = 4\pi C_0 \sigma$, where C_0 is the internal capacity of the empty container in e.s.u., it being assumed that the electric field in the container has the same form in all cases.

Hence

$$\begin{aligned}\frac{Z}{R} &= \frac{\cot \theta_1 + \cot \theta_2 - A}{\omega C_{\text{farad}}} \frac{4\pi n^2 \kappa C_0}{30\lambda} \\ &= \frac{\cot \theta_1 + \cot \theta_2 - A}{C' + \epsilon C_0} \cdot \frac{2\kappa \epsilon C_0}{1 - \kappa^2},\end{aligned}$$

where $C' + \epsilon C_0$ is the total capacity of the container filled with the medium of dielectric constant ϵ .

Inserting this value of $\frac{Z}{R}$ in Equation (9) and rearranging, one finds

$$(10) \quad \frac{4\kappa}{1 - \kappa^2} = \frac{C' + \epsilon C_0}{\epsilon C_0} \frac{\delta}{\cot \theta_1 + \cot \theta_2 - A} \left[(1 + \cot^2 \theta_1 + D_2) \sqrt{\frac{G_1}{G_2}} - \frac{2}{\lambda} \left(\frac{x_1}{\sin^2 \theta_1} + \frac{x_2}{\sin^2 \theta_2} \right) - \frac{2D_1}{\delta} \right].$$

This gives κ , and, except where $n^2 \kappa$ is large, A , D_1 , and D_2 may be omitted as in Equation (2).

A NEW HIGH LIGHT GATHERING POWER SPECTROGRAPH FOR AURORAL STUDIES¹

BY W. PETRIE

Abstract

The optics of the spectrograph consist of two f 2.5, 12 in. aircraft camera lenses, and a 15,000 lines per inch plane grating with ruled surface 4 in. by 4 in. The grating concentrates light in the second order spectrum; the dispersion in this order for normal incidence is 22 Å per mm. A few spectra were obtained during the spring of 1949, and the results appear to be most promising. These spectra include several interesting features, one of which is a strong radiation of wave length 4320 Å in the second order. This radiation is likely to be an intense first order infrared feature.

Introduction

There is still great need for moderate dispersion spectrograms of the aurora if we are to make full use of this phenomenon in interpreting physical conditions in the upper atmosphere. Little is known regarding the near infrared region of the spectrum, and it is especially important that we determine the intensities of numerous faint features that have been attributed to atomic oxygen and nitrogen in several stages of ionization. It is hoped that information on these and other problems will be obtained with a new spectrograph constructed at the University of Saskatchewan.

Description of the Instrument

Two aircraft camera units were purchased from U.S. War Assets. The camera lenses, film holders, and camera back are all used in the spectrograph. The lenses are 7-element, f 2.5, 12 in. focal length Ektar lenses manufactured by the Eastman Kodak Co. One lens is used as collimator and covers a section of the sky that subtends an angle of approximately 22° at the camera. All inner air-glass surfaces in these lenses are coated with a nonreflecting film that minimizes the loss of light by reflection and prevents the formation of "ghost" images of appreciable intensity. According to the literature (1), the focal plane shift for a lens of this type is approximately 0.01 mm. per 1° C. change in temperature. The few observations made to date suggest that thermostatic control of the instrument will not be necessary.

The dispersing element is a plane grating obtained from Johns Hopkins University. The ruled surface is 4 in. by 4 in., there are 15,000 lines per in., and the light is concentrated in the second order spectrum. The grating and camera lens produce a second order dispersion for normal incidence of 22 Å per mm.

The spectrograph components are mounted on an aluminum base plate and surrounded with a three ply plywood housing. The lid may be removed,

¹ Manuscript received August 9, 1949.

Contribution from the Department of Physics, University of Saskatchewan, Saskatoon, Sask.

and a 5 in. by 10 in. opening is provided on one side for loading and removing the plate holder. A 5 in. diameter circular section is cut out of an adjacent side of the housing, so that the slit and mounting may be exposed to the night sky. Both these openings can be covered from the outside by tin slides. The interior of the housing is painted black, and suitable baffles are provided to shield the optical components and the photographic plate from the regions of the first and third order spectra which are not incident on the camera lens.

A shutter mounted behind the slit may be opened and closed at specified times by the use of an electric time clock. This device makes possible the operation of the spectrograph during an auroral display without the presence of an operator.

In order that the instrument may readily be pointed at different regions of the sky, the spectrograph box is clamped to a stand in such a way that the altitude of the instrument may be varied from 0° to 90° . The stand is fitted with castors and sits on an 8 ft. by 8 ft. wooden platform on the roof of the Physics Building. This arrangement enables the stand to be turned to any direction. Figs. 1 and 2 illustrate the interior and mounting of the spectrograph.

Auroral Spectrograms Obtained with the Instrument

The spectrograph was used for the first time during the night of February 21, 1949. On this date, an intense auroral display was observed at Saskatoon (2). A four hour exposure yielded a spectrogram that showed 18 measurable features, and a number of lines or bands too weak for wave length measurement. Six other spectrograms were obtained between February 24 and April 1, but none of these were as dense as the first spectrogram secured on February 21. A list of the more intense lines and bands present in the strongest spectrogram is given in Table I.

TABLE I

Wave length, I.A.	Identification	Wave length, I.A.	Identification
3805	N ₂ , 2 P.G.	5577	OI, $^1D_2 - ^1S_0$
3915	N ₂ , N.G.	5675	?
4278	N ₂ , N.G.	5867	N ₂ , 1 P.G.
4320	?	5993	N ₂ , 1 P.G.
4652	N ₂ , N.G.	6300	OI, $^3P_2 - ^1D_2$
4709	N ₂ , N.G.	6364	OI, $^3P_1 - ^1D_2$
4861	H β	6563	H α
4992	?	6676	?
5202-5278	?	6753	?

The most interesting feature of these spectra is the appearance of a relatively strong radiation at a wave length of 4320 Å. This radiation is about as intense as the nitrogen band at λ 4709, and does not correspond to any line or band given in Vegard's tables (3) of auroral wave lengths. The writer is of the

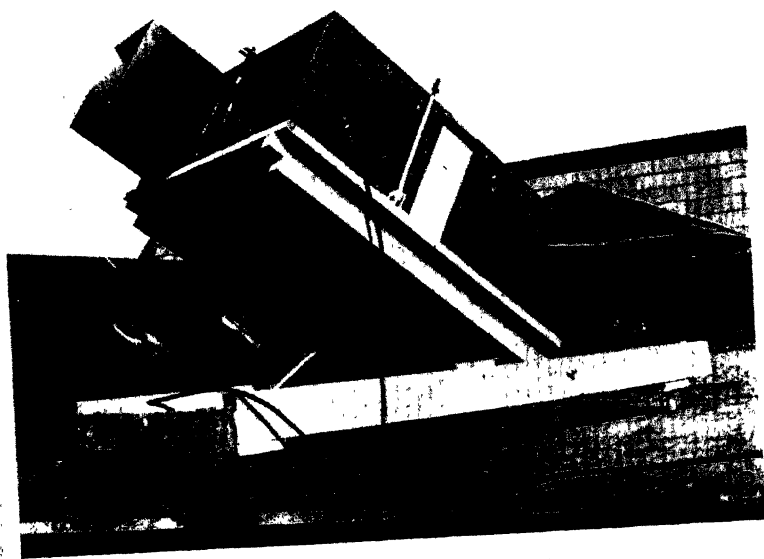
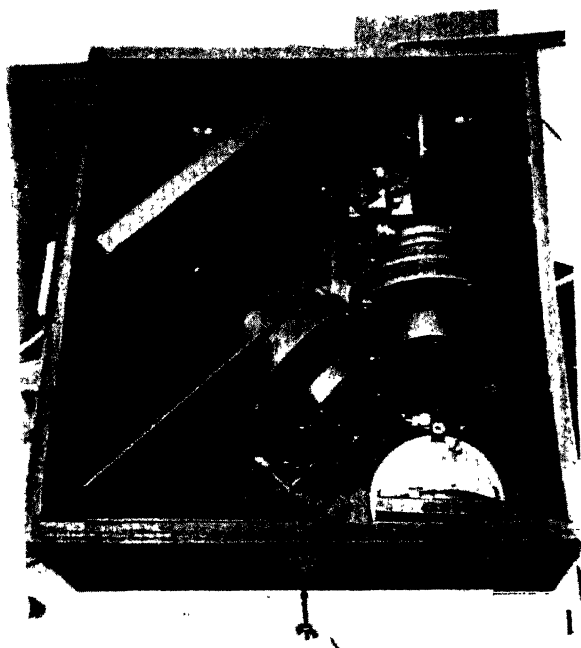


FIG. 1. *The interior of the spectrograph.*

FIG. 2. *The mounting of the spectrograph.*

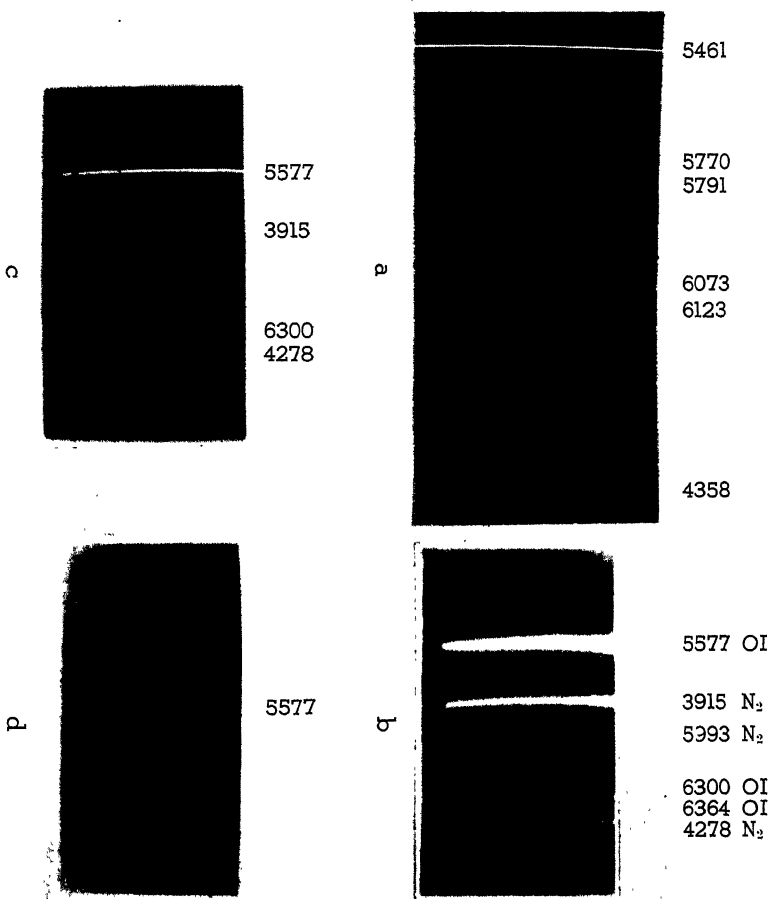


Fig. 3. (a) The mercury arc spectrum photographed with the new instrument.
 (b) Aurora, February 21, 1949. Exposure, four hours; slit, 1 mm.
 (c) Aurora, March 1, 1949. Exposure, four hours; slit, 0.25 mm.
 (d) Aurora, March 2, 1949. Exposure, 15 min.; slit, 0.25 mm.

opinion that this feature of unknown origin belongs to the first order infrared spectrum. It is our intention to obtain second order infrared auroral spectra about which little is known.

It is well to note that the first two members of the hydrogen Balmer series appear in the February 21 spectrogram. Also present are several features about whose origin the writer is undecided. A stronger spectrogram is needed before the identification of these features can be reasonably certain. Fig. 3 is a reproduction of parts of several auroral spectrograms taken with the new instrument.

The results obtained to date appear to be promising, and the instrument will be used chiefly to secure infrared spectra of the aurora. This region of the spectrum has not been examined in any detail and much remains to be done. All future plates will be calibrated with a step sector disk so that line intensities may be obtained.

Acknowledgment

The construction and operation of this instrument has been supported by a grant from the National Research Council of Canada.

References

1. KINGSLAKE, R. J. *Optical Soc. Am.* 37 : 1. 1947.
2. PETRIE, W., FORSYTH, P. A., and McCONECHY, E. *Nature*, 163 : 774. 1949.
3. VEGARD, L. and KVIFTE, G. *Geofys. Publikasjoner Norske Videnskaps-Akad. Oslo*, 16 (7) : 13. 1945.

SECTION A
INDEX TO VOLUME 27

Authors

- Armstrong, L. D.** and Grayson-Smith, H.—Specific heats of manganese and bismuth at liquid hydrogen temperatures, 9.
- Arnell, J. C.**—Permeability studies. IV. Surface area measurements of zinc oxide and potassium chloride powders, 207.
- Baird, K. M.**—Veiling glare in aerial photography, 130.
- Beals, C. S.** and Burland, M. S.—Wave lengths, equivalent widths, and line profiles in the spectrum of the star H.D. 190073, 169.
- Bunemann, O.**, Cranshaw, T. E., and Harvey, J. A.—Design of grid ionization chambers, 191.
- Burland, M. S.**—See Beals, C. S.
- Chien, W. Z.**, Infeld, L., Pounder, J. R., Stevenson, A. F., and Synge, J. L.—Contributions to the theory of wave guides, 69.
- Cranshaw, T. E.**—See Bunemann, O.
- Crawford, M. F.**, and Levinson, J.—The nuclear moments of P^{31} , 156.
- Currie, B. W.**—See Pearce, D.C.; Penn, W. D.
- Dolan, P. A.**—See Petrie, W.
- Ferguson, K.**—See Laird, E. R.
- Grayson-Smith, H.**—See Armstrong, L. D.
- Hart, K. H.**—See Langstroth, G. O.
- Harvey, J. A.**—See Bunemann, O.
- Infeld, L.**—See Chien, W. Z.
- Katz, L.**, Leverton, W. F., and Woods, S. B.—The resonance method of measuring the ratio of the specific heats of a gas C_p/C_v . VI. Carbon dioxide, nitrous oxide, and methane, 39.
- , Woods, S. B., and Leverton, W. F.—The resonance method of measuring the ratio of the specific heats of a gas C_p/C_v . V. Section A: An improved apparatus for measuring the ratio of the specific heats of a gas. Section B: The use of electronic counter circuits to measure low frequencies and a variable low frequency oscillator, 27.
- Laird, E. R.** and Ferguson, K.—Dielectric properties of some animal tissues at meter and centimeter wave lengths, 218.
- Langstroth, G. O.** and Hart, K. H.—The specific heat of Napalm-gasoline gels, 151.
- Leverton, W. F.**—See Katz, L.
- Levinson, J.**—See Crawford, M. F.
- McKinley, D. W. R.** and Millman, P. M.—Determination of the elements of meteor paths from radar observations, 53.
- Mann, K. C.** and Ozeroff, M. J.—The gamma rays of radium (B + C), 164.
- Millman, P. M.**—See McKinley, D. W. R.

Monaghan, P. A.—See Petrie, W.

Ozeroff, M. J.—See Mann, K. C.

Pearce, D. C. and Currie, B. W.—Some qualitative results on the electrification of snow, 1.

Penn, W. D. and Currie, B. W.—A recording meter for auroral radiations, 45.

Pepper, T. P.—Relative yields of the D-D reactions at low energies, 143.

Petrie, W.—A new high light gathering power spectrograph for auroral studies, 231.

———, Monaghan, P. A., and Dolan, P. A.—The spectrum of atomic oxygen in a high current a-c. discharge, 213.

Pounder, J. R.—See Chien, W. Z.

Stanley, J. P.—On the numerical calculation of the internal conversion in the *K*-shell—The electric dipole case, 17.

Stevenson, A. F.—See Chien, W. Z.

Synge, J. L.—See Chien, W. Z.

Woods, S. B.—See Katz, L.

SECTION A

INDEX TO VOLUME 27

Subjects

- Absorption coefficients** and dielectric constants of some animal tissues at meter and centimeter wave lengths, 218.
- A-c. discharge**, See Alternating current discharge.
- Aerial photography**, Veiling glare in, 130.
- Alternating current discharge**, High current, Spectrum of atomic oxygen in, 213.
- Animal tissues**, Dielectric constants and absorption coefficients of some, at meter and centimeter wave lengths, 218.
- Antennae**, See under Wave guides.
- Apparatus** for measuring ratio of specific heats, C_p/C_v , of a gas, Improved, 27.
- Area**, See Surface area measurements.
- Atomic oxygen**, Spectrum of, in a high current a-c. discharge, 213.
- Aurora**, Studies of, A new high light gathering power spectrograph for, 231.
See also Auroral radiations.
- Auroral radiations**, Recording meter for, 45.
See also Aurora.
- Bismuth** and manganese, Specific heats of, at liquid hydrogen temperatures, 9.
- Carbon dioxide**, Measurement of ratio of specific heats of, See "Resonance method" under Specific heats.
- Chambers**, Grid ionization, Design of, 191.
- Circuits**, Electronic counter, Use of, to measure low frequencies, 27.
- Counter circuits**, Electronic, Use of, to measure low frequencies, 27.
- D-D reactions**, Relative yields of, at low energies, 143.
- Deuterium**, See D-D reactions.
- Dielectric constants** and absorption coefficients of some animal tissues at meter and centimeter wave lengths, 218.
- Dipole**, See Electric dipole.
- Discharge**, See Alternating current discharge.
- Electric dipole**
On the numerical calculation of the internal conversion in the K-shell—the electric dipole case, 17.
- Electrification of snow**, Some qualitative results on, 1.
- Electronic counter circuits**, to measure low frequencies, Use of, 27.
- Electrons in K-shell**, on the numerical calculation of the internal conversion coefficient (electric dipole case) for, 17.
- K-electrons**, See Electrons.
- Elements of meteor paths**, Determination of, from radar observations, 53.
- Energy**, Relative yields of the D-D reactions at low, 143.
- Equivalent widths and line profiles** in the spectrum of the Star H.D. 190073, Wave lengths and, 169.
- Frequency**, Low, use of electronic counter circuits to measure, and a variable low frequency oscillator, 27.
- Gamma rays** of radium (B + C), 164.
- Gas**, Measurement of ratio of specific heats of a, See "Resonance method" under Specific heats.
- Gasoline-Napalm gels**, Specific heat of, 151.
- Gels**, Napalm-gasoline, Specific heat of, 151.
- Glare**, Veiling, in aerial photography, 130.
- Grid ionization chambers**, Design of, 191.
- Heat**, See Specific heat, Heat capacity, Temperature.
- Heat capacity** of gasoline, Napalm, and Napalm-gasoline gels, 151.

Hulme's formula internal conversion of γ -radiation, Simplified, Use of, in calculation of internal conversion coefficient in the electric dipole case for electrons in K-shell, 17.

Impedance, See under Wave guides.

Internal conversion in the K-shell, On the numerical calculation of, the electric dipole case, 17.

Internal conversion coefficient in electric dipole case for electrons in the K-shell, 17.

Internal conversion of γ -radiation, 17.

Ionization chambers, Grid, Design of, 191.

K-Electrons, See K-Shell.

K-Shell, Electrons in, Calculation of internal conversion coefficient (electric dipole case) for, 17.

Light, A new high light gathering power spectrograph for auroral studies, 231.

Line profiles in the spectrum of the star H.D. 190073, Wave lengths, equivalent widths, and, 169.

Manganese and bismuth, Specific heats of, at liquid hydrogen temperatures, 9.

Meteor paths, Elements of, Determination of, from radar observations, 53.

Meter, See Recording meter.

Methane, Measurement of ratio of specific heats of, See "Resonance method" under Specific heats.

Moments, Nuclear, of P^{31} , 156.

Napalm-gasoline gels, Specific heat of, 151.

Nitrous oxide, Measurement of ratio of specific heats of, See "Resonance method" under Specific heats.

Nuclear moments of P^{31} , 156.

Oscillators, Variable low frequency, Use of, in measurement of ratio of specific heats of a gas, 27.

Oxygen, Atomic, Spectrum of, in a high current a-c. discharge, 213.

P^{31} , Nuclear moments of, 156.

Permeability studies

IV. Surface area measurements of zinc oxide and potassium chloride powders, 207.

Phosphorus 31, Nuclear moments of, 156.

Photography, Aerial, Veiling glare in, 130.

Potassium chloride and zinc oxide powders, Surface area measurements of, 207.

Powders, Zinc oxide and potassium chloride, Surface area measurements of, 207.

Profiles, Line, in the spectrum of the star H.D. 190073, Wave lengths, equivalent widths, and, 169.

Radar observations, Determination of the elements of meteor paths from, 53.

Radiation

Auroral, Recording meter for, 45.

γ -, Internal conversion of, 17
See under Wave guides.

Radium (B + C), Gamma rays of, 164.

γ -Rays, See Gamma rays.

Reactions, D-D, Relative yields of, at low energies, 143.

Recording meter for auroral radiations, 45.

Resonance method for measuring ratio of specific heats of a gas. See under Specific heats.

K-Shell, Electrons in, Calculation of internal conversion coefficient (electric dipole case) for, 17.

Snow, Electrification of, Some qualitative results on, 1.

Specific heat of Napalm-gasoline gels, 151.

Specific heats

of manganese and bismuth at liquid hydrogen temperatures, 9.

Resonance method of measuring ratio of, of a gas, C_p/C_v ,

V. A: An improved apparatus for measuring the ratio of the specific heats of a gas. B: The use of electronic counter circuits to measure low frequencies and a variable low frequency oscillator, 27.

VI. Carbon dioxide, nitrous oxide, and methane, 39.

Spectrograph, A new high light gathering power spectrograph for auroral studies 231.

Spectrum

of atomic oxygen in a high current a-c. discharge, 213.

of the star H.D. 190073, Wave lengths, equivalent widths, and line profiles in the, 169.

Star H.D. 190073, Spectrum of, Wave lengths, equivalent widths, and line profiles in, 169.

Surface area measurements of zinc oxide and potassium chloride powders, 207.

Temperature

Specific heat of manganese and bismuth at liquid hydrogen temperatures, 9.

Theory of wave guides, See under Wave guides.

Tissues, See Animal tissues.

Veiling glare, in aerial photography, 130.

Wave guides, Contributions to the theory of, 69.

I. Radiation from a source inside a perfectly conducting wave guide of rectangular section, 70.

II. A general method for calculating the impedance of an antenna in a wave guide of arbitrary cross section, 91.

III. The resistance of antennae of various shapes and positions in rectangular and circular wave guides, 100.

IV. The impedance of a rectangular wave guide with a thin antenna, 109.

Wave lengths

equivalent widths, and line profiles in the spectrum of the star H.D. 190073, 169.

Meter and centimeter, Dielectric properties of some animal tissues at, 218.

Yields, Relative, of the D-D reactions at low energies, 143.

Zinc oxide and potassium chloride powders, Surface area measurements of, 207.

INDIAN AGRICULTURAL RESEARCH
INSTITUTE LIBRARY, NEW DELHI.

[illegible]

GIPNLK-H-40 I.A.R.I.-29-4- 5-15,000

